Solidification orientation relationships in Al and Mg alloys

Yi Cui

Department of Materials

Imperial College London

Submitted in part fulfilment of the requirements for the degree of Doctor of Philosophy at Imperial College London, November 2020

Abstract

This thesis explores solidification orientation relationships (ORs) in intermetallic compounds (IMCs) and Al and Mg alloys.

In the Al_3Ti-TiB_2 system, it is found that the nucleation of Al_3Ti on TiB_2 and the pushing and engulfment of TiB_2 particles by growing Al_3Ti crystals both form reproducible ORs during solidification. The nucleation OR is identified by solidifying multiple small Al_3Ti crystals on one large (0001) facet of TiB_2. Pushing and engulfment ORs are investigated by statistical analysis of EBSD measurements, DFT calculations of interface energies, and imaging of TiB_2 particles being pushed and engulfed by Al_3Ti facets. It is shown that the lowest energy OR is formed by nucleation as well as by pushing/engulfment. The higher energy ORs, formed by pushing and engulfment, correspond to local interfacial energy minima and can be explained by rotation of TiB_2 particles on Al_3Ti facets during pushing.

ORs formed by cyclic twinning of low symmetry IMCs is studied in Al_3Ti, Ag_3Sn, $Al_{45}Cr_7$ and $Al_{13}Fe_4$. It is argued that deeper undercooling induced by higher cooling rate favours the nucleation of metastable phases and/or the formation of short-range order with high symmetry in the melt, which then nucleated/transformed into stable phases with all orientation variants to the higher-symmetry parent phases.

This thesis then applies the new understanding developed in the previous chapters to explore the formation mechanism for the above-random proportion of special grain boundaries in FCC-Al and HCP-Mg after equiaxed solidification. Two main mechanisms are examined and, by combining statistical EBSD analysis and DFT calculations, it is found that the measured preferred grain boundaries with twin ORs correspond to local interfacial energy minima and, for the alloy systems studied here, it is likely due to the rotation and movement between neighbouring grains during solidification instead of nucleation from icosahedral quasicrystals and/or icosahedral short-range order.

Contents

List of Tables

List of Figures

Declaration of originality

I, Yi Cui, hereby declare that this thesis and associated research are my own work and that all sources I have used or quoted have been indicated and acknowledged by means of complete referencing.

Parts of this thesis have been published in:

Cui, Y., King, D. J. M., Horsfield, A. P., & Gourlay, C. M. (2020). Solidification orientation relationships between Al3Ti and TiB2. *Acta Materialia*, *186*, 149-161.

Copyright declaration

Acknowledgements

First of all, I would like to thank my supervisor Prof. Christopher M. Gourlay for his kind help throughout this project and I also very much appreciate his financial support during the rest of my PhD time after the CSC-imperial scholarship finished. I also would like to thank Prof. Andrew Horsfield, Dr. Daniel J M King, Dr. Sergey A. Belyakov, Dr. Jingwei Xian, Dr. Mahmoud Ardakani, and all our group members for their generous help, valuable ideas, and discussions. Finally, I would like to thank my family members and good friends for their constant support, consideration, and understanding.

Chapter 1 Introduction

1.1 Background and industrial motivation

Aluminium and magnesium are two of the lightest structural metals with large abundance in the Earth's crust, being the third most abundant element for aluminium (8.3%) and seventh for magnesium (2.4%) [1]. Aluminium alloys are widely used in aerospace, automotive, and construction industries due to their low density, low price, high corrosion resistance and high castability and formability, while magnesium alloys are mainly used as cast alloys for automotive components because of its light weight, excellent machinability and good strength-to-weight ratio. However, compared to Al alloys, low-cost Mg alloys are restricted by a number of limitations including low tensile properties (strength and ductility) and poor workability. High strength Mg alloys exist but are currently confined to military and aerospace applications due to their high cost.

To improve the processability and mechanical properties of Al and Mg products, grain refinement has become one of the most important techniques in the past century [2-5]. Whilst effective grain refiners are available for many Al alloys (e.g. Al-Ti-B, as shown in Figure 1.1 [6]) and Mg alloys that do not contain Al (e.g. Zr [7]), there remain various alloys that cannot be grain refined effectively on an industrial scale and, for these, new understanding of the fundamentals of heterogeneous nucleation and grain refinement are required. Alloy systems that would benefit from such an improved understanding include Al-Si-based [8-10] and Mg-Al-based [11, 12] alloys that make up a majority percentage of shape cast light alloys.

Moreover, new approaches to grain refinement that do not require the addition of hard embrittling compounds (e.g. TiB_2) would be welcome in industries requiring the highest performance (e.g. the aerospace industry). Similarly, industries using rolled or extruded Al or Mg alloys for aesthetic parts (e.g. smartphone and laptop covers) would prefer not to use hard TiB_2 particles (or similar) which can give a poor surface finish.

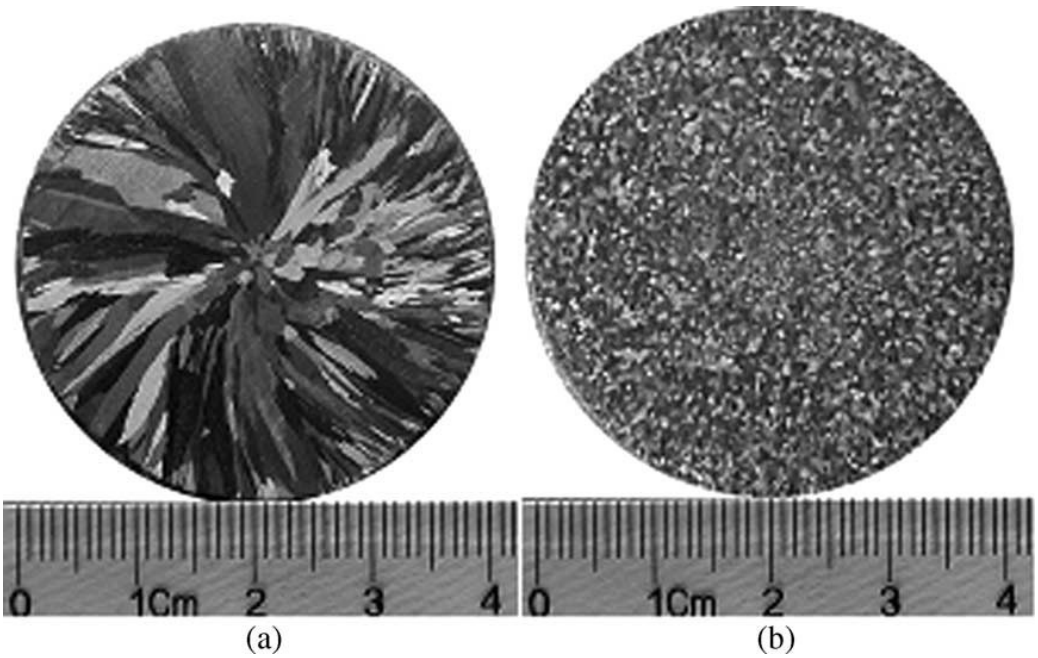

Figure 1.1 Microstructure of (a) commercial purity Al and (b) commercial purity Al grain refined by 0.2 wt.% Al-5Ti-1B master alloy. From Ref.[6]

Controlling the morphology of primary intermetallic compounds (IMCs) in recycled light alloys is another approach to improve the mechanical properties. A key reason why recycled Al alloys are not used more widely is the presence of coarse brittle IMCs due to impurity elements such as Fe [13-15]. It is not economical to reduce the impurity level [16], so there is a need to manipulate the size and shape of these IMCs to improve the tensile ductility and fatigue life of final products [17-19]. Figure 1.2 overviews some examples: Al-7Si-0.4Mg (wt.%) contaminated with 0.7wt%Fe solidifies to contain large brittle β-Al_5SiFe plates in (a) [20]. With the dilute addition of Mn, these become less embrittling α-$Al_{15}(Mn,Fe)_3Si_2$ IMCs in (b) [21], which significantly improves fatigue life. This is a low-cost approach manipulating phase equilibria and phase transformations during solidification. An alternative approach is to break-up large brittle IMCs by post-solidification deformation processing. In (c) and (e), $Al_{13}Fe_4$ and $Al_{13}Cr_2$ (also known as $Al_{45}Cr_7$) respectively, can be made much smaller by hot extrusion in (c) and (f) [22], although this is not applicable to shape cast parts.

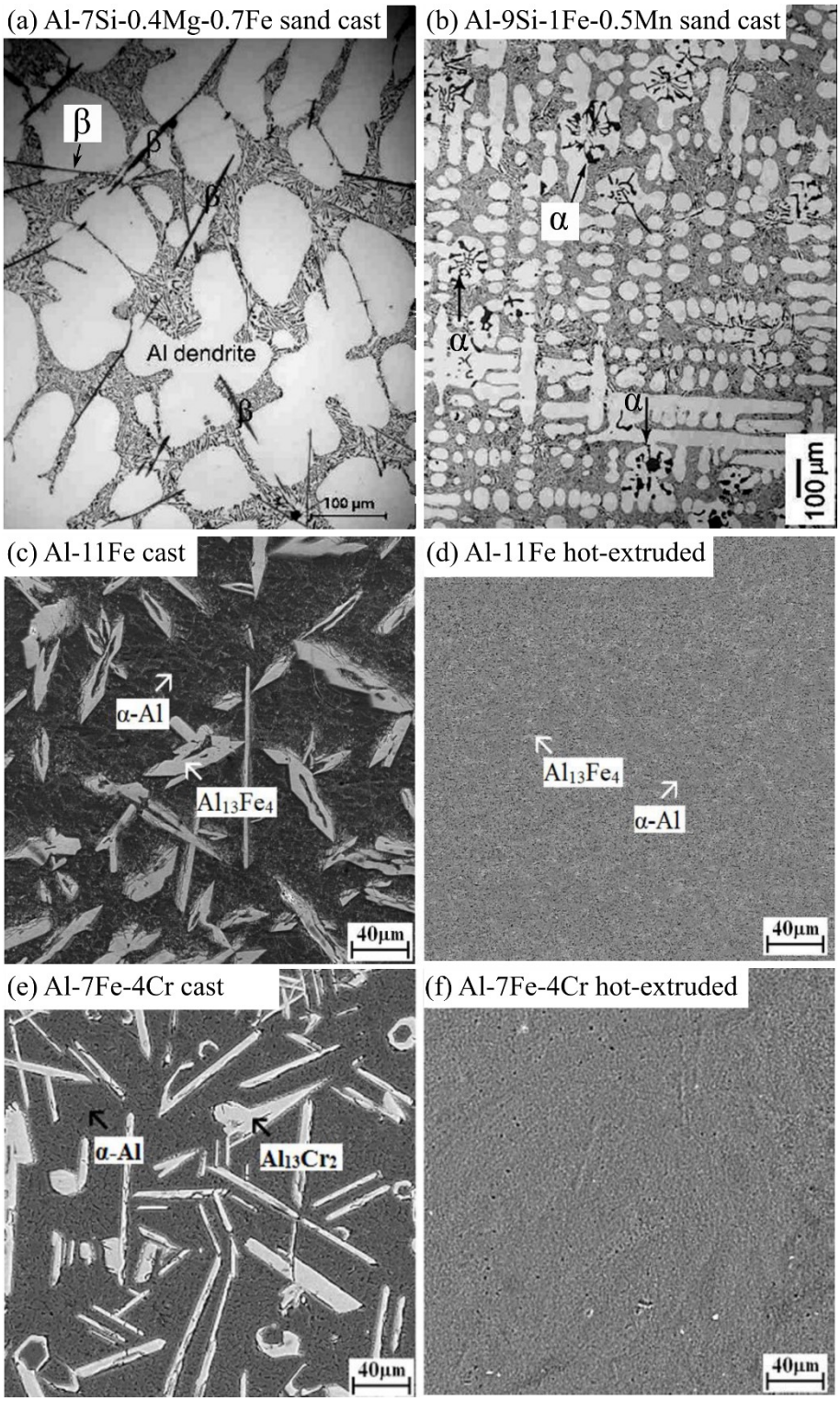

Figure 1.2 Microstructure of sand cast (a) Al-7Si-0.4Mg-0.7Fe [20] and (b) Al-9Si-1Fe-0.5Mn [21], cast (c) Al-11Fe and (e) Al-7Fe-4Cr, and hot-extruded (d) Al-11Fe and (f) Al-7Fe-4Cr [22].

1.2 Research challenges

There is intensive ongoing research into the grain refinement of alloys by inoculant additions that contain growth restricting solute and numerous heterogeneous nucleant particles. Often, the orientation relationship formed by heterogeneous nucleation and its disregistry are used as a measure of the potency of particles in a grain refiner. However, there can be more than one OR formed and multiple mechanisms can generate ORs during solidification so it is often difficult to assign each orientation relationship to a formation mechanism, and it can be highly challenging to identify the nucleating particle with certainty. Therefore, there is a need to develop new experimental approaches to link ORs to their formation mechanism during solidification, and understand how ORs form between inoculant particles and the matrix.

Research has indicated that FCC alloys may be grain refined by adding small additions that encourage icosahedral short-range order in the melt and/or cause icosahedral quasicrystals (iQCs) to form first during solidification and that the FCC phase then grows from each iQC into ten FCC orientations. Kurtuldu et al. [23-28] reported in Al-Zn-Cr and Au-Ag-Cu-Ir FCC alloys an abnormal fraction of twin, or near-twin, grain boundaries and 5-fold symmetry among neighbouring grains, and significant grain refinement. They attributed this to Cr and Ir additions promoting icosahedral short-range order in the melt and/or the formation of iQCs prior to FCC nucleation followed by the growth of ten FCC orientations from each iQC due to multiple variants of the OR between these phases. This has shown some exciting promise as it is a new mechanism causing grain refinement without the need for nucleant particles. However, few studies have been performed on this topic and it is unclear if this mechanism can be used to design alloys to harness this phenomenon.

The morphology of primary IMCs is known to strongly affect the extent to which they degrade mechanical properties (tensile ductility and fatigue life) of Al and Mg alloys. However, there is limited understanding of how the morphology of primary IMCs can be manipulated during solidification. Research has suggested that twinning may enable a route to morphology control, but this has not been explored in detail. Recently, Feng et al. [29] studied solidification twinning in primary $Al_{13}Fe_4$ and

showed that the formation of parallel twin platelets perpendicular to the growth direction promoted thickening of $Al_{13}Fe_4$ and resulted in crystals of a much lower aspect ratio. Such a morphology is desirable as it is less deleterious to mechanical properties. Similarly, Zeng et al. [30, 31] have studied how solidification twinning affects the Al_8Mn_5 growth morphology in magnesium alloys. They found that Al_8Mn_5 (rhombohedral) grows as equiaxed particles with a cyclic twin forming a combined cubic symmetry due to nucleation with four variants on a small B2-Al(Mn,Fe) (cubic) particle. In contrast, when Al_8Mn_5 grows as a single crystal, it forms long hexagonal rods which are likely to degrade tensile ductility and fatigue life. To optimise the potential benefits of solidification twinning in $Al_{13}Fe_4$ and other IMCs in Al and Mg casting alloys, there is now a need to build the understanding of the factors affecting solidification twinning in a range of transition metal aluminides.

1.3 Aims

The overall aim of this thesis is to build a deeper understanding of the mechanisms that lead to solidification ORs, solidification twinning and equiaxed solidification textures, using Al and Mg alloys as examples.

To address the research challenges above, a combination of (i) experiments centred around electron backscatter diffraction, and (ii) calculations using density functional theory (DFT), are applied with four specific objectives:

1) To develop experimental approaches that allow ORs formed between inoculant particles and the matrix to be linked with their formation mechanisms.

2) To build the understanding of solidification twinning in IMCs and its influence on growth morphology.

3) To investigate twinning induced by the iQC-mediated nucleation mechanism in FCC alloys by comparing ORs and textures in Al (FCC) and Mg (HCP) alloys after equiaxed solidification.

4) To explore the origins of crystallographic texture formed by equiaxed solidification.

1.4 Thesis structure

A unifying thread through this thesis is the study of orientation relationships formed during solidification due to the nucleation, growth and rotation of crystals, and the statistics of the interfaces formed. The structure of the thesis is as follows:

Chapter 2 is a broad review of the previous literature including nucleation theory, pushing and engulfment theory, and quasicrystal crystallography. It also reviews the published research work about quasicrystal-induced grain refinement and grain boundary formation. Finally, a brief theoretical background for density functional theory (DFT) calculations is given.

In Chapter 3, one of the most common Al grain refinement systems (Al-Ti-B) is used to explore the formation of ORs between Al_3Ti and small TiB_2 platelets. Methods are presented to link ORs to their formation mechanism by combining electron backscatter diffraction (EBSD), droplet nucleation experiments and interface energy calculations.

Chapter 4 investigates solidification twinning in transition metal aluminides with a focus on how IMC nucleation and growth can be manipulated by controlling the cooling rate (undercooling). Two types of IMCs are studied: (i) $Al_{45}Cr_7$ and $Al_{13}Fe_4$ which are monoclinic approximants of icosahedral and decagonal quasicrystals respectively; and (ii) Al_3Ti and Ag_3Sn are tetragonal and orthorhombic superlattices derived from the FCC and HCP structures. In all four IMCs, the conditions under which twinning occurs with the symmetry of the higher symmetry parent structure (icosahedral, decagonal cubic and hexagonal, respectively) is studied.

In Chapter 5, the non-random misorientation distribution and crystallographic texture of Al and Mg alloys after equiaxed solidification is investigated. A high fraction of twin boundaries between equiaxed grains are found in cast Al (Al-6Cu+TiB_2, Al-15Cu and Al-20Zn, wt%) and Mg (Mg-9Al-0.7Zn+$FeCl_3$, Mg-9Zn-0.7Zn+Al_4C_3, wt%) alloys with and without grain refiner additions. Considering the two mechanisms of forming solidification ORs in Chapters 3 and 4, (i) the interaction and movement between two contacting grains and/or (ii) nucleation on atomic clusters with icosahedral short-range order in the melt, could both produce the observed twin boundaries. By detailed grain boundary analysis and interface calculations, the mechanisms that form the high fraction of twin boundaries and equiaxed solidification texture in both Al and Mg alloys are investigated and discussed.

Chapter 6 summarises the main findings of the thesis and provides conclusions for this work. The thesis ends with suggestions for future research.

Chapter 2 Literature review

2.1 Nucleation theories

2.1.1 Homogeneous nucleation theory

In classical homogeneous nucleation theory [32-36], a pure homogeneous liquid is considered. It is possible for atoms to form small clusters with a crystalline structure due to random fluctuations. Assuming the formation of a spherical cluster with radius R, the Gibbs free energy change of the system can be written as:

$$\Delta G = \Delta G_V + \Delta G_S = \frac{4}{3}\pi R^3 \cdot \left(G_v^s - G_v^l\right) + 4\pi R^2 \cdot \sigma = -\frac{4}{3}\pi R^3 \cdot \Delta G_v + 4\pi R^2 \cdot \sigma \quad \textit{Equation 2.1}$$

Where G_v^s and G_v^s are the Gibbs free energy of the solid and liquid per unit volume, respectively. ΔG_v is the Gibbs free energy change per unit volume and it is defined as $(G_v^l - G_v^s)$, and σ is the solid/liquid interfacial energy induced by the formation of the solid cluster. For a small undercooling, ΔG_v can be expressed as:

$$\Delta G_v = \Delta H_v - T\Delta s_v \cong L_v - T\frac{L_v}{T_f} = L_v\frac{\Delta T}{T_f} \quad \textit{Equation 2.2}$$

Where ΔH_v is the enthalpy change per unit volume, Δs_v is the entropy change per unit volume, T_f is the melting point of the melt and ΔT is the undercooling defined as: $\Delta T = T_f - T$. L_v is the latent heat of fusion per unit volume which can also be expressed in terms of Δs_v: $L_v = \Delta s_v T_f$. Thus, Eq. 2.2 can be expressed as:

$$\Delta G_v = \Delta s_v \Delta T \quad \textit{Equation 2.3}$$

Substituting Eq. 2.3 into Eq. 2.1 gives:

$$\Delta G = \Delta G_V + \Delta G_S = -\frac{4}{3}\pi R^3 \cdot \Delta s_v \Delta T + 4\pi R^2 \cdot \sigma \quad \textit{Equation 2.4}$$

When $\Delta T < 0$, i.e., $T > T_f$, both terms on the right hand side of Eq. 2.4 are positive, which means it is energetically unfavourable to form solid clusters with crystalline structure and they will melt back instead of growing. Oppositely, when $\Delta T > 0$, i.e., $T < T_f$, the first term on the right hand side is negative which corresponds to the energy decrease by solidification of the undercooled liquid. The

second term is positive and corresponds to the energy penalty for the formation of the solid-liquid interface. In this case, the energy change of the system for pure Al is plotted in Figure 2.1. The thermodynamic values for Al are listed in Table 2.1.

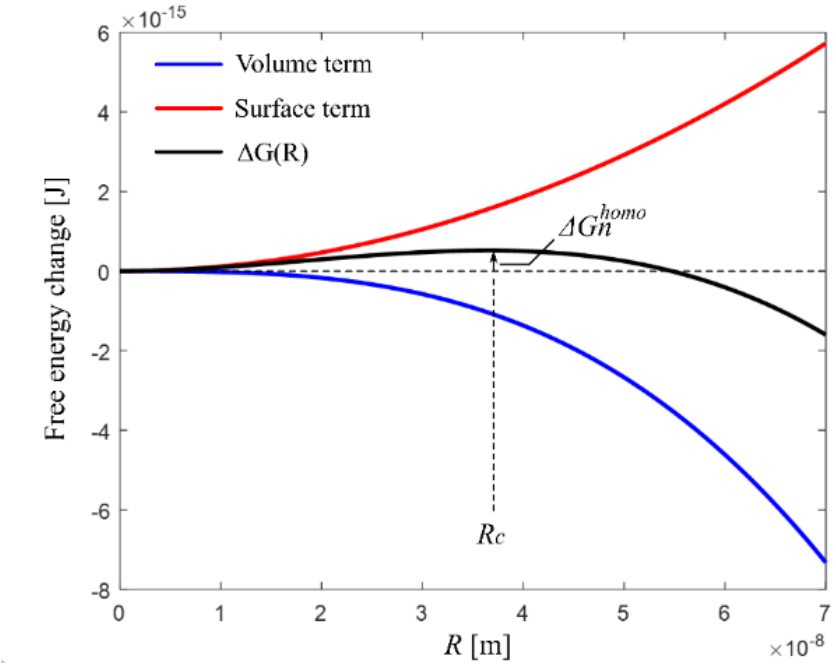

Figure 2.1 Surface energy, bulk energy and total free energy change of Al cluster as a function of its radius for homogeneous nucleation. The undercooling is set to be 5°C. After Ref. [37]

Table 2.1 Thermodynamic properties for Al [37]

Parameters	Symbol	Value	Units
Melting point of Al	T_f	933	K
Solid-liquid interfacial energy	σ	0.1	J/m^2
Entropy change per unit volume	Δs_v	1.02×10^6	J/(m^3·K)
Molar volume of Al	V^m	1.138×10^{-5}	m^3/mol
Atomic vibration frequency at 933K	ν_0	10^{13}	s^{-1}
Probability of capturing an atom at the surface	p_c	1	
Boltzmann constant	k_B	1.38×10^{-23}	J/K
Avogadro constant	N_A	6.02×10^{23}	mol^{-1}

In Figure 2.1, the surface energy penalty exceeds the volumetric energy release for small R, whereas the energy decrease from the volumetric term dominates at large R, creating a maximum value in ΔG which is called the homogeneous nucleation barrier ΔG_n^{homo}. The radius R_c corresponding to ΔG_n^{homo} can be determined by differentiating Eq. 2.4 with respect to R and finding the turning point. The result is:

$$R_c = \frac{2\sigma}{\Delta s_v \Delta T} \qquad \textit{Equation 2.5}$$

And the homogeneous nucleation barrier can be calculated by:

$$\Delta G_n^{homo} = \frac{16\pi}{3}\frac{\sigma^3}{\Delta s_v^2 \Delta T^2} \qquad \textit{Equation 2.6}$$

It is energetically favourable for clusters with $R < R_c$ to melt back, and clusters with $R > R_c$ to keep growing. Therefore, embryos with radius R_c are called critical nuclei.

In addition, assuming that the energy of atoms in liquid follows a Maxwell-Boltzmann distribution, the density of clusters with radius R can be written as:

$$n(R) = n_0 exp(-\frac{\Delta G(R)}{k_B T}) \qquad \textit{Equation 2.7}$$

n_0 is the total number of atoms per volume in the liquid and equals to $\frac{N_A}{V^m}$ where N_A is the Avogadro constant and V^m is the molar volume. k_B is the Boltzmann's constant. For clusters with critical size, the number density can be calculated by setting $\Delta G(R) = \Delta G_n^{homo}$ in Eq. 2.7:

$$n_c = n_0\, exp\left(-\frac{\Delta G_n^{homo}}{k_B T}\right) = n_0 exp(-\frac{16\pi}{3}\frac{\sigma^3}{(\Delta s_v \Delta T)^2 k_B T}) \qquad \textit{Equation 2.8}$$

A nucleus of critical size R_c will grow if it manages to add one more atom, and the occurrence rate of this is proportional to the atomic vibration frequency ν_0 and the probability of capturing an atom at the surface p_c. Therefore, the rate to form homogeneous nucleai, I^{homo}, is:

$$I^{homo} = \nu_0 p_c n_c = \nu_0 p_c n_0 exp(-\frac{16\pi}{3}\frac{\sigma^3}{(\Delta s_v \Delta T)^2 k_B T}) \qquad \textit{Equation 2.9}$$

It is clear that the homogeneous nucleation rate depends strongly on temperature: on one hand an increasing undercooling lowers the nucleation barrier, ΔG_n^{homo}, but on the other hand decreased

temperature leads to the decreasing mobility of atoms. Therefore, the two competing factors lead to a maximum nucleation rate at a certain temperature. The change of I^{homo} for pure Al with respect to temperature is plotted in Figure 2.2: the homogeneous nucleation rate reaches the maximum value around 300K with ~700K undercooling, which is much deeper than the measured undercooling for Al alloys. Therefore, other nucleation process happens in real situations before the homogeneous nucleation is triggered.

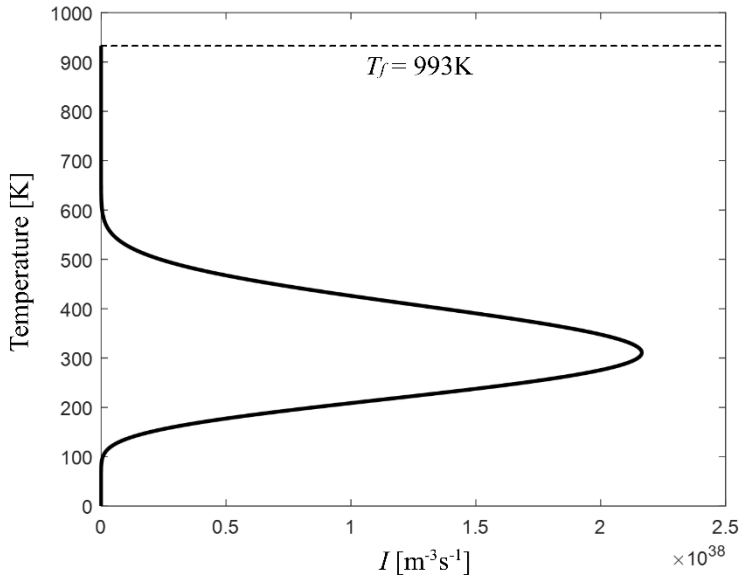

Figure 2.2 The homogeneous nucleation rate of α-Al as a function of temperature.

2.1.2 Heterogeneous nucleation theory

In real situation, there are always some solid phases like oxide layers, impurity particles, added grain refiners and even container walls that share interfaces with liquid where heterogeneous nucleation can happen [38-40]. Assuming the critical nucleus forming on the flat existing solid surface is a spherical cap, the geometry of the heterogeneous nucleation process is shown in Figure 2.3.

Considering the equilibrium state of the surface energy [41]:

$$\gamma_{fl} = \gamma_{fs} + \gamma_{sl} cos\theta \qquad \textit{Equation 2.10}$$

Where γ_{fl} is the interfacial energy between the foreign substrate and the liquid, γ_{fs} is the interfacial energy between the foreign substrate and the newly formed solid, γ_{sl} is the interfacial energy between the solid and the liquid, and θ is the contact angle (also known as wetting angle).

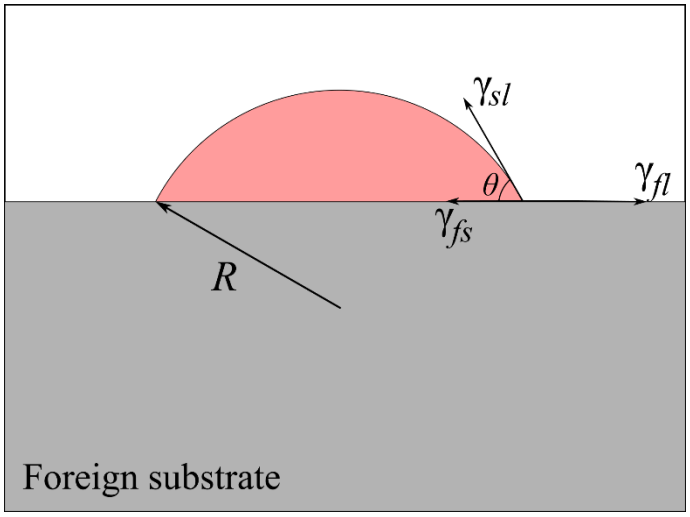

Figure 2.3 The nucleation of a spherical solid cap on a foreign substrate. After Ref. [41]

In this case, the Gibbs energy change of the system due to the formation of the solid spherical cap is given by:

$$\Delta G = \Delta G_V + \Delta G_S = V_s \cdot \left(G_v^s - G_v^l\right) + A_{sl} \cdot \gamma_{sl} + A_{fs}(\gamma_{fs} - \gamma_{fl}) \qquad \textit{Equation 2.11}$$

Where V_s is the volume of the solid nucleus, A_{sl} is the area of the newly formed solid-liquid interface, and A_{fs} is the area of the interface between the solid and foreign substrate. For a spherical cap with radius R, V_s, A_{sl} and A_{fs} can be written as:

$$V_s = \frac{\pi R^3}{3}(2 + cos\theta)(1 - cos\theta)^2 \qquad \textit{Equation 2.12}$$

$$A_{sl} = 2\pi R^2(1 - cos\theta) \qquad \textit{Equation 2.13}$$

$$A_{fs} = \pi R^2(1 - cos^2\theta) \qquad \textit{Equation 2.14}$$

Substituting Eq. 2.10, Eq. 2.12, Eq. 2.13 and Eq. 2.14 into Eq. 2.11, and applying $\Delta G_v = \Delta s_v \Delta T$, the equation can be written as:

$$\Delta G = (-\frac{4}{3}\pi R^3 \cdot \Delta s_v \Delta T + 4\pi R^2 \cdot \gamma_{sl}) f(\theta) \qquad \textit{Equation 2.15}$$

Where $f(\theta)$ is a geometry factor given by:

$$f(\theta) = \frac{V_s}{4\pi R^3/3} = \frac{(2+cos\theta)(1-cos\theta)^2}{4} \qquad \textit{Equation 2.16}$$

Comparing Eq. 2.15 (heterogeneous nucleation) with Eq. 2.4 (homogeneous nucleation), the Gibbs energy change appears in the same form except multiplied by the $f(\theta)$ factor in heterogeneous nucleation. The critical radius can be derived by differentiating Eq. 2.15 with respect to R and setting it to zero, and yields the same result as in homogeneous nucleation:

$$R_c = \frac{2\gamma_{sl}}{\Delta s_v \Delta T} \qquad \textit{Equation 2.17}$$

And the heterogeneous nucleation energy barrier can be calculated by:

$$\Delta G_n^{hetero} = \frac{16\pi}{3}\frac{\gamma_{sl}^3}{\Delta s_v^2 \Delta T^2} f(\theta) = \Delta G_n^{homo} f(\theta) \qquad \textit{Equation 2.18}$$

The range of the geometry factor $f(\theta)$ with respect to the contact angle θ is plotted in Figure 2.4. For $\theta = 0^\circ$, the function $f(\theta) = 0$, which means complete wetting of solid phase on substrate and there is no nucleation barrier in this case. For $0^\circ < \theta < 180^\circ$, the function $f(\theta)$ is between 0 and 1, indicating that the energy barrier for heterogeneous nucleation is lower than homogeneous nucleation. With wetting angle increasing, the compatibility between the solid phase and the substrate decreases. For non-wetting conditions ($\theta = 180^\circ$): $f(\theta) = 1$, the energy changes are the

same for heterogeneous and homogeneous nucleation because in this situation solid nuclei form from liquid instead of substrate.

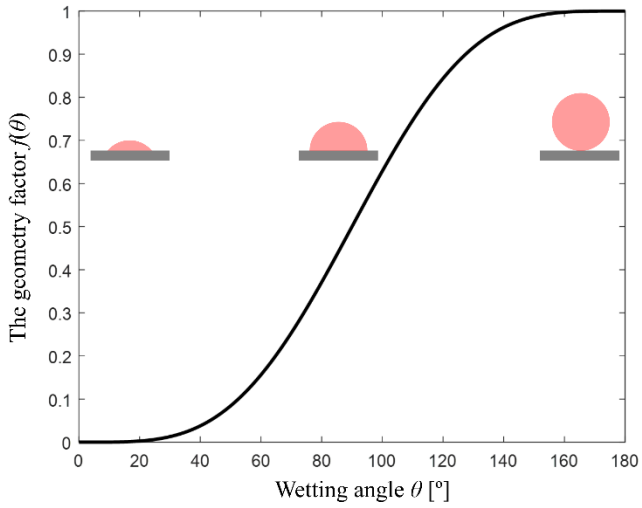

Figure 2.4 The range of $f(\theta)$ with respect to the wetting angle

Considering the heterogeneous nucleation rate, with the knowledge of the free energy barrier, Eq. 2.9 can be rewritten as:

$$I^{hetero} = \nu_0 p_c n_p exp(-\frac{16\pi}{3}\frac{\gamma_{sl}^3}{(\Delta s_v \Delta T)^2 k_B T} f(\theta)) \qquad \textit{Equation 2.19}$$

Where n_p is the density of inoculants in the melt for heterogeneous nucleation. Compared to homogeneous nucleation, we expect $n_p \ll n_0$. Now assuming n_p =10^9 m^{-3} with ν_0 and p_c being the same as in homogeneous nucleation, the change of heterogeneous nucleation rate with respect to temperature and wetting angle in Al melt is plotted in Figure 2.5. The nucleation rate for homogeneous nucleation is also plotted for comparison. For most metallurgical process the undercooling of melt is less than 100K, which would trigger a large amount of heterogeneous nucleation with wetting angle less than 60°. Therefore, even though the pre-exponential term for heterogeneous nucleation is much smaller than homogeneous nucleation, the $f(\theta)$ factor appearing in the nucleation barrier makes heterogeneous nucleation much more favourable.

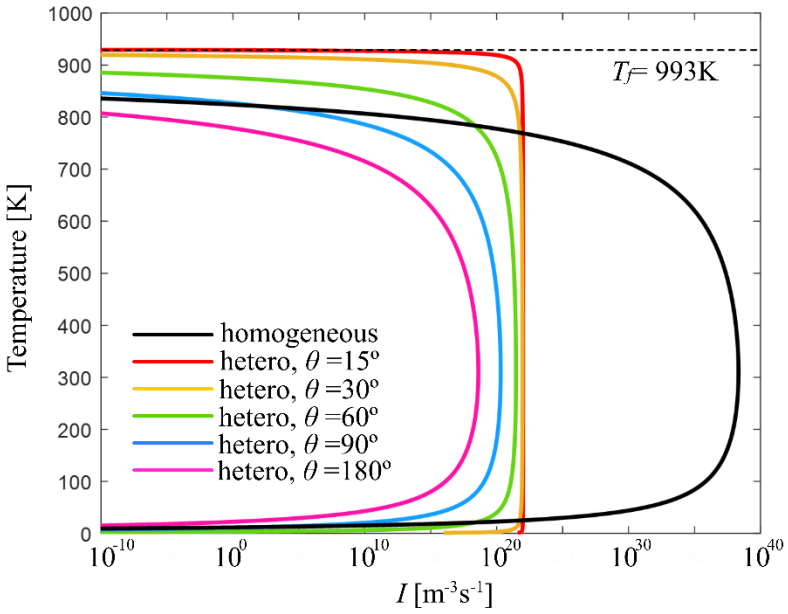

Figure 2.5 The nucleation rate as a function of temperature and wetting angle for Al. After Ref. [37]

2.1.3 Nucleant potency

2.1.3.1 Lattice matching theory

The classical nucleation theory implies little about the atomic mechanism of heterogeneous nucleation. In order to examine how nucleant potency is affected by its orientation relationship with the forming solid, the lattice coherency between the substrate and the growing solid is considered in various models that quantify the disregistry. Three major approaches are discussed here: (i) the Turnbull-Vonnegut linear disregistry [42], (ii) the Bramfitt planar disregistry [43] and (iii) the Zhang-Kelly edge-to-edge model [44-46].

According to Turnbull and Vonnegut, the nucleant potency is in the order of the reciprocal of the disregistry (δ) between the nucleant and forming solid on their low index planes with similar atomic arrangement [42]:

$$\delta = \Delta a_0 / a_0 \qquad \textit{Equation 2.20}$$

Where Δa_0 is the difference between the lattice parameters for the nucleant and the forming solid on a low index plane, and a_0 is the lattice parameter for the forming solid. Through experiment, the linear disregistry model successfully explained the measured undercooling for various nucleants (nitrides and carbides) that share the same crystal structure as the forming phase (δ Fe). But for nucleants with different atomic arrangement, the prediction from linear disregistry is not consistent with experiments. Bramfitt proposed a more accurate model to describe the lattice mismatching between the substrate and forming solid, known as planar disregistry model, by averaging the linear disregistry in the three lowest-index directions and considering the adjustment of angular difference between the matched directions [43]. The form of the planar disregistry can be written as:

$$\delta_{(hkl)_n}^{(hkl)_s} = \frac{1}{3} \cdot \sum_{i=1}^{3} \frac{\left| \left(d_{[uvw]_s}^{\,i} cos\theta \right) - d_{[uvw]_n}^{\,i} \right|}{d_{[uvw]_n}^{\,i}} \times 100\% \qquad \textit{Equation 2.21}$$

Where $(hkl)_s$ and $(hkl)_n$ are low index planes of the substrate and nucleated solid, $[uvw]_s$ and $[uvw]_n$ are low index directions in $(hkl)_s$ and $(hkl)_n$, $d_{[uvw]_s}$ and $d_{[uvw]_n}$ the interatomic spacing along $[uvw]_s$ and $[uvw]_n$, and θ is the angle between $[uvw]_s$ and $[uvw]_n$.

In Al casting, TiB_2 is considered as a potent nucleant for Al_3Ti [47-53]. Figure 2.6 plots the atomic matching between these two compounds at the interface with the orientation relationship reported in previous literature [50-52]:

$$\{112\}_{Al_3Ti} \parallel \{0001\}_{TiB_2}, \text{with } <\bar{2}01>_{Al_3Ti} \parallel <11\bar{2}0>_{TiB_2} \qquad \textit{Equation 2.22}$$

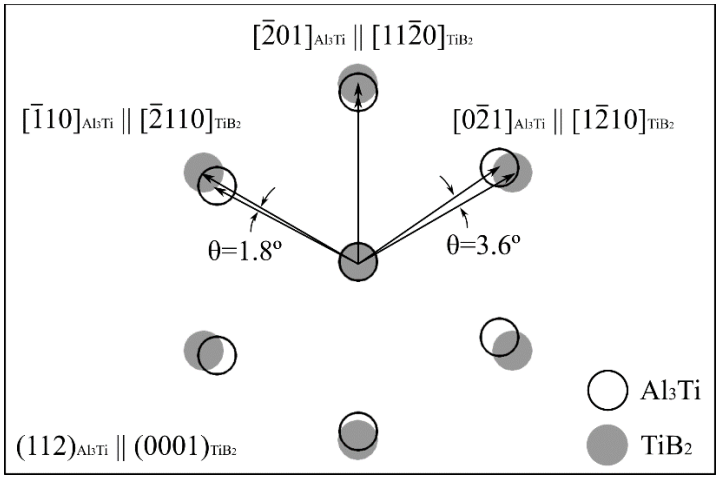

Figure 2.6 Bramfitt planar lattice matching between Al_3Ti and TiB_2 at the interface

Table 2.2 lists the calculated results of the Bramfitt planar disregistry for the orientation relationship between Al_3Ti and TiB_2 in Eq. 2.22. With consideration of the linear disregistry in three directions and taking the angular difference into account, Bramfitt planar disregistry makes a better prediction than the linear disregistry model. Bramfitt used a similar argument to show that the planar disregistry gives a better prediction of nucleant potency for WC to nucleate δFe [43].

Table 2.2 Bramfitt planar disregistry between Al_3Ti and TiB_2 in the (112)||(0001) interface plane

Directions	Angular difference θ	Linear disregistry δ_i	Planar disregistry δ
$[\bar{2}01]_{Al_3Ti} \parallel [11\bar{2}0]_{TiB_2}$	0	5.03%	6.98%
$[0\bar{2}1]_{Al_3Ti} \parallel [11\bar{2}0]_{TiB_2}$	3.6°	4.82%	
$[\bar{1}10]_{Al_3Ti} \parallel [11\bar{2}0]_{TiB_2}$	1.8°	11.10%	

More recently a new model has been developed by Kelly and Zhang considering the matching of close packed or nearly close packed atomic rows along the edge of the planes meeting at the interface [44]. Therefore, this model is termed the edge-to-edge matching theory. Figure 2.7 schematically plots the edge-to-edge matching and planar matching models. For plane-on-plane matching, the coherent or partially coherent interface between A and B are normally close packed or nearly close packed planes, while for edge-to-edge matching, the interface is the intersection plane of the matching planes containing the close packed or nearly close packed directions being the 'edges'.

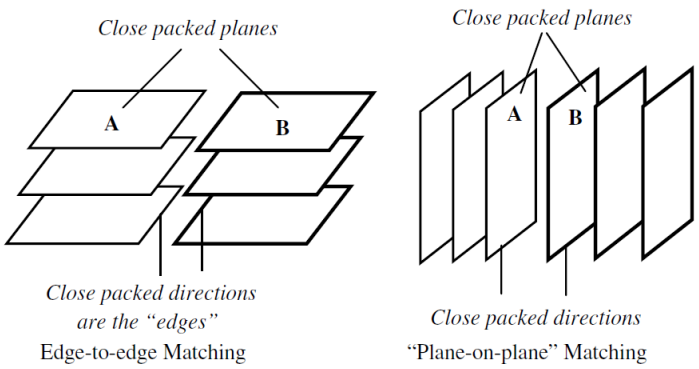

Figure 2.7 Schematically illustration of the edge-to-edge matching and plane-on-plane matching. From Ref. [45]

Through the application of this matching model, not only can it make good predictions for the effectiveness of the known nucleant in Al and Mg-Al based alloys [45, 46], but also it has given an explanation on the poisoning effect of Si on Al-Ti-B grain refiners [54]. In Al-Si casting practice it has been known that excess Si solute (>2 wt.%) poisons the potency of Al-Ti-B grain refiners. Using the edge-to-edge matching model this is likely due to the formation of a shell of Ti_5Si_3 on Al_3Ti, which prevents the highly potent Al_3Ti substrate from nucleating α-Al and thus causing the poisoning of the Al-Ti-B grain refiners.

2.1.3.2 Free growth model

The free growth model was first proposed by Quested and Greer [55-57] which demonstrated that the potency of grain refiners is also determined by its size distribution. In this model the undercooling temperature depends on the size and geometry of the foreign particles. In classical nucleation theory an embryo could grow into stable nucleus at any temperature as if the thermal fluctuation could overcome the corresponding energy barrier. But in the free growth model, the morphology of the particles completely dictates the undercooling temperature at which the stable embryo will grow out of it. The stable grain will not form until the critical temperature is reached. Therefore foreign particles with different size and geometry will have different potency.

As shown in Figure 2.8(a), the initial growth of α-Al on the {0001} facet of TiB_2 continuously reduces its radius of curvature until it reaches the critical hemispherical cap with minimum radius (d/2), after which the radius of curvature start to increase with further growth. According to classical nucleation theory, the undercooling required to form an embryo with radius *R* can be calculated:

$$\Delta T = \frac{2\gamma_{sl}}{\Delta s_v R} \qquad \textit{Equation 2.23}$$

Therefore, for a TiB_2 particle with diameter *d*, the critical undercooling above which α-Al can grow freely is fully determined by its size and can be expressed as following:

$$\Delta T_c = \frac{4\gamma_{sl}}{\Delta s_v d} \qquad \textit{Equation 2.24}$$

Figure 2.8(b) plots the size distribution of TiB_2 particles in Al-5Ti-1B master alloy measured by the image analysis of SEM [57]. The distribution can be well fitted to a log normal function with most TiB_2 particles at small diameter side. However, as discussed above, it is the TiB_2 particles with larger diameter (shaded black in Figure 2.8(b)) that correspond to lower critical undercooling and are likely to be activated during practical casting while the rest will be stifled due to recalescence.

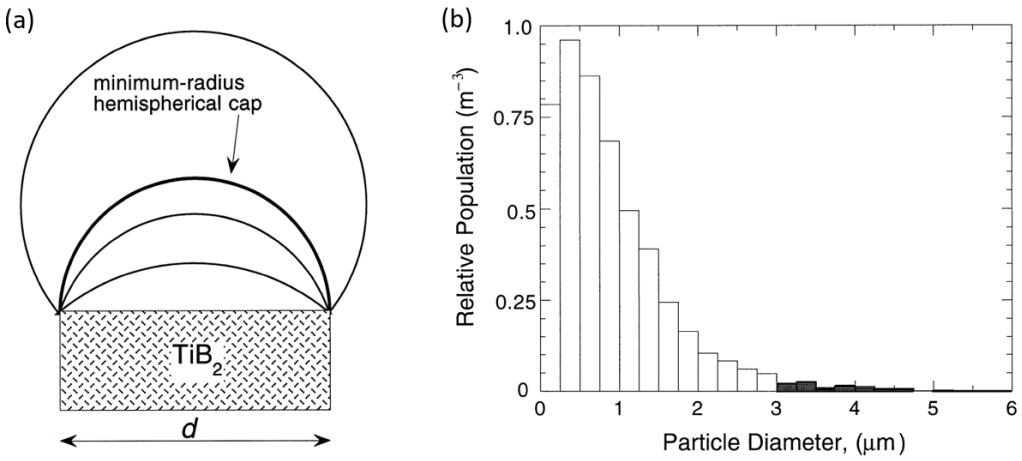

Figure 2.8 (a) α-Al growth on the {0001} facet of TiB_2 particles. Thickening of the growing crystal reduces the radius of curvature of its interface with the liquid. (b) Size distribution of TiB_2 particles in Al-5Ti-B master alloy determined by the image analysis of SEM. From Ref. [57]

2.2 Nucleation mechanism in TiB_2-Al_3Ti-Al system

Grain refinement of Al alloys has been widely studied for over half a century [58-62]. One of the most commonly used grain refiners is the Al-Ti-B master alloy. Although the addition of heterogeneous nuclei to achieve significant grain refinement in this case was first proposed by Cibula in 1949 [63], the exact refinement mechanism of the Al-Ti-B grain refiners is still debated and many theories have been proposed.

2.2.1 Nucleant-Particle theory

The nucleant-particle theory was first postulated by Cibula who attributed the grain refinement from the master alloys to the nucleation on borides (TiB_2 and AlB_2) [58, 63]. Normally when the Al-Ti-B master alloy is added in practice, the Ti content is at hypoperitectic level (<0.13 wt%) and most particles in the melt are borides. Figure 2.9 plots the Al-Ti phase diagram at Al-rich side. Examination shows that some boride particles, or more commonly, boride clusters or agglomerates, can be located in the centre of α-Al grains [64, 65], suggesting that nucleation is likely to happen on these particles. However, calculations made by the lattice matching models show that there is large lattice disregistry between the borides and α-Al [45], and it has been observed that most borides are pushed to the grain boundaries [47, 66-68], suggesting that borides are poor nucleants. More importantly, it has been confirmed that no grain refinement is observed when there is no excess Ti in the solute [47], indicating that borides alone do not cause the grain refinement.

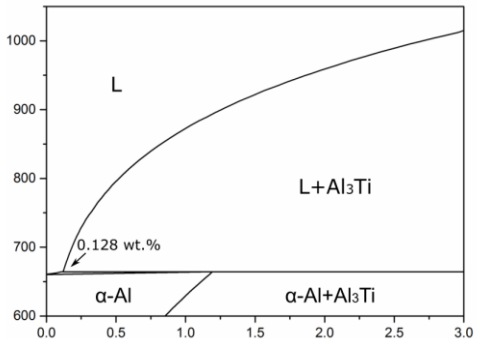

Figure 2.9 Al-rich side of the Al-Ti phase diagram from Thermo-Calc database TCTI2 version 2.0.

2.2.2 Phase-Diagram theory

Compared to TiB_2, Al_3Ti is known as a highly potent nucleant for α-Al and phase-diagram theories were developed to explain how Al_3Ti could be active at hypoperitectic concentrations. It has been suggested that with the addition of boron, the peritectic point moves to low titanium concentration [69-71]. Marcantonio and Mondolfo suggested that there is a ternary eutectic (Al-(Al,Ti)B_2-Al_3Ti) at the Al corner of the Al-Ti-B equilibrium phase diagram at 0.05 wt% Ti and 0.01 wt% B around 659.5°C [69]. The grain refinement occurred due to the formation of primary Al_3Ti crystals which triggered the nucleation of α-Al. However, there is no reported observation of the same phenomenon by other researchers and theoretical thermodynamic calculations show that boron has virtually no effect on the Al-Ti peritectic point [60, 72, 73]. It appears that the phase-diagram theories cannot be used to explain the observed grain refinement.

2.2.3 The Peritectic hulk theory

This theory was proposed by Backerud and Dong [74, 75] and supported by Vader et al.[76]. It accepts that Al_3Ti is a more powerful nucleant, and instead of forming primary Al_3Ti crystals, Al_3Ti particles may remain undissolved in the melt when the master alloy is added. The peritectic hulk theory suggests that the borides form a shell around Al_3Ti and slow down the dissolution due to the difficulty of diffusion through the borides shell. When Al_3Ti finally dissolve, there is Ti-rich liquid left inside the shell and when temperature drops the peritectic reaction takes place to form α-Al. Although this theory seems to be consistent with some of the experiment evidence, one of its major problems is the assumption that the borides dissolve in the melt and reprecipitate to form the boride shell. In reality, however, borides are much more stable in the melt than Al_3Ti [77]. Normally Al_3Ti can dissolve within minutes at high temperature even with borides present in the master alloy. Furthermore, Johnsson et al. [78] found that the grain refinement efficiency does not change after a number of cycles of melting and solidifying, which in theory should decrease if the peritectic hulk theory is operative as Ti would diffuse out of the hulk. Therefore, the peritectic hulk theory is not likely to be the main refinement mechanism.

2.2.4 The Duplex nucleation theory

Of all the grain refinement theory proposed so far, the duplex nucleation theory is the most promising. It was first proposed by Mohanty et al. [47, 68, 79, 80] and strongly supported by Schumacher and Greer [48-51, 81]. The theory postulates that a thin layer of Al_3Ti forms on the surface of TiB_2 particles which nucleates α-Al. By adding the master alloy into an $Al_{85}Y_8Ni_5Co_2$ glassy matrix and then rapidly quenching, Schumacher et al. found the TiB_2 basal plane was covered by a thin layer of Al_3Ti which was surrounded by α-Al, which demonstrated the same sequence as that proposed during nucleation [81]. The close packed planes and directions of TiB_2, Al_3Ti and α-Al are parallel and highlighted in Figure 2.10. The orientation relationship can be written as:

$$\{0001\} < 11\bar{2}0 >_{TiB2} \; || \; \{112\} < 1\bar{1}0 > \text{or} < \bar{2}01 >_{Al3Ti} \; || \; \{111\} < 1\bar{1}0 >_{Al} \qquad \textit{Equation 2.25}$$

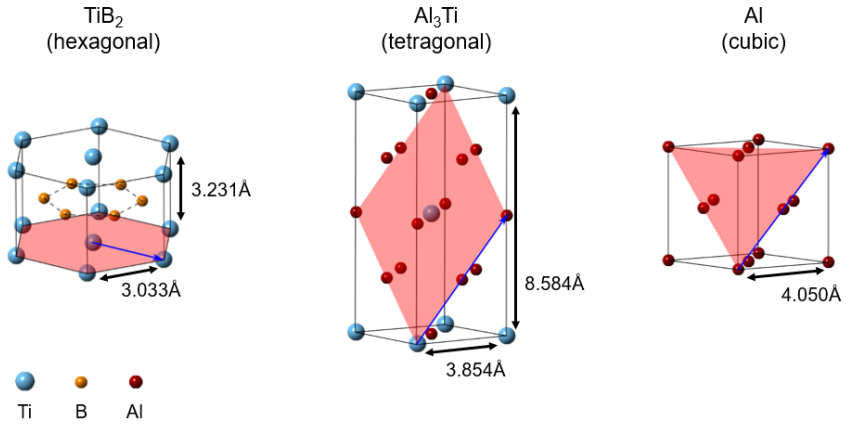

Figure 2.10 The orientation relationships between TiB_2, Al_3Ti and α-Al. Their close packed planes and directions are highlighted in red and blue, respectively.

Mohanty et al. suggested that the formation of the Al_3Ti layer is caused by a concentration gradient of Ti towards the TiB_2 particles. Considering the local equilibrium near the TiB_2 particles, the Al_3Ti might be stable and thus nucleate α-Al. Similarly, the hypernucleation theory proposed by Jones [82, 83] suggested that the Ti solute can segregate to the melt-TiB_2 interface and form a stable pseudocrystals which nucleate α-Al.

Recently, with high resolution TEM, a Ti-rich monolayer has been observed on the TiB_2 {0001} surface and the same OR is suggested between TiB_2 particles and this Al_3Ti two-dimensional compound (2DC) [52]. Atomic level simulations on the stability of this thin Al_3Ti layer have been performed through density functional theory (DFT) calculations and molecular dynamics (MD) simulations. Through DFT calculations there is a high interfacial energy between TiB_2 and α-Al, suggesting that TiB_2 is a poor nucleant for α-Al, while an Al_3Ti-like thin layer could be thermodynamically stable on the TiB_2 surface [84]. However, according to Wearing et al. [85], α-Al nucleation directly on a Ti terminated TiB_2 substrate is a more favoured mechanism and a thin Al_3Ti layer appears to be more stable on B-terminated TiB_2. MD simulations show a considerable degree of FCC-like ordering at the Ti terminated TiB_2-liquid interface, but the thin ordering layer is also possible to be strained Al atoms with lattice parameters similar to Al_3Ti [86, 87].

2.3 Particle pushing and engulfment in solidification

Mohanty et.al. found that TiB_2 particles were pushed to the α-Al grain boundaries when there was no excess Ti solute in the melt [47], suggesting a high interfacial energy between TiB_2 and α-Al. According to the prediction of the free growth model, only a small percentage (1-10%) of TiB_2 particles from the grain refiner can trigger nucleation events [88, 89]. The remaining TiB_2 particles are either pushed to the grain boundaries or engulfed and retained within α-Al grains during solidification. The crystallographic analysis performed by Schaffer et al. [90] showed that very few TiB_2 particles pushed to the grain boundaries share any reproducible orientation relationships with surrounding α-Al, while 70% of the engulfed particles showed one of two simple ORs, indicating that the formation of low energy interfaces assists engulfment.

Multiple models have been developed in order to study pushing and engulfment of second-phase particles in the growth front [91-97]. It was first observed by Uhlmann in 1964 [91] that there is a critical velocity of the growing front below which the particles are rejected and continuously pushed by the interface, and above which they are engulfed and trapped in the solid. In 1976 Omenyi and Neumann [98] proposed the thermodynamic criterion for pushing-engulfment transition that when the interface moves slowly (a few micrometres per second), the thermodynamic (equilibrium) conditions will predominate at the interface and the pushing/engulfment process is solely dependent on the net change in free energies of the system:

$$\Delta\sigma = \sigma_{SP} - (\sigma_{LP} + \sigma_{SL}) \qquad \textit{Equation 2.26}$$

Where σ_{SP} is the solid-particle interfacial energy, σ_{LP} is the liquid –particle interfacial energy and σ_{SL} is the solid-liquid interfacial energy. For $\Delta\sigma < 0$, the particles are engulfed by the interface, while for $\Delta\sigma > 0$ the pushing-engulfment transition then depends on the growth velocity of the interface.

The expression format of the critical velocity has been continuously adapted by taking different factors into account including: the thermal gradient in the liquid [99], the roughness of particles [92], the shape/curvature of the interface [92, 100-102], and the effect of agglomeration [103]. The effect of

the interface shape was first investigated by Bolling and Cisse [92]. The growing front was treated as a flat planar interface in previous models but they provided the rigorous mathematical proof that near the particles the interface must be a smooth shallow indentation. The same morphology was applied in later models and numerical simulations [101, 102, 104-106]. Figure 2.11 shows a numerical model for the SiC particle engulfment during silicon solidification [107].

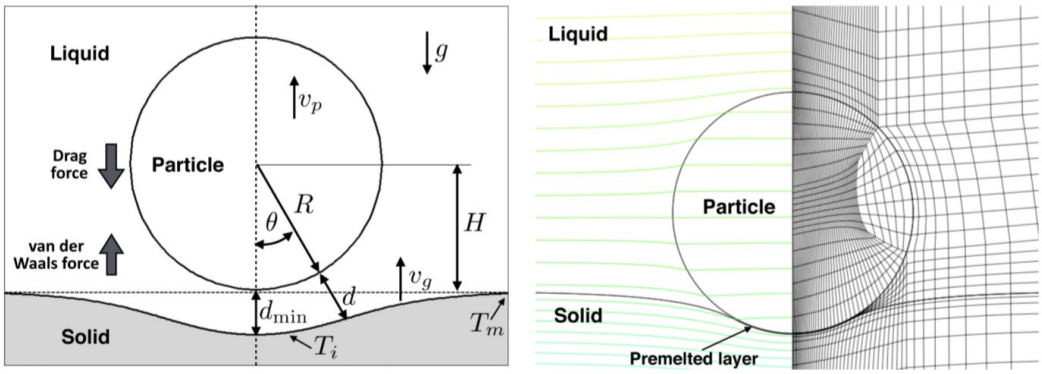

Figure 2.11 (a) A schematic depiction of particle pushing and engulfment during solidification. (b) The numerical model of a SiC particle being pushed by a silicon growth front (The temperature isotherms are plotted on the left and the finite element mesh are plotted on the right). From Ref. [107]

However, most traditional pushing and engulfment models are built based on the assumption that the second-phase particles are inert, while in most metallurgical processes many of the foreign particles are active inoculants that can interact with the growing solid. Analysis for TiB_2 particles engulfed inside equiaxed α-Al grains by Schaffer et al. [90] revealed two preferred ORs, which they attributed to the interaction between TiB_2 particles and the α-Al growth front. Therefore, apart from the factors studied in traditional pushing and engulfment theory, it is important to consider such interaction between active particles and the growth front, which affects the relative orientation and distribution of the second-phase particles, and furthermore the mechanical properties of the alloy.

2.4 Quasicrystalline symmetry and icosahedral short-range order in supercooled melt

2.4.1 Quasicrystal symmetry

It has been well known in crystallography that fivefold symmetry cannot exist in crystals considering the three-dimensional translation operation. But it is first found by Shechtman in 1984 [108] that a metallic solid from the rapidly quenched Al-14 at.%Mn alloy showed the icosahedral symmetry ($m\bar{3}\bar{5}$) [109], which is inconsistent with lattice translations and thus aperiodic in space. It was later proposed by Pauling [110-112] that the material is actually an 'icosatwin', which is a composite of twenty identical crystalline particles twinned together forming a combined icosahedral symmetry. However, that hypothesis was not consistent with analysis of the X-ray [113, 114], electron [115, 116] and neutron [117, 118] diffraction data, and it was postulated that the metallic phase is quasicrystalline and atoms are arranged with icosahedral symmetry [119]. Polyhedrons with standard icosahedral symmetry contains twofold (15), threefold (10) and fivefold (6) symmetry axes in each hemisphere, as shown in Figure 2.12 [120] using three polyhedrons with icosahedral symmetry as examples.

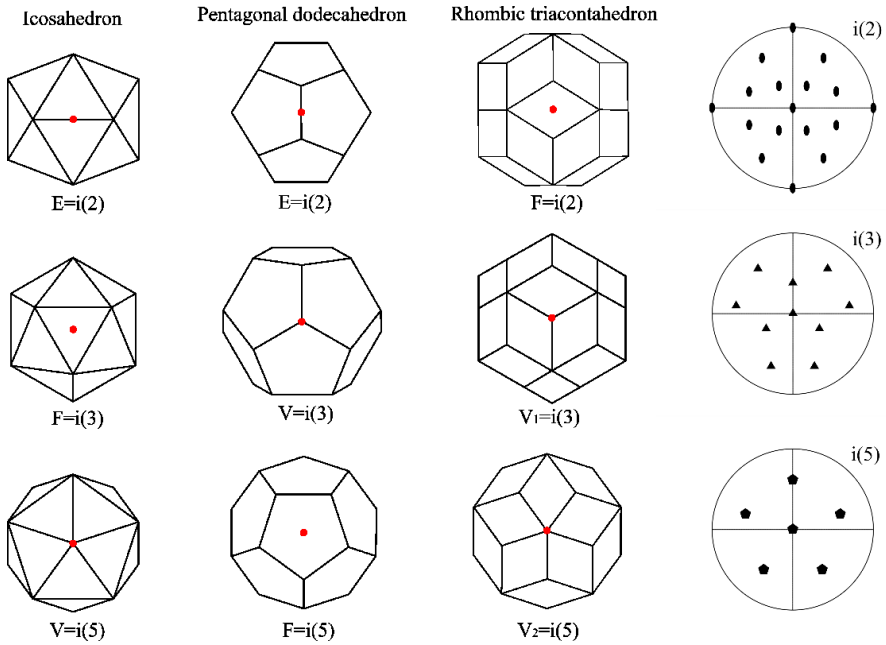

Figure 2.12 Polyhedrons with icosahedral symmetry: icosahedron, pentagonal dodecahedron and rhombic triacontahedron. The twofold, threefold and fivefold axes are highlighted in the polyhedrons and corresponding pole figures. E means edges, F means faces and V means vertices.

After the first observation of the icosahedral quasicrystal in rapidly quenched Al-Mn alloys [108], other similar quasicrystals have been found in many Al-transition metal element (TM) alloys [114, 121-124]. For example, in a rapidly solidified Al_7Cr alloy, the icosahedral quasicrystal was found to coexist with the monoclinic $Al_{45}Cr_7$ intermetallic phase, with a definite orientation relationship linking the icosahedral quasicrystals and the pseudo-icosahedral building blocks in $Al_{45}Cr_7$ [125]. Many stable crystalline Al (rich)-TM intermetallics contain icosahedral units in their crystal structure, and such icosahedral quasicrystal approximant nature indicates the short-range icosahedral symmetry of the atomic arrangement in the undercooled liquid. Figure 2.13 plots the icosahedral atomic clusters in three Al-TM intermetallic compounds: $Al_{45}Cr_7$, HT-$Al_{11}Mn_4$ and $Al_{13}Fe_4$; the distorted icosahedral clusters are all centred with TM atoms. Their crystal structure and lattice parameters are listed in Table 2.3.

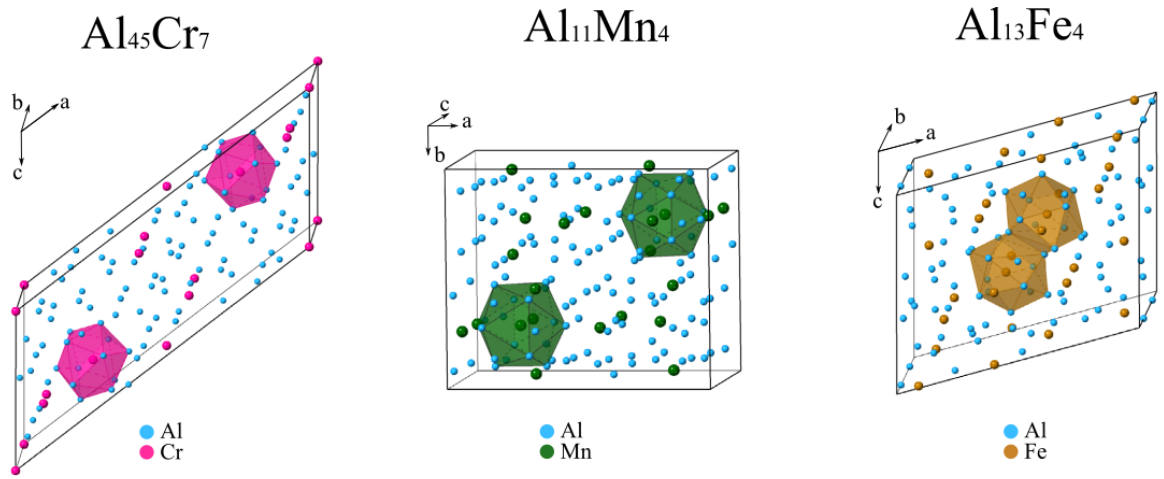

Figure 2.13 The TM-centred icosahedral atomic clusters in three Al-TM intermetallic compounds: $Al_{45}Cr_7$, HT-$Al_{11}Mn_4$ and $Al_{13}Fe_4$.

Table 2.3 The crystal structure of $Al_{45}Cr_7$, HT-$Al_{11}Mn_4$ and $Al_{13}Fe_4$

Intermetallic	Crystal system	Space group	Lattice parameters						Ref
			a(Å)	b(Å)	c(Å)	α(°)	β(°)	γ(°)	
$Al_{45}Cr_7$	Monoclinic	C2/m	25.2	7.6	11.0	90	128	90	[126]
HT-$Al_{11}Mn_4$	Orthorhombic	Pnma	14.8	12.3	12.5	90	90	90	[127]
$Al_{13}Fe_4$	Monoclinic	C2/m	15.5	8.0	12.5	90	108	90	[128]

Decagonal quasicrystals are another main group of the quasicrystals, which are aperiodic on the tenfold plane, but periodic along the decagonal axis (10/mmm) [109]. It has been found that decagonal quasicrystals are common in the rapidly cooled Al-Fe system, together with the monoclinic $Al_{13}Fe_4$ tenfold twins [129, 130]. The tenfold axis of the decagonal quasicrystal is parallel to the pseudo-tenfold [010] twin axis. The {010} plane of the monoclinic $Al_{13}Fe_4$ is shown in Figure 2.14: there are local pentagonal rings formed by Fe atoms, and there is twofold rotational symmetry coincident with the <010> in monoclinic structure, which gives $Al_{13}Fe_4$ a pseudo-tenfold symmetry around <010> [131, 132]. This intermetallic compound is also known as a decagonal-quasicrystal approximant.

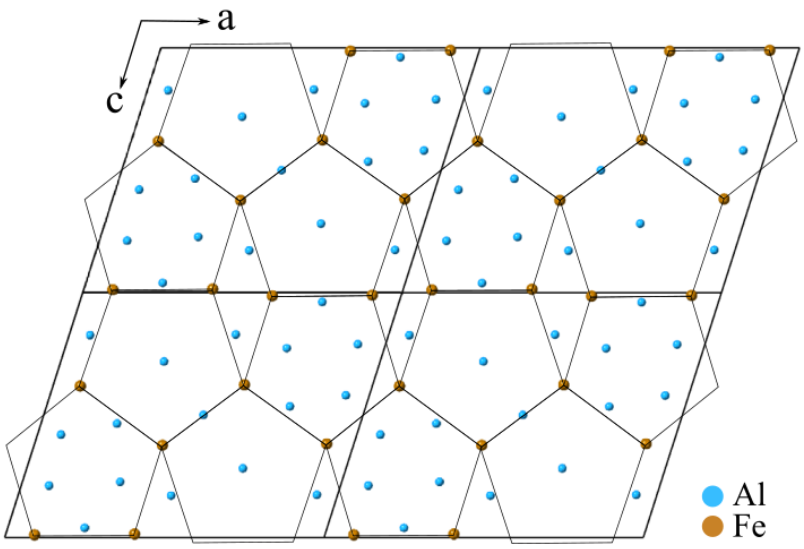

Figure 2.14 The local pentagonal atomic rings in {010} plane in $Al_{13}Fe_4$

2.4.2 Icosahedral short-range order in supercooled melt

It has been known for over a half century that substantial undercooling (~0.2T_m) can be achieved in small metallic droplets in the absence of catalytic inclusions [34]. Frank [133] postulated icosahedral short-range order (ISRO) in the melt and performed topological calculation showing such geometry has lower energy (8.4%) than other close packed FCC or HCP structures, considering the atomic interactions following a Lennard-Jones potential. More recently, combining containerless processing of high purity melts with electromagnetic levitation, ISRO was proved to be prevailing in supercooled Fe, Zr, Ni and Co pure metal melts by neutron diffraction and synchrotron radiation [134, 135]. Moreover, in these experiments such ISRO was revealed already above T_m and became more pronounced with deeper undercooling.

Although the ISRO was initially proposed for the monoatomic liquid, it was also observed in alloy systems. Topologically the interatomic distance between first-neighbour atoms on the icosahedron surface is 5% larger than the distance from the centre to the surface [136]. Combining with the chemical affinities, the ISRO may even be favoured by a small concentration of slightly smaller or larger atoms. In an undercooled Al-Fe-Co melt, ISRO was measured with significant chemical order in which the first coordinate shell of the icosahedron tends to be Al atoms centred with TM atom [137]. Similar to the pure metal liquid, the topological and chemical short-range order was enhanced with increasing undercooling. Molecular dynamics simulation of a supercooled $Cu_{64.5}Zr_{35.5}$ melt shows that the icosahedral clusters grow into larger shells with deeper undercooling [138]. For the alloys that form quasicrystals and approximants, the same tendency for the ISRO was observed in the liquid above and below T_L for $Al_{13}Fe_4$ [139], $Al_{74}Co_{26}$ [139], $Al_{88.5}(Mn_xCr_{1-x})_{11.5}$ [140] and $Al_{72.1}Pd_{20.7}Mn_{7.2}$ [141] melts. Furthermore, a metastable icosahedral quasicrystal phase was observed through in-situ X-ray diffraction by Kelton et al. in deeply undercooled $Ti_{39.5}Zr_{39.5}Ni_{21}$ melt for a few seconds before it transformed into the stable C14 Laves phase [142].

2.4.3 Nucleation from icosahedron quasicrystals and/or icosahedral short-range order

It has been known for over half a century that Ir can cause strong grain refinement in yellow gold alloys [143-145], but the mechanism remained unclear. Recently it was proposed by Kurtuldu et al. [24] that icosahedral quasicrystals and/or icosahedral short-range order forming in the undercooled melt act as a potent nucleant for FCC-Au. The iQC-mediated nucleation mechanism is illustrated in Figure 2.15 from their work.

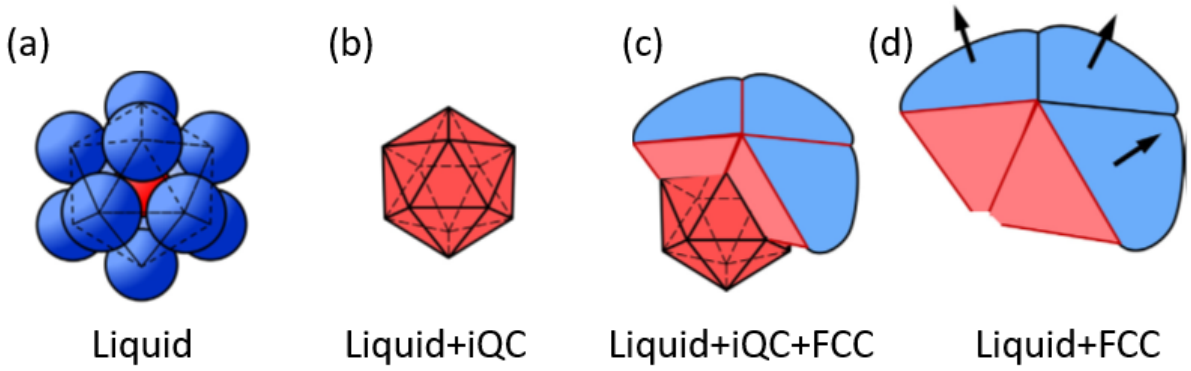

Figure 2.15 iQC-mediated nucleation mechanism: (a) Frank's icosahedral short-range order of atoms in the liquid; (b) formation of iQC in the liquid; (c) heteroepitaxy of the FCC phase on the iQC facets; (d) growth of the FCC phase and dissolution of the iQC during cooling due to the peritectic nature of the phase diagram. From Ref. [24]

A significant above-random proportion of 60° {111} twinned boundaries was measured by Kurtuldu et al.[24] between neighbouring Au grains, which was proposed to result from the FCC variants of the reported OR between the FCC unit cell and iQC: {111}||i(3) with three in-plane <110>||i(5), as shown in Figure 2.16. The same OR was also suggested between FCC Al and Cr-induced iQC in Al-Zn alloys [23].

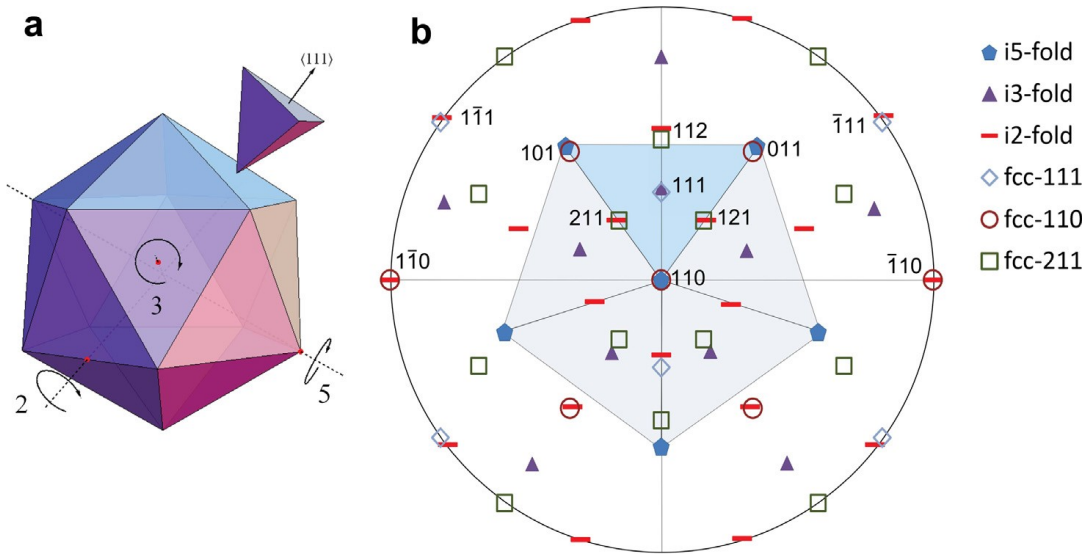

Figure 2.16 The crystallographic orientation relationship between FCC unit cell and icosahedral quasicrystals. From Ref. [24]

The crystallographic orientation relationships between icosahedral quasicrystals and a metal matrix have been studied extensively. Singh and Tsai reported the epitaxial orientation relationships between α-Mg and Mg-Zn-Y iQC precipitates, as well as between Pb, Bi and Sn particles embedded in an icosahedral Al–Cu–Fe matrix [146]. According to Bolliger and Luscher [147, 148], the vapor-deposited Al films on the fivefold symmetry surface of the Al–Pd–Mn icosahedral quasicrystals exhibit an epitaxial orientation relationship between the FCC phase and iQCs, which is the same as in Figure 2.16: one of the FCC <111> direction parallel to one of the icosahedral threefold axes.

Apart from the most commonly observed OR (OR1) between FCC phase and icosahedral quasicrystals, four more ORs have been reported between the iQC and aluminium matrix, as OR2-OR5 listed in Table 2.4. OR1-OR3 were found between the Al-Mn iQC and Al matrix by Beeli et al.[149], and OR1-OR4 were reported in the Al-Li-Cu-Mg system by Loisseau and Lapasset [150, 151]. OR5 was originally observed between an iQC and cubic rational approximants [119, 152-154], but it has also been found between the dodecahedron shaped Al-Mn icosahedral precipitates and the aluminium matrix [155]. Among all five ORs, OR1 is the best fit between the FCC phase and iQC, according to Singh and Tsai [156], as most of the major axes and planes of these two phases match to each other.

Table 2.4 Orientation relationships between icosahedral quasicrystal and FCC Al

OR	Icosahedron axes/planes	Corresponding FCC Al directions/planes
1	Twofold	<111>(3), <110> (3), <112>(3)
	Fivefold	<110>(3), <113> (3)
2	Twofold	<100>(2), <111>(1), <110>(1), <112>(1)
	Fivefold	<100>(1), <112>(2), <315>(2), <221>(1)
3	Twofold	<100>(1), <110>(2), <112>(4)
	Fivefold	<111>(2), <112>(2), <113>(2)
4	Twofold	<110>(1), <112>(4), <221>(1)
	Fivefold	<111>(1), <112>(2)
5	Twofold	<100>(3), <112>(3), <123>(3)
	Fivefold	<012>(3)

2.5 Grain boundary formation in equiaxed solidification

2.5.1 Grain coalescence and grain boundary migration

At the last stage of solidification, with thin liquid films left, grains start to impinge and form grain boundaries. This process is termed 'coalescence'. The thermodynamic criterion for grain coalescence to happen was deduced by Rappaz et al. [157]:

$$\Delta T = \frac{\Delta \Gamma}{\delta} = \frac{\gamma_{gb} - 2\gamma_{sl}}{\Delta s_f} \cdot \frac{1}{\delta} \qquad \textit{Equation 2.27}$$

Where ΔT is the undercooling for approaching planar liquid/solid interfaces to coalesce into a grain boundary. $\Delta\Gamma$ is the difference between the grain boundary energy, γ_{gb}, and twice the solid-liquid interfacial energy, $2\gamma_{sl}$, divided by the entropy of fusion, Δs_f. δ is a measure of diffuse interface thickness (typically ~ 2nm). If $\gamma_{gb} < 2\gamma_{sl}$, $\Delta T < 0$ and the liquid film is unstable. The two liquid-solid interfaces coalesce into grain boundaries immediately as they get close enough (at a distance on the order of δ). This situation is referred to as 'attractive', typically for two dendritic arms belonging to the same grain ($\gamma_{gb} = 0$) or grains that form low angle grain boundaries, as shown in Figure 2.17 [158]. If $\gamma_{gb} = 2\gamma_{sl}$, $\Delta T = 0$ and this situation is referred to as 'neutral'. If $\gamma_{gb} > 2\gamma_{sl}$, $\Delta T > 0$ and the liquid film is stable between the neighbouring grains until the undercooling exceeds ΔT. Although the value of γ_{gb} depends strongly on the misorientation between the impinging grains, this 'repulsive' situation applies to the coalescence of most high angle grain boundaries (Figure 2.17(b)) as Miller and Chadwick [159] indicated the average grain boundary energy $\gamma_{gb,ave} \approx 2.2\gamma_{sl}$.

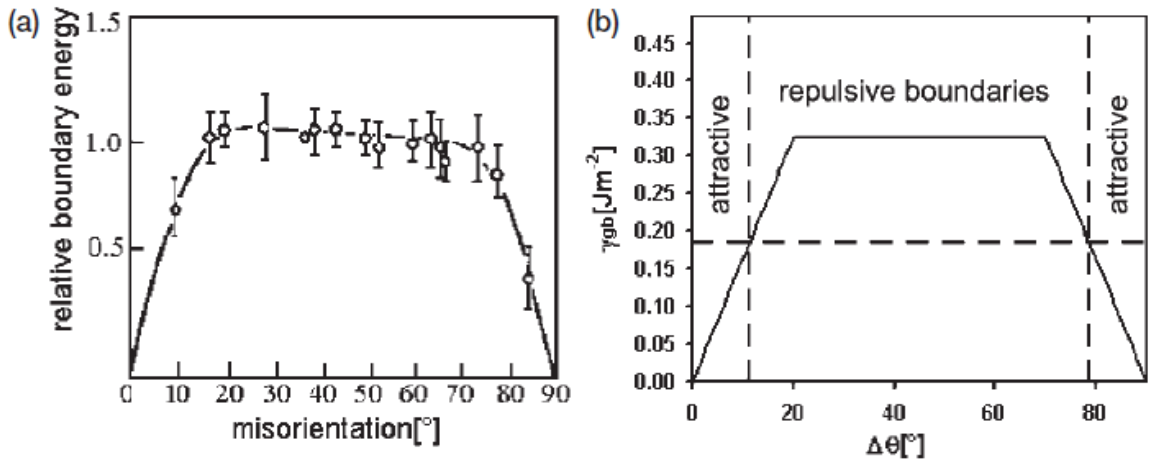

Figure 2.17 (a) The measured relative grain boundary energy for symmetric interface of Al <100> tilting. Note that 1.0 on the y-axis corresponds to 0.324 J/m^2, and the 'misorientation' on x-axis means tilting angle, not necessarily the real misorientation between two FCC unit cell [160]. (b) The simplified grain boundary energy distribution used for Mathier's coalescence model [158], where the attractive region corresponds to low angle grain boundaries and repulsive region corresponds to high angle grain boundaries.

A detailed model of an equiaxed mushy zone was developed to describe the transition from a continuous liquid film network into a fully coherent solid by Vernede et al. [161, 162]. The model assumes the simultaneous nucleation of grains at random nucleation centres with random orientations, and the smooth grain boundaries between adjacent grains are approximated into straight line segments. Complete diffusion was assumed in the liquid while back-diffusion in the solid was computed according to a Landau transformation. The undercooling for coalescence was calculated based on Eq. 2.25 and the grain boundary energy was simplified into Read-Shockley distribution [163]. Figure 2.18 shows the result for the directional solidification of Al-1wt% Cu [161]. On the left are simulated local microstructures from the four black rectangles. The black areas between grains are liquid channel and grains with 'dry' interface (no liquid) are coloured with the same grey scale. On the right are the changes of temperature and solid fraction across the sample. For (a) and (b) ($0<g_s<0.97$), most of the grains are isolated, and for (c) ($0.97<g_s<0.99$), large grain clusters/aggregates are formed. Final continuous solid is formed in (d) when $g_s>0.99$.

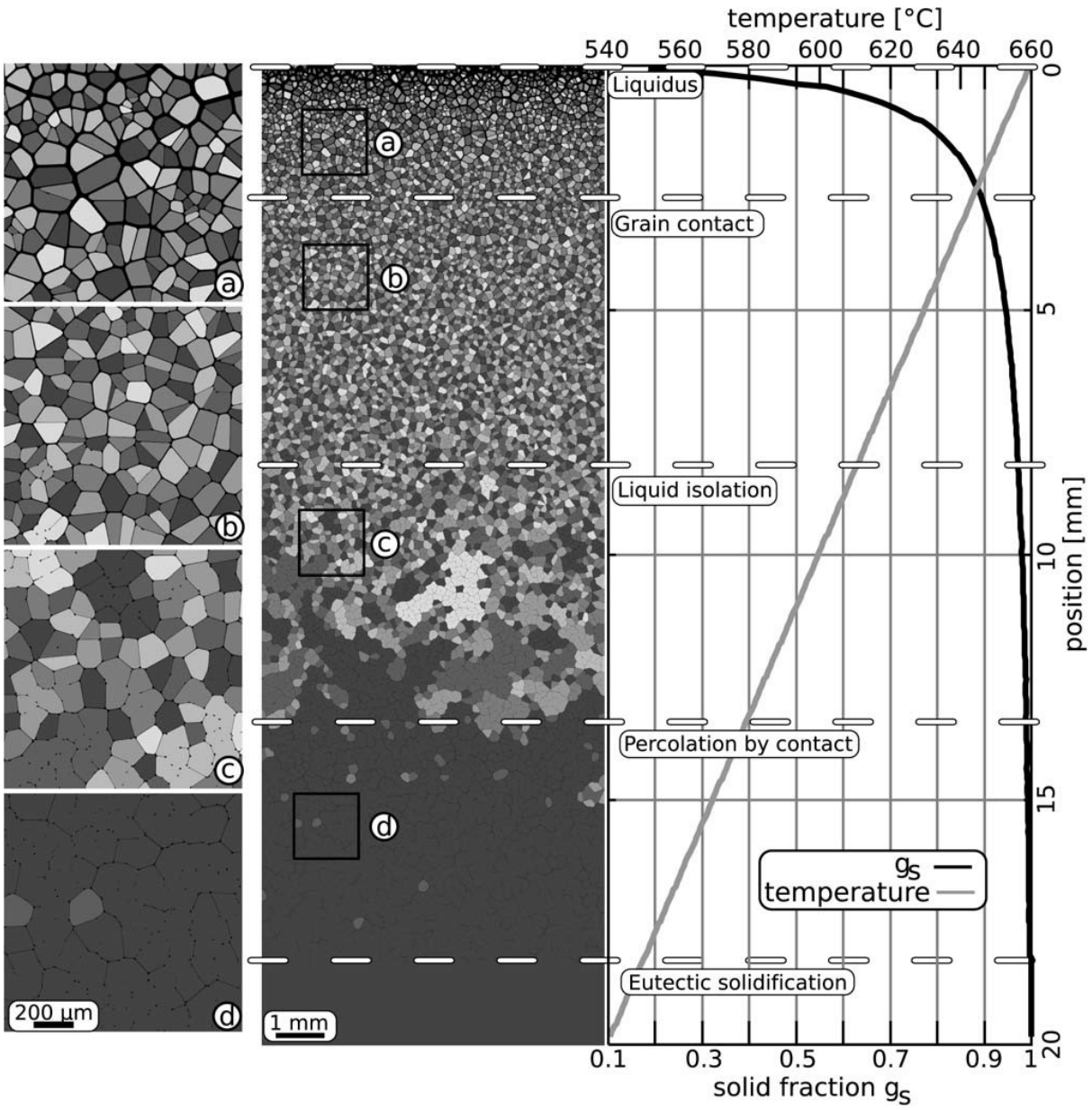

Figure 2.18 Calculated mushy zone for an Al–1 wt.% Cu alloy cooled at 1K/s in a gradient of 6000 K/m. Liquid channels are coloured in black, and grain clusters (no liquid film) are shaded with the same grey level. On the left: a, b, c, d are the close views of the black square areas from the simulated result in the middle. From Ref. [161]

Moreover, after grain coalescence, in some alloys grain boundaries can migrate in the very last-stage of solidification. It was first proposed by Biloni in 1961 [164] that solidification grain boundary migration in Al changed its grain structures. Subsequently more observations of grain boundary migration during solidification were reported in Al-0.28wt% Fe [165], Al-0.2wt% Cu [166], Ti-6 wt% Cr [167] and AM50 (Mg-4.9wt% Al-0.34wt% Mn) [168]. It was suggested that the migration occurs rapidly

near the solidus temperature of the alloy [169-171], and after migration the grain boundary energy decreases [172, 173]. A proposed grain boundary migration model during solidification is plotted in Figure 2.19(a) [167]. Atoms in part of grain 2 (blue) change their orientation into grain 1 (yellow), and the initial grain 2 is divided into 3 separate grains at the final state. The dendritic segregation profile is retained through this process, which can be directly observed from the optical image of the as-cast Ti-6 wt.% Cr in Figure 2.19(b) and (c) [167].

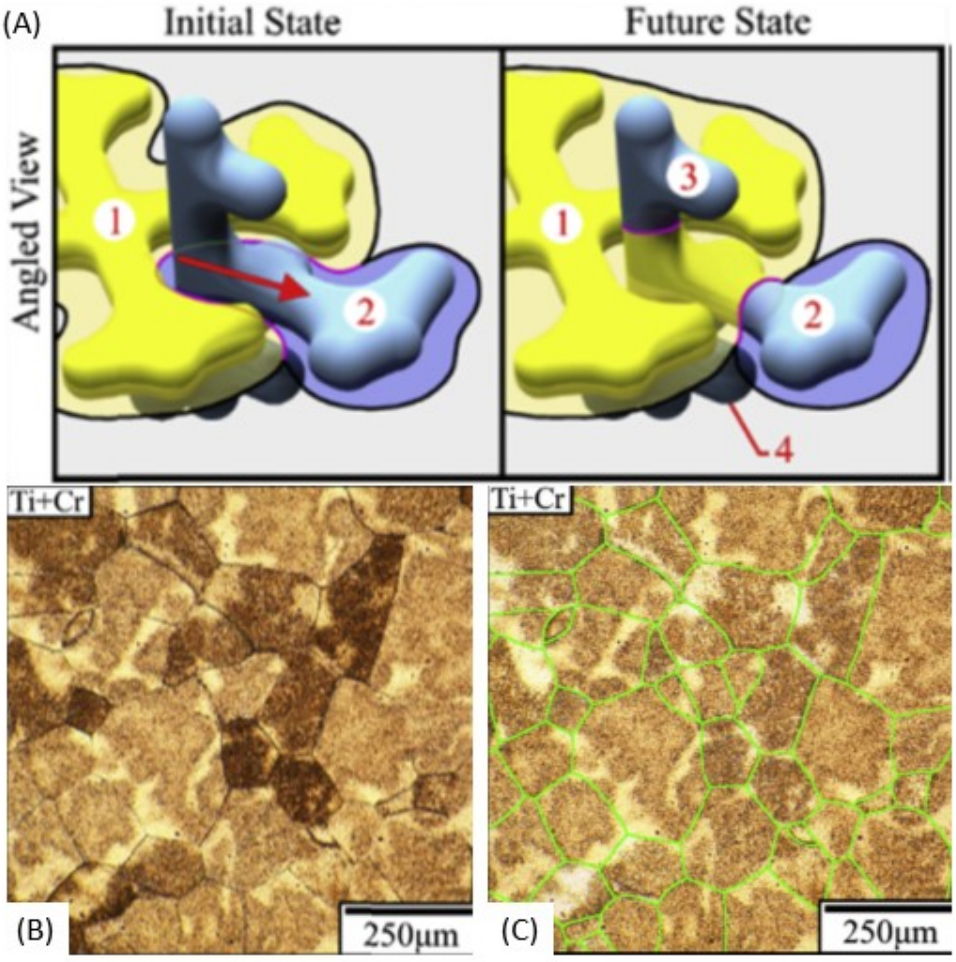

Figure 2.19 (A) A theorised grain boundary migration pathway. (B) Optical image of as-cast Ti-6wt% Cr after etching, revealing the dendritic segregation due to chemical composition. (C) Microstructure of B superimposed with the highlighted grain boundaries (green). From Ref. [167]

2.5.2 Grain collision and movement under external shear/forced convection

In high pressure die casting (HPDC) of Al and Mg alloys, agglomeration and bending of grains caused by grain collisions under external mechanical stress can produce a texture different to the theoretical prediction for a random orientated microstructure [174]. Compared to statically cooled AlSi4MgMn, HPDC produces a higher frequency of grain boundaries at low angle (5°-10°) and high angle (55°-60°). For Mg alloys, HPDC AM50 alloy has higher fraction of α-Mg grain boundaries at various angles from 0° to 90° compared to the statically cooled sample. Moreover, for Al-6.5wt.% Si alloy that has been sheared in the semi-solid state with 0.2 solid fraction and quenched, the investigation of the orientation relationships between the neighbouring α-Al grains in agglomerates revealed that the α-Al grains were related either by low angle grain boundaries with misorientation less than 10° or by misorientation of near 60° about {111} which corresponding to a coherent twin [175]. Therefore, it appears that, under external shear in the mushy zone, collisions between grains can form certain preferred boundaries and produce a texture which is different to the theoretical prediction for total random microstructure.

More recently, with the help of 3D X-ray diffraction microscopy, direct observation of grain rotation to form preferred boundaries was made during the annealing of semisolid Al-Cu alloy with 0.7 solid fraction [176, 177]. Without any external force, grains were found to rotate to lower the grain boundary energy, and the final texture depends on the grain boundary energy landscape. Figure 2.20 shows the rotations of two reconstructed grains before (a) and after (b) annealing, and a computed tomography (CT) slice across the two grains. After rotation the misorientation between the two grains decreases from 10.1° to 7.4°. As indicated in the CT slice, the crystal lattice of the two grains were in direct contact, and there is no visible liquid film between them.

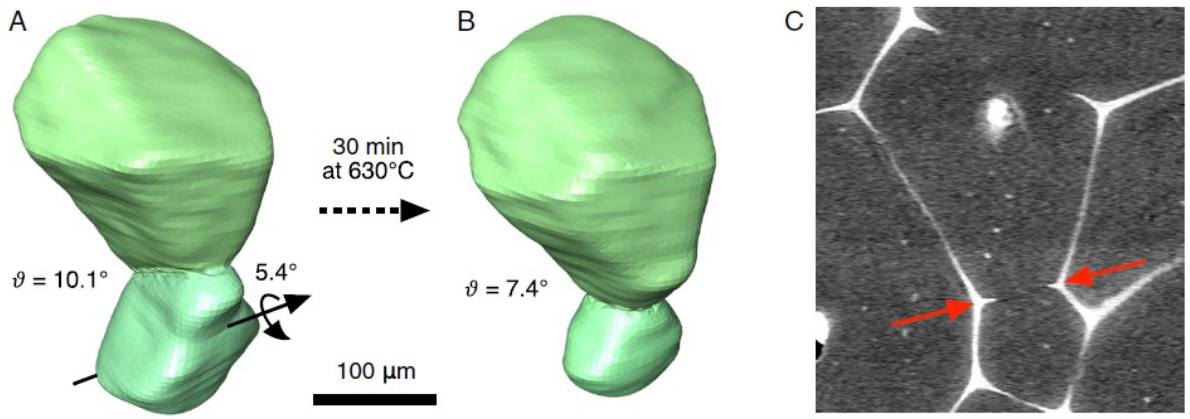

Figure 2.20 The rotation of Al grains in Al-5wt% Cu holding at 630°C for 30 min. (A) Initial and (B) final 3D reconstructed morphology of two grains. (C) X-ray computed tomography image of the two grains showing 'dry' interface. From Ref. [176]

2.5.3 Grain boundary defects

From microscopic perspective, there are three parameters which are represented by a vector characterising a rigid body translation from one grain to the other [178]. The translations are independent of the macroscopic parameters which will be discussed in the next section, but are controlled by the minimisation of grain boundary energy to generate the atomic structure of the grain boundary under actual external conditions such as temperature, pressure and chemical compositions [179].

As mentioned above, individual atoms at grain boundaries are likely to be rearranged and shifted from their regular crystal positions. For the grain boundary between two different phases (nucleant and growing solid), Turnbull and Vonnegut proposed different interface structure according to the disregistry (δ) between the two lattice, as shown in Figure 2.21. For small disregistry the atoms of growing solid can precisely fit the atoms of nucleant with a certain amount of strain (ε). In this situation, the interface form coherently between the two crystals. For larger disregistry some regions in the interface are in good fit, while in other regions the atoms cannot perfectly match through a certain amount of strain. Therefore, there will be dislocations forming at grain boundary to release the accumulated stress. The interface could be pictured as good fit regions separated by a dislocation gridwork and the dislocation density is proportional to (δ-ε).

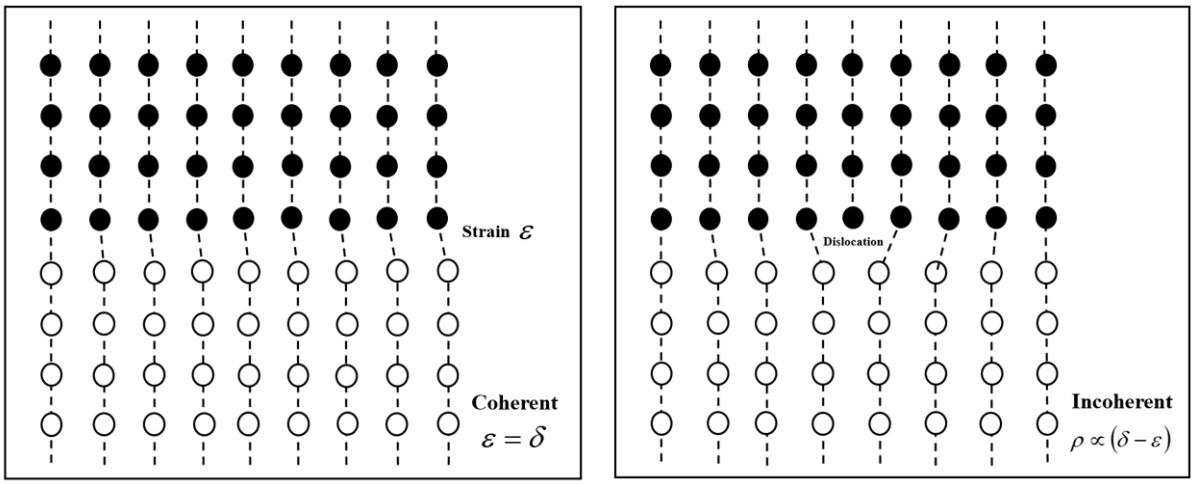

Figure 2.21. The grain boundaries between nucleant and growing solid with different lattice matching.

2.6 Grain boundary plane distribution & Grain boundary character distribution

2.6.1 Five macroscopic parameters characterisation

A grain boundary segment can be seen as a function of lattice misorientation and grain boundary plane orientation, $\lambda(\Delta g, \vec{n})$, and therefore it requires five macroscopic parameters (three for the lattice misorientation and two for the grain boundary plane orientation) to fully describe the character of grain boundaries [180-182]. The definition of the five parameters is plotted in Figure 2.22. The first three angles $(\varphi_1, \Phi, \varphi_2)$ makes the transfer matrix to rotate from orientation A to B:

$$g(\varphi_1, \Phi, \varphi_2) = \begin{pmatrix} c\varphi_1 c\varphi_2 - s\varphi_1 \varphi_2 c\Phi & s\varphi_1 c\varphi_2 + c\varphi_1 s\varphi_2 c\Phi & s\varphi_2 s\Phi \\ -c\varphi_1 s\varphi_2 - s\varphi_1 c\varphi_2 c\Phi & -s\varphi_1 s\varphi_2 + c\varphi_1 c\varphi_2 c\Phi & c\varphi_2 s\Phi \\ s\varphi_1 s\Phi & -c\varphi_1 s\Phi & c\Phi \end{pmatrix} \quad \textit{Equation 2.28}$$

Where c and s means cosine and sine, respectively. The last two angles describe the grain boundary plane normal, $\vec{n}(\phi, \theta)$, which is shown in Figure 2.22 (b). The first angle, ϕ, is the angle between the grain boundary trace normal and x-axis on the cross section, and the second angle, θ, is the angle between the plane normal and the z-axis in 3D space.

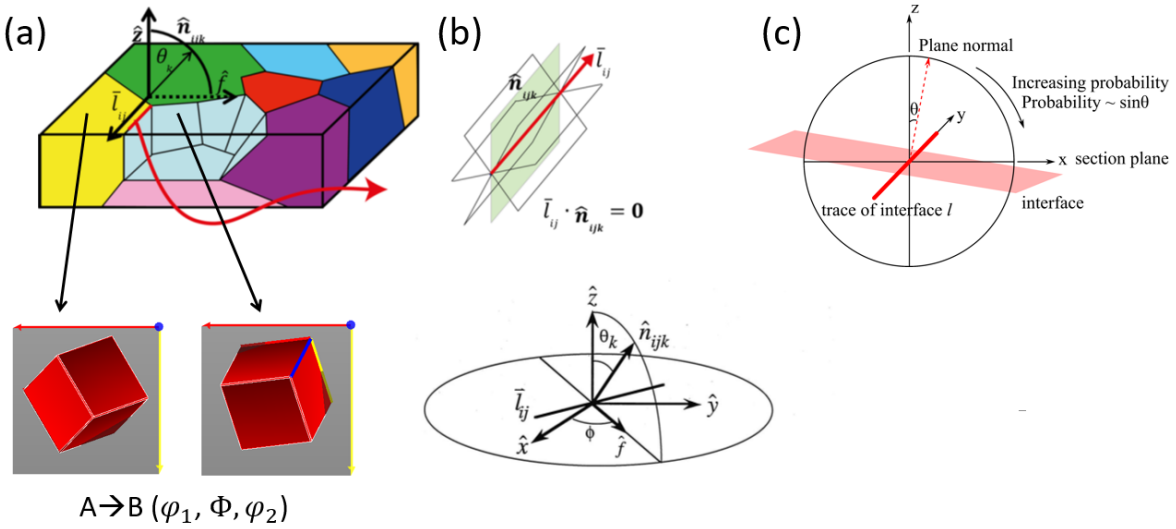

Figure 2.22 Definition of the five macroscopic parameters for grain boundaries characterisation. From Ref.[183]

The first four parameters out of five can be precisely obtained through the analysis of an EBSD dataset, while for the last one, the precise value can be determined through 3D EBSD analysis, or it can be assessed by considering the probability from 2D EBSD mapping, as illustrated in Figure 2.22(c). For a sectioned grain boundary trace l, all possible grain boundary planes must contain this segment, i.e. all possible planes must be in the zone of l. For all these possible grain boundary planes, the plane perpendicular to the sectioned plane has the highest probability, while the plane parallel to the sectioned plane has the lowest probability. The probability of these planes is proportional to $\sin(\theta)$ (θ is the angle between the grain boundary plane normal and z-axis). For every grain boundary segment observed, it corresponds to a set of possible planes, containing a true interfacial plane with a set of incorrect planes. The probability of the true plane in the set is always 1 while the probability of any incorrect planes in the set is less than 1. After considering a large enough grain boundary dataset, the frequency of true grain boundary planes will greatly exceed other incorrect ones, and provide useful information about the real interface between neighbouring grains.

Considering the distribution of interfacial planes at all grain boundaries, $\lambda(\vec{n})$, gives us a grain boundary plane distribution (GBPD), while considering the distribution of interfacial planes at the grain boundaries with certain misorientation, or more precisely, with certain orientation relationships between the neighbour lattice, gives us a grain boundary character distribution (GBCD), $\lambda(\Delta g, \vec{n})$. For example, in FCC alloys, the $\lambda(\vec{n}|60^o/[111])$ describes the distribution of interfacial planes at all 60° [111] twin grain boundaries.

2.6.2 GBPD and GBCD in Al and Mg alloys

The GBPD and GBCD analysis has been carried out on polycrystalline specimen from various materials [184-194]. In cold rolled and annealed CP-Al alloy, the grain boundary plane distribution (Figure 2.23(a)) shows that the {111} planes are preferred to be the grain boundary plane [195]. The peak is 25% higher than the random distribution. Figure 2.23(b) and (c) are the grain boundary character distributions for two special grain boundaries: the 60° {111} twin and 50° <110> twin. For the 60° {111} twinning boundaries, the {111} common plane is highly preferred (~28 times higher than random) to be the interfacial plane due to the perfect atomic matching at the interface. The same for 50° <110> twinning boundaries with {113} common plane to be the interface. In cast and annealed Mg-3Al-1Zn (AZ31) alloy, there is a high preference for 56° and 64° grain boundaries between Mg grains [196]. With further GBCD analysis, twinned grain boundaries with preferred coherent interfaces that correspond to low interfacial energy were identified at these two misorientation angle: 56° $[11\bar{2}0]\{1\bar{1}01\}$ and 64° $[11\bar{2}0]\{1\bar{1}03\}$.

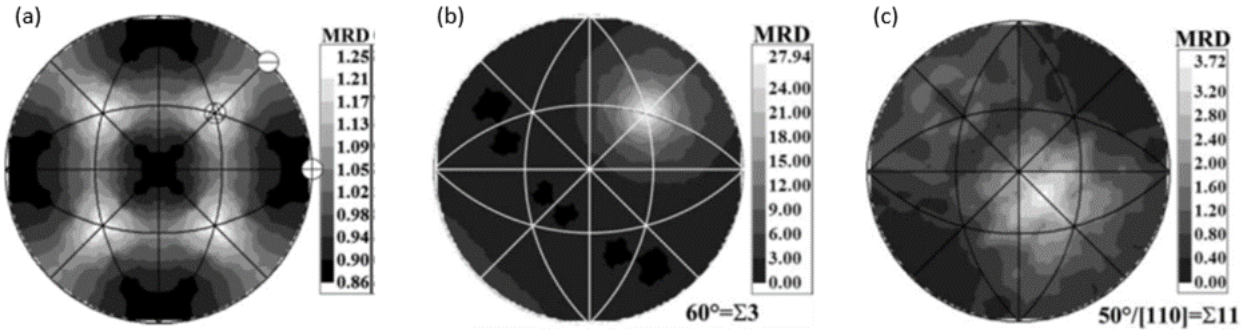

Figure 2.23 (a) GBPD of the cold rolled and annealed CP Al. (b) GBCD for 60° {111} twin grain boundaries showing the {111} plane to be the interface. (c) GBCD for 50° <110> twin grain boundaries showing the {113} plane to be the interface. [195]

As indicated above, in order to form low energy boundaries during annealing, two mechanisms are likely to happen between grains: (i) rotation of grains which involves the first three parameters and; (ii) the motion of the interface (straightening and rotation) which involves the last two parameters. A more direct result is plotted in Figure 2.24 showing that the lower the interfacial energy the higher

frequency it is observed for symmetric boundaries tilting along <110> in annealed CP-Al [197]. Note that the 'misorientation' angle in the x-axis means the tilt angle along the <110> direction, not the misorientation between two unit cells. For 60° {111} twinning, it corresponds to 70.5° tilt along the common <110> direction, while 50° {113} twinning corresponds to 129.5° tilt along the common <110> direction. These two low energy interfaces, together with the low angle boundaries, are preferred to form during CP Al annealing.

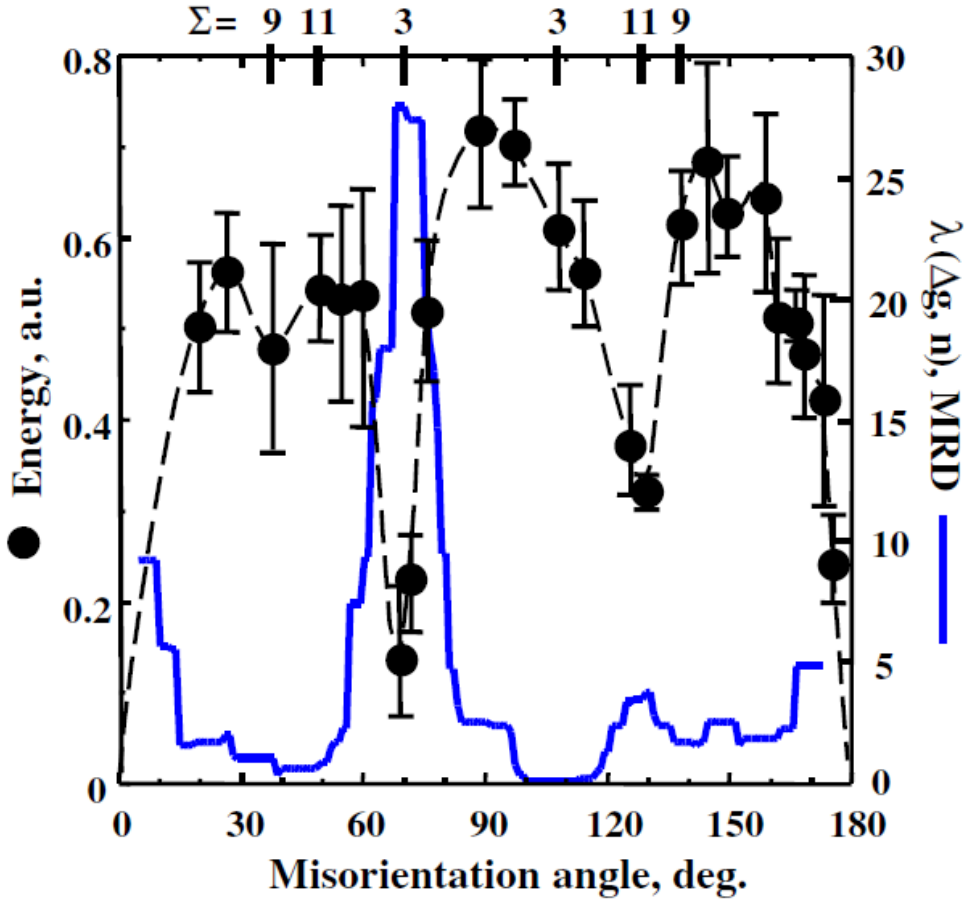

Figure 2.24 Comparison of measured energies (dashed line) to populations (solid line) for symmetric [110] tilt boundaries. The misorientation angle is the tilting angle along the common [110] direction. [197]

2.7 Density Functional Theory (DFT)

Crystals are formed by a collection of well-defined atoms, and each atom contains two parts: the nucleus and electrons. The atomic nuclei are much heavier than electrons, which means the electrons are highly mobile and respond much faster to the change of surroundings than nuclei. In order to compute the energy of atoms, the question is split into two parts: first the atomic nuclei position is fixed and the ground state energy for electrons moving in the field of the fixed nuclei needs to be calculated. The ground state energy is a function of the nuclei positions: $E(\vec{R}_1, \vec{R}_2, \dots, \vec{R}_M)$. After we obtain this energy function, we can know the energy change when we move atoms, and find the lowest energy configuration [198].

2.7.1 The Schrodinger Equation

In quantum mechanics [199], one simple form of the time-independent Schrodinger equation [200] that describes the states of quantum particles can be written as:

$$H\psi = E\psi \qquad \textit{Equation 2.29}$$

Where H is the Hamiltonian operator, ψ is the wave functions of the quantum particles and E is the energy. There is a set of solutions, known as eigenstates, ψ_n, and each ψ_n has a corresponding E_n value which is an eigenvalue. When $n = 0$, E_0 is known as the ground state energy. The detailed expression of the Hamiltonian depends on the physical system. For a collection of well-defined atoms in a crystal, multiple electrons are interacting with multiple nuclei and the Schrodinger equation is in a more complicated form:

$$\left[-\frac{\hbar^2}{2m}\sum_{i=1}^{N}\nabla_i^2 + \sum_{i=1}^{N}V(\vec{r}_i) + \sum_{i=1}^{N}\sum_{j<i}U(\vec{r}_i, \vec{r}_j)\right]\psi = E\psi \qquad \textit{Equation 2.30}$$

Here, $\hbar$ is the reduced Planck constant and m is the electron mass. The three terms in the brackets correspond to the kinetic energy of each electron, the interaction energy between each electron and the whole collection of nuclei, and the interaction energy between electrons. ψ is the electron wave

function which describes the spatial positions of the N electrons: $\psi = \psi(\vec{r}_1, \vec{r}_2, \dots, \vec{r}_N) = \psi_1(\vec{r})\psi_2(\vec{r}) \dots \psi_N(\vec{r})$.

Considering the definition of the Hamiltonian above, the electron-electron interaction term is the most critical one in terms of solving the equation. The wave function of an individual electron $\psi_i(\vec{r})$ cannot be determined without simultaneously considering the wave functions of other electrons. Therefore, the Schrodinger equation is a many-body problem and it is extremely difficulty to solve the equation considering N can be huge in real problems.

2.7.2 Electron density

According to quantum mechanics, the electron wave functions at certain position cannot be observed directly. The quantity that can be measured in principle is the probability of finding electrons at a certain position, i.e., the electron density:

$$n(\vec{r}) = 2\sum_i \psi_i^*(\vec{r})\psi_i(\vec{r}) \qquad \textit{Equation 2.31}$$

The term inside the summation refers to the probability of finding an electron in an individual wave function ψ_i at position $\vec{r}$, and the summation covers all the individual electron wave functions that are occupied by electrons. The factor 2 comes from the spin of electrons and the Pauli exclusion principle points out that each electron wave function can only be occupied by two electrons with different spins. From Eq. 2.29 it is clear that the electron density that contains a great amount of information is a function of only three coordinates, which is much simpler compared to the full wave function solution of the many-body Schrodinger equation in Eq. 2.28. If we sum the electron density throughout the whole material, we have the total number of electrons, N:

$$\int n(\vec{r})d\vec{r} = N \qquad \textit{Equation 2.32}$$

2.7.3 Density functional theory

The entire density functional theory is built on two fundamental theorems that were proved by Hohenberg and Kohn in 1964 [201]. The first theorem is: The ground-state energy from the Schordinger equation is a unique functional of the electron density. That is to say, the electron density uniquely determines all properties, including the energy and the wave function, of the ground state. The second Hohenberg-Kohn theorem is: The electron density that minimises the energy of the overall functional is the true electron density corresponding to the full solution of the Schrodinger equation. Therefore, instead of solving the Schrodinger equation by finding the wave functions of $3N$ variables, the ground-state energy can be obtained by finding the corresponding electron density which only contains 3 spatial variables.

The Hohenberg-Kohn theorem shows that the ground-state energy of many electrons is a functional of the electron density, but it does not give any forms of this functional. Kohn and Sham incorporated the electron density to modify the single electron Schrodinger equation, which is the Kohn-Sham equation [202]:

$$\left[-\frac{\hbar^2}{2m}\nabla^2 + V(\vec{r}) + V_H(\vec{r}) + V_{XC}(\vec{r})\right]\psi_i(\vec{r}) = \varepsilon_i\psi_i(\vec{r}) \qquad \textit{Equation 2.33}$$

In the brackets, the four terms are, in order, the kinetic energy of the single electron, the interaction energy of the single electron with the whole collection of atomic nuclei, the interaction energy between the single electron with the whole collection of electrons, and the exchange-correlation energy. The third term, $V_H(\vec{r})$, which is called the Hartree potential, is defined as:

$$V_H(\vec{r}) = e^2 \int \frac{n(\vec{r}')}{|\vec{r}-\vec{r}'|} d\vec{r}' \qquad \textit{Equation 2.34}$$

This potential represents the Coulomb repulsion between the single electron and the total electron density. But there is a self-interaction contribution in the Hartree potential because the single electron described in the Kohn-Sham equation is also part of the total electron density. This self-interaction is unphysical, and the correction for it, together with other effects, is included into the last term $V_{XC}(\vec{r})$ in Eq. 2.31, which describes the exchange and correlation contribution.

The fundamental principle of density functional theory calculation to find the ground-state electron density and corresponding energy is based on an iterative algorithm:

1. Define an initial trial electron density, $n(\vec{r})$;
2. Solve the Kohn-Sham equation (Eq. 2.31) with the trial electron density to find the single electron wave function, $\psi_i(\vec{r})$;
3. Calculate the electron density with the Kohn-Sham single electron wave function from step 2: $n'(\vec{r}) = 2\sum_i \psi_i^*(\vec{r})\psi_i(\vec{r})$ (Eq. 2.29);
4. Compare the calculated electron density, $n'(\vec{r})$, with the initial electron density, $n(\vec{r})$. If they are the same, then this is the ground-state electron density, and use it to calculate the ground-state energy. Otherwise, update the trial electron density and repeat from step 2.

There are many detailed operations in this process, e.g., how to define the initial trial electron density, what is the approximation form of the exchange-correlation term, to what extent the two electron density can be considered the same, how to update the trial electron density etc. These details are out of the scope of the research, and thus are not presented here.

Chapter 3 Solidification orientation relationships between Al_3Ti & TiB_2

3.1 Introduction

Orientation relationships (ORs) can form during solidification by a variety of mechanisms. Often, the OR formed by heterogeneous nucleation and its disregistry are used as a measure of the potency of particles in a grain refiner. However, there can be more than one OR formed and multiple mechanisms can generate ORs during solidification so it is often difficult to assign each orientation relationship to a formation mechanism, and it can be highly challenging to identify the nucleating particle with certainty. To build a deeper understanding of the mechanisms that lead to solidification ORs, here new approaches are presented to link ORs to their formation mechanism using a model system containing numerous potent nucleant particles. In this Chapter, TiB_2 and Al_3Ti were selected to study OR formation for the following reasons:

1. Both are faceted phases with simple growth facets which simplifies the interpretation of pushing and engulfment processes;

2. There are crystallographic similarities between these hexagonal and tetragonal phases [203, 204] which allows low energy interfaces and multiple ORs to form;

3. These phases are important in the grain refinement of Al alloys, where a thin layer of Al_3Ti forms on TiB_2 particles followed by the nucleation of α-Al.

As shown in Equation 2.22 in the Literature Review, the reported OR between Al_3Ti and TiB_2 can be written as:

$$\{112\}_{Al3Ti} \parallel \{0001\}_{TiB2}, \text{with } <\bar{2}01>_{Al3Ti} \text{ (or } <1\bar{1}0>_{Al3Ti}) \parallel <11\bar{2}0>_{TiB2} \quad (OR1)$$

In this Chapter, analytical SEM studies and DFT calculations are combined to study the solidification ORs between Al_3Ti and TiB_2 with three main aims: (i) identify the preferred ORs between Al_3Ti and TiB_2; (ii) distinguish ORs formed by different mechanisms and (iii) understand the active interactions between TiB_2 particles and the growing Al_3Ti front.

3.2 Methods

3.2.1 Sample preparation

Orientation relationships between Al_3Ti and TiB_2 were studied in three types of sample. First, in commercial Al-5Ti-1B and Al-3Ti-1B (wt%) grain refiner rods containing ~0.2-0.8 μm TiB_2 particles. Second, in samples of remelted and solidified master alloy. Third, in samples of Al-0.8wt%Ti with added ~50-100 μm TiB_2 particles in which numerous Al_3Ti particles had solidified on each large TiB_2 particle.

The Al-5Ti-1B and Al-3Ti-1B rods were supplied by the London and Scandinavian Metallurgical Company. For the partial-remelting and casting of the Al-3Ti-1B rod, the alloy was re-heated to 980°C in a BN-coated clay-bonded graphite crucible in a resistance furnace. After holding for 4 hours, the melt was stirred with an Al_2O_3 rod and then poured into a 300°C BN-coated steel mould of inner height 60 mm and inner diameter 50 mm.

To make Al-0.8wt%Ti with large TiB_2 particles, a procedure to grow TiB_2 particles was developed, exploiting the relatively low melting point of the Fe-TiB_2 eutectic. First, 400 g of Fe-10.10Ti-3.86B (wt%) alloy was made by arc melting 99.9% Fe flake, 99% B pellets and 99.99% Ti ingot. Arc melting was conducted in 30 mTorr vacuum, back-filled with Ar on a water-cooled Cu plate. The alloy was melted, flipped, remelted and then cast into a rectangular copper mould. The casting consisted of primary TiB_2 (~20% vol%) in a matrix of Fe+TiB_2 eutectic similar to Ref. [205]. The Fe was then dissolved in 37% HCl at 50°C to release the 50-100 μm primary TiB_2 crystals. 50g of Al-0.8wt%Ti alloy was then arc-melted using CP 99.6% Al ingots and 99.99% Ti ingot with the TiB_2 particles extracted from the Fe-10.10Ti-3.86B alloy made above. The alloy was melted, flipped three times, and then the power was stopped and the alloy solidified on the water-cooled Cu plate.

To prepare cross-sections, samples were mounted in Struers VersoCit acrylic cold mounting resin and then ground to 4000 grit with SiC paper followed by polishing with colloidal silica on a nap cloth for 5 minutes.

To study the 3D morphology of the intermetallic compounds, the α-Al phase was selectively etched in anhydrous 1-butanol under an Ar atmosphere at 117°C for approximately 4 hours to remove the Al matrix. Intermetallic crystals were collected and placed on a stub for further study by analytical scanning electron microscopy (SEM).

For crystallographic investigation on both cross-sections and extracted crystals, a Zeiss Auriga field emission gun SEM fitted with a Bruker e-FlashHR electron backscatter diffraction (EBSD) detector was used. Bruker Esprit 2.0 software, combined with MTEX 4.4 toolbox within MATLAB™9.2 (Mathworks, USA) [206], were applied to analyse and plot the orientation relationships between different phases. The Orientation Imaging Microscopy (OIM™) Data Analysis software were used to index the Kikuchi pattern. Throughout this thesis, all unit cell wireframes in figures were plotted from Euler angles (ϕ_1, Φ, ϕ_2) measured by Bruker Esprit 2.0 software. With the Euler angles under Bunge convention (ZXZ), the orientation matrix for a crystal to rotate from the reference crystal frame into the sample frame is:

$$O = R_Z(\phi_2)R_X(\Phi)R_Z(\phi_1) \qquad \textit{Equation 3.1}$$

Where R_Z and R_X are two rotation matrices of rotating along Z and X axis, respectively:

$$R_Z(\theta) = \begin{pmatrix} cos\theta & sin\theta & 0 \\ -sin\theta & cos\theta & 0 \\ 0 & 0 & 1 \end{pmatrix} \qquad \textit{Equation 3.2}$$

$$R_X(\theta) = \begin{pmatrix} 1 & 0 & 0 \\ 0 & cos\theta & sin\theta \\ 0 & -sin\theta & cos\theta \end{pmatrix} \qquad \textit{Equation 3.3}$$

3.2.2 DFT calculation

In order to compare the interfacial energy corresponding to each OR measured in this work, DFT calculations were performed using the Vienna Ab Initio Simulation Package (VASP) framework [207]. A planewave basis set and projector augmented wave (PAW) pseudopotentials [208] were used. The generalised gradient approximation (GGA) in the formalism of Perdew-Burke-Ernzerhof (PBE) was chosen for the exchange and correlation energy functional [209]. All parameters were converged to satisfy a criterion of 10^{-4} eV for each element: B, Al and Ti, in their pure form, where $2s^2 2p^1$, $3s^2 3p^1$ and $3p^6 3d^2 4s^2$ electrons respectively were treated explicitly (they are not included in the core when forming the pseudopotentials). It was determined that an energy cutoff of 350 eV, *k* point density of ~0.025 $Å^{-1}$ and Methfessel Paxton smearing width of 0.1 eV [210] were sufficient for all species and were kept consistent for the calculations.

The bulk simulations were performed under constant pressure conditions in the most stable forms at 0K for all phases, and the results are listed in Table 3.1, with comparison to previous studies [85, 203, 204, 211-217]. The lattice parameters (neglecting zero point motion) match well with experiments, with all differences being less than 1%. The calculated formation energies for Al_3Ti and TiB_2 (for Al, Ti and B in their pure bulk phases it is defined as zero) are in good agreement with previous calculations and experiment results, with differences less than 5%.

Table 3.1 The lattice parameters and formation energies from DFT calculations and experiments

Phase	Crystal structure	Lattice parameter (Å)		Formation energy (kJ/mol)	
		Calculated	Experimental	Calculated	Experimental
Al	Cubic	a=4.045	c=4.045[211]	-	-
Ti	Hexagonal	a=2.932 c=4.651	a=2.951[212] c=4.684	-	-
B	Trigonal	a=4.894 c=12.539	a=4.908[213] c=12.559	-	-
Al_3Ti	Tetragonal	a=3.846 c=8.600	a=3.854[204] c=8.584	-154 -155[85], -153[214]	-150[215] -157[216]
TiB_2	Hexagonal	a=3.033 c=3.231	a=3.024[203] c=3.220	-306 -310[85]	-322[217]

For surface calculations, constant volume simulations were performed to preserve the vacuum. Two methods are used to calculate the surface energy. The first is the traditional method of subtracting the bulk energy from the internal energy and then dividing by the surface area. Four surfaces were simulated in this study. The supercells were converged at 8 layers for the Al_3Ti {112} surface (32 atoms) and 7 layers for the Al_3Ti {100}, {001} and TiB_2 {0001} surfaces (28, 14 and 20 atoms, respectively) to maintain bulk properties in the centre, and the vacuum added between the slabs was as thick as the slab itself to prevent interaction between surfaces. For TiB_2 {0001} and Al_3Ti {001} surfaces, there are two different possible terminations (as shown in Figure 3.1(a) and (c)), indicating their surface energies are functions of the chemical potential of the relevant element. Using the methodology described in previous literature [218], the surface energy was obtained using Eq. 3.1, where TiB_2 has been used as an example:

$$\sigma_{TiB_2} = \frac{1}{2A}\left[E_{slab} - \frac{N_B}{2}E^m_{TiB_2} - \left(N_{Ti} - \frac{N_B}{2}\right)\mu^{slab}_{Ti}\right] \qquad \textit{Equation 3.4}$$

Here σ is the surface energy, A is the surface area, E_{slab} is the internal energy of a fully relaxed slab, $E^m_{TiB_2}$ is the calculated bulk energy for a TiB_2 unit, N_{Ti} and N_B are the numbers of Ti and B atoms in the slab, and μ^{slab}_{Ti} is the chemical potential of Ti in the slab. Figure 3.1 shows the results for TiB_2 {0001} (Figure 3.1(b)) and Al_3Ti {001} (Figure 3.1(d)) surfaces, in comparison with other published work [85, 214].

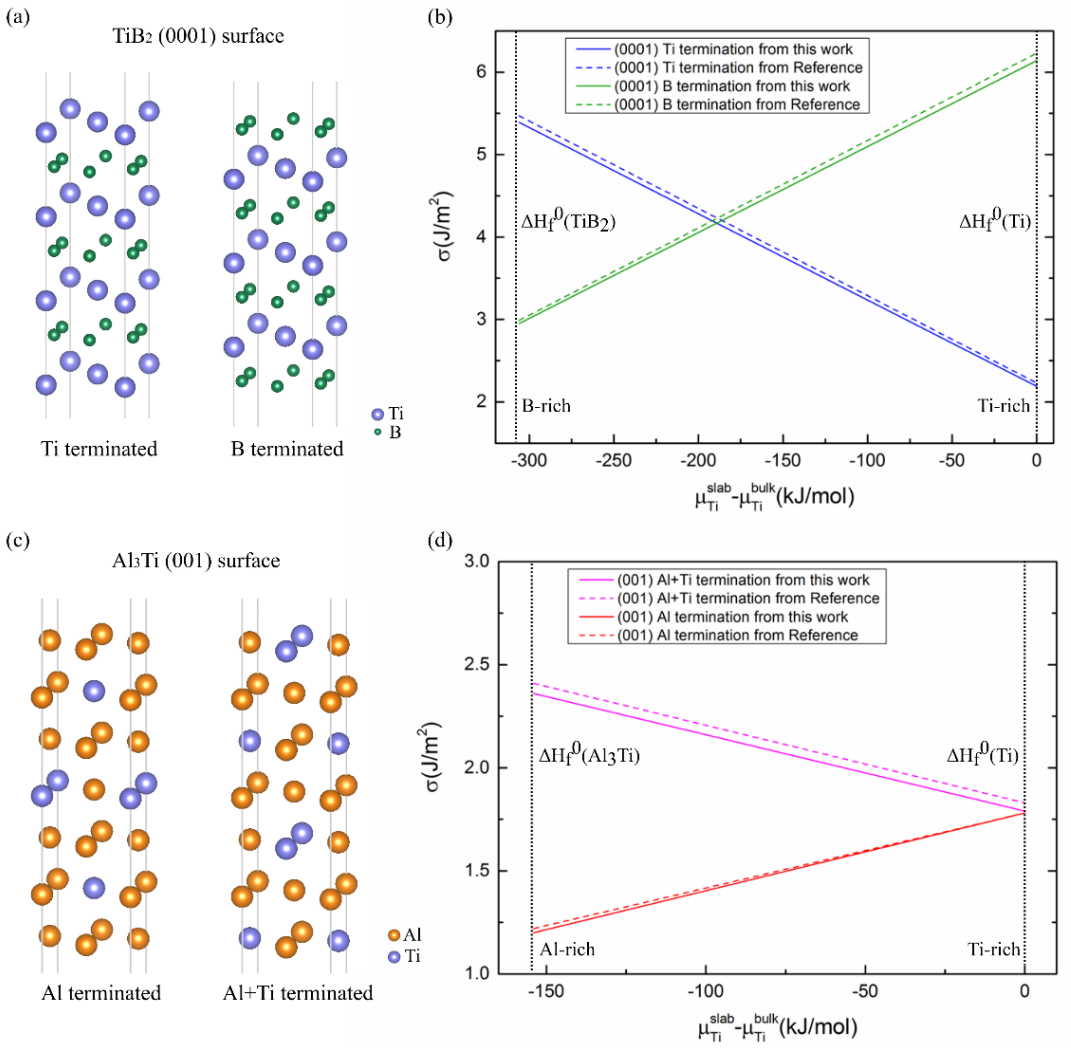

Figure 3.1 (a) Slab model for Ti terminated and B terminated TiB_2 (0001) surface. (b) Surface energies for TiB_2 (0001) surface from DFT calculation. (c) Slab model for Al terminated and Al+Ti terminated Al_3Ti (001) surface. (d) Surface energies for Al_3Ti (001) surface after DFT calculation. The formation energies, ΔH_f^o, for TiB_2, Al_3Ti and pure Ti are shown by the vertical dotted lines. Calculations from past work [85, 214] are shown for comparison.

The second method is an average of the calculation results at various thickness for each surface. In simple cases like Al_3Ti {112} and {100} surfaces, the internal energy of a slab model consists of two parts: the bulk energy and the surface energy:

$$E_{slab} = n_{Al_3Ti} \cdot E^m_{Al_3Ti} + E_{surface} \qquad \textit{Equation 3.5}$$

Here E_{slab} is the internal energy of a fully relaxed slab, $E^m_{Al_3Ti}$ is the bulk energy for an Al_3Ti unit, n_{Al_3Ti} is the number of Al_3Ti units in the slab, and $E_{surface}$ is the surface energy. The bulk energy was

calculated from the slope of the straight line fit to the internal energy E_{slab} as a function of n_{Al_3Ti} and the surface energy corresponds to the intercept (Figure 3.2(a)). For TiB_2 {0001} and Al_3Ti {001} surfaces, different terminations correspond to different fitting lines (Figure 3.2(b)), and the intercept now consists of the surface energy and the chemical potential from the extra atoms. Taking the Ti terminated TiB_2 {0001} surface as an example, the internal energy can be written as:

$$E_{slab} = n_{TiB_2} \cdot E^m_{TiB_2} + (E_{surface} + 2 \cdot \mu^{slab}_{Ti}) \qquad \textit{Equation 3.6}$$

Here E_{slab} is the internal energy of a fully relaxed slab, $E^m_{TiB_2}$ is the bulk energy for a TiB_2 unit, n_{TiB_2} is the number of TiB_2 units in the slab, $E_{surface}$ is the surface energy and μ^{slab}_{Ti} is the chemical potential of Ti in the slab.

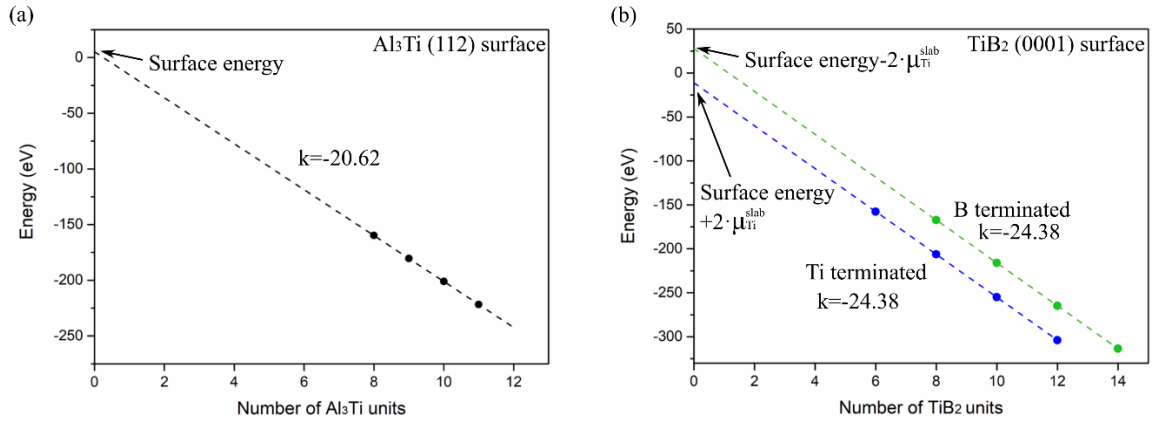

Figure 3.2. Second method for surface energy calculation. (a) The internal energy of Al_3Ti (112) surface model versus number of Al_3Ti units where the intercept is the Al_3Ti (112) surface energy. (b) The internal energy of TiB_2 (0001) surface model versus number of TiB_2 units where the intercept include the surface energy and the chemical potential of extra Ti atoms in the slab.

The slopes of the straight lines correspond to the bulk energy for Al_3Ti and TiB_2 according to Eq. 3.2 and 3.3. The slopes in Figure 3.2(a) and (b) give the same results as the constant pressure bulk simulation where the calculated bulk energy for Al_3Ti and TiB_2 are -20.62 eV/unit and -24.38eV/unit. The surface energies calculated using these two methods are listed in Table 3.2, together with results from past work. It can be seen that the values are very close using these two methods for all four surfaces, and they are all in good agreement with previous work where available. The interfacial

energies were then calculated by the common method [84, 219, 220] of subtracting the bulk energy, dividing by the area, and then subtracting away any surface energy. Overall, the bulk and surface energy calculations are in good agreement with previous work and, together, they form the basis of the interfacial calculations performed in this study.

For the Al-Ti-B master alloys, excess Ti becomes solute in the liquid (2.88wt% for Al-5Ti-1B) before Al_3Ti solidification, and raises the Ti chemical potential. The range of Ti chemical potential during Al_3Ti solidification is calculated in section 3.3.2, from which we can determine the stable terminations for the TiB_2 {0001} and Al_3Ti {001} in interface slabs.

Table 3.2 DFT calculated surface energy with comparison to published work

Surface		Relaxed surface energy σ (J/m^2)		
		First method	Second method	Published work
Al_3Ti(112)		1.48	1.49	1.563[214]
Al_3Ti(100)		1.80	1.79	-
Al_3Ti(001)	Al termination	1.20-1.78	1.22-1.79	1.22-1.78[214]
	Al+Ti termination	2.36-1.79	2.37-1.80	2.41-1.83[214]
TiB_2(0001)	Ti termination	5.39-2.19	5.39-2.20	5.47-2.23[85]
	B termination	2.95-6.14	2.94-6.13	2.99-6.23[85]

3.3 Results and discussion

3.3.1 Three preferred ORs between Al_3Ti and TiB_2

Al_3Ti crystals extracted by selective etching of the Al-5Ti-1B master alloy are shown in Figure 3.3(a) and (b). They have the same morphology as in Ref [65]. The unit cell wireframe in Figure 3.3(a) was plotted using the Euler angles from EBSD performed directly on the facets of the extracted crystal, and confirms that the main facets are {001} and {101}. Figure 3.3(c) shows typical small TiB_2 hexagonal plates with {0001} and $\{1\bar{1}00\}$ facets on the Al_3Ti {001} facets with Al_3Ti ledges surrounding them. Similar Al_3Ti and TiB_2 crystals were also found in the Al-3Ti-1B master alloy. Figure 3.3(d)-(f) are crystals etched out from the re-cast Al-3Ti-1B alloy. The Al_3Ti crystal now has a faceted dendritic morphology similar to Ref. [65] with a major {001} facet and {100} edges. On the Al_3Ti {001} surface, Al_3Ti growth ledges can be seen around the hexagonal TiB_2 platelets (Figure 3.3(f)).

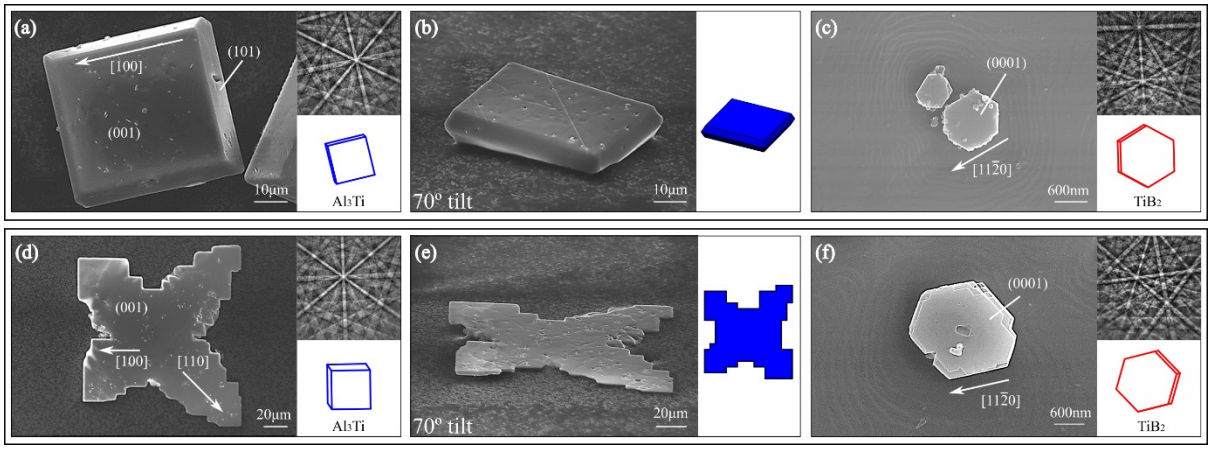

Figure 3.3 Typical Al_3Ti and TiB_2 crystal morphologies after selective etching of the α-Al matrix. (a)-(c) were extracted from the Al-5Ti-1B master alloy. (d)-(f) were extracted from the re-cast Al-3Ti-1B master alloy. Kikuchi patterns were obtained from EBSD directly on the extracted crystals from which the facets, directions and unit cell wireframes were plotted.

Figure 3.4(a)-(g) and (h)-(n) show the same OR measured between Al_3Ti and TiB_2 in Al-3Ti-1B master alloy and re-cast Al-3Ti-1B alloy. In Figure 3.4(a) and (h) TiB_2 particles are on the Al_3Ti {001} surfaces, with similar growth ledges as in Figure 3.3(c) and (f). EBSD patterns from these two phases are shown in Figure 3.4(b)-(c) and (i)-(j), and selected parallel planes and directions are indexed in Figure 3.4(d)-

(e) and (k)-(l), respectively. Pole figures for these parallel planes and directions of these two crystals are superimposed in Figure 3.4(f) and (m). It can be seen that the $\{001\}_{Al3Ti}$ is near-parallel with $\{0001\}_{TiB2}$ and one of the $<110>_{Al3Ti}$ is near-parallel with one of the $<11\bar{2}0>_{TiB2}$. The OR can be written as:

$$\{001\}_{Al3Ti} \parallel \{0001\}_{TiB2}, \text{with } <110>_{Al3Ti} \parallel <11\bar{2}0>_{TiB2} \quad (OR2) \qquad \textit{Equation 3.7}$$

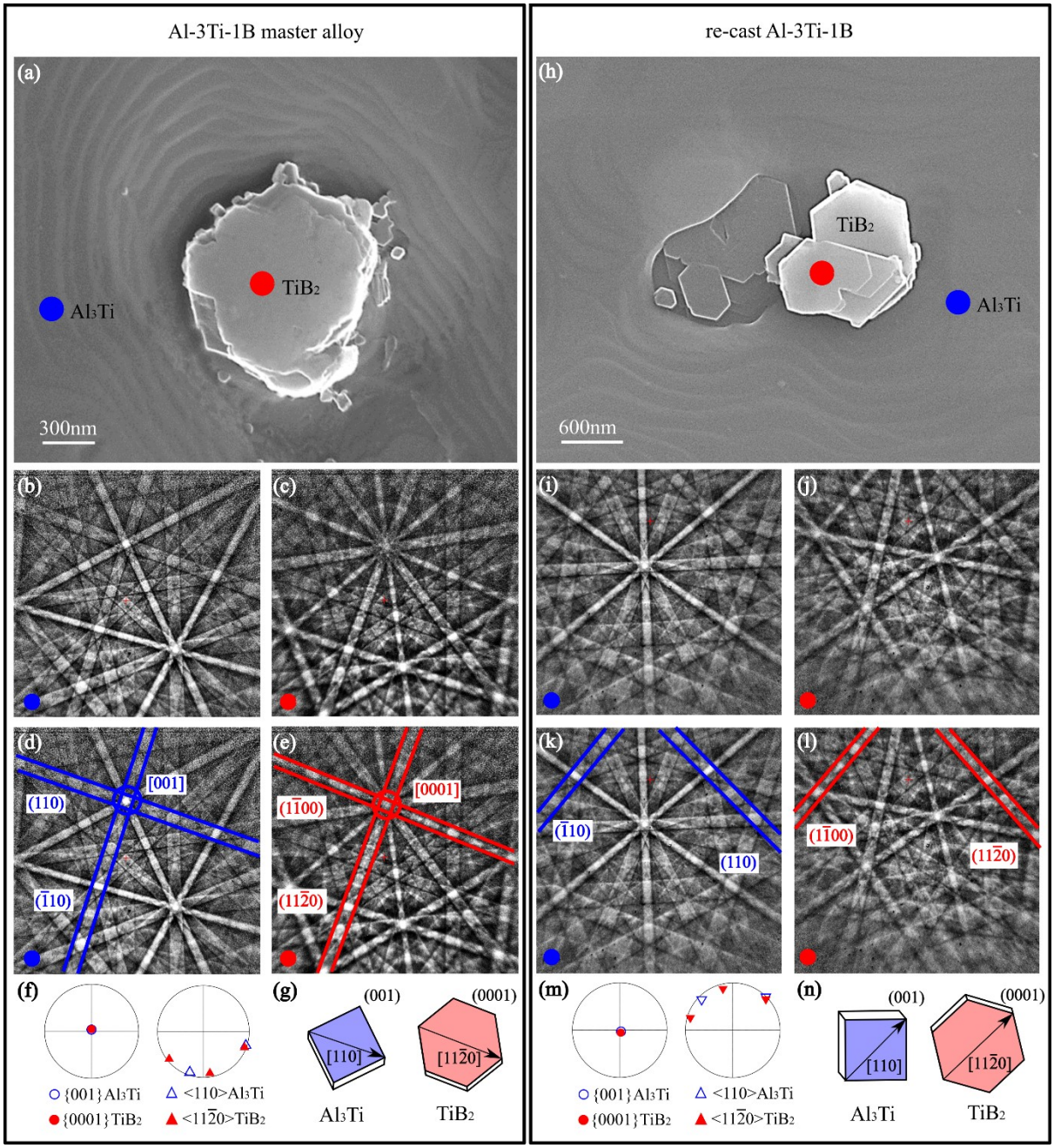

Figure 3.4 Typical TiB_2 particles on the Al_3Ti {001} surface with OR2. (a)-(g) are from the Al-3Ti-1B master alloy. (h)-(n) are from re-cast Al-3Ti-1B. The two phases are marked in red and blue. (b)-(c) and (i)-(j) are Kikuchi patterns from the TiB_2 and Al_3Ti crystals in (a) and (h). In (d)-(e) and (k)-(l) selected parallel planes and directions are indexed on the Kikuchi patterns. (f) and (m) are superimposed pole figures of parallel planes and directions of these two phases. (g) and (n) show unit cell wireframes of the two crystals with highlighted parallel planes and directions.

Note that this OR is different from OR1 in the introduction. EBSD analysis of 580 TiB_2 particles sharing an interface with Al_3Ti in the Al-5Ti-1B and Al-3Ti-1B master alloys identified three preferred ORs between Al_3Ti and TiB_2. Figure 3.5 is an example of a single Al_3Ti crystal with multiple TiB_2 inside where all three ORs are present. In Figure 3.5 there are two TiB_2 particles having each OR with the Al_3Ti in this cross section, where each OR is marked as a triangle(OR1), diamond(OR2) and rectangle(OR3) in Figure 3.5(b), respectively. Pole figures showing parallel planes and directions in each OR are plotted in Figure 3.5(c)-(e), together with the unit cell wireframes below. In addition to OR1 and OR2 written previously, the third OR can be written as:

$$\{100\}_{\mathrm{Al3Ti}} \parallel \{0001\}_{\mathrm{TiB2}}, \text{with } <010>_{\mathrm{Al3Ti}} \parallel <11\bar{2}0>_{\mathrm{TiB2}} \quad (OR3) \qquad \textit{Equation 3.8}$$

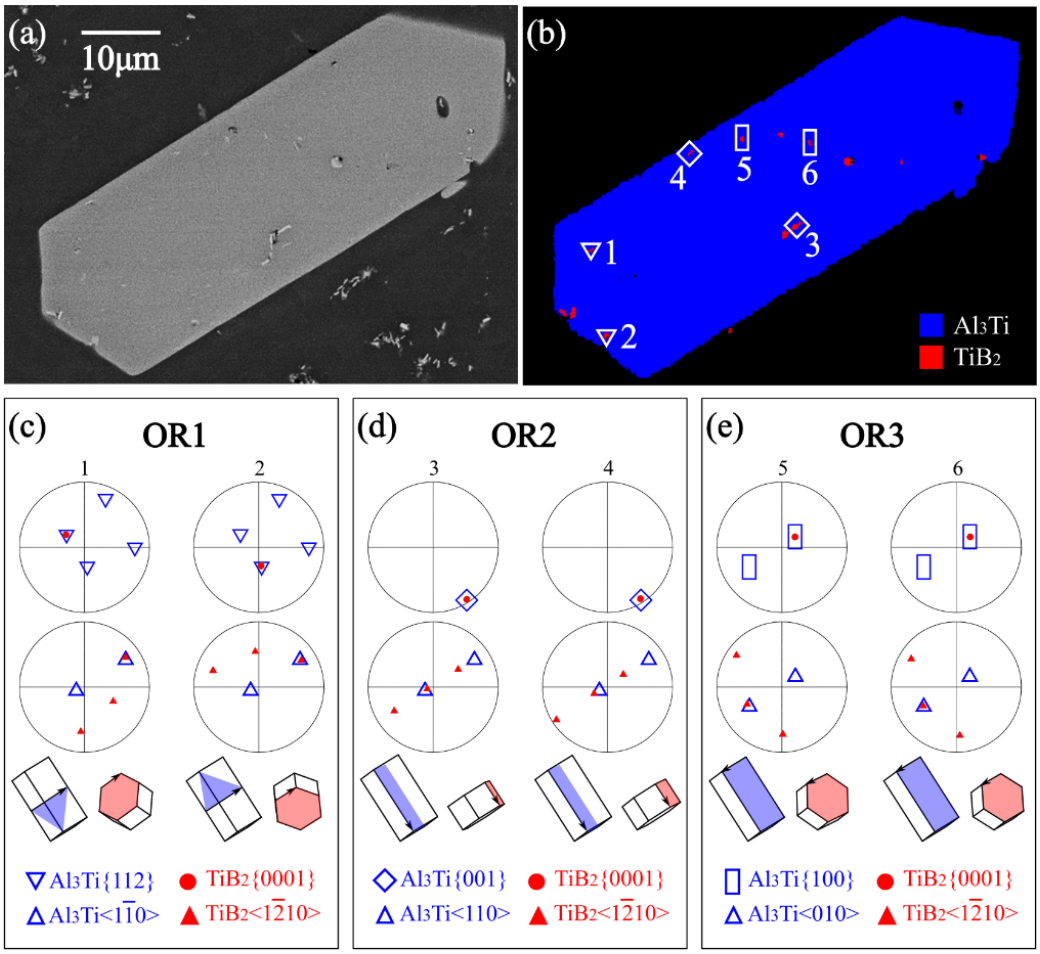

Figure 3.5. Multiple TiB_2 particles sharing different ORs with an Al_3Ti crystal. (a) Backscattered electron image of a typical Al_3Ti crystal in Al-5Ti-1B with multiple TiB_2 particles embedded inside. (b) EBSD phase map of the Al_3Ti crystal in (a). Blue is Al_3Ti. Red is TiB_2. (c) Two TiB_2 particles marked with triangles in (b) sharing OR1 with the Al_3Ti. (d) Two TiB_2 particles in diamonds in (b) sharing OR2 with the Al_3Ti. (e) Two TiB_2 particles in rectangles in (b) sharing OR3 with the Al_3Ti.

Among all 580 TiB_2 particles analysed in the Al-5Ti-1B and Al-3Ti-1B master alloys, 33 had OR1, 49 had OR2 and 9 had OR3 when the maximum deviation for parallelism was set as 5°. The ORs between these TiB_2 and Al_3Ti are projected into pole figures in Figure 3.6. In each OR, because there are three different <11$\bar{2}$0> directions in TiB_2 with 120° between them, the three corresponding Al_3Ti directions cannot be strictly parallel to the three <11$\bar{2}$0> at the same time. However, the angle between these three Al_3Ti directions are close to 120° (the difference is < 5°), so it is reasonable to compare their deviations in pole figures in this way. The standard deviations from the three ORs are small and closer examination indicates that the parallelism of the interfacial planes is tighter than the directions at the

interface for all three ORs. The relative geometry of the two crystals in terms of unit cells and crystal morphology (habit) for the three ORs are plotted at the bottom of Figure 3.6 for clarity.

For simplicity through the whole analysis in this chapter we set the deviation angle between the parallel planes and directions to be less than 5° as the threshold for the 3ORs. A more rigorous criterion is to characterise ORs using a deviation from the ideal OR based misorientation matrix. This can be written in terms of an axis-angle, and from this the OR can be tested using an angular tolerance. In this case, the number of OR2 changes slightly from 49 to 45, while the number of OR1 and OR3 stay the same.

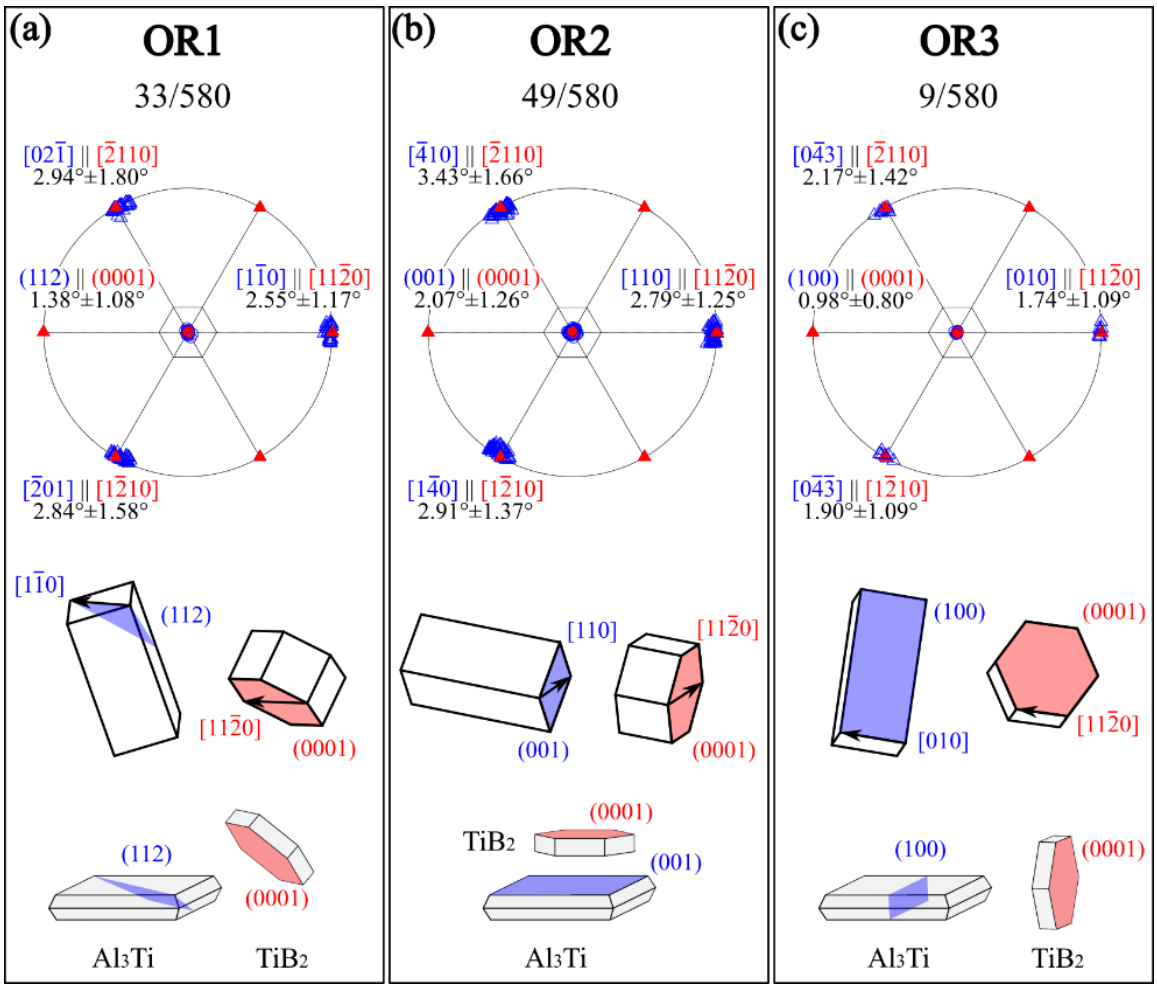

Figure 3.6. Summary of the three ORs between 580 TiB_2 particles and 132 Al_3Ti crystals. Orientations of Al_3Ti are projected onto pole figures with respect to the orientations of TiB_2 for (a) OR1, (b) OR2 and (c) OR3. Red circles are $\{0001\}_{TiB2}$, red triangles are $<11\bar{2}0>_{TiB2}$ and equivalent blue symbols are the corresponding planes and directions of Al_3Ti in each OR. The relative geometry of the unit cells and the

crystal morphology of the two crystals in each OR are plotted underneath, with parallel planes and directions highlighted.

Considering the thin plate-like hexagonal shape of TiB_2 in the master alloy rods, the {0001} is the main facet that forms interfaces with Al_3Ti crystals. To explore the reproducibility of interfaces between Al_3Ti and the TiB_2 {0001} facet, the direction of {0001} is projected into an Al_3Ti inverse pole figure in Figure 3.7(a) for 278 TiB_2 particles in the Al_3Ti interior and 302 TiB_2 particles on the Al_3Ti surface. For TiB_2 that was totally engulfed inside, three planes in Al_3Ti: {112}, {001} and {100}, are preferred to form contact planes with the TiB_2 {0001} facet, corresponding to the three ORs we discovered above. While for TiB_2 on the Al_3Ti surface, according to the contour figure, only one of the three contact planes is preferred: $\{001\}_{Al3Ti} || \{0001\}_{TiB2}$. The percentage of these three contact planes and ORs are plotted for interior TiB_2 and surface TiB_2 in Figure 3.7(b) and the statistical data is listed in Table 3.3. In Figure 3.7(b), note that cross-hatched regions refer to the full OR (parallel plane and parallel direction) whereas coloured regions refer only to the contact plane (parallel plane only).

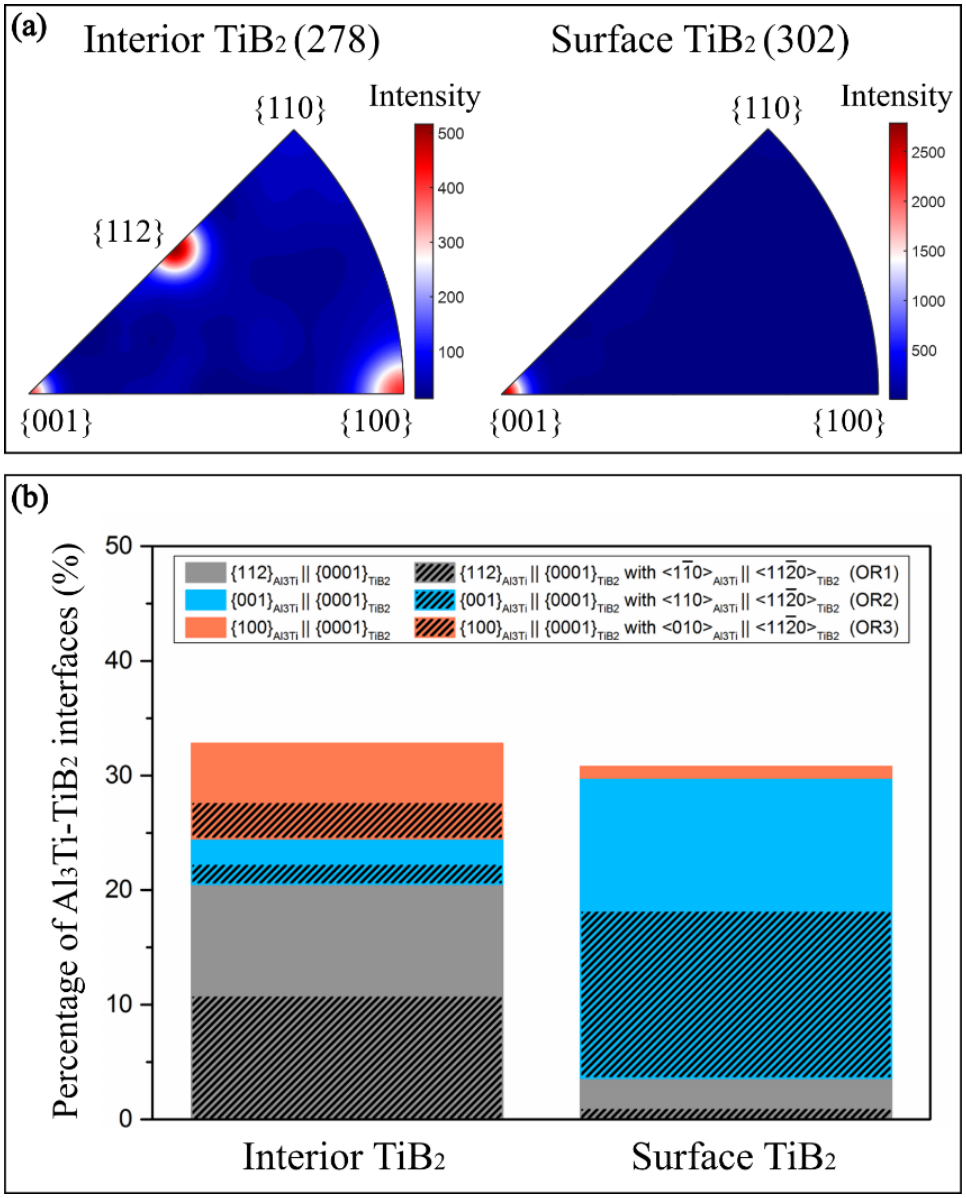

Figure 3.7. (a) Projection of $\{0001\}_{TiB2}$ into the inverse pole figure of Al_3Ti for 278 TiB_2 particles fully embedded inside and 302 TiB_2 particles on the Al_3Ti surface. (b) Percentage of different Al_3Ti-TiB_2 interfaces for TiB_2 particles embedded inside and on the surface Al_3Ti. Note that cross-hatched regions are for orientation relationships (parallel plane and direction) whereas colour-only regions are for parallel planes only.

In Figure 3.7(b), for TiB_2 inside Al_3Ti, the $\{112\}_{Al3Ti}$ || $\{0001\}_{TiB2}$ contact plane (the grey region) and the related OR1 (the grey cross-hatched region) are dominant. The third contact plane $\{100\}_{Al3Ti}$ || $\{0001\}_{TiB2}$ (the orange region) has higher occurrence frequency than the second one $\{001\}_{Al3Ti}$ || $\{0001\}_{TiB2}$ (the blue region) when TiB_2 is fully embedded inside Al_3Ti. On the contrary, for TiB_2 on the Al_3Ti surface, the second contact plane (blue), together with OR2 (the blue cross-hatched region),

becomes significantly preferred, and only few TiB_2 with OR1 (the grey cross-hatched region) and none with OR3 (the orange cross-hatched region) were observed.

Table 3.3 The statistical data for the parallelism between Al_3Ti and TiB_2 particles within 5°

	Number of Al_3Ti	Number of TiB_2	$\{112\}_{Al3Ti}\|\|\{0001\}_{TiB2}$	$\{001\}_{Al3Ti}\|\|\{0001\}_{TiB2}$	$\{100\}_{Al3Ti}\|\|\{0001\}_{TiB2}$	Other
Interior TiB_2	100	278	57 (20.5%)	11 (4.0%)	23 (8.3%)	67.2%
			$\langle 1\bar{1}0\rangle_{Al3Ti}\|\|\langle 11\bar{2}0\rangle_{TiB2}$ **(OR1)**	$\langle 110\rangle_{Al3Ti}\|\|\langle 11\bar{2}0\rangle_{TiB2}$ **(OR2)**	$\langle 010\rangle_{Al3Ti}\|\|\langle 11\bar{2}0\rangle_{TiB2}$ **(OR3)**	
			30 (10.8%)	5 (1.8%)	9 (3.2%)	
	Number of Al_3Ti	**Number of TiB_2**	$\{112\}_{Al3Ti}\|\|\{0001\}_{TiB2}$	$\{001\}_{Al3Ti}\|\|\{0001\}_{TiB2}$	$\{100\}_{Al3Ti}\|\|\{0001\}_{TiB2}$	**Other**
Surface TiB_2	32	302	11 (3.6%)	79 (26.2%)	3 (1.0%)	69.2%
			$\langle 1\bar{1}0\rangle_{Al3Ti}\|\|\langle 11\bar{2}0\rangle_{TiB2}$ **(OR1)**	$\langle 110\rangle_{Al3Ti}\|\|\langle 11\bar{2}0\rangle_{TiB2}$ **(OR2)**	$\langle 010\rangle_{Al3Ti}\|\|\langle 11\bar{2}0\rangle_{TiB2}$ **(OR3)**	
			3 (1%)	44 (14.6%)	0	

3.3.2 DFT calculations of interfacial energy for 3ORs

In DFT calculations, the surface and interfacial energies are usually related to the chemical potential of the relevant element in the melt [84, 214, 218-220]. To determine the Ti chemical potential corresponding to the composition in Al-5Ti-1B master alloy, thermodynamic calculations were performed in Thermo-Calc using the Ti database and the results are shown in Figure 3.8. Figure 3.8(a) is the Al-Ti phase diagram at the Al rich side. For the Al-5Ti-1B master alloy, the Ti concentration in the melt is 2.88 wt% (1005°C) before Al_3Ti nucleates if we consider TiB_2 to be insoluble in liquid Al. With the nucleation and growth of Al_3Ti, the Ti content within the liquid decreases along the liquidus line until it reaches the minimum level, 0.13 wt%, at the peritectic temperature (665°C). Figure 3.8(b) shows the change of Ti chemical potential along the liquidus line from 1005°C to 665°C: the range of $(\mu_{Ti}^{slab} - \mu_{Ti}^{bulk})$ lies between -88 kJ/mol and -115 kJ/mol. The value of $(\mu_{Ti}^{slab} - \mu_{Ti}^{bulk})$ is calculated from Thermo-Calc through chemical activity:

$$a_{Ti} = exp\left(-\frac{\mu_{Ti}^{slab} - \mu_{Ti}^{bulk}}{RT}\right) \qquad \textit{Equation 3.9}$$

Therefore, when Al_3Ti is first stable, $(\mu_{Ti}^{slab} - \mu_{Ti}^{bulk})$ is -88 kJ/mol, and the value decreases on cooling with Ti depletion in the melt. After applying this chemical potential range to the calculated surface energies in Figure 3.1, the Ti terminated TiB_2 {0001} and Al terminated Al_3Ti {001} are energetically favourable during Al_3Ti solidification, and we will only consider these two terminations for TiB_2 {0001} and Al_3Ti {001} when performing interface calculations.

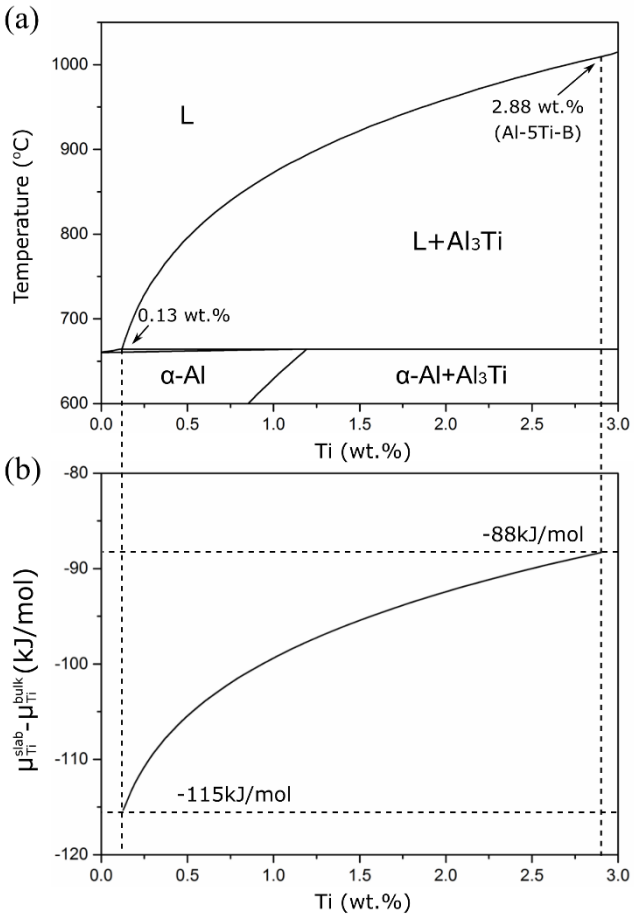

Figure 3.8. (a) Al-rich side of the Al-Ti phase diagram from the Thermo-Calc database TCTI2 version 2.0. (b) Chemical potential of Ti in the Al-Ti melt along the Al_3Ti liquidus line.

Figure 3.9(a) shows the interface slab model for OR1 $((112)_{Al3Ti}||(0001)_{TiB2}$ with $[1\bar{1}0]_{Al3Ti}||[11\bar{2}0]_{TiB2})$. The calculated interfacial energy for OR1 as a function of chemical potential is plotted in grey line in Figure 3.9(b). Due to the different DFT codes used for the calculation, the current result of OR1 is about 0.14 J/m^2 lower than Wearing's study [85]. This is a typical difference magnitude between DFT studies; for example Wearing's study has a difference of 0.13-0.21 J/m^2 in Al/TiB_2 interfacial energy with Ref.[84]. The DFT results for the other two ORs are also plotted in blue and orange lines in Figure 3.9(b). At the early stage of solidification, OR1 has the lowest energy, and it has the highest frequency for the interior TiB_2 particles in Figure 3.7(b), while OR3 has much higher interfacial energy than OR1 and OR2 and yet was commonly observed for the interior TiB_2. Moreover, there is a significant preference of OR2 when TiB_2 is on the Al_3Ti surface (Figure 3.7(b)), despite OR1 having the lowest

interfacial energy over most of the Al_3Ti solidification range. This shows that factors in addition to interfacial energy play a key role in the formation of ORs and contact planes between TiB_2 particles and Al_3Ti during Al_3Ti nucleation and growth.

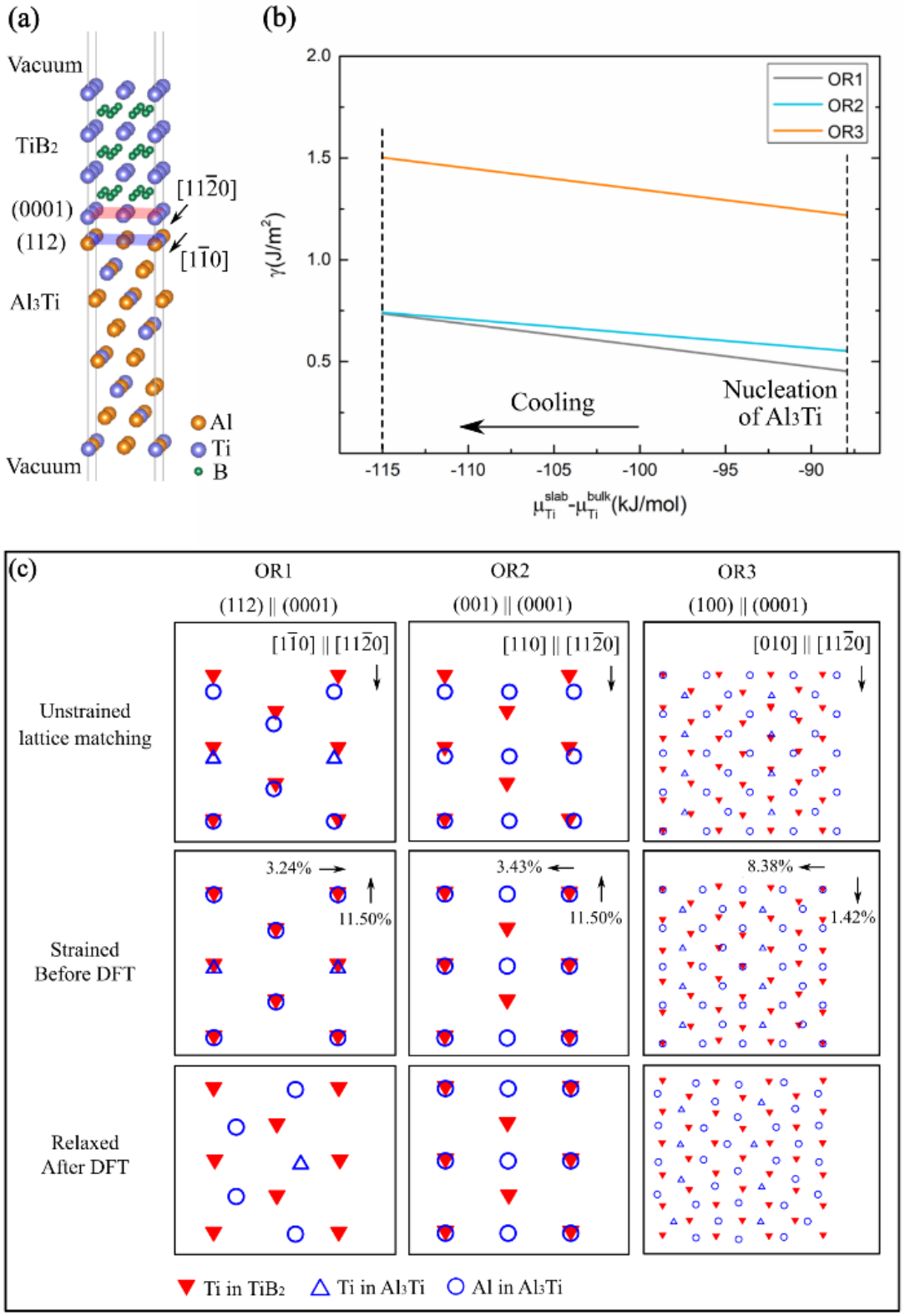

Figure 3.9. DFT calculations on Al_3Ti-TiB_2 interfaces. (a) Interface slab model for OR1. (b) Interfacial energy of the three ORs versus Ti chemical potential. (c) Interface projection of the three ORs: unstrained, strained before DFT calculation (the strain is calculated referred to 0K), and relaxed after DFT calculation. Red triangles are Ti atoms in TiB_2, blue triangles and circles are Ti and Al atoms in Al_3Ti.

Figure 3.9(c) are plots of the atomic positions in the interface projection of the slab models for the three ORs before and after relaxation using DFT. The first row shows the unstrained lattice matching, and OR1 has the best atomic matching in the three ORs. In order to apply periodic boundary conditions, Al_3Ti has been strained to match the unit cell parameters of the stiffer TiB_2 phase at the interface in each case, as shown in second row. For OR1 before atomic relaxation, the Al and Ti atoms in Al_3Ti are sitting on top of Ti atoms in TiB_2, while after the calculation all atoms in Al_3Ti moved to the vacant centre of Ti atoms in TiB_2, which is the expected stacking sequence for close packing. For OR2 before the calculation, Al atoms sit on top of or in the vacant centre between Ti atoms of TiB_2 {0001}, and their positions do not change after the calculation, indicating the input arrangement is very close to the lowest energy geometry for this interface. For OR3, a large input model was required due to the relatively poor lattice matching at the interface, which partially explains its high interfacial energy compared to the other two ORs. After DFT calculation of this interface the overall movement of atoms in Al_3Ti seems to have the tendency to fill the vacant gaps between the Ti atoms in TiB_2.

We note that the DFT interfacial energy values refer to 0K which will not be identical to the values at elevated temperatures. However, experimentally measured interfacial energies have been shown to follow the same trend as the 0K DFT calculated energies [221]. Moreover, thermal expansion at elevated temperature (e.g. 800K) changes the lattice parameters for Al_3Ti [222] and TiB_2 [203] by less than 1%, and the changes of strain at the calculated interfaces are less than 0.8%. Therefore, the 0K calculated interfacial energy can be used as a useful approximant to the real value in this work, especially since our main goal here is a comparison between different ORs.

3.4 Identification of OR formation mechanisms

To understand the mechanisms that lead to the formation of the preferred contact planes and OR1, OR2 and OR3, we next study OR formation by (1) characterising small Al_3Ti crystals that solidified on the facets of large TiB_2, (2) examining the microstructures (similar to Figure 3.3-Figure 3.5) around TiB_2 particles on the Al_3Ti surfaces and embedded within Al_3Ti, and (3) calculating the interfacial energy at different rotation angles on the three contact planes and comparing the results with the measured occurrence frequencies.

3.4.1 Nucleation OR between TiB_2 and Al_3Ti

In Al-0.8Ti arc melted with large TiB_2 particles, multiple Al_3Ti crystals formed on the TiB_2 {0001} surface of each TiB_2 plate, as shown in the example in Figure 3.10(a). EBSD orientation map is shown in Figure 3.10(b), where the 11 labelled Al_3Ti crystals attached to a single TiB_2 crystal have six different orientations which correspond to the six crystallographic variants of OR1 with the TiB_2 plate. Their Kikuchi patterns, plotted in Figure 3.10(c), share many similarities, especially between 1&4&6(2&3&5), but there are also some clear differences in terms of the relative intensity and angle between certain bands which enable correct indexing of the orientations. The presence of six variants of OR1 can be seen in the pole figures by noting that, for each of the Al_3Ti grains, one of the $\{112\}_{Al3Ti}$ planes is parallel to the $\{0001\}_{TiB2}$ plane and one of the $<110>_{Al3Ti}$ directions is parallel to one of the $<11\bar{2}0>_{TiB2}$, and all permutations are present.

Figure 3.10(d) shows a typical TiB_2 plate with multiple small Al_3Ti on the $\{0001\}_{TiB2}$ surface after selectively etching the α-Al matrix. Their unit cells are plotted in Figure 3.10(e) from the measured Euler angles and there are in total six different orientations of the Al_3Ti crystals, each corresponding to a variant of OR1. In Figure 3.10(f) all six orientations share a common $\{112\}_{Al3Ti}$ plane that is parallel to the $\{0001\}_{TiB2}$. Every two orientations share a common $<110>_{Al3Ti}$ direction, and all three shared $<110>_{Al3Ti}$ directions are parallel to three $<11\bar{2}0>_{TiB2}$. The other $<110>_{Al3Ti}$ direction from each orientation forms a combined 6-fold symmetry around the common $\{112\}_{Al3Ti}$ plane. The small angle

between the other $\{112\}_{Al3Ti}$ planes is because there is no threefold symmetry on the $\{112\}_{Al3Ti}$ plane since c/a≠2 for Al_3Ti. The six Al_3Ti unit cells are plotted with the TiB_2 unit cell in Figure 3.10(g) using the measured Euler angles, where the combined 6-fold symmetry of Al_3Ti comes from the hexagonal TiB_2 basal plane.

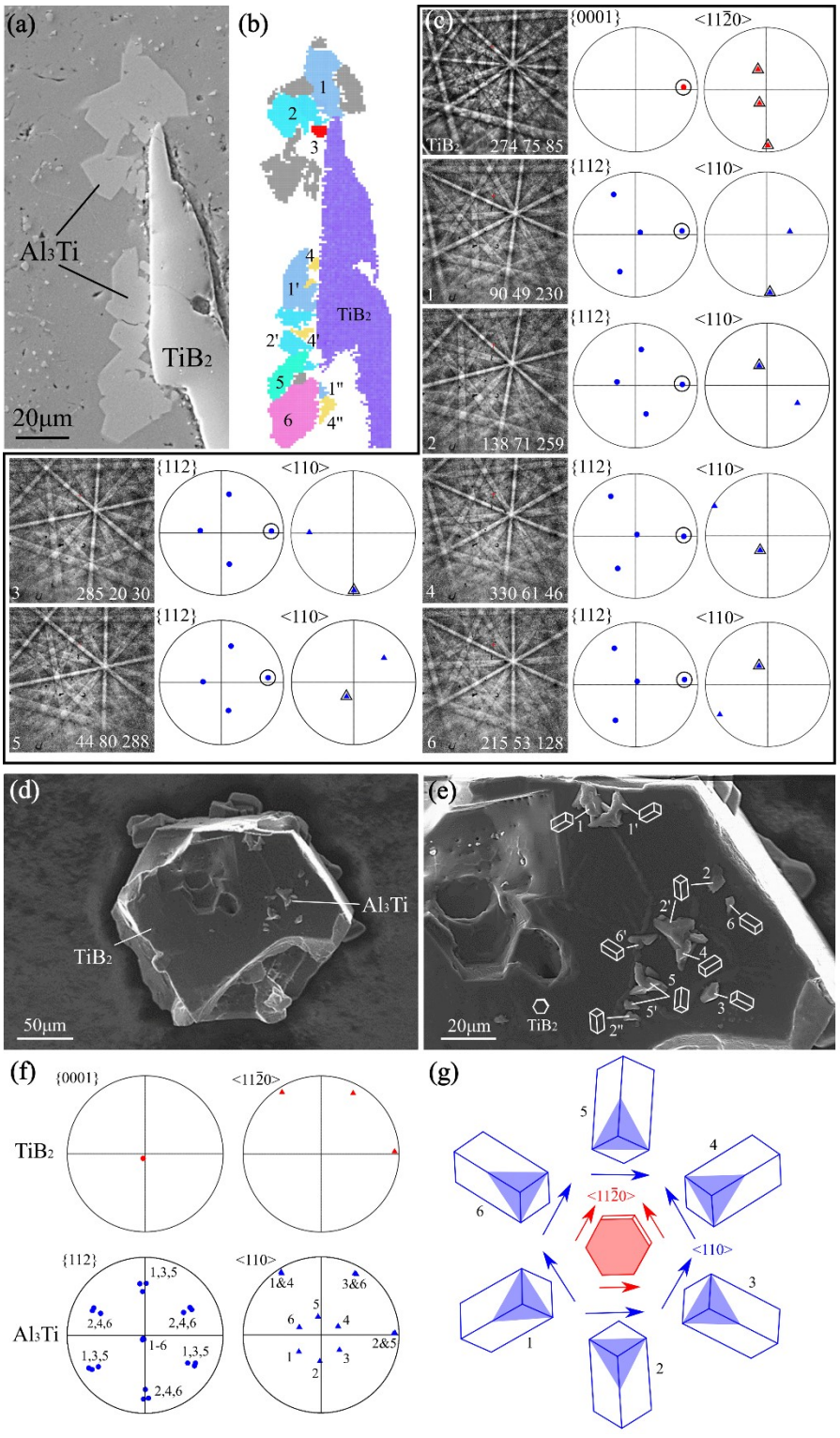

Figure 3.10. Nucleation of small Al_3Ti on large TiB_2 crystals (a) SEM image of multiple Al_3Ti crystals on a cross sectioned TiB_2 (0001) surface. (b) EBSD orientation map of the Al_3Ti and TiB_2 crystals in (a). (c) Kikuchi patterns and Euler angles for the TiB_2 and six Al_3Ti orientations in (b), together with pole figures showing $\{0001\}_{TiB2}$ || $\{112\}_{Al3Ti}$, with $<11\bar{2}0>$ || $<1\bar{1}0>$ (OR1) for all six Al_3Ti orientations. (d) Another TiB_2 particle with multiple Al_3Ti crystals on the {0001} facet after selective etching of α-Al. (e) Magnified region from (d), with TiB_2 and Al_3Ti unit cell wireframes plotted showing six different Al_3Ti orientations. (f) {0001} and $<11\bar{2}0>$ pole figures of TiB_2 and superimposed {112} and <110> pole figures of all six Al_3Ti orientations in (e) showing all Al_3Ti have OR1. (g) All six Al_3Ti unit cell wireframes plotted with the TiB_2 unit cell wireframe in (e), with parallel planes and directions highlighted.

From Figure 3.10 it is known that Al_3Ti crystals on the TiB_2 {0001} surface can have six different orientations, each a variant of OR1 with the TiB_2 plate, and many Al_3Ti crystals have the same orientation even when they are geometrically far away, strongly indicating that they each nucleate on the TiB_2 {0001} surface independently. 27 out of 28 Al_3Ti crystals that shared an interface with large TiB_2 crystals had OR1 and none had OR2 or OR3. These combined findings prove that OR1 is the Al_3Ti-TiB_2 nucleation OR. This is consistent with OR1 having the lowest interfacial energy when ($\mu_{Ti}^{slab} - \mu_{Ti}^{bulk}$) is -101kJ/mol at 846°C (the Al_3Ti liquidus temperature of Al-0.8Ti) as shown in Figure 3.9(b).

The other Al_3Ti crystals without OR1 are the grey coloured Al_3Ti crystals at the top of Figure 3.10(b). Most of them (7 out of 8) do not share an interface with the TiB_2 plate, and none of them have a simple or reproducible OR with the TiB_2, indicating they may be Al_3Ti crystals that fell (settled) into the surface during solidification.

In Figure 3.5 more than one TiB_2 particle has OR1 with the same Al_3Ti single crystal, which indicates that measuring a simple OR to a particle within a crystal does not equate to identifying a nucleant particle or a nucleation OR. The nucleation experiment presented here of growing a TiB_2 particle to a large size and solidifying small droplets of Al_3Ti on a large TiB_2 particle made the nucleant clear and isolated the nucleation OR from other mechanisms.

In order to estimate the probability of sectioning the TiB_2 nucleant particle on an Al_3Ti 2D random surface, a digital sectioning calculation was performed. As shown in Figure 3.11(a), Al_3Ti is set to be a 50*50*20µm plate while TiB_2 is designated to be a hexagonal plate with side 500nm and thickness

200nm, similar to our experiments. A stochastic point O in Al_3Ti is set to be the origin of the Cartesian coordinate system and O' is the geometric centre of the TiB_2 particle. O' is limited in the 10*10*10μm blue cubic space located at the centre of the Al_3Ti because the nucleant is usually near the centre of the growing crystal. The XY plane is set to be the sectioning plane. In Figure 3.11(b), Al_3Ti and TiB_2 are rotated under the stochastic Euler angles and by examining the coordinates of the 12 TiB_2 corners, it can be determined if the TiB_2 is crossed by the sectioning plane.

Table 3.4 shows the number of sectioning planes and how many of them contain the TiB_2 nucleant. With increasing the number of sectioning planes, the probability of sectioning the nucleant becomes stable at about 2.5%. Thus, for the 100 Al_3Ti 2D cross sections we studied (Table 3.3), the TiB_2 nucleant particle is only likely to have been sectioned in 2-3 Al_3Ti crystals and the remaining 28-27 (out of 30) TiB_2 particles in Table 3.3 are likely to have developed OR1 by other mechanisms (discussed in the next section). Therefore, there is an underlying difficulty of identifying the particle that triggered nucleation or determining the nucleation OR in a random 2D cross section.

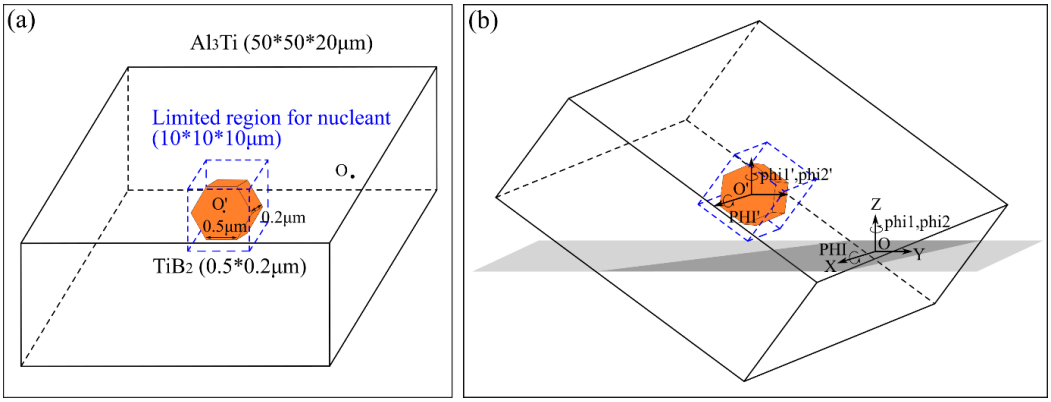

Figure 3.11. Model for the digital sectioning experiment (a) before rotation and (b) after rotation.

Table 3.4 The chances of sectioning TiB_2 nucleant

Number of sections	Number of section planes containing TiB_2	Chances of sectioning TiB_2 nucleant (%)
100	0	0
1000	26	2.6%
10,000	256	2.56%
100,000	2486	2.48%
1000,000	25148	2.51%

3.4.2 Pushing & Engulfment on contact planes during Al_3Ti growth

Since Al_3Ti and TiB_2 are both significantly denser than the liquid and will have different settling rates due to their different sizes and densities, TiB_2 particles are likely to come into contact with growing Al_3Ti crystals as they both settle in the melt. From the relative crystal morphology (habit) of these two crystals drawn at the bottom of Figure 3.6, the basal plane of TiB_2 is likely to land on and then be continuously pushed by Al_3Ti {001} facets. Figure 3.7(b) shows that, the second contact plane $\{001\}_{Al3Ti}$ || $\{0001\}_{TiB2}$ (blue) is most common (26.2%) on the Al_3Ti {001} surface, and less common (4.0%) inside Al_3Ti crystals. Micrographs of both situations are shown in Figure 3.12(a) and (b) respectively. It can be seen in the cross-section of Figure 3.12(a) that the growth front of Al_3Ti is curved and has a depression containing the TiB_2 particles. The view from above after selective etching of α-Al in Figure 3.12(c) shows that this depression consists of multiple Al_3Ti ledges around the TiB_2 particles, the same as observed in Figure 3.3 and Figure 3.4.

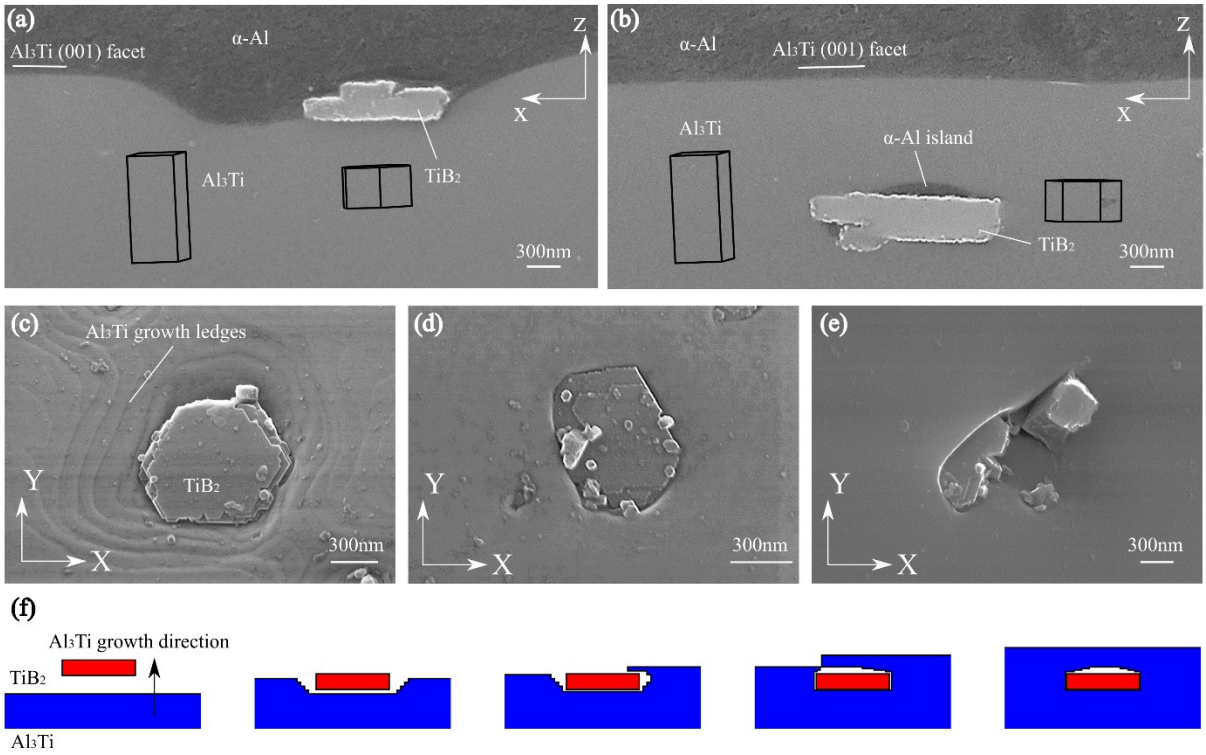

Figure 3.12. Pushing and engulfment of TiB_2 on the $\{001\}_{Al3Ti}$ facet. (a) TiB_2 particle on an Al_3Ti surface with $\{001\}_{Al3Ti}$ || $\{0001\}_{TiB2}$ in cross section, superimposed with the unit cell wireframes from EBSD. (b) TiB_2 particle fully embedded underneath the Al_3Ti {001} surface with $\{001\}_{Al3Ti}$ || $\{0001\}_{TiB2}$ in cross section, superimposed with the unit cell frames from EBSD. (c)-(e) TiB_2 particles on the Al_3Ti {001} facet being gradually engulfed. (f) Schematic illustration of the pushing and engulfment process of a TiB_2 particle leading to $\{001\}_{Al3Ti}$ || $\{0001\}_{TiB2}$ contact planes and OR2.

The concave Al_3Ti interface around TiB_2 particles is expected to be promoted by impeded solute diffusion since, when the flat Al_3Ti facet grows and starts to push a TiB_2 plate, there will be a thin gap (several to tens of atomic radii [91, 92, 223, 224]) between them where it is difficult for the rejected Al solute from the Al_3Ti growth front to diffuse away, causing the Al_3Ti growth rate behind the TiB_2 to be slower than the Al_3Ti region around it. Consequently, the Al_3Ti front is depressed near the pushed TiB_2 particle and the ledges are formed due to its faceted growth mechanism. At some point, if the growth rate of the Al_3Ti {001} facet exceeds a certain value, it will grow out over the TiB_2 particle and engulf it gradually, as shown from Figure 3.12(c)-(e), and that critical velocity corresponds to the pushing-engulfment transition [224]. Eventually some TiB_2 particles will be totally engulfed and a small amount of liquid Al is likely to be sealed in front of TiB_2 plates and become α-Al islands after solidification, as shown in Figure 3.12(b). Figure 3.12(f) illustrates the whole process from pushing to engulfment, together with the formation of Al_3Ti ledges around TiB_2 at the beginning and the formation of an α-Al island at the end. The Al_3Ti growth ledges surrounding TiB_2 particles in Al-3Ti-B (Figure 3.4(a)) and Al-5Ti-B (Figure 3.12(a)) master alloys and re-cast Al-3Ti-B (Figure 3.4(h)) provide new information of the pushing process. Such a concave growth front has been mathematically expected in past pushing and engulfment theories and models [92, 104, 106, 107, 225, 226], and our imaging provides direct proof of this. For TiB_2 particles that have been engulfed, the α-Al island at one side is another proof for the engulfment process. A similar liquid pool has also been proposed in the previous literature [225, 226], and it is clear through our imaging that it was formed during engulfment.

Figure 3.13(a) shows a similar α-Al island in front of a TiB_2 plate with the third contact plane: $\{100\}_{Al3Ti}$ || $\{0001\}_{TiB2}$, suggesting it can be created by the same pushing and engulfment mechanism. However,

different from the second contact plane, the final shape of Al_3Ti in the master alloy did not usually include {100} facets. Examples of rare $\{100\}_{Al3Ti}$ facets are given in Figure 3.13(b) and (c). To explore the dependence of the third contact plane frequency on position within Al_3Ti crystals, Figure 3.13(d) projects the relative position of 23 interior TiB_2 particles in Table 3.3 with the third contact plane into a normalised Al_3Ti cross section. In order to separate different distances to the origin, ellipses with various values from 0.2 to 1.0 of function $(x/a)^2+(y/b)^2$ are drawn in Figure 3.13(d). The origin represents the growth centre and the closer the TiB_2 is located to the origin, the earlier it was engulfed during Al_3Ti growth. It can be seen that most of the TiB_2 (over 80%) in Figure 3.13(d) are located inside the first two ellipses and the percentage of TiB_2 particles located at different distances to the growth centre are plotted in Figure 3.13(e), confirming that most TiB_2 particles with $\{100\}_{Al3Ti}$ || $\{0001\}_{TiB2}$ contact plane were engulfed by Al_3Ti {100} facets in the early stages of Al_3Ti growth. From this result, it might be that the {100} facet was more common during early growth of Al_3Ti.

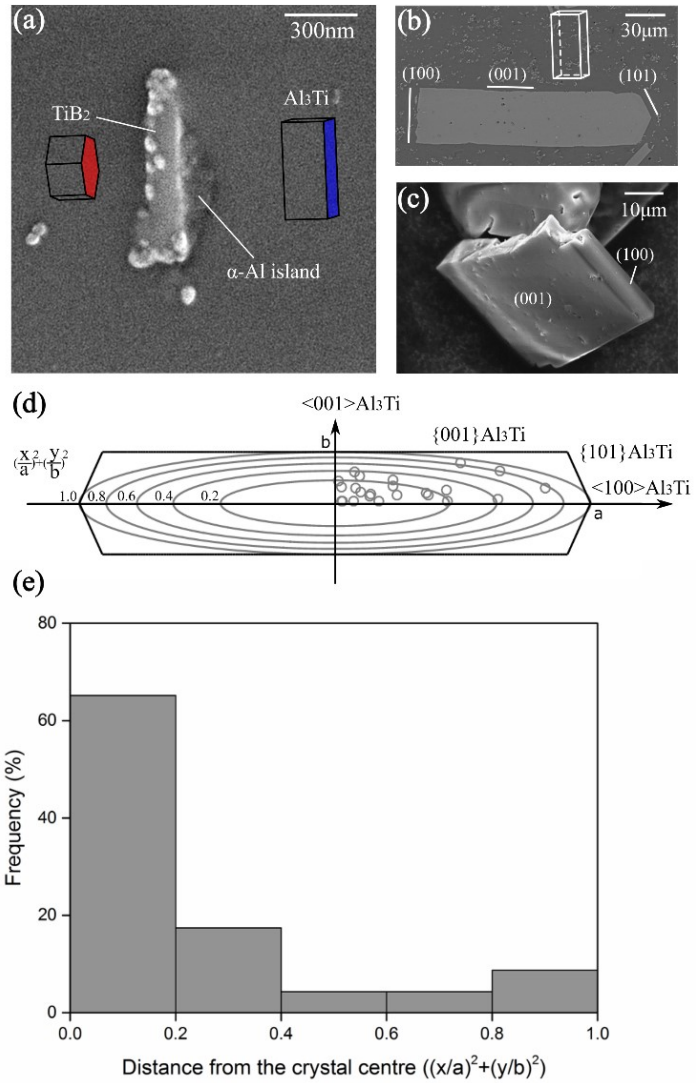

Figure 3.13. (a) Cross section of a TiB_2 particle fully embedded inside Al_3Ti with $\{100\}_{Al3Ti}$ || $\{0001\}_{TiB2}$. Contact planes are highlighted in the unit cell wireframes. (b) A rare cross section of an Al_3Ti crystal with (100), (001) and (101) facets, with unit cell wireframe from EBSD superimposed. (c) Extracted Al_3Ti from Al-5Ti-1B with a (100) facet. (d) Relative positions of 23 TiB_2 particles embedded in Al_3Ti with $\{100\}_{Al3Ti}$ || $\{0001\}_{TiB2}$. Ellipses with various radius represent different distances from the Al_3Ti growth centre. (e) Percentage of TiB_2 particles at different distances to the Al_3Ti centre in (d).

Other factors such as liquid flow and the thermal gradient are also likely to play a role. For example, Stefanescu et al. [96] have discussed how melt flow affects pushing and engulfment: for low convection, flow into the interface generated by solidification produces a drag force to push the particle into the interface, whereas flow parallel to the interface induced by natural convection produces a lift force to push the particle away from the interface. In these cases, engulfment occurs when the S-L interface velocity exceeds a critical value whereas, when there is significant melt

convection, no engulfment occurs. For the low melt convection condition studied here, melt flow effects are expected to be small. Figure 3.7 shows that the third contact plane, $\{100\}_{Al3Ti}$ || $\{0001\}_{TiB2}$, was mainly observed inside Al_3Ti crystals while the second one, $\{001\}_{Al3Ti}$ || $\{0001\}_{TiB2}$, was mainly on the Al_3Ti surface. From Figure 3.3 it is clear that Al_3Ti crystals grow faster in the <100> direction than the <001> direction, which means during pushing the {100} facet is more likely to exceed the critical velocity and cause engulfment than the {001} facet. Therefore, for the third contact plane, $\{100\}_{Al3Ti}$ || $\{0001\}_{TiB2}$, TiB_2 has higher chance to be engulfed (8.3%) while for the second one, $\{001\}_{Al3Ti}$ || $\{0001\}_{TiB2}$, TiB_2 is more likely to be pushed by the advancing Al_3Ti facet (26.2%).

3.4.3 Rotation on contact planes during pushing

For the three types of contact plane in Figure 3.7(b), only some of them also have the preferred parallel directions in the three ORs. To explore the frequency of the angular arrangement, the orientations on three contact planes are plotted as histograms at the top of Figure 3.14(a)-(c), using interior TiB_2 for contact planes 1&3, and surface TiB_2 for contact plane 2 because most TiB_2 particles with contact plane 2 remained on the surface due to the low growth rate of Al_3Ti {001} facet. Because of the sixfold symmetry of the TiB_2 {0001} plane and the fourfold symmetry of the Al_3Ti {001} plane, the invariant rotation range is 30° for contact planes 1&3 and 15° for contact plane 2, as indicated by the green and purple arrows in Figure 3.14(b).

For all three contact planes, 0° away from the 3ORs was the most commonly measured deviation angle. When the deviation angle increases, the frequency continuously decreases as it reaches 15° (15° away from the OR on the contact plane). For contact plane 2, the situation between 15° and 30° is symmetric to 15° and 0°, while for the other two, the frequency rises again from 15° to 30° but eventually it does not reach the same level as 0°.

It has also been simulated that between 10000 totally random Al_3Ti and TiB_2 orientations only a very small fraction have the parallel planes: 1.2% for contact plane 1, 0.35% for contact plane 2 and 0.71% for contact plane 3, which is much smaller compared to our measurement in Table 3.3. As for the deviation angle on the parallel planes, the difference is less than 0.15%. Therefore, the contribution from random orientation background can be ignored through our analysis.

The interfacial energy for the three preferred contact planes at various deviation angles was calculated by DFT and the results are plotted at the bottom of Figure 3.14(a)-(c) for $(\mu_{TiB2}^{slab} - \mu_{TiB2}^{bulk})$=-88kJ/mol (for each contact plane the shape of the curve is almost the same for the $(\mu_{TiB2}^{slab} - \mu_{TiB2}^{bulk})$ range from -88kJ/mol to -115kJ/mol). It can be seen that, generally, the geometry with highest frequency in the experiments is energetically favoured. For each contact plane, the lowest energy happens at 0°, which corresponds to the three ORs observed in section 3.3.1, and the change of frequency matches the

energy trend along the deviation angle very well, confirming that the 3ORs are local energy minima and TiB_2 particles can rotate towards the 3ORs to lower the interfacial energy when it is being pushed.

We argue that the measured deviation angles are highly likely to have been created by rotation of the TiB_2 particles on the relevant Al_3Ti facet to minimise their interfacial energy since it is improbable that they would form this distribution of deviation angles by randomly falling onto the Al_3Ti facet, and such in-plane rotation preference during pushing can be explained from an energy perspective. In the traditional pushing and engulfment theory, the pushing particle is treated as inert and it is passively pushed by the growth front. But in this study, the foreign particles are active inoculants that can interact with the growing Al_3Ti. With the combination of statistical experimental data and theoretical calculations, it can be seen that TiB_2 particles can have the degree of freedom to rotate with respect to the growth front during pushing to lower the energy and produces simple ORs.

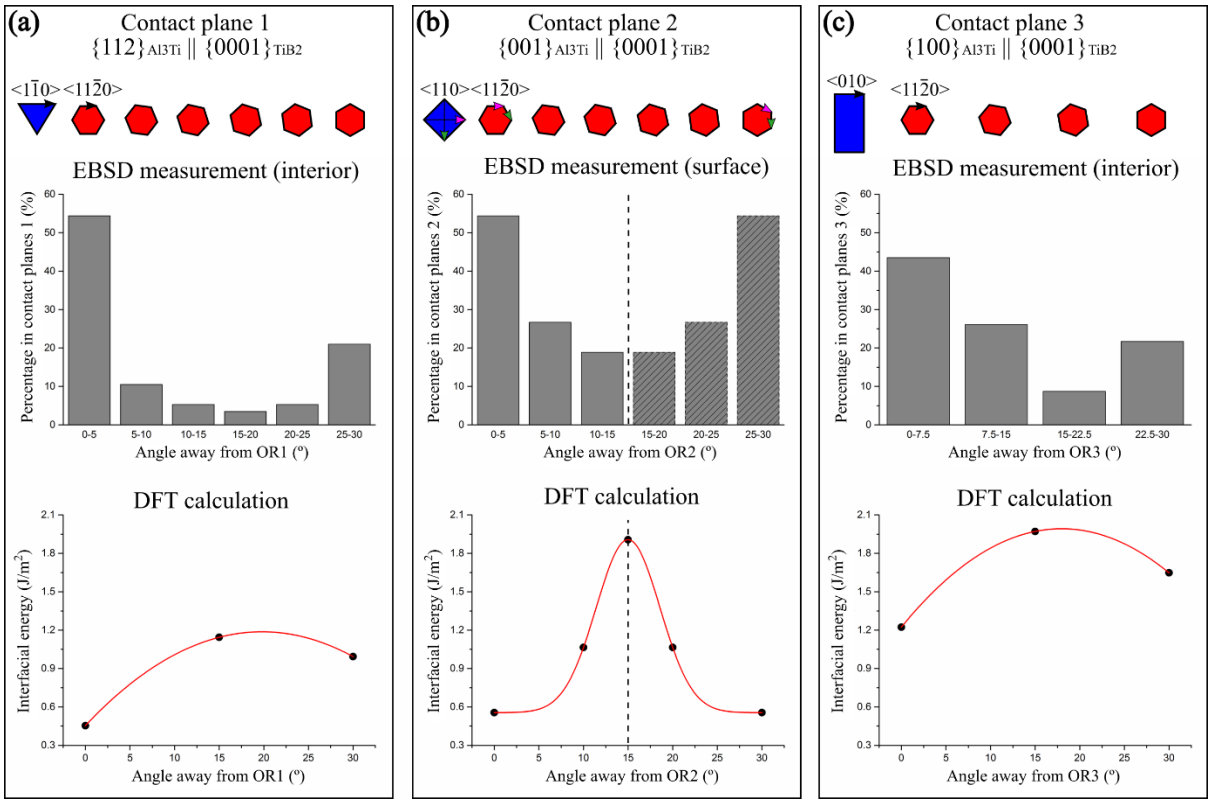

Figure 3.14. In-plane rotation (restricted rotation on the contact plane) of TiB_2 with respect to Al_3Ti on three contact planes. (Top) The frequency of different rotation angles measured by EBSD. (Bottom) The corresponding interfacial energies calculated by DFT when ($\mu_{TiB2}^{slab} - \mu_{TiB2}^{bulk}$)=-88kJ/mol. (a) $\{112\}_{Al3Ti}$ || $\{0001\}_{TiB2}$, (b) $\{001\}_{Al3Ti}$ || $\{0001\}_{TiB2}$ and (c) $\{100\}_{Al3Ti}$ || $\{0001\}_{TiB2}$.

3.4.4 Out-of-plane rotation and interface optimisation

From the shape of Al_3Ti crystals, there is another facet, {101} (Figure 3.3(a)), and if pushing and engulfment of TiB_2 particles happen on this facet we should expect to observe another preferred contact plane: $\{101\}_{Al3Ti}$ || $\{0001\}_{TiB2}$. However, this was never measured in this work as highlighted in the contour inverse pole figures in Figure 3.7. Therefore, along with planar rotation during pushing and engulfment, there should be another active process to change the orientation of TiB_2.

Figure 3.15(a) shows a case where TiB_2 with OR3 is close to a {101} surface of Al_3Ti, indicating this TiB_2 was possibly pushed and engulfed on the {101} facet at a late stage of growth. Instead of $\{101\}_{Al3Ti}$ || $\{0001\}_{TiB2}$, the contact plane $\{100\}_{Al3Ti}$ || $\{0001\}_{TiB2}$ was produced (i.e. OR3), which suggests a non-uniform growth of Al_3Ti happened as it pushed the TiB_2 particle, forcing an out-of-plane rotation of this TiB_2 particle. Figure 3.15(b) illustrates schematically the combined processes of continuous pushing, rotation and engulfment due to Al_3Ti growth that could cause the formation of OR3 in this case. As in Figure 3.12, this mechanism also creates a small α-Al island left behind by the growth front. Similar to the in-plane rotation in section 3.4.3, this out-of-plane rotation is also believed to be driven by interfacial energy minimisation, where TiB_2 rotation caused by Al_3Ti growth optimises the interface.

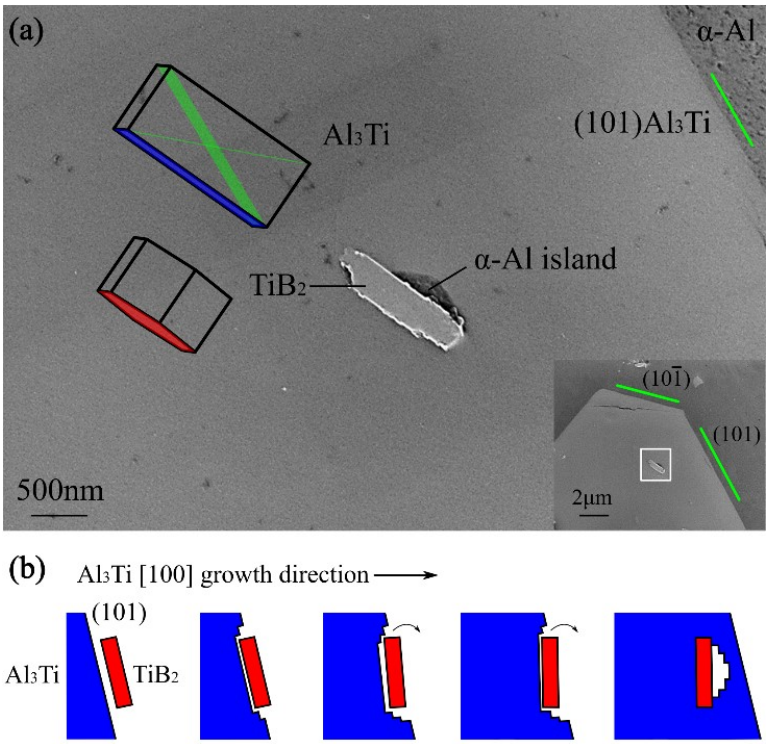

Figure 3.15. Out-of-plane rotation during the pushing and engulfment process for contact plane 3: $\{100\}_{Al3Ti}$ || $\{0001\}_{TiB2}$. (a) TiB_2 particle fully embedded underneath the Al_3Ti {101} facet with $\{100\}_{Al3Ti}$ || $\{0001\}_{TiB2}$ in cross section. The parallel planes are highlighted in the unit cell frames from EBSD. (b) Schematic illustration of out-of-plane rotation during the pushing and engulfment of a TiB_2 particle on a Al_3Ti {101} facet forming $\{100\}_{Al3Ti}$ || $\{0001\}_{TiB2}$.

Similarly, TiB_2 particles with OR1 in Figure 3.5(b) (1&2) are also very close to the {101} facets, and since there can only be one TiB_2 nucleant for a single Al_3Ti crystal, not all OR1 interfaces we measured were caused by nucleation. In Figure 3.14(a) TiB_2 particles have varying rotation angle on contact plane 1 with respect to OR1, indicating the planar rotation can happen on contact plane 1 during the pushing and engulfment process. Since the {112} facet is never observed in Al_3Ti crystals, the out-of-plane rotation process is required to orientate $\{0001\}_{TiB2}$ parallel to $\{112\}_{Al3Ti}$ followed by in-plane rotation to OR1 which gives the lowest interfacial energy. The rotation angle required from $\{101\}_{Al3Ti}$ || $\{0001\}_{TiB2}$ to contact plane 1,2 and 3 are 40.17°, 65.8° and 24.2° respectively, indicating a possible preference for TiB_2 to reorient to contact plane 1&3 followed by in-plane rotation to OR1 and OR3.

In Al grain refinement, it is widely accepted that the largest TiB_2 particles trigger nucleation first and that recalescence then stifles nucleation on smaller TiB_2 particles [227, 228]. It is likely that similar phenomena happen with the nucleation of Al_3Ti, although this could not be studied here since the size of TiB_2 could not be determined with confidence in 2D sections, and particles with OR1 could have formed by nucleation or by pushing/engulfment.

Figure 3.7(b) also shows that about 70% of TiB_2 particles did not have any of these three contact planes. They are likely to be clustered or trapped in other less favoured local energy minima and engulfed before there was enough uneven Al_3Ti growth to help reach an orientation relationship with lower interfacial energy. From this, it can be seen that while pushing and engulfment can generate preferred orientation relationships, engulfment can also occur when a higher energy interface is present.

3.5 Conclusions

A detailed study of the solidification orientation relationships between Al_3Ti and TiB_2 in the Al-Ti-B master alloys and in Al-0.8Ti containing large TiB_2 crystals has been conducted, combining experiment (EBSD) and simulation (DFT calculation). The following main conclusions can be drawn:

- Three reproducible ORs were measured between Al_3Ti and TiB_2 in Al-5Ti-1B and Al-3Ti-1B, both in master alloy rods and in remelted and cast samples:

$$\{112\}_{Al3Ti} \parallel \{0001\}_{TiB2} \text{ with } <\bar{2}01>_{Al3Ti} \parallel <11\bar{2}0>_{TiB2} \quad \text{(OR1)}$$

$$\{001\}_{Al3Ti} \parallel \{0001\}_{TiB2} \text{ with } <110>_{Al3Ti} \parallel <11\bar{2}0>_{TiB2} \quad \text{(OR2)}$$

$$\{100\}_{Al3Ti} \parallel \{0001\}_{TiB2} \text{ with } <010>_{Al3Ti} \parallel <11\bar{2}0>_{TiB2} \quad \text{(OR3)}$$

- DFT calculation shows OR1 has the lowest interfacial energy, OR2 has a slightly higher energy, and OR3 has a substantially higher interfacial energy, consistent with a simple lattice matching analysis.
- OR1 was most frequent (10.8%) inside Al_3Ti while OR2 was common (14.6%) on the Al_3Ti (001) facet. OR3 only existed inside Al_3Ti. Multiple TiB_2 particles were found to share all three ORs within a single Al_3Ti crystal; only one TiB_2 particle can have nucleated the Al_3Ti crystal and the other particles formed ORs by pushing/engulfment.
- By solidifying small Al_3Ti crystals on the (0001) facet of large TiB_2 crystals, OR1 was confirmed to be the nucleation OR between Al_3Ti and TiB_2. All six variants of OR1 were measured for multiple Al_3Ti crystals nucleating on the TiB_2 (0001) facet. OR2 and OR3 were never measured in these nucleation experiments.
- Micrographs of TiB_2 particles at different stages of pushing and engulfment by Al_3Ti growth facets, showed that TiB_2 plates lie with their (0001) on the Al_3Ti facet and cause a depression in the surrounding Al_3Ti growth front. Engulfment occurred by Al_3Ti ledges overgrowing a TiB_2 particle, leaving an α-Al island adjacent to the TiB_2 particle.

- A statistical analysis of EBSD data from 580 TiB_2 particles indicated that TiB_2 can rotate with respect to Al_3Ti during pushing. The frequency of the in-plane rotation angle measured by EBSD matched well with the interfacial energy calculated by DFT, showing that the rotation occurs to minimise the interfacial energy. This is the main origin of OR2 on (001) Al_3Ti facets, and occasionally of OR3 on rare (100) Al_3Ti facets.
- OR1 also occurred by a pushing and engulfment mechanism. However, unlike OR2, out-of-plane rotation is required to form OR1 (and OR3 on {101} facets) during pushing by the main Al_3Ti growth facets. Thus, combined in-plane and out-of-plane rotations during the pushing and engulfment process are required to optimise the interface and create OR1 and OR3 in most cases.
- More broadly it can be concluded that, for a faceted intermetallic (Al_3Ti) solidifying in the presence of numerous particles of a potent nucleant (TiB_2), the great majority of particles develop a simple OR by pushing/engulfment and the minority develop their OR by nucleation.

Chapter 4 Solidification twinning in IMCs: metastable nucleation in undercooled melts

4.1 Introduction

In Chapter 3, it was seen that six Al_3Ti orientations nucleated and grew from a single TiB_2 nucleant crystal; these were the six variants of OR1 and the combined six Al_3Ti orientations inherited an overall hexagonal symmetry from the TiB_2 nucleant (Figure 3.10). More generally, during solidification, when heterogeneous nucleation occurs on a nucleant phase with higher symmetry than the new solid, multiple variants of the nucleation OR exist and the resulting multiple orientations have a twinning relationship with each other. For example, the nucleation OR of FCC-Al on hexagonal TiB_2 has two variants and FCC-Al grains that nucleated with these two orientations have a twin OR with each other, a 60° rotation around a common {111} [229]. In another example, the nucleation OR of rhombohedral Al_8Mn_5 on cubic B2-Al(Fe,Mn) has eight variants and the resulting Al_8Mn_5 form cyclic twins with overall cubic symmetry [31]. Similar behaviour has been reported where the nucleant phase is a metastable precursor. For example, in electrostatically levitated NiZr droplets, a metastable decagonal quasicrystal formed in an undercooled melt and growth of the stable orthorhombic NiZr phase from this had a tenfold cyclic twinned structure [230]. There are many other examples of cyclic twinning in IMCs where the mechanism is not well understood. This chapter explores the solidification conditions under which cyclic twinning occurs in four IMCs where previous work has shown signs of cyclic twinning. The IMCs were selected using the following criteria:

1. There should be a low volume fraction of the primary IMCs to enable growth with their preferred morphology without interference from their neighbours.

2. After solidification, the remaining volume should mostly contain a simple metallic phase (e.g. α-Al or β-Sn) that is well-suited to selective etching to extract the primary IMCs for 3D SEM studies.

3. They should be either (i) ordered superstructures derived from simple close packed disordered phases, where the superstructure is from a different crystal system to the parent phase (e.g. orthorhombic ↔ HCP, or tetragonal ↔ FCC).

4. Or (ii) low symmetry IMCs that are quasicrystal approximants.

5. The selected IMCs should span a wide range of crystal structures and pseudo-symmetries.

Based on these criteria, the selected IMCs were: $D0_{22}$-Al_3Ti, a tetragonal superstructure derived from FCC; $D0_a$-Ag_3Sn, an orthorhombic superstructure derived from HCP; monoclinic $Al_{45}Cr_7$, an icosahedral quasicrystal approximant; and monoclinic $Al_{13}Fe_4$, a decagonal quasicrystal approximant. The phase diagrams of the four systems are plotted in Figure 4.1 at the Al-rich (from the Thermo-Calc TCTI2 database) or Sn-rich (from the Thermo-Calc TCSLD3.2 database) sides, with the compositions used in this study highlighted. The structure and lattice parameters of the four IMCs are listed in Table 4.1.

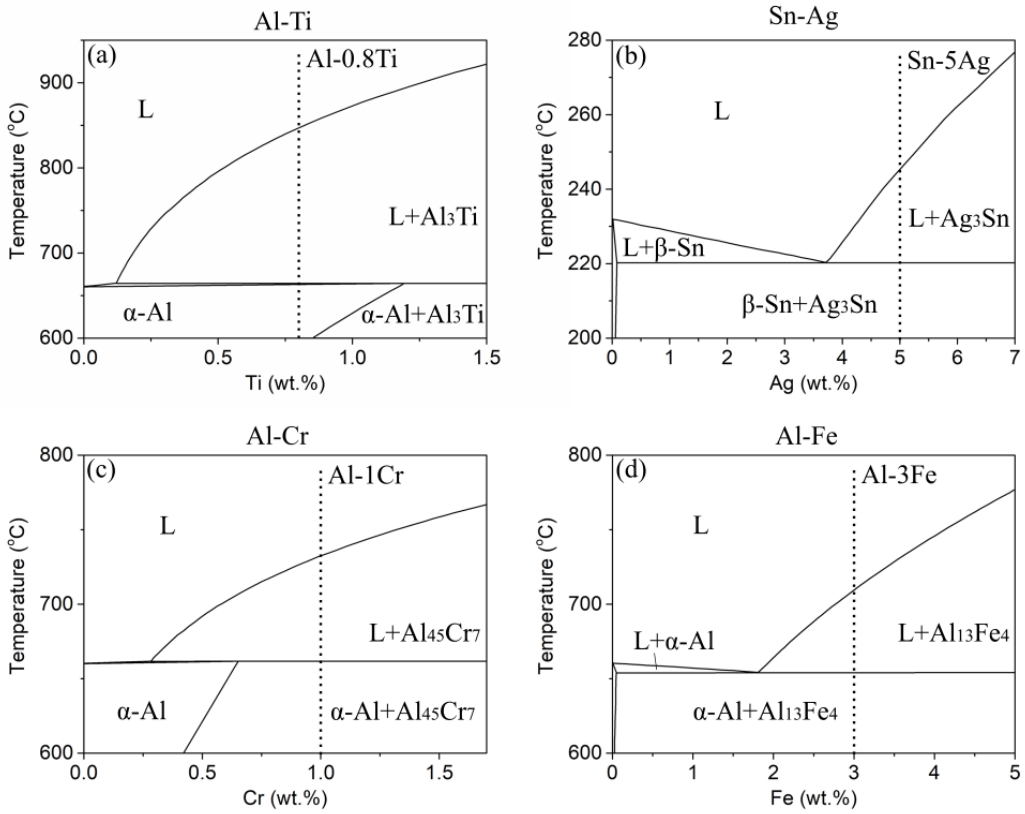

Figure 4.1 Phase diagram for (a) Al-Ti, (b) Sn-Ag, (b) Al-Cr and (d) Al-Fe system at Al (Sn for Sn-Ag) rich side.

Table 4.1 Crystal structures of the four IMCs

Crystals	Space group	Pearson symbol	Lattice parameters	Ref.
Al_3Ti	I4/mmm	*tI8*	a=3.8537Å, c=8.5839Å	[204]
Ag_3Sn	PmmnZ	*oP8*	a=4.7823Å, b=5.9975Å, c=5.1639Å	[231]
$Al_{45}Cr_7$	C2/m	*mS104*	a=25.196Å, b=7.574Å, c=10.949Å, β=128.72°	[126]
$Al_{13}Fe_4$	C2/m	*mS102*	a=15.492Å, b=8.078Å, c=12.471Å, β=107.69°	[128]

Past solidification studies on $Al_{13}Fe_4$ and $Al_{45}Cr_7$ sometimes report (untwinned) single crystals, single twins and multiple twins [29, 125, 232-234]. One aim of this work was to explore the effect of cooling rate and melt undercooling on the types and number of twins, to help us understand the origin of solidification twinning in these crystals. By studying four IMCs with significantly different symmetries, the aim was to further build the understanding of the factors affecting cyclic twinning rather than the specific behaviour of one crystal structure.

4.2 Methods

4.2.1 Sample preparation

160g of Sn-5Ag alloy was made by melting 99.999% Sn with 99.9% Ag. The mixture was heated to 300°C in a clay-bonded graphite crucible in a resistance furnace. After holding for 2 hours, the melt was stirred with an Al_2O_3 rod and then poured into the steel mould. The alloy was rolled to ~30µm foils, punched into Ø 1.6mm discs and reflowed in a ROL-1 tacky flux on a hotplate at 280°C to form 500µm diameter spheres due to surface tension. The balls were then reflowed in a Mettler Toledo DSC in aluminium pans under a nitrogen atmosphere. The heating rate was 20 K/min and the peak temperature was 280 °C. After holding at the peak temperature for 10 minutes, solder balls were then cooled at one of five cooling rates: 0.05, 0.2, 1.2, 5 and 20K/min ($8.3x10^{-4}$, $3.3x10^{-3}$, $2.0x10^{-2}$, $8.3x10^{-2}$ and $3.3x10^{-1}$ K/s).

50g of Al-1wt% Cr, Al-0.8wt% Ti and Al-3wt% Fe alloys were made by arc melting CP Al ingots (Table 4.2) with 99.9% Cr pellets, 99.99% Ti sponge and Al-10Fe master alloy respectively. Arc melting was conducted in 30mTorr vacuum, back-filled with Ar on a water-cooled Cu plate. The alloys were melted, flipped three times, and then the power was stopped and the alloy solidified on the water-cooled Cu plate. The cooling rate has been estimated to be approximately 5K/s from thermal imaging after switching off the arc [235]. For comparison, 15g of these three alloys were re-melted at 980°C in an alumina boat coated with a layer of boron nitride in a resistance furnace. After holding for 6 hours, the power was turned off and the melt cooled down slowly inside the furnace resulting in a cooling rate of 1.2K/min (0.02K/s), measured by an immersed K-type thermocouple in a separate experiment.

Table 4.2 The composition of commercial purity (CP) Al used in this work

Elements	Al	Fe	Si	Mn	Mg	Ni	Ti	Cu	Zn
Composition (wt. %)	Bal.	0.229	0.015	0.0039	0.0023	0.0158	0.0043	0.0015	0.0007

All alloys were mounted in Struers VersoCit acrylic cold mounting resin and then ground to 4000 grit with SiC paper followed by polishing with colloidal silica on a nap cloth for 6 minutes. For

crystallographic investigation, a Zeiss Sigma field emission gun SEM fitted with a Bruker e-FlashHR electron backscatter diffraction (EBSD) detector was used. Bruker Esprit 2.0 software, combined with the MTEX 4.4 Toolbox within MATLAB^{TM}9.2 (Mathworks, USA) [206], were applied to analyse the growth habits of single crystal intermetallics, and the orientation relationships in twinned crystals. Throughout this chapter, all unit cell wireframes in Figures were plotted based on the Euler angles measured by EBSD.

To study the 3D morphology of the intermetallic compounds, α-Al was selectively etched in anhydrous 1-butanol under an argon atmosphere at 117°C for approximately 4 hours, and β-Sn was selectively etched in the solution with 5% NaOH and 3.5% orthonitrophenol at 80°C for approximately 6 hours. Intermetallic crystals were collected and placed on a stub for further study by analytical SEM.

4.2.2 DSC analysis

Figure 4.2 shows a typical heating and cooling curve of a Sn-5Ag ball from DSC to demonstrate the method used to determine the nucleation temperature of the Ag_3Sn phase. In this case, the heating rate was 20K/min and the cooling rate was 1.2K/min. On both heating and cooling, one large peak at lower temperature and one small peak at higher temperature can be seen. The small peak is hotter than the eutectic temperature and is associated with the melting or solidification of primary Ag_3Sn. The nucleation point of primary Ag_3Sn is the temperature at which latent heat release first occurs on cooling, but it is difficult to determine accurately. Therefore, the onset temperature for primary Ag_3Sn nucleation was determined by the extrapolation method shown in the inset in Figure 4.2.

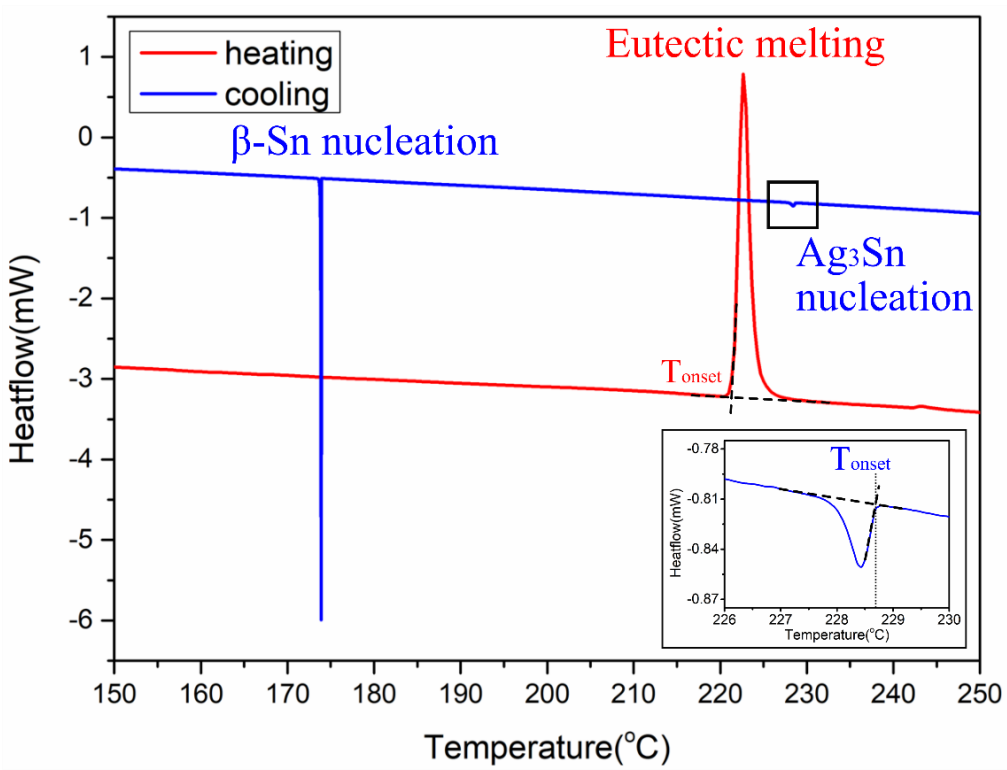

Figure 4.2 A typical heating (20K/min) and cooling (1.2K/min) curve from one Sn-5Ag solder ball, with the onset temperature for eutectic melting and Ag_3Sn nucleation determined by the extrapolation method.

For high heating and cooling rates in DSC, there can be a lag between the recorded temperature and the real temperature of thermal events due to heat transfer through the DSC pan. In order to check for the extent of such lag, five heating rates (0.05, 0.2, 1.2, 5, 20K/min) were applied to the same

solder ball and the heating curves in Figure 4.3 were recorded. The onset of melting was determined by the same extrapolation method as in Figure 4.2. Figure 4.3 focusses on the onset of eutectic melting since there is a large peak and there is negligible barrier for eutectic melting so, in theory, the onset temperature should be constant for all heating rates. It was found in Figure 4.3 that the onset temperature for eutectic melting at all five heating rates differs by less than 1°C. This is substantially smaller than the effects discussed in this Chapter and, therefore, the influence of the lag in data recording can be ignored.

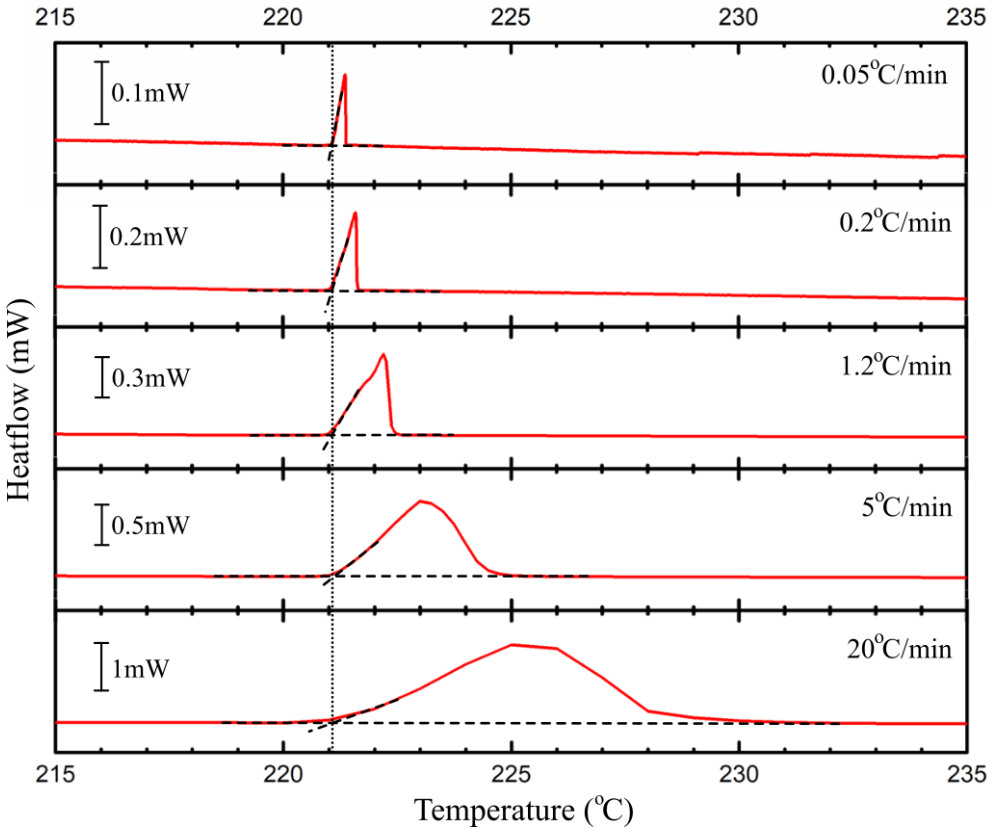

Figure 4.3 The heating curves of eutectic melting in a Sn-5Ag ball at different heating rate.

4.3 Results

4.3.1 Solidification twinning in the four IMCs

4.3.1.1 Al_3Ti

4.3.1.1.1 Single crystal of Al_3Ti

In Al-0.8Ti alloy cooled at 1.2K/min, all Al_3Ti solidified as plate-like single crystals. A typical Al_3Ti plate extracted from Al-0.8Ti alloy is shown in Figure 4.4. At this slow cooling rate, crystals grew into large size (>1mm) with high aspect ratio (thin plate-like shape). EBSD examination confirms that the main facet is {001} with multiple {100} edge facets. The thin direction of the plate is the long direction of the tetragonal unit cell.

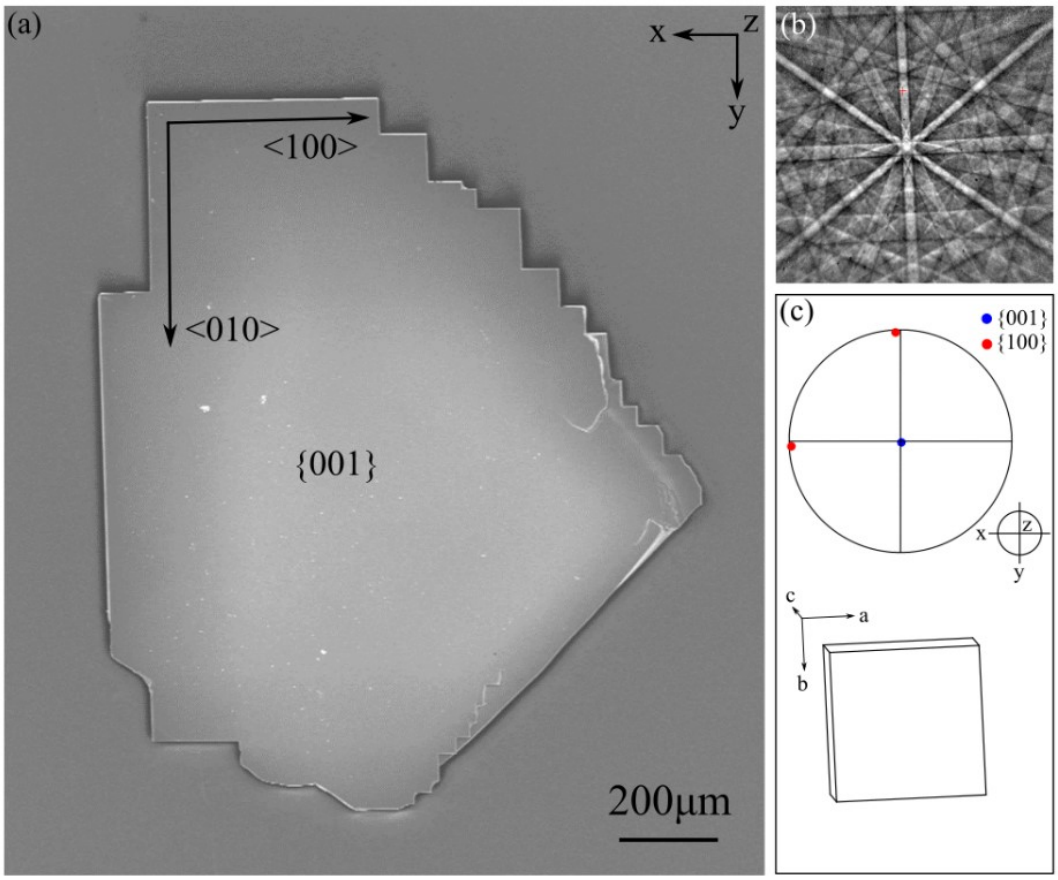

Figure 4.4 (a) Single Al_3Ti crystal extracted from slow cooled Al-0.8Ti with large {001} facet and {100} edges. (b) EBSD pattern from the Al_3Ti crystal in (a). (c) {001} and {100} pole figure of the crystal in (a) with the unit cell wireframe showing the orientation.

4.3.1.1.2 Cyclic twinning in Al_3Ti with combined cubic symmetry

In arc-melted (~5K/s) Al-0.8Ti alloy, Al_3Ti crystals were much smaller (~20μm) and, with EBSD examination, none were single crystals. Twinned Al_3Ti crystals consisted of three perpendicular plates penetrating each other, as shown in Figure 4.5(a). The EBSD IPF-Y map in Figure 4.5(b) shows there are three orientations inside the crystal and the main facet of each plate is {001}. The three orientations are at 90° to each other rotated about the <100> directions, causing every two of them to share a common {100} plane which is parallel to the {001} of the third one, as shown in pole figures in Figure 4.5(c). Together the three orientations form an overall cubic symmetry. Such triple twinning is obvious from the 3D morphology of extracted Al_3Ti crystals, as shown in Figure 4.5(d)-(f). The cubic orientation is plotted in Figure 4.5(f), surrounded by the three tetragonal unit cells corresponding to the three orientations in Figure 4.5(d). The three tetragonal unit cells are the three variants of one orientation relationship with a cubic unit cell. The unit cells of Al_3Ti in DO_{22} is plotted in Figure 4.5(g), as well as the related cubic $L1_2$ structure and the disordered FCC solid solution [236]. Compared to the large Al_3Ti plates from slow cooling in Figure 4.4, the twinned Al_3Ti crystals from arc melting are over 50 times smaller and the twins produce a blocky equiaxed shape.

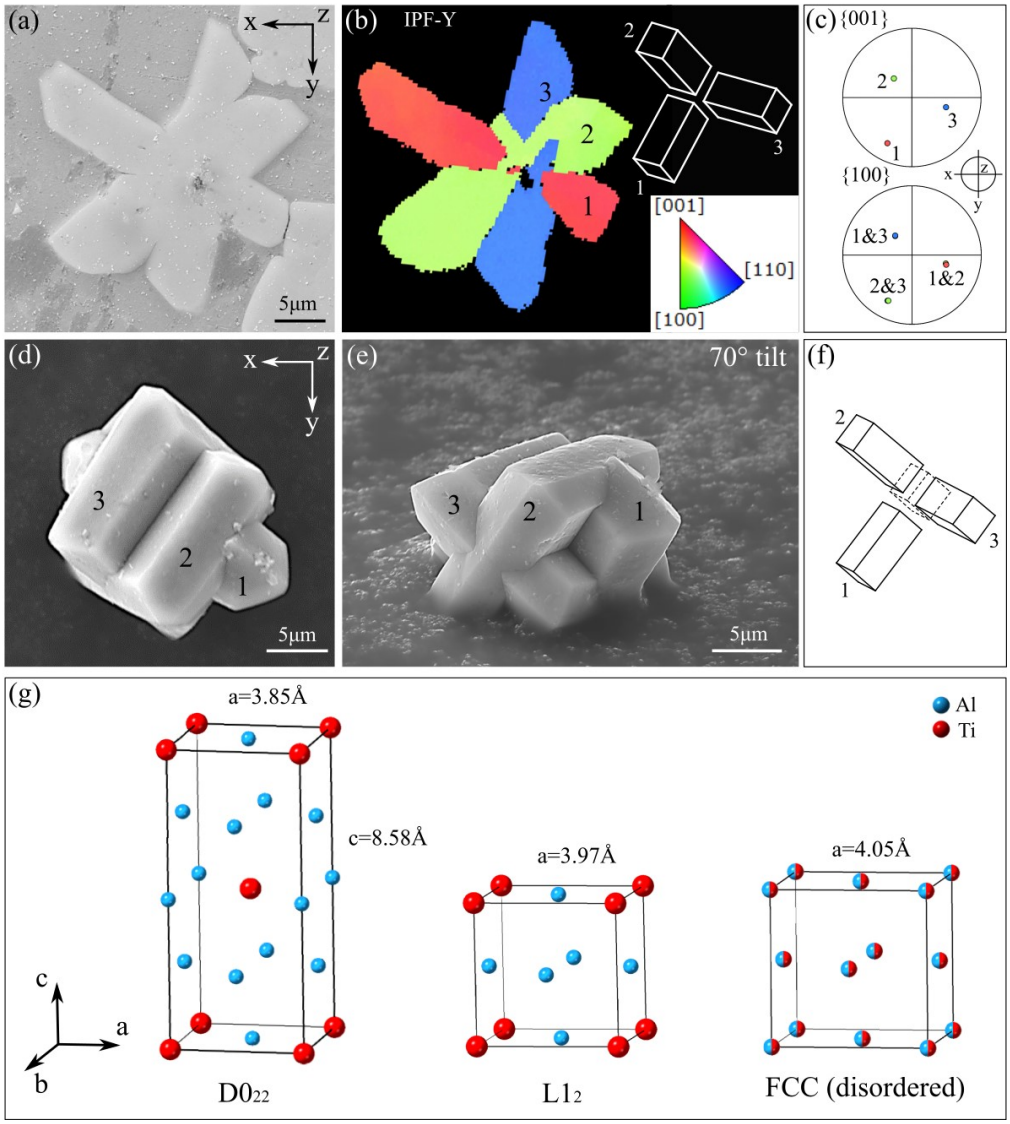

Figure 4.5 Triple twinning in Al_3Ti from arc-melted Al-0.8Ti alloy. (a) Al_3Ti crystal in cross section with three plates penetrating into each other. (b) EBSD IPF-Y map of the crystal in (a) showing three orientations inside the crystal, together with their unit cell wireframes. (c) {001} and {100} pole figures of the three orientations showing they are 90° to each other. (d) An extracted Al_3Ti crystal from arc-melted Al-0.8Ti alloy with the same triple twinning in (a)-(c). (e) 70° tilt view of the extracted crystal in (d). (f) The unit cell wireframes of the three orientations in (d) forming a combined cubic symmetry. The cubic orientation is plotted in the centre of the three tetragonal unit cells. (g) Unit cell of Al_3Ti in $D0_{22}$, $L1_2$ and disordered FCC solid solution structure.

4.3.1.2 Ag_3Sn

4.3.1.2.1 Single crystal of Ag_3Sn

When solidified at 0.05K/min, all Ag_3Sn in Sn-5Ag solder balls were single crystals. Figure 4.6(a) shows a typical Ag_3Sn single crystal cooled at 0.05K/min, and Figure 4.6(b) is the EBSD phase map of the solder ball. There is only one orientation in the large Ag_3Sn plate, and its Kikuchi pattern is shown in Figure 4.6(c). The {001} pole figure and the unit cell wireframe in Figure 4.6(d) indicate that the main facet of the primary Ag_3Sn plate is {001}. Figure 4.6(e) is a large Ag_3Sn plate extracted from the Sn-5Ag solder ball cooled at 0.05K/min. The EBSD IPF-Z map indicates that it is a single crystal with its {001} nearly parallel to the z-axis. The Kikuchi pattern from its top surface is shown in Figure 4.6(g). The {001} pole figure and the unit cell wireframe confirm the {001} is the main facet of the Ag_3Sn plate with {100} and {010} being the edges.

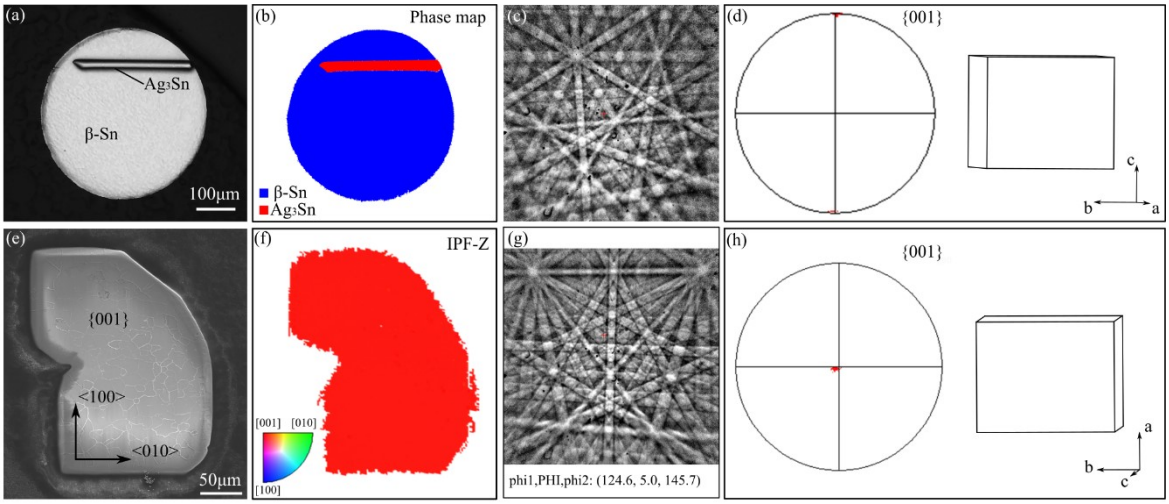

Figure 4.6 (a) Optical microscope image of an Ag_3Sn single crystal in a Sn-5Ag solder ball cooled at 0.05K/min. (b) EBSD phase map of the cross section in (a). Red is Ag_3Sn and blue is β-Sn. (c) The Kikuchi pattern from the Ag_3Sn in (a). (d) {001} pole figure with unit cell wireframes of the Ag_3Sn orientation in (a). (e) SEM image of an Ag_3Sn crystal extracted from a Sn-5Ag solder ball cooled at 0.05K/min. (f) EBSD IPF-Z map of the crystal in (e). (g) The Kikuchi pattern from the Ag_3Sn in (e) with Euler angles. (h) {001} pole figure with unit cell wireframes of the Ag_3Sn orientation in (e).

4.3.1.2.2 Cyclic twinning in Ag_3Sn with combined hexagonal symmetry

Compared to the single crystals from 0.05 K/min cooling rate, most Ag_3Sn (70%) were found to be twinned at 1.2K/min. Figure 4.7 shows a typical example of three twinned Ag_3Sn plates. The polarised optical micrograph reveals three different colours of the three plates, indicating that each one of them corresponds to a different crystallographic orientation (Figure 4.7(a)). Three Ag_3Sn orientations were measured by EBSD mapping but, as shown in the IPF-X map in Figure 4.7(c), there is a heavy misindexing problem between the three orientations in this map. According to the morphology analysis of the Ag_3Sn single crystal under the same cooling rate in Figure 4.6, the main facet of each plate is {001}. Therefore, the corresponding orientation for each plate can be assigned, as plotted next to the plate in Figure 4.7(c). There is a cyclic twinning relationship between the three Ag_3Sn orientations by a 60° rotation about the common <100> direction, and the three twinned orthorhombic orientations form a combined hexagonal symmetry, as shown in Figure 4.7(d). Pole figures of the three twinned orientations are plotted in Figure 4.7(e) showing the shared <100> direction with three {001} facets being at 60° to each other. In terms of the atomic arrangement, Figure 4.7(f) is the hcp lattice (grey) superimposed with the three orthorhombic unit cells with Sn and Ag atoms coloured in blue and orange. The whole hcp lattice can be occupied by the three twinned Ag_3Sn unit cells with chemically ordered atomic arrangement and small lattice distortion (as will be discussed later). Figure 4.7(g) is a comparison between the orthorhombic Ag_3Sn unit cell and the disordered hcp structure. The OR between the orthorhombic and hcp unit cells is: $\{001\}_{ortho}$ || $\{1\bar{1}00\}_{hcp}$, with $<100>_{ortho}$ || $<0001>_{hcp}$, and the three measured orthorhombic orientations correspond to the three variants of this OR.

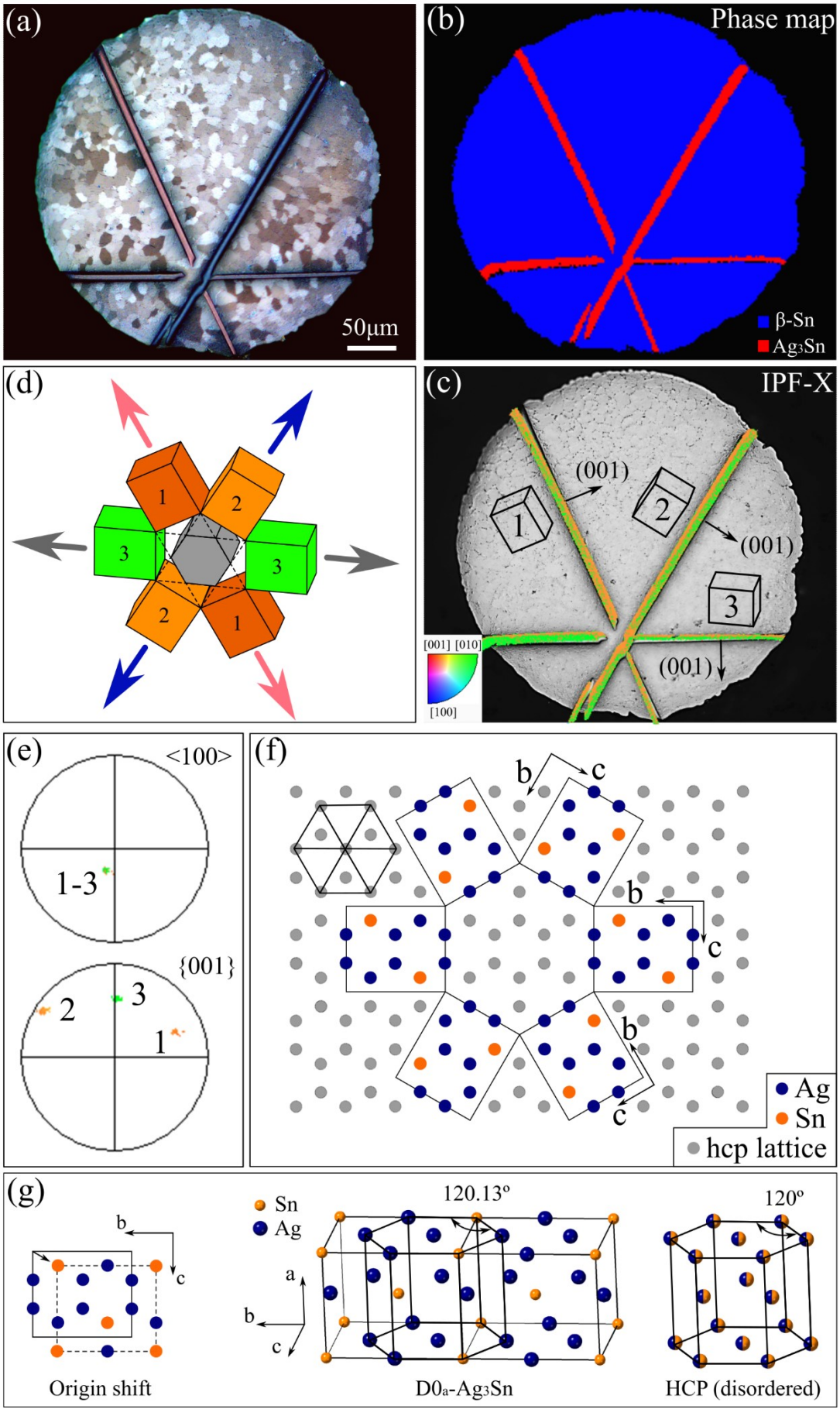
(a)
50μm
(b)
Phase map
β-Sn
Ag3Sn
(d)
1
2
3
3
2
1
(c)
IPF-X
(001)
(001)
(001)
1
2
3
[001] [010]
[100]
(e)
<100>
1-3
{001}
2
3
1
(f)
b
c
b
c
b
c
Ag
Sn
hcp lattice
(g)
b
c
Origin shift
Sn
Ag
a
b
c
120.13°
D0a-Ag3Sn
120°
HCP (disordered)

Figure 4.7 Cyclic twinning of Ag_3Sn in Sn-5Ag solder balls. (a) Polarised optical microscope image of twinned Ag_3Sn crystals in a Sn-5Ag solder ball cooled at 1.2K/min. (b) EBSD phase map of the cross section in (a). Red is Ag_3Sn and blue is β-Sn. (c) EBSD IPF-X map of the Ag_3Sn crystals superimposed on the optical microscope image with unit cell wireframes plotted next to each plate. (d) A combined hexagonal symmetry formed by the three Ag_3Sn unit cell wireframes from (c). The growth direction is highlighted based on the colour of the plates in (a). (e) <100> and {001} pole figures of the three cyclic twinned Ag_3Sn orientations. (f) HCP lattice (grey) superimposed with ordered Ag (blue) and Sn (orange) atoms from three cyclic twinned Ag_3Sn unit cells. (g) Unit cell of $D0_a$-Ag_3Sn and disordered HCP structure.

4.3.1.3 $Al_{45}Cr_7$

4.3.1.3.1 Single crystal of $Al_{45}Cr_7$

In Al-1wt% Cr alloy solidified at 1.2K/min, about 40% of $Al_{45}Cr_7$ were single crystals with hexagonal rod-like shape, as shown in Figure 4.8. Figure 4.8(a) is a transverse sectioned plane of an $Al_{45}Cr_7$ rod embedded inside mounting resin. The EBSD IPF-Z map (Figure 4.8(b)) confirms that it is a single crystal, and the pole figure (Figure 4.8(c)) shows that the three main facets are (001)(magenta), (110)(red) and $(11\bar{1})$(blue), and the long direction is $[1\bar{1}0]$. Figure 4.8(d) shows another $Al_{45}Cr_7$ single crystal extracted from the alloy with the same shape. Figure 4.8(e) is a geometric model of the crystal morphology plotted using the (001), (110) and $(11\bar{1})$ planes, and the pole figure in Figure 4.8(f) shows the long direction of this crystal is almost in the plane of the paper. The unit cell orientation is also plotted with the long $[1\bar{1}0]$ direction highlighted.

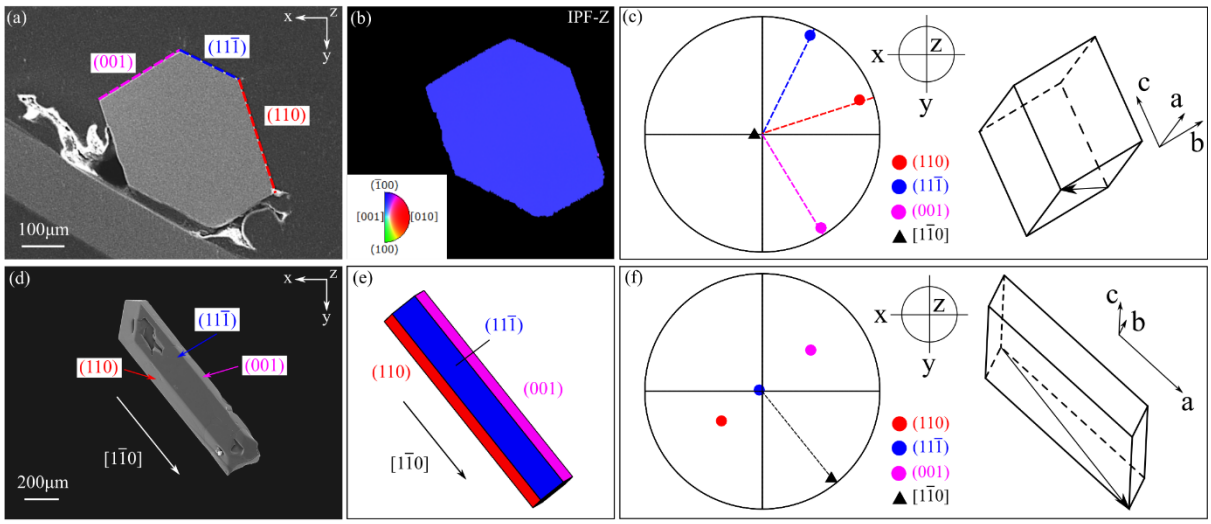

Figure 4.8 (a) A transverse cross section of $Al_{45}Cr_7$ rod with the main facets indexed as (001)(magenta), (110)(red) and $(11\bar{1})$(blue). (b)EBSD IPF-Y map of the crystal in (a). (c)Pole figure of the three main facets, (001), (110) and $(11\bar{1})$, and the $[1\bar{1}0]$ long direction of the crystal in (a), together with the unit cell wireframe with long direction highlighted. (d) A typical $Al_{45}Cr_7$ crystal extracted from Al-1Cr alloy, with three main facets and long direction indexed. (e) A schematic illustration of the crystal morphology with (001), (110) and $(11\bar{1})$ facets coloured in magenta, red and blue, respectively. (f) Pole figure of the three main facets, (001), (110) and $(11\bar{1})$, and the $[1\bar{1}0]$ long direction of the crystal in (d), together with the unit cell wireframe with long direction highlighted.

4.3.1.3.2 Two types of twinning in $Al_{45}Cr_7$

The remaining 60% of $Al_{45}Cr_7$ crystals solidified at 1.2K/min were twinned. Some twinned $Al_{45}Cr_7$ crystals contained two types of twinning in the same rod, as shown in Figure 4.9. Figure 4.9(a) is a transverse cross section of a long rod-like crystal with re-entrant corners. There are four orientations in this crystal, as shown in the EBSD orientation map in Figure 4.9(b). The Kikuchi patterns from these four domains are given in Figure 4.9(c)-(f), and it is clear that they share some similarities and some obvious differences. In Figure 4.9(g) the four orientations share a common <110> long direction that is almost perpendicular to the sectioning plane. Between grain 1&2 (3&4) the common {110} plane is the interface, and it is indicated (red) in Figure 4.9(a). The twin is a 180° rotation about the common <110> axis. Such twinning can also be observed directly in the extracted crystal (Figure 4.9(i)) with the clear {110} interface. Figure 4.9(h) and (j) shows another type of twinning: between grain 1&4 (2&3) there is a common <101> direction with the common $\{11\bar{1}\}$ plane being the interface, and the twinning can be seen as a 70.9° rotation about the common <101> direction. The interface is also indicated in Figure 4.9(a) in blue. Such twinning with its interface can also be seen in the extracted crystals (Figure 4.9(j)).

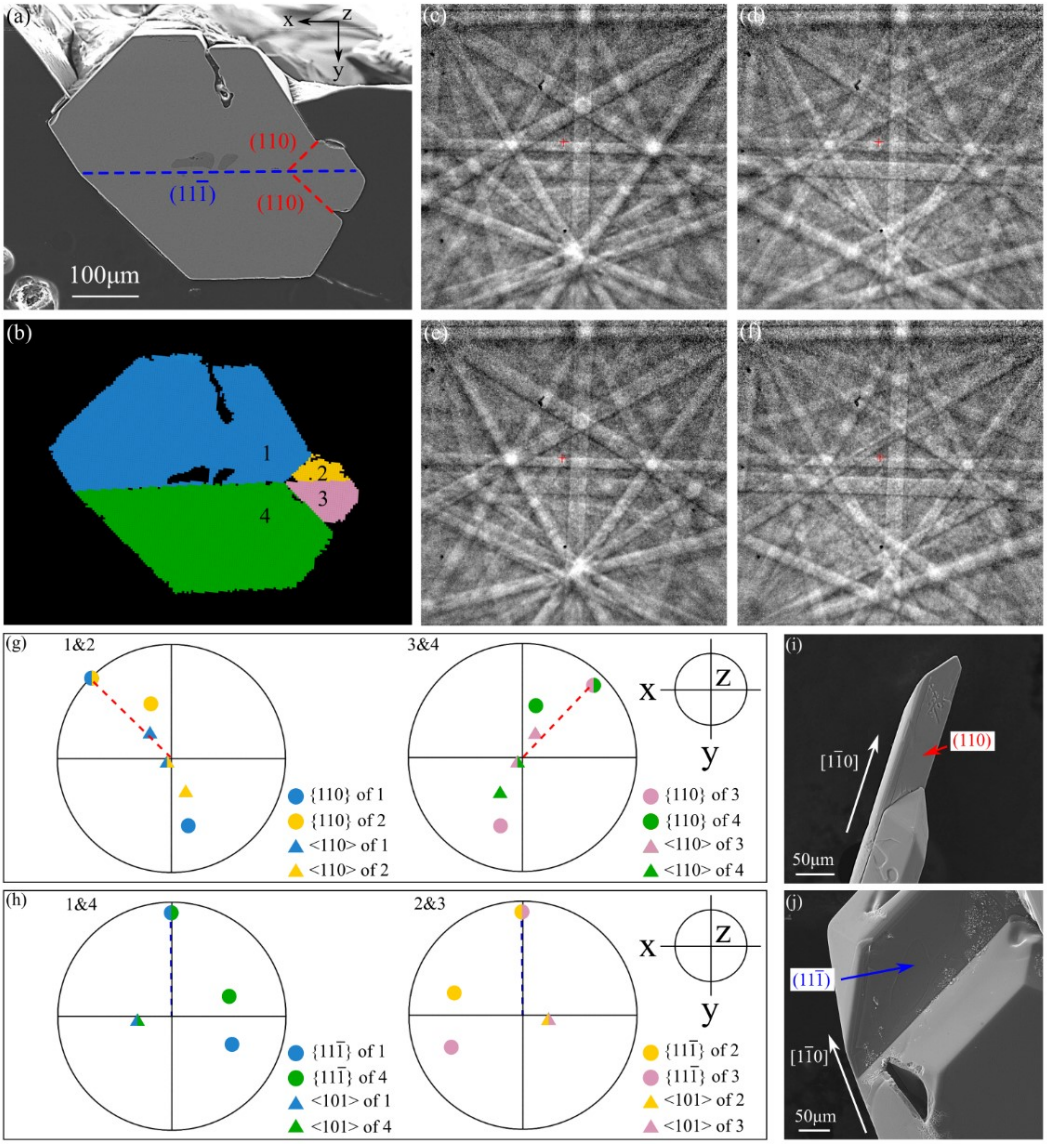

Figure 4.9 (a) A transverse cross section of $Al_{45}Cr_7$ long rod-like crystal. (b) The orientation map of the crystal in (a) showing four orientations. (c)-(f) The Kikuchi pattern corresponding to the Orientation 1,2,3 and 4 in (b). (g) The Type 1 twinning: 180° [1$\bar{1}$0] (110) between 1&2 and 3&4. (h) The Type 2 twinning: 70.9° [101] (11$\bar{1}$) between 1&4 and 2&3. (i) A typical extracted $Al_{45}Cr_7$ crystal with Type 1 twinning. The (110) interface is indexed. (j) A typical extracted $Al_{45}Cr_7$ crystal with Type 2 twinning. The (11$\bar{1}$) interface is indexed.

$Al_{45}Cr_7$ is an icosahedral quasicrystal approximant and contains distorted Cr-centred icosahedron building blocks in its unit cell, as shown in Figure 4.10(a). The twinning can be understood from the pseudo-icosahedral symmetry of this phase. An OR between $Al_{45}Cr_7$ and an icosahedron is plotted in Figure 4.10(a) with the monoclinic unit cell aligned so that its [101] is pointing out of the paper. It can

be seen that the *i*(5), *i*(3) and *i*(2) axes are approximately parallel with the pseudo-*i*(5), pseudo-*i*(3) and pseudo-*i*(2) axes in $Al_{45}Cr_7$ whose indices are labelled on the plot.

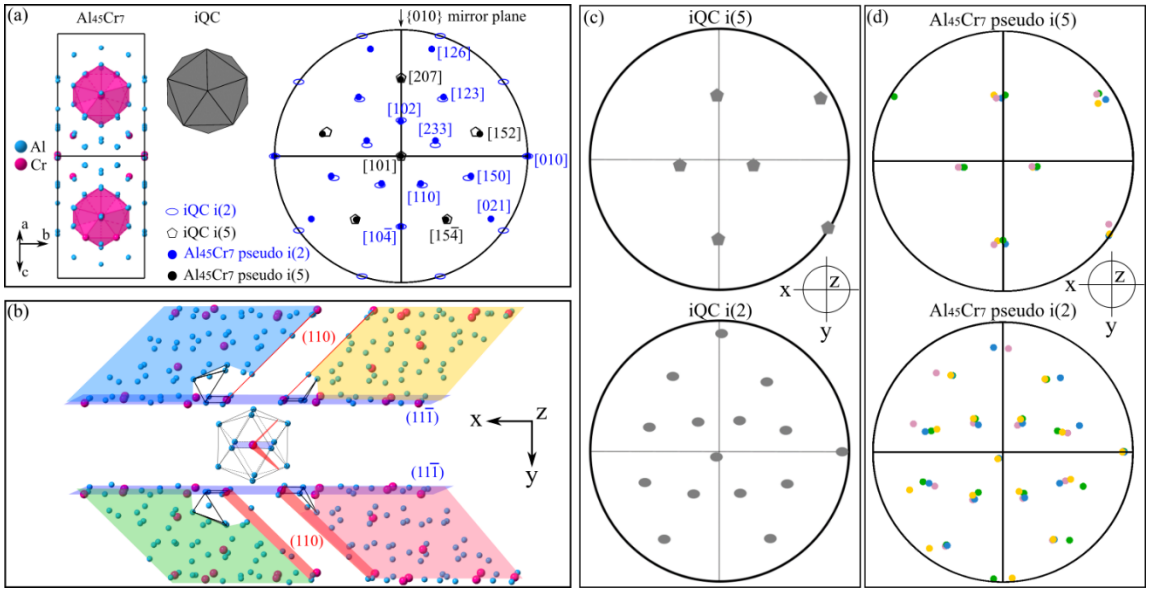

Figure 4.10 (a) Orientation relationship between $Al_{45}Cr_7$ and iQC: the Cr1 icosahedral building block in $Al_{45}Cr_7$ is parallel to the icosahedron in iQC. The $Al_{45}Cr_7$ is aligned so that one of the pseudo-fivefold directions, [101], is pointing out of the paper and one of the pseudo-twofold directions, [010], is pointing east. (b) The atom configuration at the junction of the four domains in Figure 4.9(b). Each domain is shaded in the same colour as in Figure 4.9(b). The interfaces are highlighted and indexed. A Cr-centred icosahedron is formed at the centre of the four domains. (c) Pole figures of the twofold and fivefold axes of the icosahedron in (b). (d) Pole figures of the pseudo-fivefold and pseudo-twofold directions of the four $Al_{45}Cr_7$ orientations in Figure 4.9(b).

Assuming the OR plotted in Figure 4.10(a), Figure 4.10(b) shows the atom configuration at the interfaces for all four orientations in Figure 4.9(b). Note that the orientation of the icosahedrons are different in (a) and (b): an *i*(5) is perpendicular to the paper in (a) to display the OR in a simple crystallographic way, while an *i*(2) is nearly perpendicular to the paper in (b) to be parallel to the measured rod axis $[1\bar{1}0]$. At the centre of the four domains is a shared common Cr-centred icosahedron, indicating they all have the same OR to that icosahedron. The fivefold and twofold axes of this icosahedral orientation are plotted in Figure 4.10(c). For comparison, the pseudo-fivefold directions of $Al_{45}Cr_7$ (<101>, <207>, <152> and <15$\bar{4}$>) from the four orientations are plotted in Figure 4.10(d) and they are all near-parallel to each other, and near-parallel to the fivefold axes of the

icosahedron orientation in Figure 4.10(b). The same is true for all the pseudo-twofold directions (<010>, <110>, <102>, <123>, <233>, <150>, <021>, <126> and <10$\bar{4}$>), and the common [1$\bar{1}$0] long direction is one of the pseudo-twofold directions. Among all 30 variants of the OR, only these four orientations share this common elongated direction. This OR between the icosahedron and $Al_{45}Cr_7$ is an icosahedron-on-icosahedron OR with the Cr1-centred distorted icosahedron in $Al_{45}Cr_7$, which is at the centre of the centrosymmetric $Al_{45}Cr_7$ unit cell. In past work, $Al_{45}Cr_7$ has been studied in coexistence with its parent icosahedral quasicrystal after reheating quasicrystals up to 450°C, and the measured OR between the iQC and $Al_{45}Cr_7$ was the same as that deduced in Figure 4.10 [125].

The same twinning geometry and the resulting re-entrant corners were observed in numerous slow cooled $Al_{45}Cr_7$ crystals in this work. Further examples are shown in Figure 4.11, with the common <110> long direction highlighted with triangles.

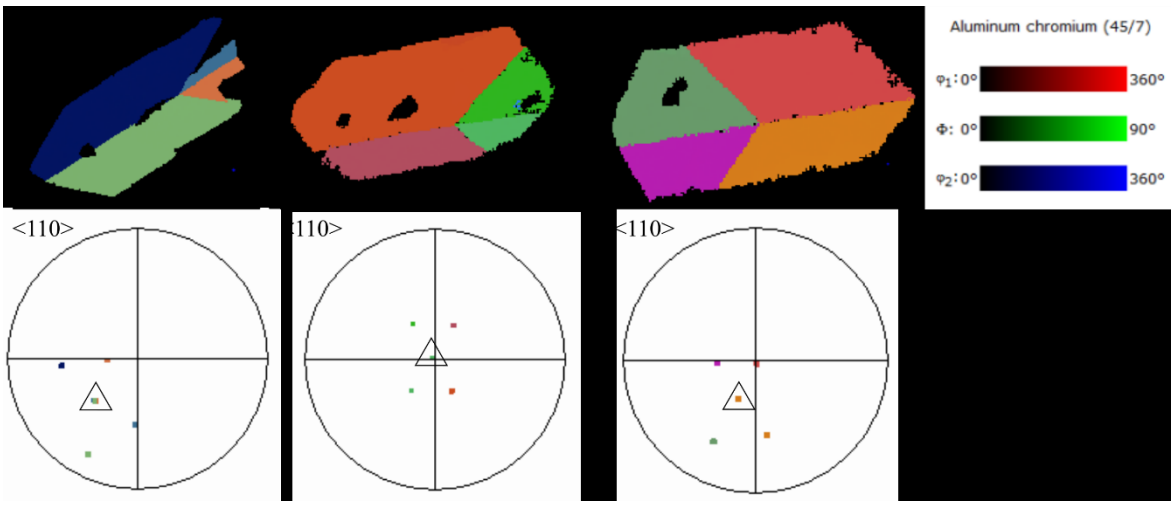

Figure 4.11 EBSD Euler angle map of the $Al_{45}Cr_7$ crystals with four twinned orientations, and their corresponding pole figures for <110> directions, together with the colour scheme for $Al_{45}Cr_7$ Euler angle map.

4.3.1.3.3 Multiple twinning in $Al_{45}Cr_7$ forming combined icosahedral symmetry

In arc-melted (~5K/s) Al-1wt% Cr alloy, the $Al_{45}Cr_7$ were much smaller with a more complicated shape. There was no long preferred direction and they never grew as single crystals. Figure 4.12(a) shows a typical $Al_{45}Cr_7$ crystal after arc-melting. EBSD revealed 12 orientations in the cross section, as shown in the EBSD Euler angle map in Figure 4.12(b). Figure 4.12(c) shows the enlarged area near the crystal centre, and due to the limit of the EBSD step size, there is a high rate of unindexed points near the complex centre. Multiple twinned boundaries exist between certain orientations and the twin laws are either one of the two types of twinning discussed with Figure 4.10 previously, indicating shared <101> (pseudo-fivefold) or <110> (pseudo-twofold) directions. Figure 4.12(d) plots all the <101> and <110> directions of the 12 measured orientations. Note that there are only six different <101> spots in the pole figure for the 12 orientations because some of them are shared, the same for the <110> directions. It is highlighted in the <110> pole figure that orientation 1-4, 5-8 and 8-11 share common <110> directions respectively, which means every group of the four orientations are in the same OR as in Figure 4.9-Figure 4.11 . The unit cell wireframes of the 12 orientations are plotted in Figure 4.12(e) and they are arranged in the same way as they are distributed geometrically inside the crystal. Figure 4.12(g) shows the Cr1-centred icosahedron building block in the unit cell of orientation 3, and all the other 11 orientations share the same orientation of the Cr1 icosahedron in their unit cells. A standard icosahedron with the same orientation is also plotted in Figure 4.12(g), with pole figures of its *i*(5) and *i*(2) plotted in Figure 4.12(f). The comparison between pole figures in Figure 4.12(d) and (f) shows that all 12 orientations form a combined icosahedral symmetry, and they all share the same OR to this single icosahedral orientation: the <101> direction is parallel to one of the fivefold axes and two <110> directions are parallel to two twofold axes. There are in total 30 possible (i.e. calculated) $Al_{45}Cr_7$ orientation variants with respect to a single icosahedron orientation in this OR, and the empty circles in the <110> pole figure in Figure 4.12(d) belong to the missing orientations not present in this cross section. It seems likely that all 30 twinned orientations are present in the full 3D crystal although this could not be confirmed in this work.

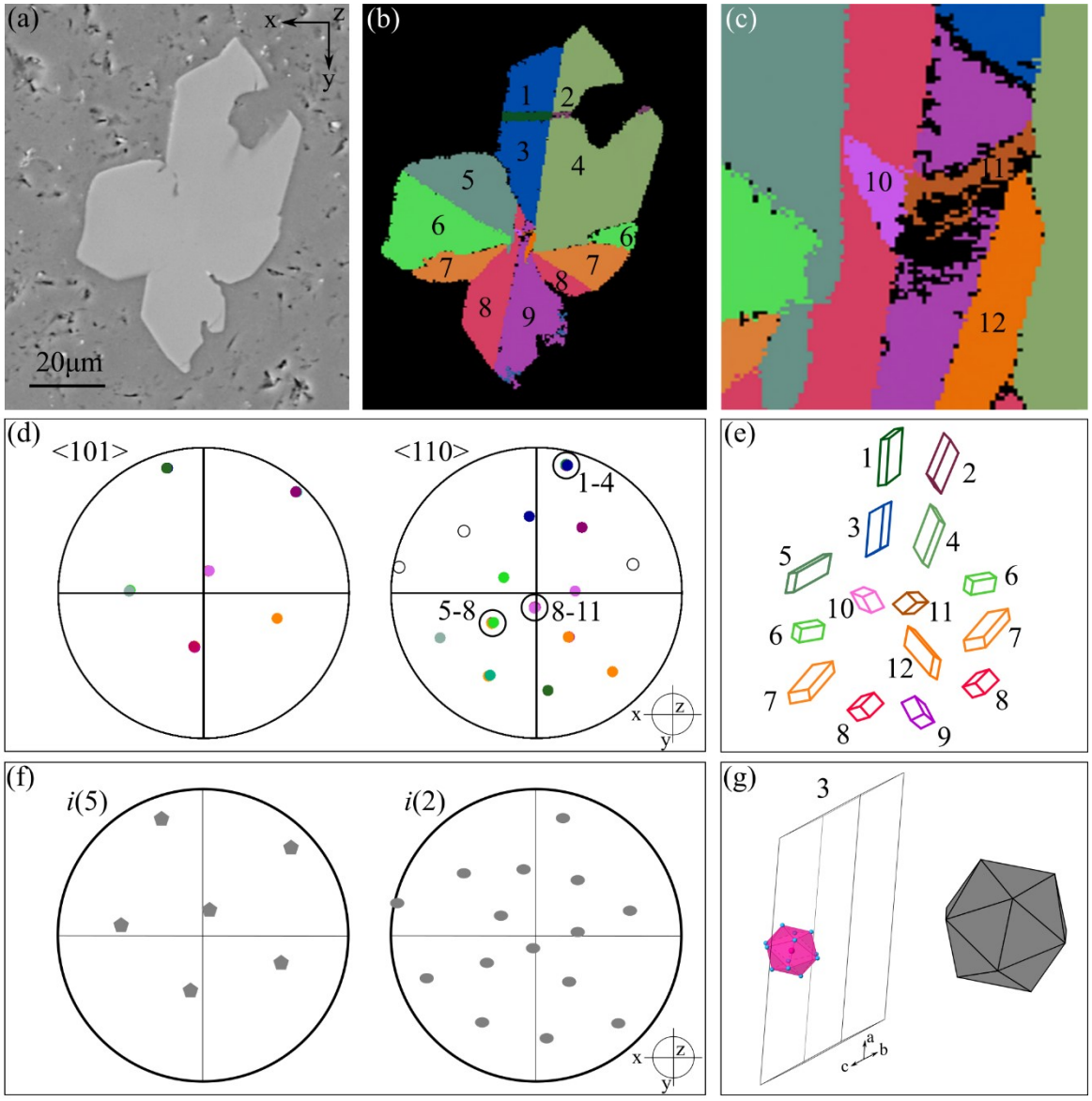

Figure 4.12 (a) The cross section of $Al_{45}Cr_7$ in arc-melted Al-1Cr. (b)-(c) EBSD Euler angle map of the crystal in (a) showing in total 12 orientations. The colour scheme is the same as in Figure 4.11. (c) is the enlarged Euler angle map at the crystal centre in (b). (d) Pole figure of the <101> and <110> directions of all 12 orientations in (b). (e) The unit cell wireframes of the 12 orientations in (b). (f) Pole figures of the fivefold and twofold axes of the standard icosahedron in (g). (g) The Cr1 icosahedral building block in the unit cell of orientation 3 in (b), and a standard icosahedron with the same orientation.

Figure 4.13 is a 3D $Al_{45}Cr_7$ crystal extracted from arc-melted Al-1Cr alloy. As indexed by the number, EBSD shows there are four orientations on the surface (2-2' and 3-3' share the same orientations). Figure 4.13(b) are the Kikuchi patterns from the four orientations with many similarities and clear differences to each other. The <101> and <110> pole figures plotted in Figure 4.13(c) show that every

two of the four orientations (1&2, 2&3, 3&4) share the 180° [$1\bar{1}0$] twinning relationship. All <101> and <110> directions from the four orientations partially form a combined icosahedron symmetry with a small deviation (the angle between two [110] and [$1\bar{1}0$] are 33.46° instead of 36°), in comparison with the fivefold and twofold axes from a standard icosahedron. Figure 4.13(e) are the unit cell wireframes of the four $Al_{45}Cr_7$ orientations with the standard icosahedron in the orientation of Figure 4.13(d). The four monoclinic unit cells are arranged spatially according to the parallelism between their <101> and the *i*(5) of the icosahedron, and such distribution is consistent with their real geometry in Figure 4.13(a).

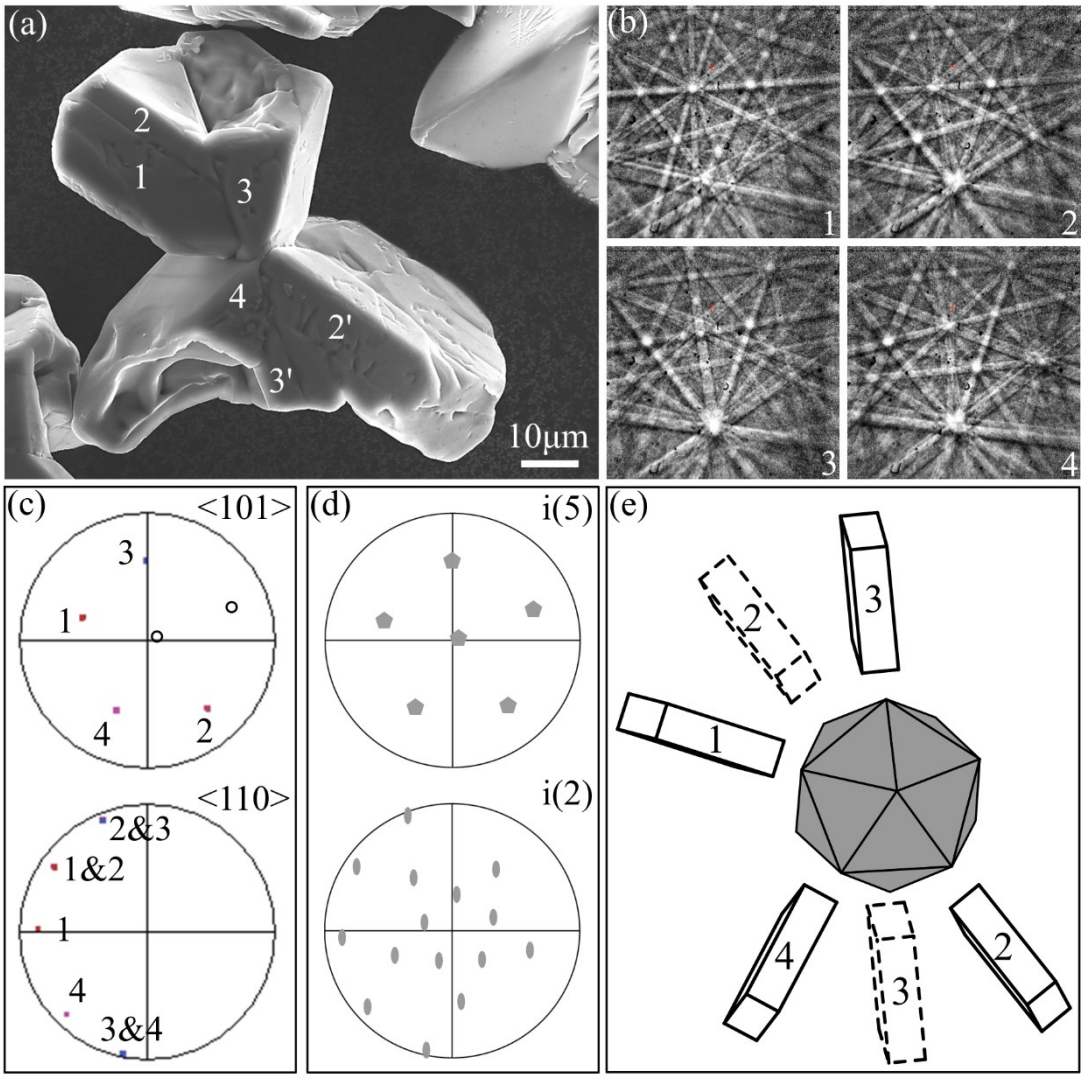

Figure 4.13(a) Extracted $Al_{45}Cr_7$ crystal from arc-melted Al-1Cr alloy with four orientations on the top surface. (b) The Kikuchi pattern from the four orientations in (a). (c) <101> and <110> pole figures of the four orientations in (a). (d) Pole figues of i(5) and i(2) of an icosahedral orientation. (e) Unit cell wireframes of the four $Al_{45}Cr_7$ orientations centred with the icosahedral orientation in (d).

Compared to the long (~800µm) rod-like shape from slow cooling, $Al_{45}Cr_7$ has a much smaller size (~60µm) with a more blocky morphology through arc-melting. Figure 4.14 shows EBSD Euler angle maps of other $Al_{45}Cr_7$ crystals from the arc-melted Al-1Cr alloy, each containing multiple twinned orientations with the same combined icosahedral symmetry. The corresponding icosahedral orientations are plotted below, where all $Al_{45}Cr_7$ orientations in each crystal share the same OR to the plotted icosahedrons. Similar to Figure 4.14, pole figures confirmed that all the pseudo-fivefold <101> and pseudo-twofold <110> directions of $Al_{45}Cr_7$ are parallel to the fivefold and twofold axes of the icosahedrons. Geometrically, the twin boundaries are commonly coincident with edges and re-entrant corners of the crystals, indicating that the twinned domains, cooperatively and competitively, attain their final forms through the growth advantages of these geometric features.

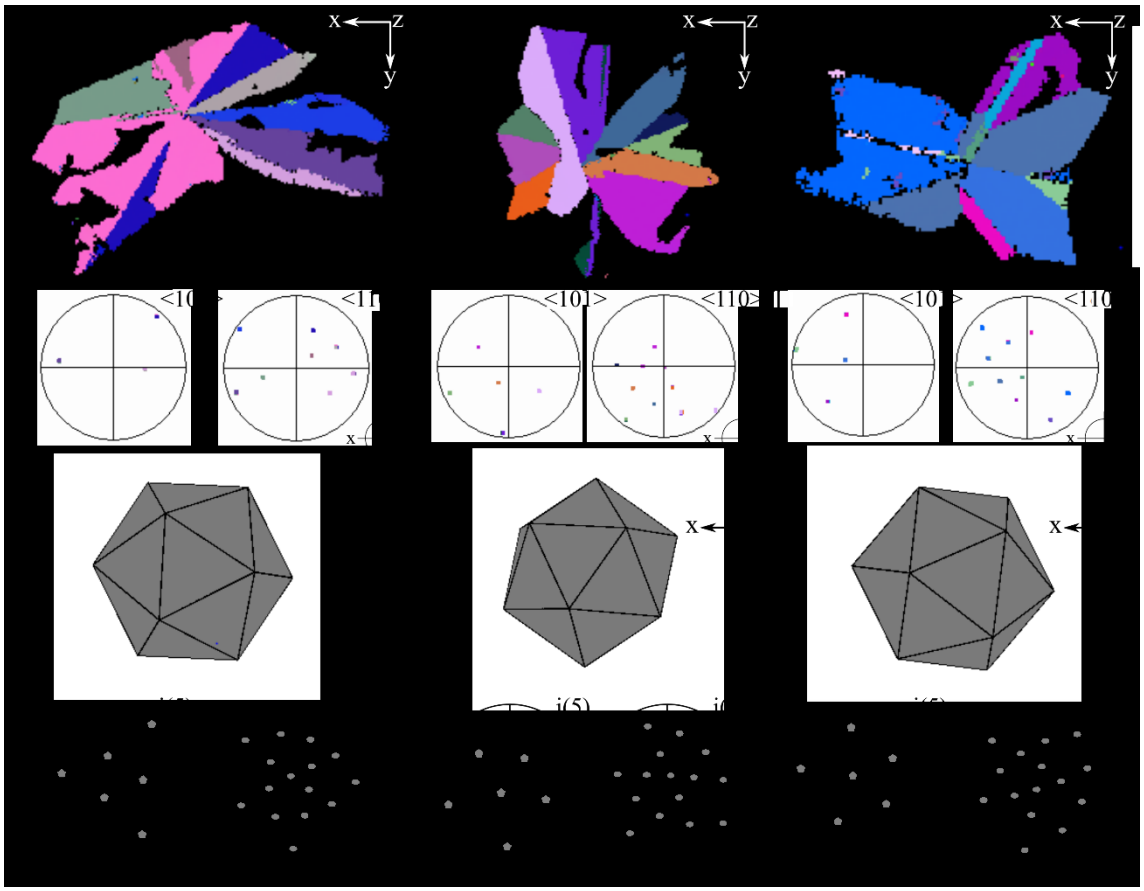

Figure 4.14 EBSD Euler angle maps of the $Al_{45}Cr_7$ crystals from arc-melted Al-1Cr alloy with multiple twinned orientations forming icosahedral symmetry, with pole figures for the pseudo-fivefold (<101>) and pseudo-twofold (<110>) directions plotted below. The corresponding icosahedral orientations are plotted too, with pole figures for the fivefold and twofold axes. The colour scheme for the Euler angle map is the same as in Figure 4.11.

4.3.1.4 $Al_{13}Fe_4$

4.3.1.4.1 Single crystal of $Al_{13}Fe_4$

For Al-3wt% Fe alloy solidified at 1.2K/min, about 40% of $Al_{13}Fe_4$ were single crystals with large (~600μm) hexagonal rod-like shape. Two types of single crystal growth crystallography were found for $Al_{13}Fe_4$, one with <010> (~70%) in the long rod direction and the other with <001> (~30%) in the long rod direction, as overviewed in Figure 4.15 and Figure 4.16 respectively. For the first type, the crystal in Figure 4.15(a) has its long directions almost perpendicular to the paper, and the example in Figure 4.15(d) has its long direction near-parallel to the paper. The EBSD IPF-Z map in Figure 4.15(b) confirms only one orientation in the transverse cross section in Figure 4.15(a). Pole figures in Figure 4.15(c) and (f) show that the three main facets are {001}(red), {100}(blue) and $\{\bar{2}01\}$(orange), and the long direction is <010>. The unit cell wireframes are also plotted in Figure 4.15(c) and (f).

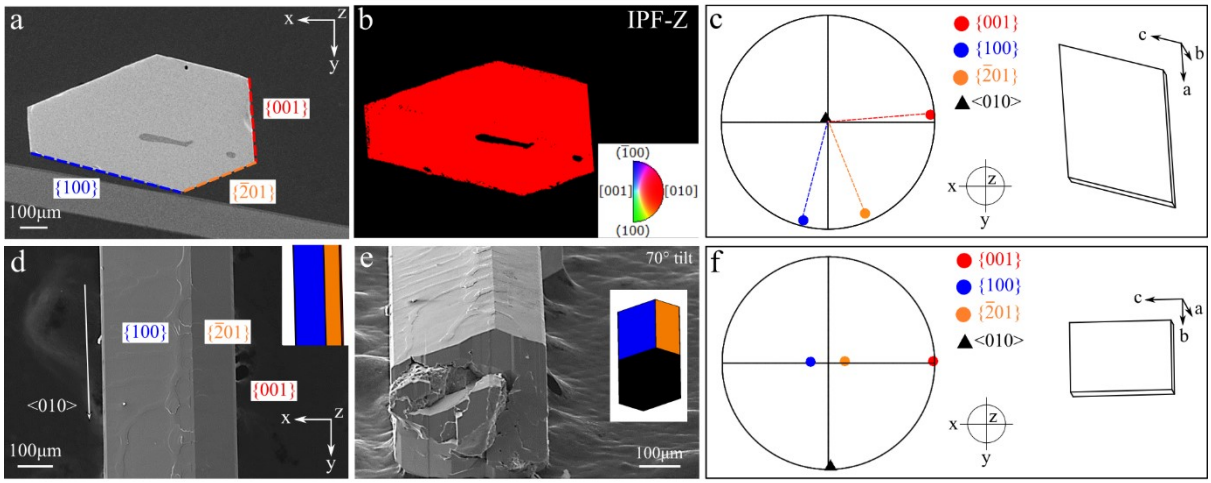

Figure 4.15 $Al_{13}Fe_4$ single crystals from slow cooling with <010> long direction. (a) A transverse cross section of an $Al_{13}Fe_4$ hexagonal rod. (b) EBSD IPF-Z map of the crystal in (a). (c) Pole figure of the {001}(red), {100}(blue) and $\{\bar{2}01\}$(orange) planes, and the <010> direction, together with the unit cell wireframe. (d) Extracted $Al_{13}Fe_4$ crystal with <010> long direction, with an illustration of the crystal morphology based on the growth habits. (e) 70° tilt view of the crystal in (d), with the illustration of morphology in (a) tilted by 70°. (f) Pole figure of the {001}(red), {100}(blue) and $\{\bar{2}01\}$(orange) planes, and the <010> direction, together with the unit cell wireframe.

The second $Al_{13}Fe_4$ single crystal growth morphology had <001> long direction, as in the example in Figure 4.16. Figure 4.16(a) and (d) show two $Al_{13}Fe_4$ crystals with their long direction perpendicular

and parallel to the paper. Pole figures in Figure 4.16(c) and (d) show that the main facets are {110}(green) and {100}(blue), and the long direction is <001>.

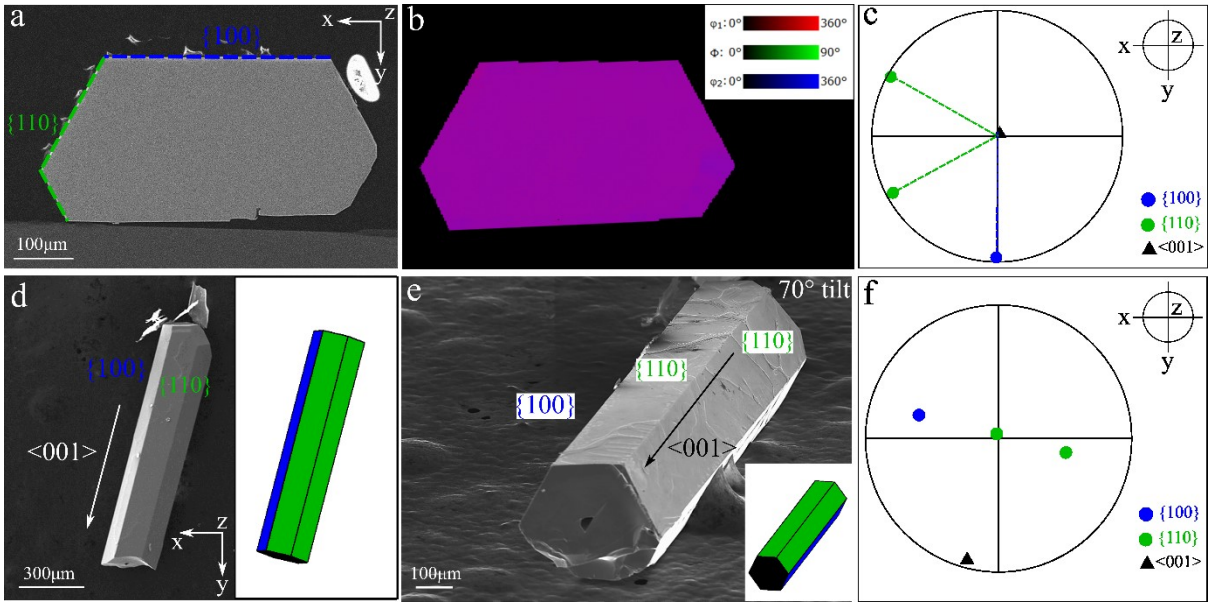

Figure 4.16 $Al_{13}Fe_4$ single crystals from slow cooling with <001> long direction. (a) A transverse cross section of an $Al_{13}Fe_4$ hexagonal rod. (b) EBSD Euler angle map of the crystal in (a). (c) Pole figure of the {110}(green) and {100}(blue) planes, and the <001> direction. (d) Extracted $Al_{13}Fe_4$ crystal with <001> long direction, with a geometric model of the crystal morphology based on the growth habits. (e) 70° tilt view of the crystal in (d), with the illustration of morphology in (d) tilted by 70°. (f) Pole figure of the {110}(green) and {100}(blue) planes, and the <001> direction for the orientation in (d).

4.3.1.4.2 <001>{100} twinning in $Al_{13}Fe_4$

Around 60% of $Al_{13}Fe_4$ crystals were twinned for rods with either <010> or <001> long direction. Figure 4.17(a) shows an $Al_{13}Fe_4$ crystal with <010> long direction and nearly symmetrical morphology with a re-entrant corner. The EBSD IPF-Y map in Figure 4.17(b) shows two orientations in this crystal and the interface passes through the re-entrant corner. Kikuchi patterns from the two orientations are shown in Figure 4.17(c) and (d) with multiple near-parallel bands and zone axes, and some clear differences. The pole figure in Figure 4.17(e) shows that the two orientations share the common <010> long direction perpendicular to the paper, and the main facets on both sides are consistent with Figure 4.15. This is one of the three types of twinning reported previously in $Al_{13}Fe_4$ [233]: 180° rotation around the <001> axis with {100} being the interface (i.e. {100} twinning). The twinning relationship is plotted using the two unit cell wireframes in Figure 4.17(e).

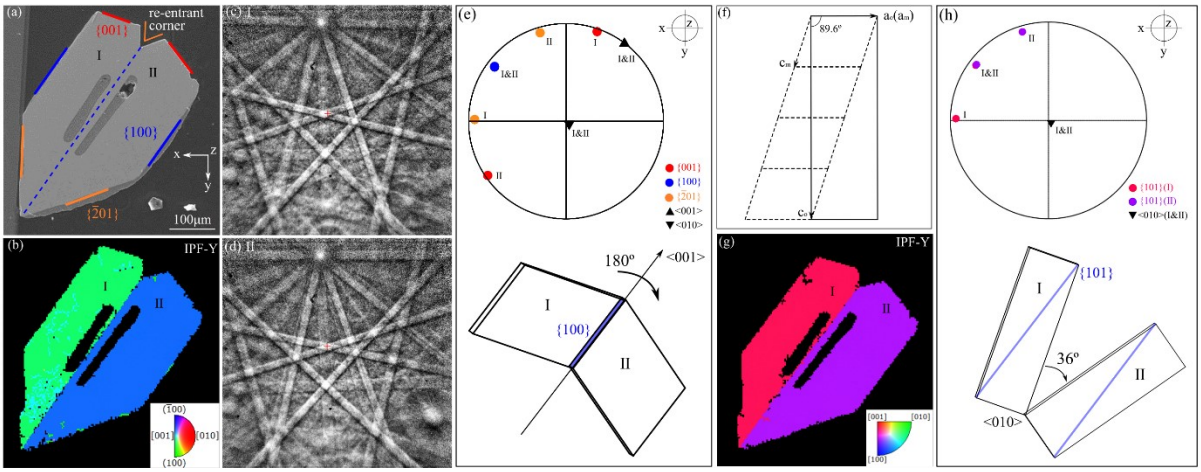

Figure 4.17 $Al_{13}Fe_4$ {100} type twinning in a <010> long rod from slow cooling. (a) A transverse cross section of a twinned $Al_{13}Fe_4$ rod with <010> long direction. The main facets are indexed. (b) EBSD IPF-Y map of the crystal in (a) showing two orientations with interface passing through the re-entrant corner. (c)-(d) The Kikuchi pattern from the two orientations in (b). (c) Pole figures of the main facets and long direction of the crystal in (a) showing the common {100} plane as the interface. The unit cell wireframes are also plotted showing the twinning relationship. (f) The transformation from $Al_{13}Fe_4$ monoclinic unit cell into pseudo-orthorhombic unit cell. (g) EBSD IPF-Y map of the crystal in (a) indexed with the orthorhombic structure. (h) Pole figure of the {101} planes and <010> direction of the two orthorhombic orientations in (g), with the unit cell wireframes and the twinning relationship between the orthorhombic unit cells.

$Al_{13}Fe_4$ has a pseudo-orthorhombic symmetry [237]. The transformation from the monoclinic unit cell into the pseudo-orthorhombic unit cell is plotted in Figure 4.17(f) with four monoclinic unit cells aligning along their c_m axis. The angle between the new a_0 and c_0 is changed from 89.60° to be exactly 90° after the transformation. The transformation matrix for crystallographic planes is:

$$\begin{pmatrix} a \\ b \\ c \end{pmatrix}_{orthorhombic} = \begin{pmatrix} 1 & 0 & 0 \\ 0 & 1 & 0 \\ 1 & 0 & 4 \end{pmatrix} \begin{pmatrix} a \\ b \\ c \end{pmatrix}_{monoclinic} \qquad \textit{Equation 4.1}$$

Figure 4.17(g) shows the EBSD IPF-Y map of the twinned $Al_{13}Fe_4$ crystal in (a) indexed with the orthorhombic structure. There are two orthorhombic orientations corresponding to the two monoclinic orientations in Figure 4.17(b), showing that the pseudo-orthorhombic symmetry does not cause the {100} type twinning in $Al_{13}Fe_4$. After transformation, the {100} and $\{\bar{2}01\}$ planes in the monoclinic unit cell merge into {101} planes in the orthorhombic unit cell, as shown in pole figure in Figure 4.17(h). It has been mentioned previously that the atomic structure on these two planes, {100} and $\{\bar{2}01\}$, are similar in $Al_{13}Fe_4$ [238]. For the orthorhombic unit cell, the twinning becomes a 36° rotation around the common <010> direction and the twin plane becomes {101}.

The same twinning was also observed in the $Al_{13}Fe_4$ rods with <001> long direction, as shown in Figure 4.18. Figure 4.18(a) is a typical cross section of an $Al_{13}Fe_4$ hexagonal rod. The IPF-X map of this crystal is plotted in Figure 4.18(b), and there are two orientations with a sharp interface parallel to the facets. There are both strong similarities and some clear differences between their Kikuchi patterns in Figure 4.18(c) and (d). Similar to Figure 4.16, the main facets for twinned $Al_{13}Fe_4$ <001> rods are {100} and {110}. Pole figures of the {100} (blue) and {110} (green) planes and <001> directions for the two orientations are plotted in Figure 4.18(e), together with their unit cell wireframes. It is clear that the two orientations share the common <001> long direction, and the {100} and {110} facets are all parallel to each other, which are highlighted in Figure 4.18(a), together with the {100} interface. Between the twinned orientations, it is a 180° rotation around the common <001> direction, which is the same twin type as in Figure 4.17. The {100} interface is highlighted in the unit cell wireframes, as well as the common {110} planes and <001> direction.

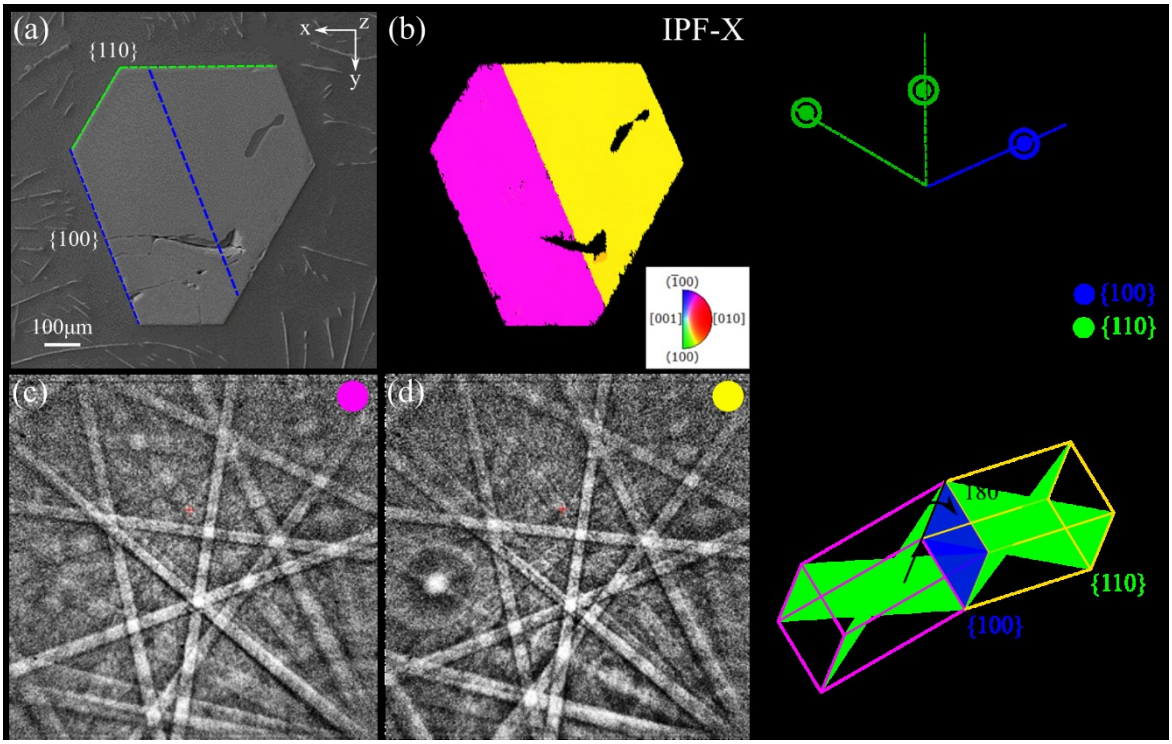

Figure 4.18 $Al_{13}Fe_4$ {100} type twinning in a <001> long rod from slow cooling. (a) A typical cross section of $Al_{13}Fe_4$ hexagonal rod. (b) The IPF-X map of the crystal in (a). (c)-(d) Selected Kikuchi patterns of the two orientations in (b). (e) Pole figure of the <001> direction and {100} and {110} planes of the two orientations in (b), and their unit cell wireframes.

4.3.1.4.3 Cyclic twinning in $Al_{13}Fe_4$ with combined decagonal symmetry

In the arc-melted (~5K/s) Al-3wt% Fe alloy, $Al_{13}Fe_4$ became much smaller (~50μm) with more twinned orientations. The long direction was <010> and the shape was more complicated with multiple facets. It was confirmed here by EBSD that all $Al_{13}Fe_4$ crystals after arc-melting were multi-twinned forming an overall decagonal symmetry, as shown in Figure 4.19. Figure 4.19(a) is a cross section of a typical $Al_{13}Fe_4$ crystal with multiple re-entrant corners from the arc-melted alloy, and Figure 4.19(b) shows the EBSD pattern quality map where the crystal is divided into many regions with a common origin and sharp interfaces. The orientation map in Figure 4.19(c) shows that there are seven monoclinic orientations in this cross-section of the crystal and their unit cell wireframes are plotted in Figure 4.19(d), together with three other undetected orientations to form the whole decagonal ring. Note that the colours in Figure 4.19(c) and (f) are manually chosen to separate different orientations without any meaningful indication of how the unit cells are oriented in space. The real orientations are shown by the unit cell wireframes in Figure 4.19(d) and (g). All ten monoclinic orientations share a common <010> direction, which is the pseudo-tenfold axis in the $Al_{13}Fe_4$ crystal structure. All three types of twinning known in $Al_{13}Fe_4$ [233] are observed in this crystal: the {100} pole figure shows between 2&3, 4&5 and 6&7 it is the {100} twinning; the $\{\bar{2}01\}$ pole figure shows between 1&2 and 3&4 it is the $\{\bar{2}01\}$ twinning; and the {001} pole figure shows between 3&6 and 4&7 it is the {001} twinning.

Considering the pseudo-orthorhombic symmetry discussed with Figure 4.17(f), the crystal was also indexed with the orthorhombic unit cell and the orientation map is shown in Figure 4.19(f). There are in total five orthorhombic orientations all at 36° to each other, forming a decagonal symmetry along the <010> direction (Figure 4.19(g)). Comparing the pole figures in Figure 4.19(e) and (h), the {100} and $\{\bar{2}01\}$ merge into one family, {101}, in the orthorhombic structure and the two corresponding twinning types become one, with {101} being the twin interface. The {001} twinning disappeared in the orientation map due to the same orthorhombic orientations for 3&6 and 4&7, respectively,

indicating that this twinning is caused by the pseudo-orthorhombic symmetry of $Al_{13}Fe_4$. As for the monoclinic {100} and {$\bar{2}$01} twinning, it is related to the pseudo-decagonal symmetry.

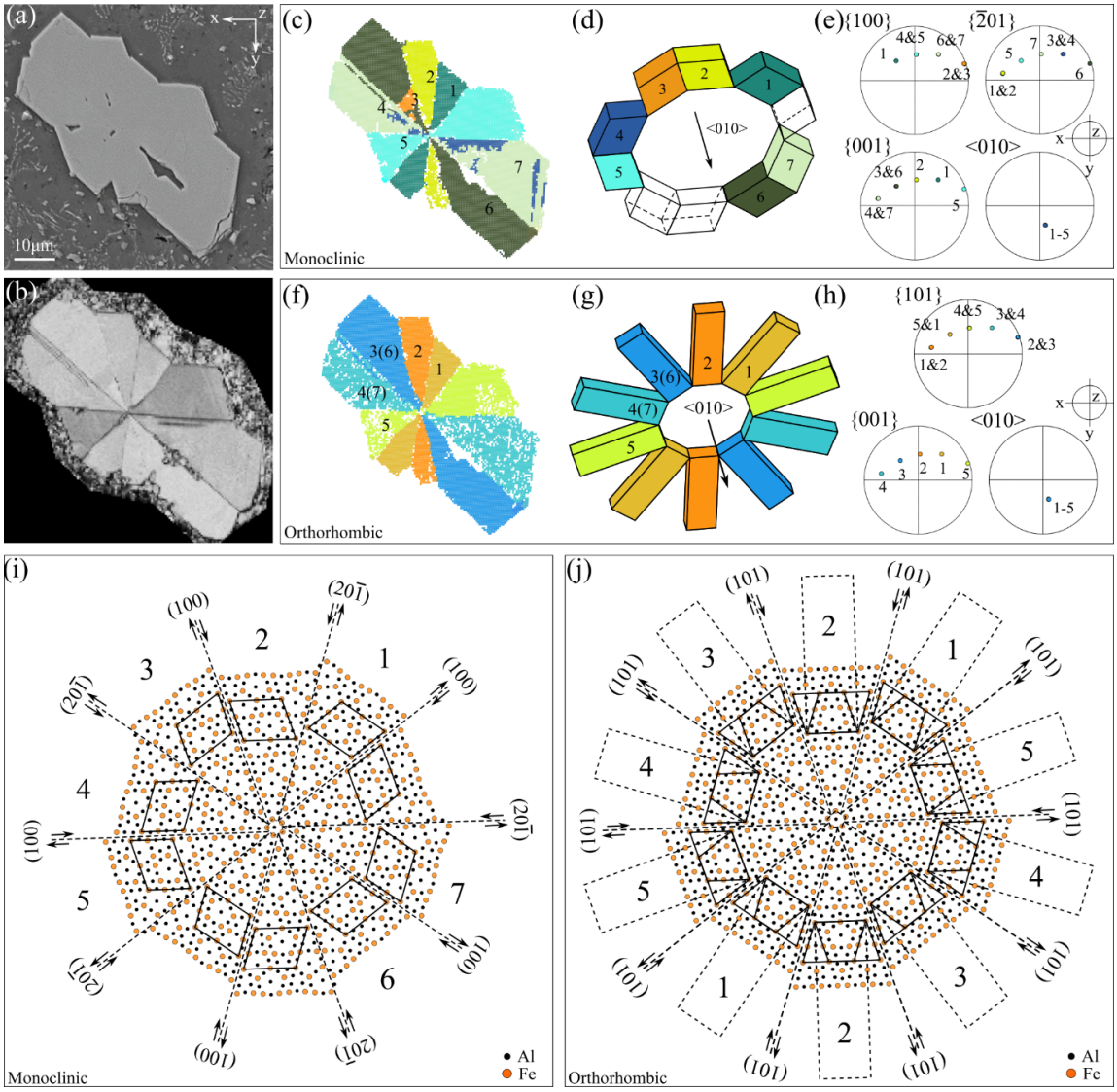

Figure 4.19 Multiple twinning in arc-melted $Al_{13}Fe_4$. (a) SE-SEM image of a cross section. (b) EBSD pattern quality map of the crystal in (a). (c) Orientation map of the crystal in (a) showing seven monoclinic orientations. (d) Monoclinic unit cell wireframes (with three orientations missing) forming a decagonal ring. (e) Pole figures of {100}, {$\bar{2}$01}, {001} and <010> for the seven monoclinic orientations. (f) The orientation map of the crystal in (a) indexed with orthorhombic unit cell. 3&6 and 4&7 correspond to the same orthorhombic orientations. (g) The five orthorhombic unit cells in (f) forming a complete decagonal ring with every orientation occurring twice on opposite sides. (h) Pole figures of {101}, {001} and <010> for the five orthorhombic orientations. (i) The atomic configuration of the $Al_{13}Fe_4$ {010} plane in monoclinic structure forming the decagonal ring in (d). (j) The atomic configuration of the {010} plane in orthorhombic structure forming the decagonal ring in (g), with every orthorhombic orientation corresponding to two monoclinic orientations. Note that the colours in (c) and (f) are manually chosen to separate different orientations without any meaningful indication of how the unit cells are oriented in space. The real orientations are shown by the unit cell wireframes in (d) and (g).

A glide-reflection model in {100}-{$\bar{2}$01} twinning was first proposed by Black [234] and later confirmed by high resolution electron microscopy [233, 239]. By applying such mechanism to all ten monoclinic orientations a complete ring can be formed with {100} and {$\bar{2}$01} being the interfaces, as shown in Figure 4.19(i) [240]. The ten unit cell wireframes are plotted and numbered with comparison to the ones above. The atomic arrangement shows that the ten monoclinic unit cells form a decagonal structure with certain glides at the interface.

Figure 4.20 shows the same decagonal twinned symmetry in an extracted $Al_{13}Fe_4$ crystal, showing the 3D morphology of the cyclic twinned crystal. There are multiple facets along the common <010> direction, and EBSD mapping shows that the five facets on top correspond to five monoclinic or orthorhombic orientations, respectively (Figure 4.20(b) and (c)). The five orthorhombic unit cells are plotted in Figure 4.20(e), with pole figures showing the common <010> direction and five common {101} planes.

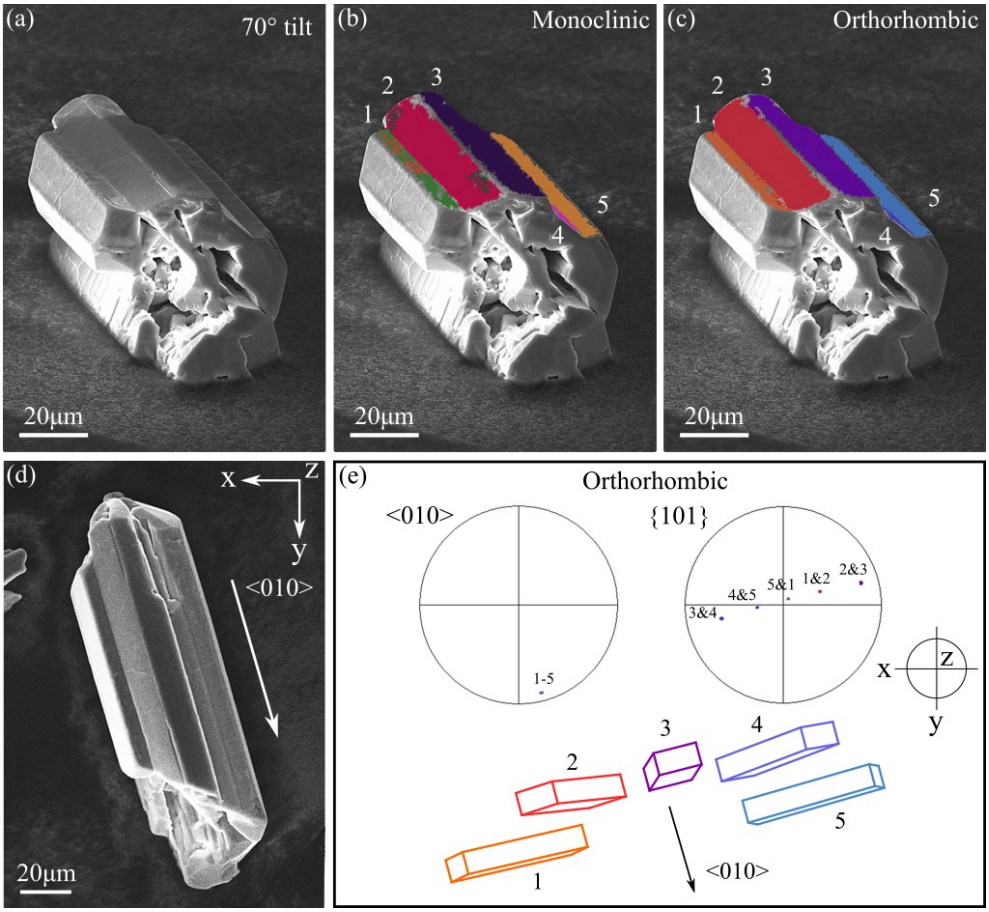

Figure 4.20 The extracted $Al_{13}Fe_4$ crystal with cyclic twinning forming decagonal symmetry. (a) 70° tilt view of an extracted $Al_{13}Fe_4$ from arc-melted Al-3Fe. (b) EBSD Euler angle map indexed with monoclinic structure superimposed on (a). (c) EBSD Euler angle map indexed with orthorhombic structure superimposed on (a). (d) Top view of the crystal in (a) with the <010> long direction highlighted. (e) <010> and {101} pole figures of the five orthorhombic orientations in (c) showing 36° rotation along <010> (decagonal symmetry).

4.3.1.5 Summary of measured twin types

The results of solidification twinning in Al_3Ti, Ag_3Sn, $Al_{45}Cr_7$ and $Al_{13}Fe_4$ measured at low and 'high' cooling rates are summarised in Table 4.3, including the percentage of twinned crystals, the measured twin type and the number of twin variants are also listed in the brackets at high cooling rate.

For slow cooling (1.2 K/min, 0.02K/s for the Al-bearing IMCs and 0.05K/min, 0.0008 K/s for Ag_3Sn), all Al_3Ti and Ag_3Sn crystals were single crystals with {001} being the main facets. In $Al_{45}Cr_7$ crystals, two types of twinning were observed among 60% and there were up to four orientations in the twinned crystals. In $Al_{13}Fe_4$, only one of the three reported twin types was observed and there were only two orientations measured in the twinned crystals.

At higher cooling rates (~5K/s for the Al-bearing IMCs and 0.33K/s for Ag_3Sn), all IMCs were cyclic twinned. For Al_3Ti and Ag_3Sn, both were triple twinned forming combined cubic and hexagonal symmetry, respectively. For $Al_{45}Cr_7$, the twin types remained the same as at low rate but grew along multiple common <110> directions from the twinned orientations; the number of all possible twinned orientations can be up to 30. For $Al_{13}Fe_4$, all three twin types were observed within each crystal with up to 10 possible orientations in the twinned crystal. Furthermore, compared to the two possible growth directions (<010> and <001>) observed in slow cooling, $Al_{13}Fe_4$ only grew along <010> in arc-melted samples.

Table 4.3 The growth twinning of the four IMCs from different cooling rates

IMCs	Slow-cooled (0.05K/min for Ag_3Sn and 1.2K/min for Al_3Ti, $Al_{45}Cr_7$ and $Al_{13}Fe_4$)			Fast-cooled (20K/min for Ag_3Sn) or Arc-melted (~5K/s for Al_3Ti, $Al_{45}Cr_7$ and $Al_{13}Fe_4$)		
	Percentage of twins	Twin type	Number of variants observed	Percentage of twins	Twin type	Number of variants observed
Al_3Ti	0%	-	-	100%	90°<100>	3(3)
Ag_3Sn	0%	-	-	100%	60°<100>	3(3)
$Al_{45}Cr_7$	~60%	180°$[1\bar{1}0](110)$ 70.9°$[101](11\bar{1})$	4	100%	180°$[1\bar{1}0](110)$ 70.9°$[101](11\bar{1})$	12(30)
$Al_{13}Fe_4$	~60%	180°[001](100)	2	100%	180°[001](100) 180°[102]{$\bar{2}$01} 180°[100]{001}	7(10)

4.3.2 The role of cooling rate and undercooling

It has been widely reported previously that cooling rate has a significant influence on how deeply the melt can be undercooled prior to nucleation. It has been observed in many systems, including Al [241] and Sn [242, 243] alloys, that the higher the cooling rate, the deeper the undercooling that can be achieved in the melt. In order to examine the relationship between undercooling and cooling rate and to attempt to decouple them, Ag_3Sn was chosen for thermal analysis in DSC due to its low nucleation temperature in Sn-5Ag alloy (liquidus temperature ~245°C) compared to the other three IMCs (liquidus temperature >700°C) and the relative ease with which the melt undercools with respect to Ag_3Sn.

4.3.2.1 DSC study of Ag_3Sn

Cooling curves for Ag_3Sn nucleation at different cooling rates are plotted in Figure 4.21. It is clear that the onset temperature for Ag_3Sn nucleation decreases with increasing cooling rates. The mean nucleation temperature for Ag_3Sn from over 10 balls for each cooling rate are plotted in grey in the histogram in Figure 4.22(a). For each cooling rate, 10 samples with a range of undercoolings were polished to examine the microstructure of Ag_3Sn by SEM imaging and EBSD. The results are indicated by the red (single crystal) and blue (twinned crystal) circles in Figure 4.22(a) with respect to their Ag_3Sn nucleation onset temperature. At low cooling rate (0.05K/min), all Ag_3Sn were single crystals. With increasing cooling rate (0.2, 1.2 and 5K/min), more Ag_3Sn grew as twinned crystals which tended to form at lower temperature compared to the single crystals, i.e. the twinned crystals formed with deeper undercooling. At the highest cooling rate (20 K/min), all Ag_3Sn formed as twinned crystals.

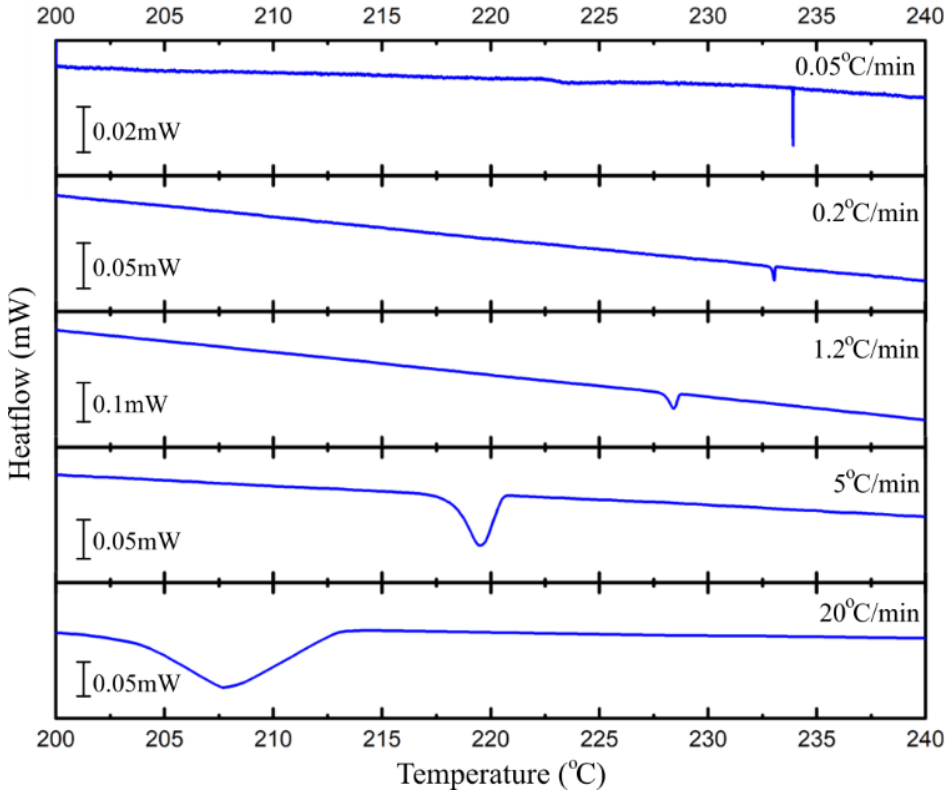

Figure 4.21 The cooling curves of Sn-5Ag balls at different cooling rate.

For Ag_3Sn, the mean undercooling at different cooling rates was obtained from Figure 4.22(a) assuming that the liquidus temperature for Ag_3Sn in Sn-5Ag is 245°C (using the Thermo-Calc TCSLD3.2 database). Figure 4.22(b) quantifies the relationship between the twinning frequency and undercooling: the deeper the undercooling, the more likely that Ag_3Sn grows as a twinned crystal. In order to visualise the nucleation temperature data, Figure 4.22(c) shows box plots for all the nucleation onset temperatures collected from the five cooling rates. We can see that although, for each cooling rate, there is a wide range between the minimum and maximum value, the median and the mean value from each group give a clear trend that with the increasing cooling rate, the onset temperature for Ag_3Sn nucleation decreases.

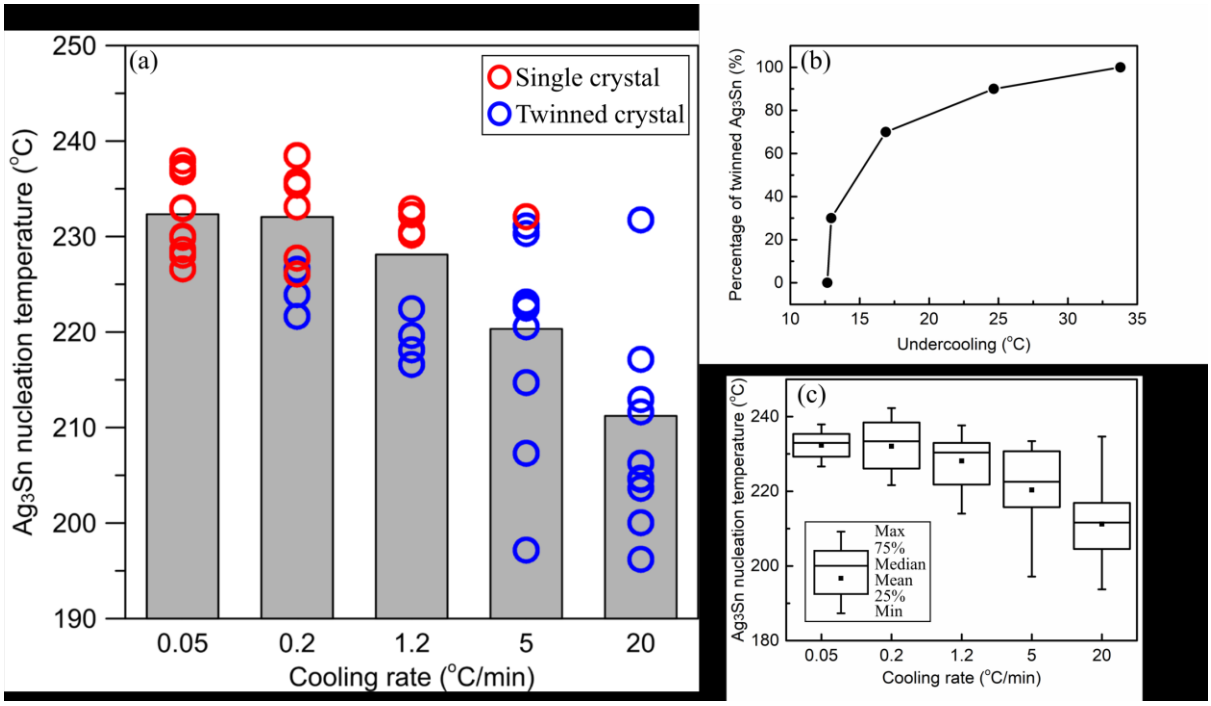

Figure 4.22 (a) Histogram of the mean nucleation temperature for Ag_3Sn at different cooling rate, superimposed with the nucleation temperature of Ag_3Sn from 10 individual samples in red (single crystal) and blue (twinned crystal) circles with corresponding microstructure.(b) The percentage of twinning Ag_3Sn with respect to the mean undercooling from the five cooling rate in (a). (c) Box plot of all the Ag_3Sn nucleation temperature obtained at the five cooling rate.

In Figure 4.22(c), the range of Ag_3Sn nucleation temperatures at each cooling rate indicates the stochastic nature of the nucleation event in these small (~500µm diameter) balls. Figure 4.23 further confirms the stochastic nature of Ag_3Sn nucleation through cyclic melting-cooling experiments. Figure 4.23(a) shows the cooling curve of Ag_3Sn nucleation from a Sn-5Ag solder ball through 10 successive melting-cooling cycles with 5K/min cooling rate. It is clear that the nucleation onset for Ag_3Sn varies from cycle to cycle. Figure 4.23(b) is the measured onset temperature for Ag_3Sn nucleation from three samples through the 10 cycles. It can be seen that the Ag_3Sn nucleation temperature is rather random with respect to the cycle number, suggesting that the nucleation of Ag_3Sn at each cycle is independent and stochastic. However, although the individual nucleation event appears to be stochastic, the whole group of statistical data in Figure 4.22(c) still reveal a clear relationship between the undercooling of Ag_3Sn and cooling rate: the higher the cooling rate, the deeper the undercooling that can be achieved in the melt.

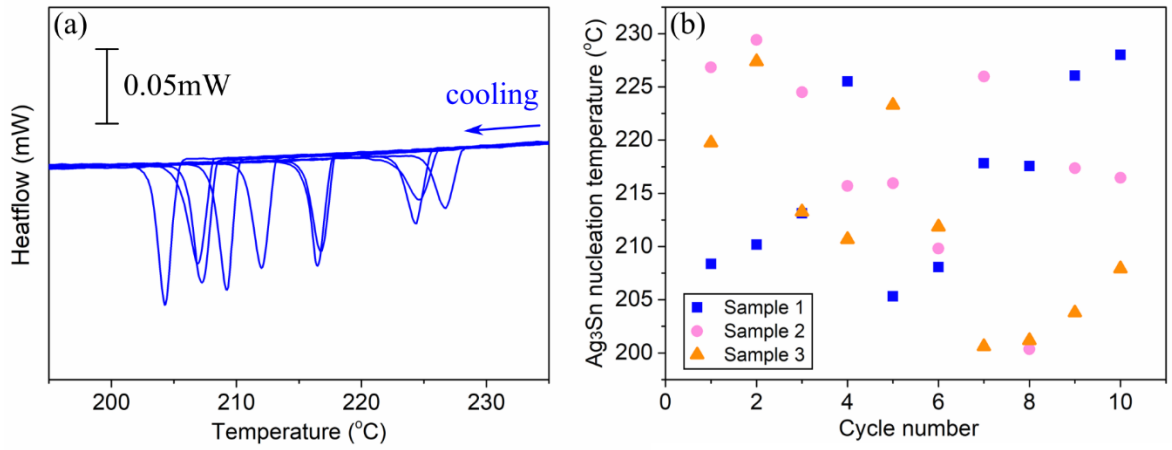

Figure 4.23 The stochasticity of Ag_3Sn nucleation. (a) The cooling curve of Ag_3Sn nucleation from a Sn-5Ag solder ball through 10 successive melting-cooling cycles with cooling rate at 5K/min. (b) Ag_3Sn nucleation temperature from three samples through the 10 successive melting-cooling cycles.

The relationship between the measured undercooling for Ag_3Sn and cooling rate are plotted in Figure 4.24: the mean undercooling increases with cooling rate with a near-linear increase of $\ln\Delta T_c$ with respect to $\ln\Delta\dot{T}$, as shown in the inset plotted using logarithmic coordinates at the right bottom corner in Figure 4.24. This relationship is consistent with past work on other systems [244-246].

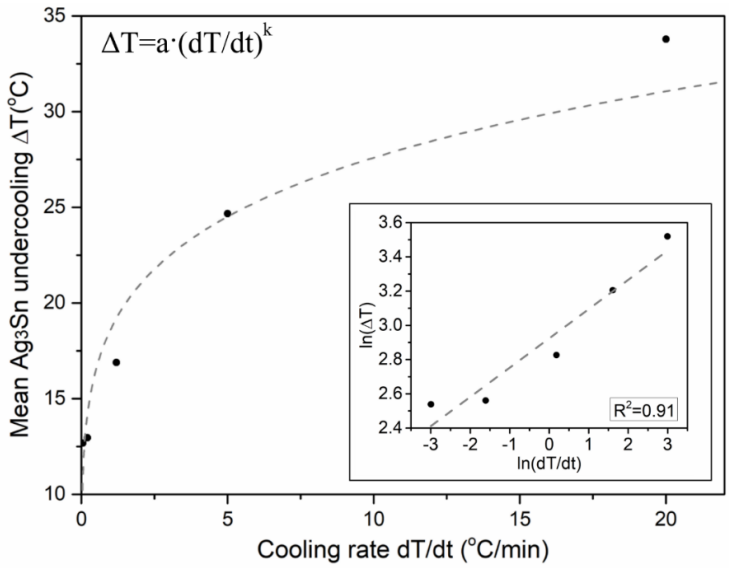

Figure 4.24 The relationship between mean undercooling for Ag_3Sn nucleation and cooling rate. (a=18.6, k=0.17 for the fitting curve)

4.3.3 Summary

It has been found that crystals of Al_3Ti (tetragonal), Ag_3Sn (orthorhombic), $Al_{45}Cr_7$ (monoclinic) and $Al_{13}Fe_4$ (monoclinic) tend to form cyclic twins with overall cubic, hexagonal, icosahedral and decagonal symmetry, respectively, at higher cooling rate. For Ag_3Sn, DSC experiments at different cooling rate show that such cyclic twinning tends to form when Ag_3Sn nucleates at lower temperature (i.e. deeper undercooling). It has also been confirmed that the mean nucleation temperature decreases with increasing cooling rate, i.e. the higher the cooling rate, the deeper the undercooling that is likely to be achieved in the melt. Therefore, it appears that the cyclic twinning forms due to the undercooling in the melt introduced by the faster cooling rate. It is interesting to note, however, that the cooling rates and undercoolings required to trigger cyclic twinning in this work are relatively modest and much less than would exist in rapid solidification approaches. The formation mechanisms for the cyclic twinning in the four IMCs are discussed in the next section.

4.4 Discussion

Following Buerger [247], twins are often classified by their origin into growth twins, transformation twins and mechanical twins. Growth twins refer to crystallisation from a gas or liquid and include twin formation both (i) at the crystal nucleation stage and (ii) during crystal growth. In their review on the twinning of crystals, Hahn and Klapper [248] give two geometric features that are signatures of twinning at the nucleation stage: (1) all twin domains appear to originate from one point near the centre of the twinned crystal; and/or (2) the twin domains have roughly the same size. These features are clearly evident for the four IMCs solidified at the higher cooling rates in this work. For example, examining the Al_3Ti in Figure 4.5, Ag_3Sn in Figure 4.7, $Al_{45}Cr_7$ in Figure 4.12-Figure 4.14, and $Al_{13}Fe_4$ in Figure 4.19, it appears that in every twinned crystal all domains point back to a common centre (which is unlikely to be in these cross sections), indicating a shared origin. Thus, it is likely that twinning initiated at the crystal nucleation stage or in the very early stages of growth.

In each IMC studied here, the multiple-twinned orientations have the combined symmetry of the 'parent' structure to which the IMCs are superstructures or approximants: FCC, HCP, iQC or dQC. Thus, it is likely that a metastable phase with this higher symmetry (crystalline or quascisytalline) formed first in the undercooled melt and then nucleated and/or transformed into the lower-symmetry stable structure with multiple orientation variants. This is similar to the hypothesis proposed by Senechal [249], that twin formation during nucleation is likely to be caused by a metastable modification with a structure existing for very small dimensions which is different from the macroscopic stable phase. After the nucleus reaches a critical size where the translation symmetry becomes decisive, it will collapse into a twinned crystal of the stable phase with lower symmetry.

Since these IMCs have a group-subgroup relationship with their parent phase, the number of orientation variants is given by the ratio of the point group order of the parent phase to the point group order of the child phase [248, 250], listed as h/l in Table 4.4. Looking back at Figure 4.5(f), Figure 4.7(f), Figure 4.12, Figure 4.19 and Table 4.3, it can be confirmed that the number of orientation variants observed is consistent with the ratio in Table 4.4, considering that, for $Al_{45}Cr_7$ the cyclic twin

grows radially in three dimensions, and the 2D sections only revealed a plane containing 12 of the 30 variants.

Table 4.4 Group-subgroup relations for the four parent structure

IMCs	Point group	Order of point group (l)	Parent structure	Point group	Order of point group (h)	Ratio h/l
Al_3Ti	4/mmm	16	FCC	$m\bar{3}m$	48	3
Ag_3Sn	mmm	8	HCP	6/mmm	24	3
$Al_{45}Cr_7$	2/m	4	iQC	$m\bar{3}\bar{5}$	120	30
$Al_{13}Fe_4$	2/m	4	dQC	10/mmm	40	10

The formation of a multiply twinned crystal at or shortly after the nucleation stage could occur in various ways:

(A) it is possible that the nucleus itself is twinned, similar to the suggestions in Ref. [251].

(B) Alternatively, a metastable phase of high symmetry could nucleate and then transform into the stable phase to produce a multiply twinned seed crystal, with multiple orientation domains resulting from multiple variants of the orientation relationship. This is similar to many solid-state transformations involving a group-subgroup relation that produce domain twins when low symmetry crystals form from high symmetry parent phases. Examples include monoclinic η'-Cu_6Sn_5 from η-hexagonal Cu_6Sn_5 [252]; monoclinic η'-Al_8Fe_3 from orthorhombic η-Al_5Fe_2 [253]; and tetragonal $L1_0$-FePd from cubic A1-(Fe,Pd**)** [254]. The difference in the present case is that the 'solid-state' transformation occurs when only a very small fraction of solid exists and most of crystallisation is yet to occur. Here, the formation of all orientation variants is likely to minimise lattice strain. For example, in Al_3Ti with lattice parameters given in Figure 4.5(g), the length of a in tetragonal Al_3Ti is shorter than that in both cubic structures, while the half length of c (4.29Å) is longer than a in both cubic structures. Due to this tetragonal distortion, the solid phase transformation of a cubic structure into a single tetragonal orientation would involve contraction along the a and b directions, and expansion along the c direction. In comparison, through triple twinning, the c direction of one tetragonal orientation is parallel to the a and b directions of the other two orientations, which cancels out most of the

contraction and expansion in the lattice. Ag_3Sn has a small orthorhombic distortion, with $\frac{2c}{b} = 1.72$ which is 0.7% less than the value ($\sqrt{3}$) of the HCP parent structure (Figure 4.7(g)) and the formation of cyclic twinned Ag_3Sn cancels out most of the strain in the lattice. Similar effects are likely for $Al_{45}Cr_7$ and $Al_{13}Fe_4$ transforming from an iQC or dQC.

(C) Alternatively, the metastable phase could act as a nucleant particle for the stable phase with multiple variants of a nucleation OR. This is similar to heterogeneous nucleation on certain inoculant particles. For example, there are two orientation variants when FCC-Al nucleates on the (0001) facet of hexagonal TiB_2 [229], and six orientation variants when Al_3Ti nucleates on the (0001) of TiB_2 [255]. There are equivalent examples with peritectic reactions L + S1 → S2, if S1 is a higher symmetry parent phase of S2 with a group-subgroup relation, as would be the case for L + ζ-Ag→ Ag_3Sn at high Ag content since ζ-Ag is HCP. For all four IMCs studied here, the nucleation barrier on the high symmetry parent phases is expected to be small due to the small lattice disregistry. For example, Al_3Ti and Ag_3Sn differ from their parent phases only by chemical ordering and a small distortion (Figure 4.5(g) and Figure 4.7(g))), and $Al_{45}Cr_7$ and $Al_{13}Fe_4$ are likely to be similarly closely related to an iQC and dQC.

Some combination of mechanisms (A), (B) and (C) may also be feasible noting that, at very small dimensions, the differences between these mechanisms may not be clear cut.

Cooling rate had a significant influence on solidification twinning in this study. At sufficiently high cooling rate, all crystals were 'fully cyclic twinned' with all orientation variants present in all four IMCs studied. At low cooling rate, Al_3Ti and Ag_3Sn were all single crystals, and $Al_{45}Cr_7$ and $Al_{13}Fe_4$ were either single crystals or 'partially twinned' where only a subset of the orientation variants were present (Table 4.3). The DSC experiments on Ag_3Sn in Figure 4.24 showed that the role of increasing cooling rate is mostly to deepen the nucleation undercooling and, given that this relationship has been reported widely for other systems, it is expected that the increasing cooling rate also deepened the nucleation undercooling of Al_3Ti, $Al_{45}Cr_7$ and $Al_{13}Fe_4$. Based on this, it is likely that the formation of single crystals at low cooling rate is due to the stable IMCs nucleating first in the melt (and not a

metastable phase). For the fully cyclic twinned crystals at the higher cooling rates, it is likely that a metastable phase formed first and nucleated/transformed into the stable phase with all orientation variants. It is then interesting to consider why, at low cooling rate, some $Al_{45}Cr_7$ and $Al_{13}Fe_4$ were partially twinned with only a subset of the orientation variants (Figure 4.9, Figure 4.11, Figure 4.17 and Figure 4.18). One possibility is that the extent of twinning depends on the size of the metastable high symmetry phase at the moment when the stable lower-symmetry phase forms; the higher the cooling rate and/or deeper the undercooling, the larger size the metastable phase reaches before the stable phase begins growing. For nucleation on the high-symmetry phase, a larger particle has more surface area on which nucleation events could occur increasing the chances of multiple OR variants nucleating. For the transformation of the high symmetry phase into domains of the lower-symmetry phase, the larger the particle the more domains it is likely to break up into. For a large enough crystal/quasicrystal of the high symmetry phase, all OR variants would form.

Twinning during nucleation or the early stage of growth also has an influence on the subsequent crystal growth. Ag_3Sn and Al_3Ti grow as plates as single crystals. When they are cyclic twinned, they can grow as an equiaxed shape which can more easily fill 3D space. Similarly, $Al_{45}Cr_7$ grows as rods as single crystals. When $Al_{45}Cr_7$ is cyclic twinned, it grows as a more equiaxed shape that is more easily able to fill 3D space. The geometric features formed by twinned crystals, such as re-entrant corners, facilitate atomic attachment and, therefore, it is favourable to retain the twinned orientations during crystal growth.

It has been observed previously that metastable phases with the parent structure of the four IMCs in Table 4.4 can form during rapid solidification, which involves considerably higher cooling rates than those studied here. In Al-2Ti and Al-5Ti alloys rapidly solidified by melt spinning, metastable cubic $L1_2$-Al_3Ti has been observed to coexist with the FCC solid solution containing up to 4 wt.% Ti [256]. The same $L1_2$ structure has also been observed in Al_3Zr and Al_3Hf through rapid solidification, and all the cubic phases transformed into the corresponding stable tetragonal phases after reheating [257, 258].

An iQC phase has been confirmed in a rapidly solidified Al-Cr alloy through X-ray [114, 259], electron [115, 116] and neutron [117] diffraction methods. After reheating the iQC metastable phase transformed into crystalline $Al_{45}Cr_7$ with the fivefold and threefold rotational twins of $Al_{45}Cr_7$ [125]. The tenfold twins of $Al_{13}Fe_4$ have also been observed previously in coexistence with the Al-Fe decagonal quasicrystals in rapidly solidified Al-Fe alloys [260]. Since this past work has shown that these metastable phases can occur in similar alloy compositions at higher cooling rate, it seems reasonable that they may also form at the nucleation stage at the moderate cooling rates in this work but do not grow to a significant size before the stable phase forms.

To explore this further, calculations were performed using Thermo-Calc with the TCSLD3.2 and TCTI2.0 databases for the Ag-Sn and Al-Ti systems respectively. Metastable liquidus lines were calculated by suppressing the stable IMCs (Ag_3Sn and Al_3Ti) from the calculations. Figure 4.25 compares the DSC information with the stable and metastable phase diagram of the Ag-Sn system. The plot of DSC results in Figure 4.25 is the same as in Figure 4.22(a). The plot is shown here to compare with the thermodynamic calculations. If cyclic twinned crystal growth occurs when the HCP phase nucleates first in the melt, the cyclic twinned nucleation temperature must be below the metastable HCP liquidus line. The calculated metastable HCP liquidus temperature is close to the highest measured temperature at which cyclic twinning was observed, which is reasonably consistent with this interpretation. Figure 4.26 shows stable and metastable phase diagrams in the Al-Ti system. Here, the metastable liquidus lines of the A1-FCC phase and the metastable $L1_2$-Al_3Ti superstructure are shown. The $L1_2$ phase liquidus line is significantly closer to the stable $D0_{22}$-Al_3Ti liquidus and is, therefore, more likely to have nucleated than disordered FCC. According to the calculations, an undercooling of ~60K is required for the $L1_2$ phase to become metastable in an Al-3Ti melt. This is a significantly deeper undercooling than the ~15K required for HCP to be metastable in a Sn-5Ag melt, which is consistent with a higher cooling rate being required to trigger cyclic twinning in Al_3Ti than in Ag_3Sn. However, it was not possible to measure nucleation temperatures in Al-3Ti in this work so it was not possible to fully confirm this interpretation.

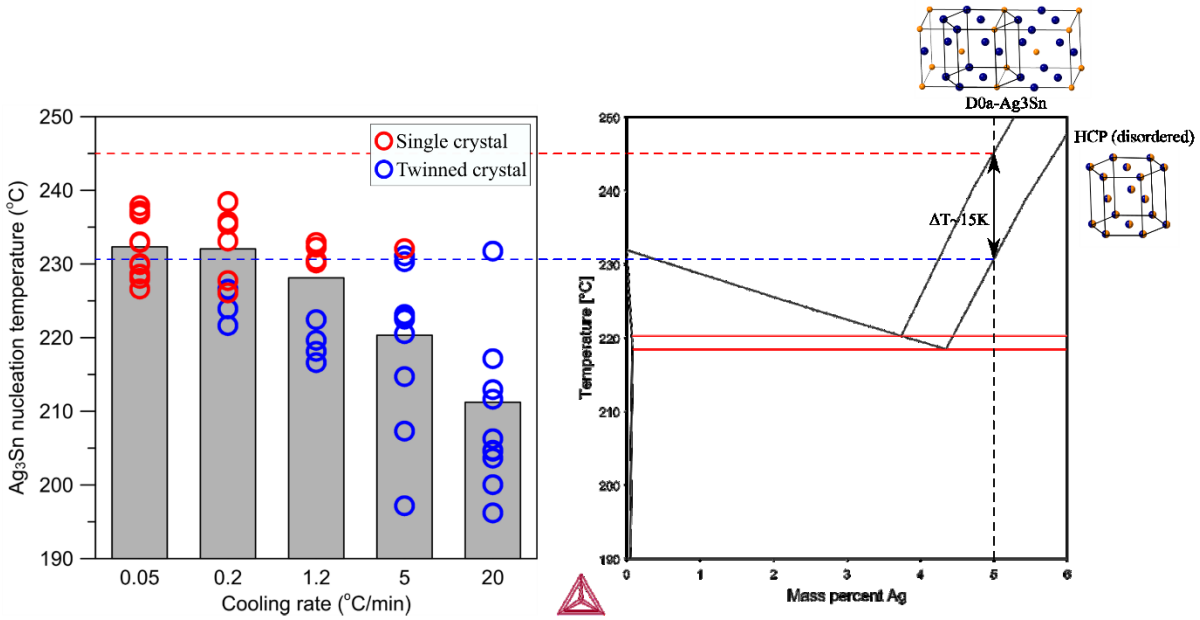

Figure 4.25 The comparison between the DSC measurement and the stable and metastable phase diagram of the Ag-Sn system from Thermo-Calc TCSLD3.2 database.

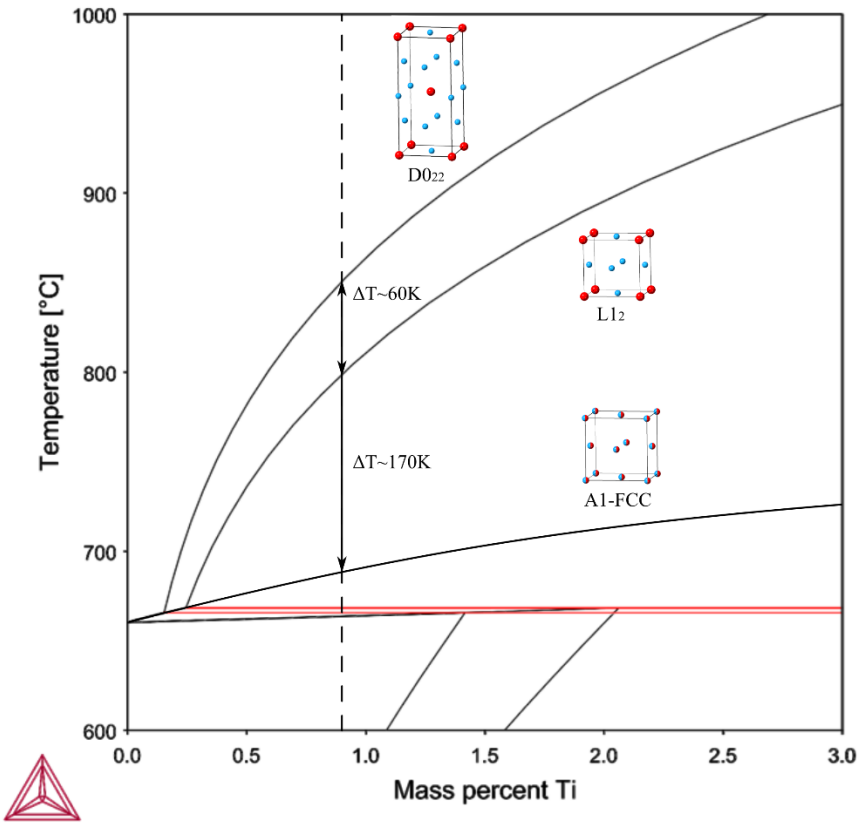

Figure 4.26 The stable and metastable phase diagrams in the Al-Ti system from Thermo-Calc TCTI2.0 database.

The iQC and dQC phases are not included in the thermodynamic databases used so similar metastable phase diagram calculations were not conducted. However, past papers have discussed the competitive nucleation of quasicrystals versus crystalline phases. It was first proposed by Frank that icosahedral short-range order is favoured in undercooled metallic melts [133]. As reviewed in Chapter 2, according to classical nucleation theory [261], the nucleation barrier for heterogeneous nucleation is:

$$\Delta G^* = \frac{16\pi}{3} \cdot \frac{{\gamma_{sl}}^3}{\Delta G^2} \cdot f(\theta) \qquad \textit{Equation 4.2}$$

Where ΔG is the Gibbs free energy difference between the solid and liquid phase, γ_{sl} is the solid-liquid interfacial energy, and $f(\theta)$ is the geometric factor for heterogeneous nucleation.

Various authors [262, 263] have shown that the nucleation barrier, ΔG^*, for an iQC is lower compared to a crystalline phase in an undercooled melt. Through undercooling experiments it was confirmed that an iQC has lower interfacial energy with the melt compared to the crystalline compounds containing polytetrahedral building blocks [262]. If the S-L interfacial energy of the metastable phase is lower than that of the more stable phase, the metastable phase can be stabilised at small size by the Gibbs-Thomson effect. Therefore, a metastable icosahedral structure, and possibly an iQC phase, is likely to form in the undercooled melt. Similar arguments have been made by Rappaz et al.[28]

According to the literature [262], the S-L interfacial energy for the Al-Fe decagonal quasicrystal (~0.112 J/m^2) is also lower than the stable $Al_{13}Fe_4$ (~0.159J/m^2), indicating that the nucleation barrier can also be lower for a decagonal quasicrystal than $Al_{13}Fe_4$ in an undercooled melt (Eq. 4.2).

For $Al_{13}Fe_4$ crystal from arc-melting, such as that in Figure 4.19, the decagonal symmetry formed by the cyclic twinning indicates that it was caused by a decagonal quasicrystal. As illustrated in Figure 4.19(i), it has been suggested that decagonal quasicrystals transform directly into monoclinic $Al_{13}Fe_4$ [240]. However, there are two features which suggest that the measured seven monoclinic $Al_{13}Fe_4$ orientations may not have grown directly from a decagonal quasicrystal: (i) in the orientation map in Figure 4.19(c), the same orientations (except 3) have been observed twice on both sides, which should

not happen if a decagonal quasicrystal directly nucleates/transforms into ten monoclinic orientations; and (ii) whilst most orientations form simple segments emanating from the crystal centre, the interfaces between 3&6 and 4&7 are quite different and might not have grown from the same centre. This issue with 3&6 and 4&7 disappears in the orthorhombic orientation map (Figure 4.19(f)), suggesting the {001} twinning may have formed through a different mechanism relating to its pseudo-orthorhombic symmetry.

There is a proposed high-temperature $Al_{13}Fe_4$ phase which has the same orthorhombic structure we studied above [237]. The geometrical feature of the sector twins is that the orientation domains share a common origin near the centre of the cross section. When the decagonal structure nucleates and/or transforms into the five orthorhombic orientations with 36° to each other at high temperature, the five orthorhombic unit cells duplicate on the opposite side around the shared centre to retain the decagonal symmetry and form sharp {101} interfaces emanating from the crystal centre (Figure 4.19(j)). Thus, the arrangement of the twin domains is consistent with an orthorhombic phase growing from a decagonal phase first and then transforming into the monoclinic phase. A similar phenomenon was observed in NiZr droplet with a single decagonal seed growing into five orthorhombic orientations in an undercooled melt through electrostatic levitation, forming tenfold twins with sharp {110} interfaces [230]. Further decreasing the temperature makes the $Al_{13}Fe_4$ orthorhombic phase transform into the stable monoclinic structure and each orthorhombic orientation breaks down into two monoclinic ones, forming {001} twinning inside the grain with different geometry. Theoretically there should be 10 monoclinic orientations, but in reality there is a chance that one orthorhombic orientation transforms into only one monoclinic orientation, and/or the other monoclinic orientations may not have been sectioned in this 2D map.

4.5 Conclusions

In this chapter, a detailed study of solidification twinning in four intermetallic compounds, Ag_3Sn, Al_3Ti, $Al_{45}Cr_7$ and $Al_{13}Fe_4$, has been conducted, combining SEM imaging, EBSD and DSC. The following main conclusions can be drawn:

1. In slow cooling (1.2K/min for Al_3Ti, $Al_{45}Cr_7$ and $Al_{13}Fe_4$, and 0.05K/min for Ag_3Sn), crystals grew into large plates (Ag_3Sn and Al_3Ti) or long rods ($Al_{45}Cr_7$ and $Al_{13}Fe_4$) with high aspect ratio. All Al_3Ti and Ag_3Sn were single crystals with their main facets being {001}. Around 60% $Al_{45}Cr_7$ and $Al_{13}Fe_4$ crystals were twinned, with two twin types for $Al_{45}Cr_7$ and only one twin type for $Al_{13}Fe_4$. For $Al_{45}Cr_7$ the long direction was $<1\bar{1}0>$, and for $Al_{13}Fe_4$ it was <010> or <001>.
2. Compared to slow cooling, Al_3Ti, $Al_{45}Cr_7$ and $Al_{13}Fe_4$ from higher cooling rate grew into much smaller size with lower aspect ratio. All crystals were twinned with more complicated morphologies. There were more twinned orientations observed in each crystal and two additional twin types were measured in $Al_{13}Fe_4$.
3. Twin boundaries were found to be commonly coincident with edges and re-entrant corners which gives growth advantage to attain the final twin form.
4. The multiple-twinned orientations in the four IMCs form the combined pseudo-symmetries of their parent structure, and the total number of the twinned variants equals the ratio of the point group order between its parent structure and the IMC.
5. The combined parent symmetry formed by the twinned orientations, and the geometrical features of their corresponding domains indicate that a metastable phase with high symmetry is likely to form first in the undercooled melt at higher cooling rate and then nucleate/transform into the stable low-symmetry crystal. In $Al_{13}Fe_4$, there were indications that this may occur in a three stage process: (i) a decagonal structure forms first in the melt, (ii) an orthorhombic phase nucleates/transforms on/from this seed and then (iii) transforms into the stable monoclinic phase.

6. The solidification orientation relationships between the stable crystals and their corresponding metastable parent phases are:

   Al_3Ti: $\{001\}_{Al3Ti}$ || $\{001\}_{FCC/L12}$, with $<100>_{Al3Ti}$ || $<100>_{FCC/L12}$;

   Ag_3Sn: $\{001\}_{Ag3Sn}$ || $\{1\bar{1}00\}_{hcp}$, with $<100>_{Ag3Sn}$ || $<0001>_{hcp}$;

   $Al_{45}Cr_7$: $<101>_{Al45Cr7}$ || *i(5)* and $<110>_{Al45Cr7}$ || *i(2)*;

   $Al_{13}Fe_4$: $<010>_{mono}$ || $<010>_{orth}$ || *d(10)*, and $<001>_{mono}$ || $<101>_{orth}$ || *d(2)*.

Chapter 5 Solidification ORs between equiaxed neighbouring grains in Al and Mg alloys

5.1 Introduction

So far we have seen different OR formation mechanisms during solidification. Between Al_3Ti and TiB_2, ORs can be formed through nucleation and pushing & engulfment processes. Twinning ORs between different domains inside an intermetallic crystal (Al_3Ti, Ag_3Sn, $Al_{45}Cr_7$ and $Al_{13}Fe_4$) can form due to the nucleation and/or solid transformation from a metastable parent structure. In this Chapter, the formation of preferred interfaces in equiaxed solidification is explored, building from past work that has shown a significant above-random population of 60° grain boundaries in FCC phases after equiaxed solidification. Kurtuldu et al. measured large amounts of 60° twinning grain boundaries and showed that clusters of these grains form overall icosahedral symmetry after equiaxed solidification in Al-Zn and Au-Ag-Cu alloys with addition of 1000 ppm Cr and 200 ppm Ir, respectively [23, 24]. According to Kurtuldu et al., this is most likely due to the nucleation of the FCC phase from icosahedral quasicrystals formed in the undercooled melt. In this Chapter, we investigate the formation mechanism for preferred grain boundaries after equiaxed solidification of different Al and Mg alloys. The alloy systems were selected based on the following criteria:

1. Equiaxed grains are formed during solidification.

2. Alloys with and without grain refiner additions.

3. Alloys with potential icosahedral nucleation activity based on past work [23].

4. Alloys with different grain size (coarse and refined) and shape (dendritic and globular).

5. Alloys that solidify with different crystal structure (FCC and HCP) to test the generality of the findings.

Based on the criteria above, three cast Al alloys (Al-20wt.%Zn, Al-15wt.%Cu and Al-6wt.%Cu inoculated with 1wt.% Al-5Ti-B master alloy) and two cast Mg alloys (Mg-9wt.%Al-0.7wt.%Zn inoculated with $FeCl_3$ powder and Mg-9wt.%Al-0.7wt.%Zn inoculated with Al_4C_3 particles) were

studied. Note that these alloys all form fully-equiaxed microstructures during solidification under gravity casting conditions due to their high solute content and, in the case of the inoculated alloys, due to the presence of heterogeneous nucleant particles. This Chapter has three main aims: (i) to compare the solidification texture with ideal random texture for both FCC and HCP structures, (ii) to identify the preferred grain boundaries and ORs between the neighbouring grains, and (iii) to explain the origin of the observed solidification ORs.

5.2 Methods

5.2.1 Sample preparation

Five cast alloys were prepeared in this study: Al-20wt.% Zn, Al-15wt.% Cu, Al-6wt.%Cu with 1wt.% Al-5Ti-B master alloy, Mg-9wt.%Al-0.7wt.%Zn with $FeCl_3$ and Mg-9wt.%Al-0.7wt.%Zn with Al_4C_3.

CP Al ingot, 99.9% Zn ingot, Al-50wt.% Cu master alloy and Al-5Ti-1B rods supplied by the London and Scandinavian Metallurgical Company were used for the casting of Al alloys. The composition for CP Al is listed in Table 4.2. The alloys were heated to 750°C in a BN-coated clay-bonded graphite crucible in a resistance furnace. After holding for 4 hours, the melt was stirred with an Al_2O_3 rod and then poured into the steel mould with BN coating pre-heated to 300°C. Three Al alloys were cast in steel moulds with three different shapes as shown in Figure 5.1: (a) inner height 100 mm and inner diameter 20 mm for Al-20wt.% Zn, (b) inner height 110 mm and inner diameter 85 mm for Al-15wt.% Cu and (c) inner height 60 mm and inner diameter 50 mm for Al-6Cu with 1wt.% Al-5Ti-1B master alloy.

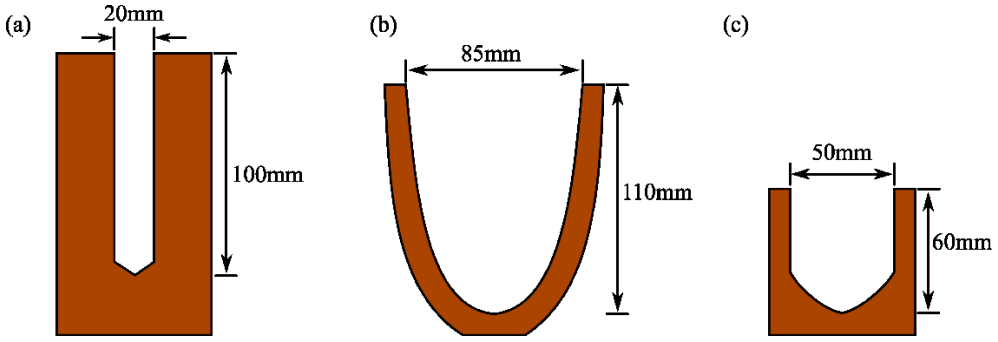

Figure 5.1 Three types of steel mould used in this study to cast Al alloys. (a) inner height 100 mm and inner diameter 20 mm for Al-20wt.% Zn, (b) inner height 110 mm and inner diameter 85 mm for Al-15wt.% Cu and (c) inner height 60 mm and inner diameter 50 mm for Al-6Cu with 1wt.% Al-5Ti-1B master alloy.

For the casting of Mg-9wt.%Al-0.7wt.%Zn, AZ91 with composition listed in Table 5.1 was used and two grain refiners were added in this study: $FeCl_3$ powder and Al_4C_3 powder. For the $FeCl_3$ addition, the melt was held at 725 °C for 1 hour. Next, 1.0 wt.% of anhydrous $FeCl_3$ powder wrapped in Al foil was plunged into the melt and stirred for 30 s with a BN-coated steel rod. After being held for 20 minutes, samples of the melt were poured at 700 °C into a 200°C Cu mould coated with a thin film of BN. For

the Al_4C_3 addition, powder with 24μm mean grain size and 99+% purity was used. The AZ91 melt was first held at 650 °C for 1 hour. Next, 3.5 wt.% of Al_4C_3 powder wrapped in Al foil was added to the melt and stirred for 1h with a BN-coated stainless steel stirrer incorporated into the furnace. Samples of the melt were then poured at 650 °C into a 200°C stainless steel mould coated with BN.

Table 5.1 The composition of AZ91 used in this work

Element	Mg	Al	Zn	Mn	Fe	Cu	Ni	Si
Composition (wt. %)	Bal.	8.97	0.74	0.15	0.002	0.002	0.003	0.01

Cast alloys were cut into small samples and metallographic polishing was carried out with colloidal silica by standard preparation methods. For EBSD characterisation, Ar-ion milling on a Gatan PECSII instrument was applied with 2kV accelerated beam at an incidence angle of 4° for 40min. For EBSD investigation, a Zeiss Sigma field emission gun SEM fitted with a Bruker e-FlashHR EBSD detector was used. Bruker Esprit 2.0 software was applied to analyse the misorientation across grain boundaries and the orientation relationship between grains. MTEX 5.2.7 toolbox within MATLAB™9.2 (Mathworks, USA) [206] was used to process EBSD data. The threshold for the misorientation inside a grain was set to be 5°.

Due to the eutectic mixture between the α-Al dendrite arms in Al-15Cu cast alloy, EBSD maps were reconstructed by MTEX to form Al-Al grain boundaries as shown in Figure 5.2 so as to examine the orientation relationships between neighbouring α-Al grains.

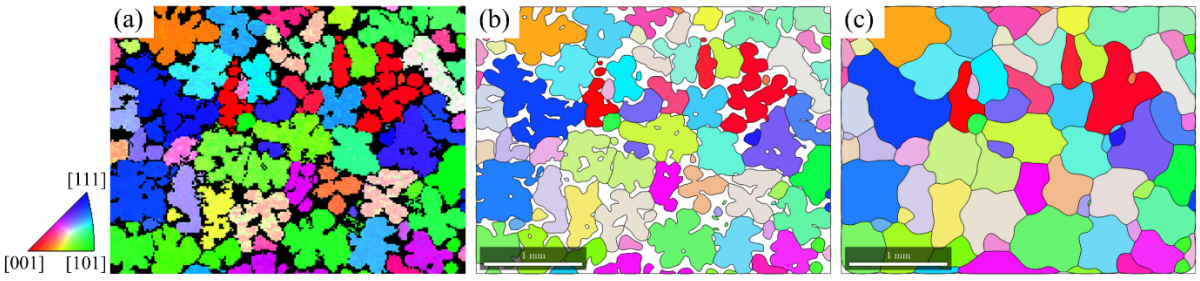

Figure 5.2 Reconstruction of α-Al dendritic EBSD mapping by MTEX. (a) EBSD IPF-Z map of α-Al dendrites in Al-15Cu alloy. (b) IPF-Z map of α-Al dendrites in (a) plotted by MTEX. (c) Reconstruction of the EBSD mapping in (b) forming grain boundaries between neighbouring α-Al grains by MTEX.

5.2.2 DFT calculations of interfacial energies

In order to compare the interfacial energy at different grain boundaries measured in this work, DFT calculations were performed for Al symmetric interfaces using the Vienna Ab Initio Simulation Package (VASP) framework [207]. A planewave basis set and projector augmented wave (PAW) pseudopotentials [208] were used. The generalised gradient approximation (GGA) in the formalism of Perdew-Burke-Ernzerhof (PBE) was chosen for the exchange and correlation energy functional [209]. All parameters were converged to satisfy a criterion of 10^{-4} eV for Al in its pure form, where $3s^2 3p^1$ electrons were treated explicitly (they are not included in the core when forming the pseudopotentials). It was determined that an energy cutoff of 350 eV, *k* point density of ~0.025 $Å^{-1}$ and Methfessel Paxton smearing width of 0.1 eV [210] were sufficient and were kept consistent for the calculations.

Four interfaces were constructed as shown in Figure 5.3 superimposed with the Al unit cell wireframes. The {111} twin boundary is formed by 70.5° tilt along <110>, and further tilt in the same direction forms {112} (109.5°), {113} (129.5°) and {114} (141.1°) twin boundaries. Reversely, the {114} twin boundary can also be formed by tilting in the opposite direction by 38.9°, and further tilt in this direction forms {113} (50.5°), {112} (70.5°) and {111} (109.5°) twin boundaries. Particularly, for {111} and {112} twins, they have the same tilt angle but in opposite directions. However, no matter which direction the unit cell is tilted to, the orientation relationship, as well as the misorientation angle, between the two unit cells is the same for the two interfaces. A more direct illustration of this is shown in Figure 5.4.

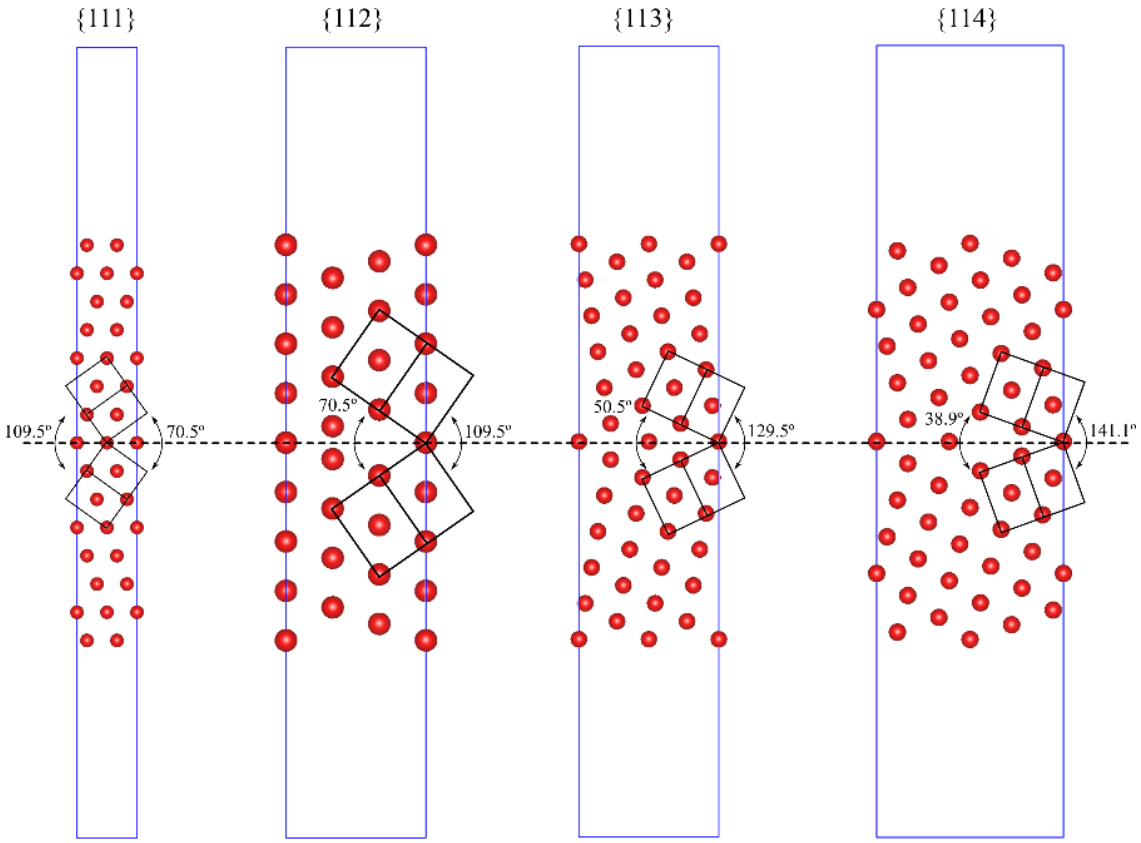

Figure 5.3 Four symmetric interfaces for DFT calculation: <110> {111}, <110> {112}, <110> {113} and <110> {114}.

In Figure 5.4(a) the formation of a series of symmetric interfaces through tilting along <110> is plotted. With increasing tilt angle, the common planes between the two cubic unit cells change. For 38.9° tilt angle, the common planes between two unit cells are {221} and {114}, and for 141.1° tilting, the orientation relationship stays the same, as well as the common planes. Similarly, for 50.5° (129.5°) tilting, the common planes are {332} and {113} and for 70.5° (109.5°) tilting the common planes are {111} and {112}, indicating the orientation relationship between two cubic unit cells is symmetric along the tilt angle from 0° to 180°, and the actual variation range is from 0° to 90°. Moreover, for any tilt angle between 0° and 90°, there are two sets of common planes that can give a coincident site lattice at the interface. For example, at 70.5° tilt angle, {111} and {112} can both form symmetric interfaces with the same OR between two unit cells. From an energy perspective, the symmetric interfaces

usually have lower interfacial energy than the asymmetric ones, and between the two possible symmetric interfaces, the one with lower interfacial energy is favoured.

The interfacial energy of the symmetric boundaries along the <110> tilt angle has been measured in previous literature [264], and the results are shown in Figure 5.4(b), together with the DFT calculation result from this work. The energy landscape is plotted with the interfaces chosen in two ways referred to Figure 5.4(a). As the first row of the unit cell wireframes tilts in Figure 5.4(a), the interfaces change from {221}, {332}, {111}, {112}, {113} to {114}, and the top figure in Figure 5.4(b) plots the interfacial energy along this sequence. The blue marks refer to the DFT calculations from this work. As for the second row in Figure 5.4(a), the sequence is reversed from {114} to {221} with increasing tilt angle, and the corresponding energy trend is reversed too in the bottom figure in Figure 5.4(b). In Figure 5.4(c) the two energy curves in Figure 5.4(b) are superimposed and, for two possible symmetric interfaces at the same tile angle, the lower energy one is chosen to describe the energy landscape. Figure 5.4(d) plots the energy landscape for the symmetric interfaces along the tilt angle varying from 0° to 90° from Figure 5.4(c). The two local energy minima correspond to the 50.5° {113} twinning and 60° {111}. Note that for an FCC unit cell, 60° rotation about a {111} plane is the same as 70.5° tilting along <110>, as will be shown later.

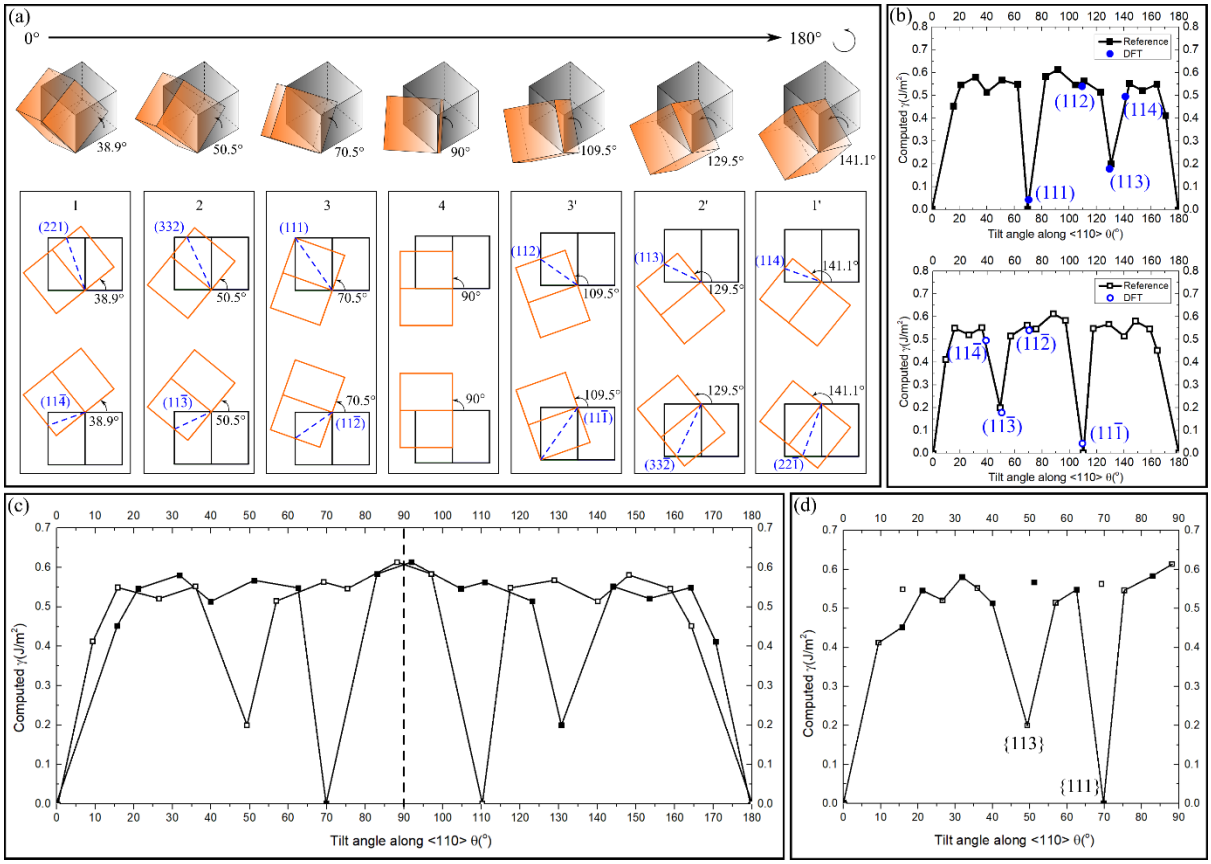

Figure 5.4 (a) Tilting an Al unit cell along a <110> direction from 0° to 180°, forming two symmetric interfaces at certain tilt angles: {221} and {114} at 38.9° (141.1°), {332} and {113} at 50.5° (129.5°), {111} and {112} at 70.5° (109.5°). (b) Interfacial energy of the symmetric boundaries tilting along <110> from 0° to 180° in two ways of choosing the interface. The black curves are from Ref. [264] and the blue marks are from the DFT calculation in this study. (c) Superimposition of the two energy curves in (b), showing the interfacial energy for two possible symmetric interfaces from 0° to 180°. (d) The lower interfacial energy comparing two possible interfaces from 0° to 90° in (c).

The interfacial energies of symmetric tilt boundaries in Mg have been calculated by DFT in previous work and those calculated values were used here (i.e. no DFT calculations were performed on Mg in this work). Figure 5.5(a) and (d) plot the tilt of the Mg unit cell along the <1$\bar{1}$00> and <11$\bar{2}$0> directions forming different common planes. For example, clockwise tilting along <1$\bar{1}$00> by 56.9°, 94.5°, 116.8° and 145.8° gives parallel {11$\bar{2}$6}, {11$\bar{2}$3}, {11$\bar{2}$2} and {11$\bar{2}$1} planes, respectively. And the interfacial energy calculated by DFT [265] for the symmetric interfaces in Mg is plotted in Figure 5.5(b). Reversely, these four parallel planes can also be formed by anti-clockwise tilting 123.1°, 85.5°, 63.2° and 34.2°, and the interfacial energy is also plotted reversely for such tilting in Figure 5.5(c). The same illustration

for tilting along the <11$\bar{2}$0> direction and the calculated interfacial energy from previous literature [266, 267] are shown in Figure 5.5(d)-(f).

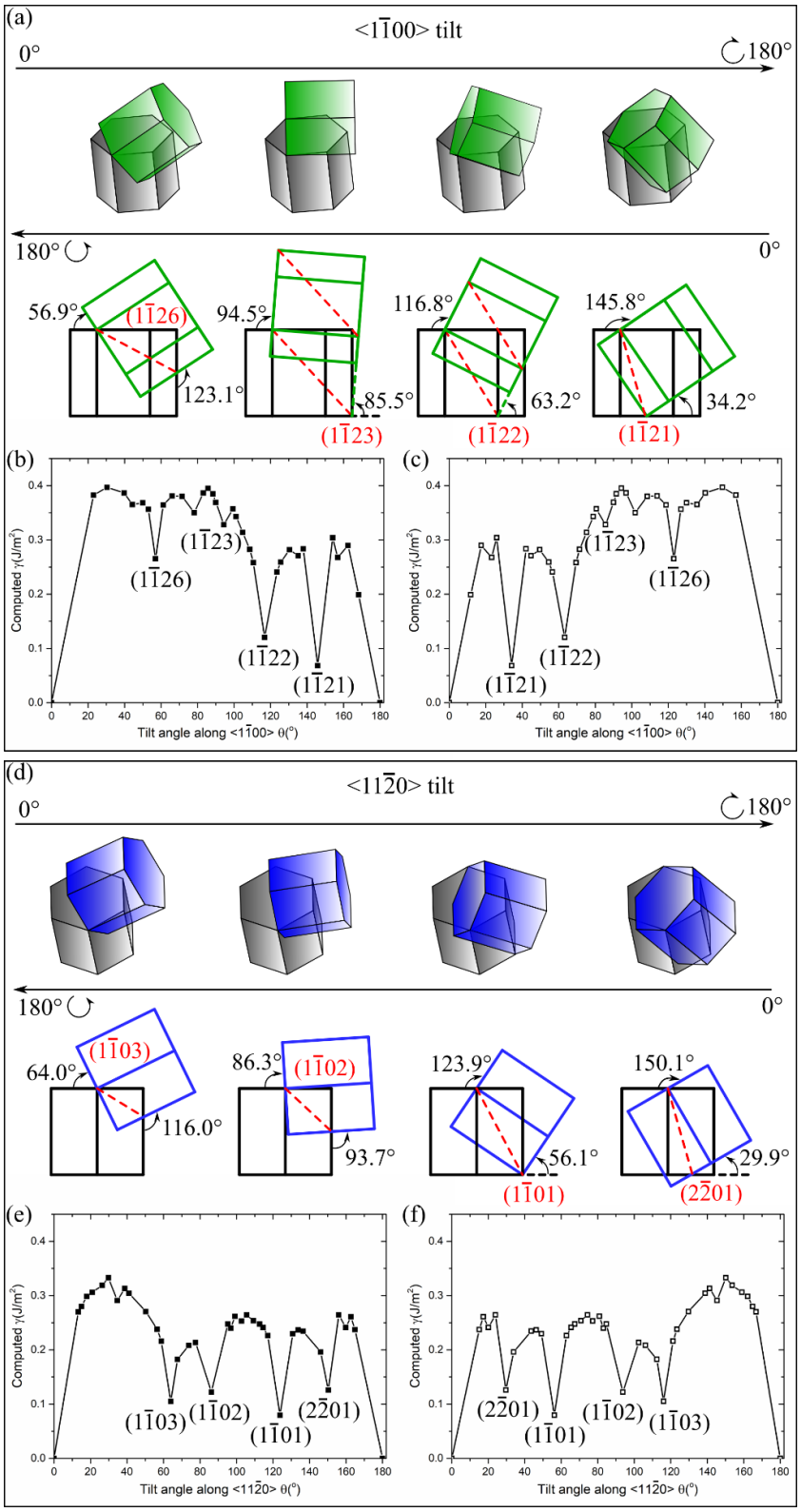

Figure 5.5 (a) Tilting of Mg unit cell along <1$\bar{1}$00> direction from 0° to 180° in clockwise and anti-clockwise directions, forming symmetric interfaces at certain tilt angles: {11$\bar{2}$6} at 56.9° (123.1°), {11$\bar{2}$3} at 94.5° (85.5°), {11$\bar{2}$2} at 116.8° (63.2°) and {11$\bar{2}$1} at 145.8° (34.2°). (b) Interfacial energy of the symmetric boundaries tilting along <1$\bar{1}$00> direction from 0° to 180° in clockwise direction. (c) Interfacial energy of the symmetric boundaries tilting along <1$\bar{1}$00> direction from 0° to 180° in anti-clockwise direction. (d) Tilting of Mg unit cell along <11$\bar{2}$0> direction from 0° to 180° in clockwise and anti-clockwise directions, forming symmetric interfaces at certain tilt angles: {1$\bar{1}$03} at 64.0° (116.0°), {1$\bar{1}$02} at 86.3° (93.7°), {1$\bar{1}$01} at 123.9° (56.1°) and {2$\bar{2}$01} at 150.1° (29.9°). (e) Interfacial energy of the symmetric boundaries tilting along <11$\bar{2}$0> direction from 0° to 180° in clockwise direction. (f) Interfacial energy of the symmetric boundaries tilting along <11$\bar{2}$0> direction from 0° to 180° in anti-clockwise direction.

Comparing Figure 5.5(b) and (c) (or Figure 5.5(e) and (f)), there are two possible symmetric interfaces for any tilting angle from 0°-90°. The lower part of the two energy curves is picked to describe the energy preference for different tilting angle, as shown in Figure 5.6(a) and (b). For tilting along the <1 $\bar{1}$ 00> direction, there are three local energy minima at 0°, 34.2° and 63.2°, the latter two corresponding to the <1$\bar{1}$00> {11$\bar{2}$1} and <1$\bar{1}$00> {11$\bar{2}$2} twins. For tilting along the <11$\bar{2}$0> direction, there are five local energy minima at 0°, 29.9°, 56.1°, 64.0° and 86.3°, and the latter four correspond to the <11$\bar{2}$0> {2$\bar{2}$01}, <11$\bar{2}$0> {1$\bar{1}$01}, <11$\bar{2}$0> {1$\bar{1}$03} and <11$\bar{2}$0> {1$\bar{1}$02} twins, respectively.

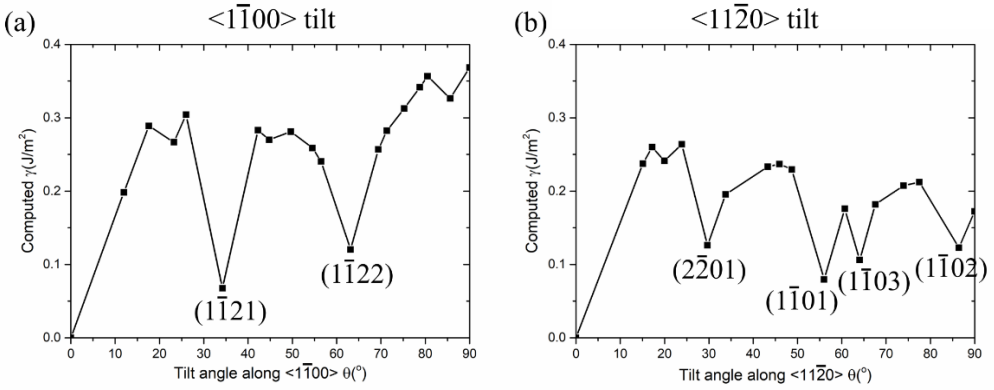

Figure 5.6 The energy landscape of Mg symmetric interfaces tilting along (a) <1$\bar{1}$00> direction and (b) <11$\bar{2}$0> direction.

5.3 Results and discussion

5.3.1 FCC Al alloys

5.3.1.1 Preferred grain boundaries in cast Al alloys

Figure 5.7(a) shows a typical EBSD IPF-Z map of the cast Al-20Zn alloy. Only one phase (FCC α-Al) is measured and the grains are equiaxed with grain size between 300-400μm. Figure 5.7(b) shows the misorientation frequency collected from 9 EBSD maps containing 4425 pairs of neighbouring α-Al grains. The Mackenzie curve is also plotted in Figure 5.7(b) showing the ideal misorientation frequency for uniform untextured FCC crystals. Compared to the Mackenzie curve, there are some preferences at certain grain boundary angles in the cast alloy. Figure 5.7(c) plots the frequency bars above the Mackenzie curve; it is clear that the preferred grain boundaries are at low angle (10°-20°) and at 50°-60°.

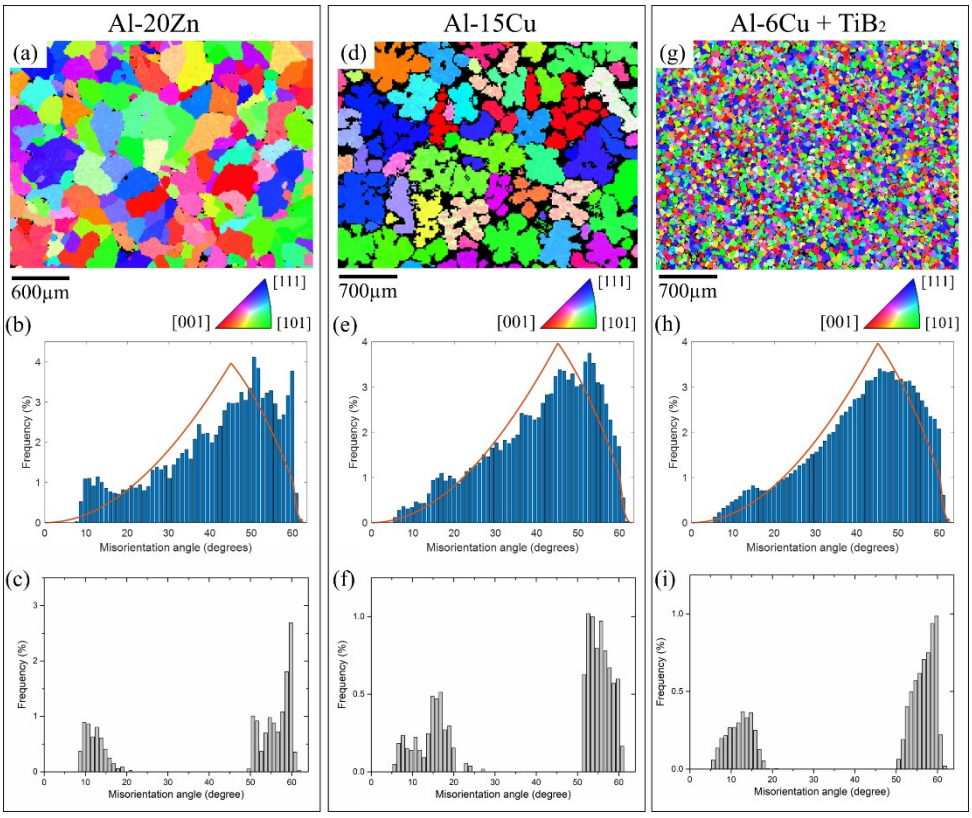

Figure 5.7 The solidification texture of cast Al-20wt.% Zn ((a)-(c)), Al-15wt.% Cu ((d)-(f)) and Al-6wt.% Cu with 1 wt.% Al-5Ti-1B ((g)-(i)). (a)(d)(g) EBSD IPF-Z map of α-Al grains in (a) Al-20wt.% Zn, (d) Al-15wt.% Cu and (g) Al-6wt.% Cu with 1 wt.% Al-5Ti-1B. (b)(e)(h) Misorientation frequency at α-Al grain boundaries superimposed with the Mackenzie curve for (b) Al-20wt.% Zn, (e) reconstructed Al-15wt.% Cu EBSD maps and (h) Al-6wt.% Cu with 1 wt.% Al-5Ti-1B. (c)(f)(i) The fraction bars above the Mackenzie curve in (b), (e) and (h).

Similar results were measured in cast Al-15Cu and Al-6Cu refined with 1 wt.% Al-5Ti-B master alloy, as shown in Figure 5.7(d)-(f) and (g)-(i). The data were collected from 3413 pairs of neighbouring α-Al grains in Al-15Cu and 43972 pairs of neighbouring α-Al in Al-6Cu with 1 wt% Al-5Ti-1B master alloy. Figure 5.7(d) and (g) are the EBSD IPF-Z maps for α-Al grains in the two alloys. It is clear that significant grain refinement is achieved with the addition of the master alloy: for Al-15Cu the coarse α-Al dendritic grains are about 500-700 μm and between the dendrite arms are filled with α-Al+θ-Al_2Cu eutectic, while for Al-6Cu cast alloy refined with TiB_2, the α-Al grains are around 70μm. For both Al-Cu cast alloys there is a preference for low angle (10°-20°) and 50°-60° boundaries compared to the Mackenzie curve, as shown in Figure 5.7(e)-(f) and (h)-(i), similar to the measurements for cast Al-20Zn.

Closer examination at the high angle boundaries in the three cast Al alloys revealed that many of them are consistent with twin boundaries. Two types of twinning are observed: 60° {111} twins and 50.5° {113} twins. Figure 5.8 shows examples of the two types of twinning in Al-20Zn alloy. For the 60° {111} twin, it is a 60° rotation on the common {111} plane forming three parallel <110> directions in the common {111} plane. For the 50.5° {113} type of twin, it is 50.5° rotation about the common <110> axis forming a common {113} plane. The common planes and directions are highlighted in the measured pole figures and in the unit cell wireframes plotted from the Euler angles for the two types of twinning. The traces of the interface between the two grains in Figure 5.8(a) and (b) are nearly perpendicular to the common plane normal in the pole figures (highlighted in dotted lines), indicating that for the two types of twinning the interfaces are likely to be the common {111} and {113} planes, respectively.

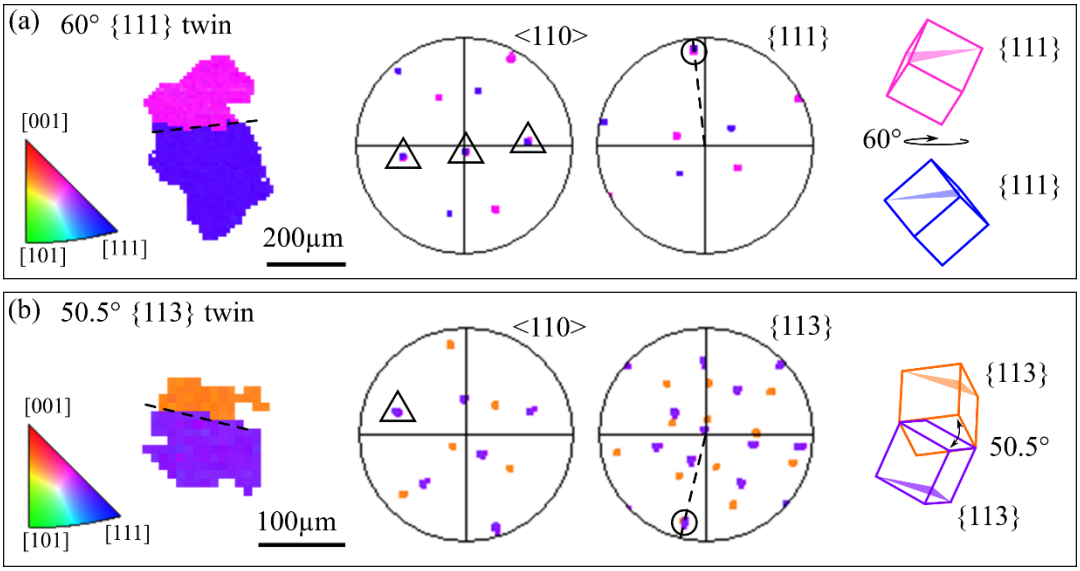

Figure 5.8 Preferred boundaries with twinning orientation relationship. (a) IPF-X map of two α-Al grains with 60° {111} twinning. The common {111} plane and three common <110> directions on the plane are marked in pole figures. The unit cell wireframes of the two orientations are plotted with the common {111} plane highlighted. (b) IPF-X map of two α-Al grains with 50.5° {113} twin. The common {113} plane and common <110> direction on the plane are marked in pole figures. The unit cell wireframes of the two orientations are plotted.

5.3.1.2 Al grain clusters with icosahedral symmetry

In the three cast Al alloys, it was found that 60° {111} twinning sometimes happened multiple times in adjacent grains. This was explored using the approach of Kurtuldu et al. [23, 24]. Figure 5.9 shows a typical example of multiple 60° {111} twinning between five α-Al grains from Al-20Zn. In Figure 5.9(a) five grains are labelled and coloured with respect to their Euler angles. There is a nearly common {111} plane with three nearly common <110> directions on the plane between 1&2, 2&3, 3&4, 4&5 and 5&1. All five orientations share a nearly common <110> direction which is highlighted in the red triangle in Figure 5.9(b)-(f). Figure 5.9(g) plots the unit cell wireframes for the five orientations. In each of the cubic unit cells, there is a tetrahedron formed with {111} being the faces and <110> being the edges. Translating all five tetrahedra along the common <110> direction with the five common {111} planes between every two of them being the interfaces, a pentagonal bipyramid is formed with small gaps because the angle between two {111} planes in a cubic unit cell is 70.5° instead of 72°. Figure 5.9(h) shows all five common {111} planes form a fivefold symmetry in space, with the common <110> direction for all five orientations lying on the plane. The same fivefold symmetry was revealed between the equiaxed α-Al grains in Al-20Zn-0.1Cr alloy by Kurtuldu [23]. Furthermore, from the pentagonal bipyramid in Figure 5.9(g) it is clear to see that, between two Al unit cells, the 60° {111} twin can also be seen as a 70.5° rotation about the common <110> direction.

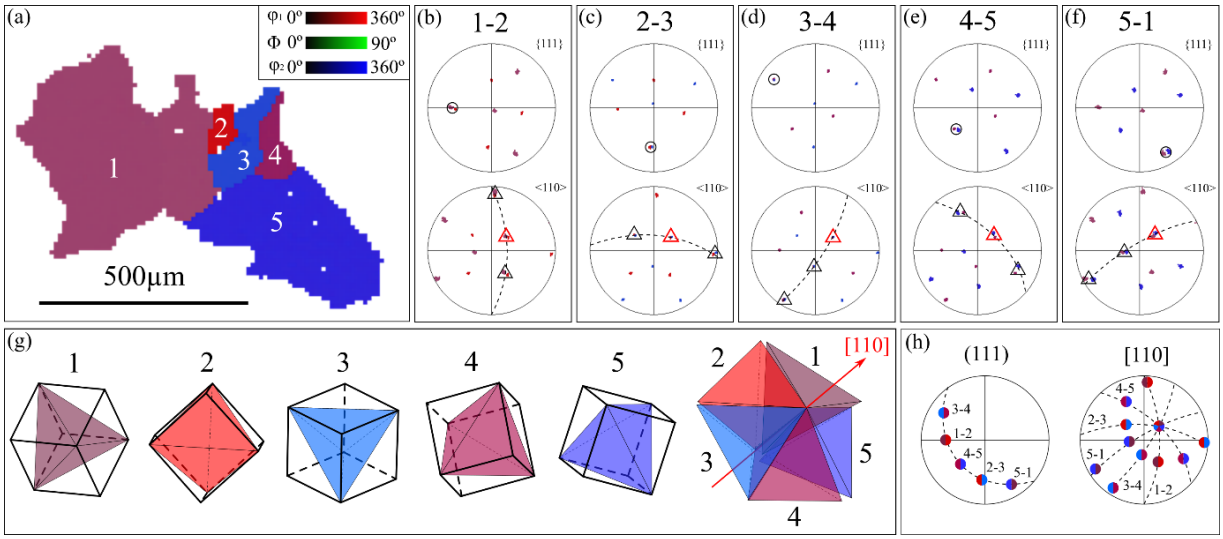

Figure 5.9 Continuous 60° {111} twin forming fivefold symmetry. (a) Five α-Al grains from Al-20wt.% Zn coloured according to their Euler angle. (b)-(f) Pole figures of every two of the five grains with 60° {111} twin. The common {111} plane and three common <110> directions on the plane are marked. All five grains share a common <110> direction highlighted in the red triangle. (g) Five tetrahedra from the cubic unit cells of the five grains forming a pentagonal bipyramid with small gaps. The fivefold axis is the common [110] direction in the red triangles in (b)-(f). The interface between every two tetrahedra is the common {111} plane. (h) Pole figures of the common (111) planes and [110] directions forming combined fivefold symmetry.

The fivefold symmetry formed by the continuous 60° {111} twinning was also observed in the two Al-Cu alloys. Figure 5.10 shows six α-Al grains from Al-6Cu refined with Al-5Ti-1B master alloy. There are five main orientations (the misorientation between 3 and 3' is 11.9°) that have the 60° twinning orientation relationship between every two of them. All five cubic unit cells share a nearly common <110> direction (highlighted in the triangles in (b)) and fivefold symmetry about this direction is formed with five nearly common {111} planes between every two of the five orientations. Translating to align along the common <110> direction, all five tetrahedra extracted from the cubic unit cells form a pentagonal bipyramid with small gaps. Note that the colours in Figure 5.10(a) are manually chosen to separate different orientations without any meaningful indication of how the unit cells are oriented in space. The real orientations are indicated by the pole figures in Figure 5.10(b).

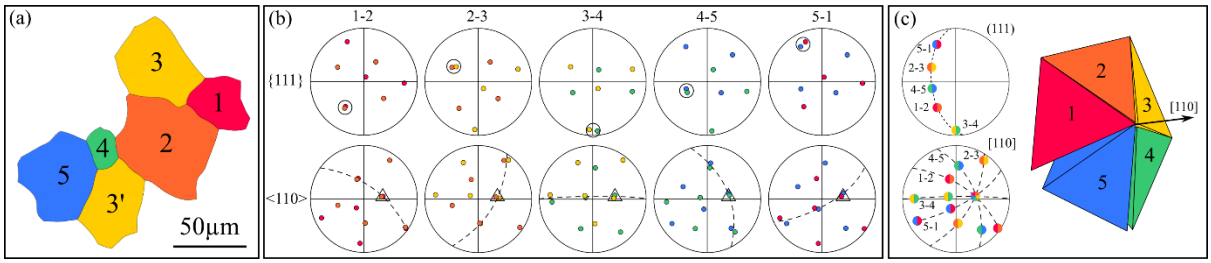

Figure 5.10 Continuous 60° <110> {111} twinning of the refined α-Al grains forming fivefold symmetry. (a) Five α-Al grains from Al-6wt.% Cu with 1 wt.% Al-5Ti-1B refiner. (b) Pole figures of five 60° <110> {111} twinning. Five common {111} planes are marked. All five grains share a common <110> direction highlighted by a triangle. (c) Five tetrahedra from the cubic unit cells of five grains forming a pentagonal bipyramid with certain gaps, with pole figures of the common (111) planes and [110] directions. Note that the colours in (a) are manually chosen to separate different orientations without any meaningful indication of how the unit cells are oriented in space. The real orientations are indicated by the pole figures in (b).

Figure 5.11 shows a more complicated situation with multiple fivefold axes formed by eight adjacent α-Al grains in Al-15Cu cast alloy. Similar to Figure 5.10(a), the colours in Figure 5.11(a) are chosen to separate different orientations without any meaningful information about the real orientations. The Euler angles for the real orientations are marked in the Kikuchi patterns for all eight grains in Figure 5.11(b). Figure 5.11(c) and (d) shows two fivefold axes formed by grain 1-5 and 4-8 respectively. For each five-grain group, they share a nearly common [110] direction with five nearly common {111} planes forming a fivefold symmetry about this direction. Similar to what was shown above, two pentagonal bipyramids can be constructed based on the five orientations in each group. Furthermore, the two pentagonal bipyramids are part of a full icosahedron and all eight tetrahedra can form a similar icosahedron with certain gaps between each other compared to a standard one with the same orientation, as shown in Figure 5.11(e). The OR between the FCC phase and the icosahedron is similar to Ref. [24]: one of the {111} || i(3) (the faces of the icosahedron) and three <110> || three i(5) (the corners of the icosahedron),

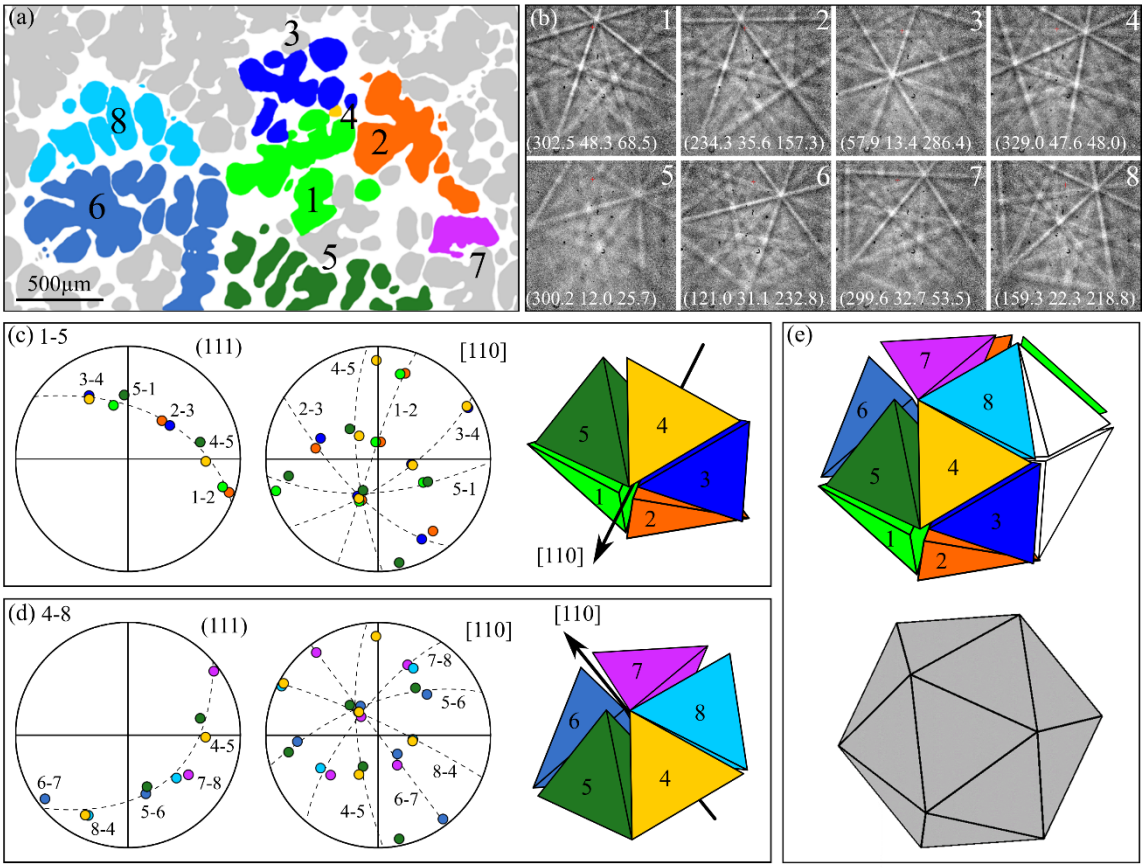

Figure 5.11 Neighbouring α-Al dendrites with continuous 60° <110> {111} twin forming icosahedron symmetry. (a) Eight α-Al grains from Al-15wt.% Cu. (b) Kikuchi patterns from the eight α-Al grains with Euler angles marked at the bottom. (c) Pole figures of the common (111) planes and [110] directions of grains 1-5 forming combined fivefold symmetry, with the five tetrahedra forming a pentagonal bipyramid. (d) Pole figures of the common (111) planes and [110] directions of grains 4-8 forming combined fivefold symmetry, with the five tetrahedra forming a pentagonal bipyramid. (e) Two pentagonal bipyramids from (c) and (d) together with two extra tetrahedra forming an icosahedron with certain gaps, in comparison with a standard icosahedron with the same orientation.

In order to identify the clusters of local aluminium grains with combined icosahedral symmetry and study the prevalence of these grain clusters, an algorithm was developed using a MATLAB code within the MTEX toolbox to process the EBSD data. The basic principle of the algorithm is searching for all grain boundaries with the 60° {111} twinning relationship (5° tolerance for the {111} common plane and three <110> common directions in the common {111} plane), filtering out the grain clusters containing more than 3 grains with the twinning boundaries, and identifying the parent icosahedron orientation. With that icosahedron orientation, all the grains contacting the cluster are then examined for the OR. The cluster keeps growing until all the grains contacting its boundary do not share the OR with the icosahedron orientation. One of the results obtained from the algorithm is shown in Figure 5.12. Figure 5.12(a) is the IPF-Z map of the α-Al in Al-6Cu refined with Al-5Ti-1B master alloy. In Figure 5.12(b) the Al clusters with icosahedral symmetry are highlighted with colour based on the IPF-Z colour scheme for the icosahedron symmetry. Figure 5.12(c) and (d) show the colour scheme for $\mathrm{m}\bar{3}\mathrm{m}$ symmetry (including FCC) and $\mathrm{m}\bar{3}\bar{5}$ icosahedral symmetry, respectively. In Figure 5.12(c) the inverse pole figure for FCC is constricted within the [001], [101] and [111] directions, and in Figure 5.12(d) the inverse pole figure for icosahedron symmetry is constricted by twofold, threefold and fivefold axes.

In Figure 5.12(c), there are 54 clusters formed by at least 3 neighbouring Al grains with icosahedral symmetry. According to the IPF-Z map, the icosahedrons have no preferred orientations and their distribution is also near-random in space. These clusters only contain less than 3% (224 out of 7646) of α-Al grains in the whole map. Thus, while it was relatively easy to find α-Al grain clusters related by

twin ORs and combined fivefold symmetry (e.g. Figure 5.10), they are rare when all grains are considered.

Kurtuldu et al. measured an above-random population of the 60° {111} twin boundaries between equiaxed α-Al grains in Al-20wt.% Zn alloy with 0.1 wt.% Cr addition [23]. They proposed this was due to the formation of Cr-centred icosahedral quasicrystals (iQC) in the undercooled melt followed by the nucleation of α-Al on the iQC with multiple variants of the OR which produced a high amount of twin boundaries with fivefold symmetry. In the case of the three Al alloys studied here (Al-20Zn, Al-15Cu, and Al-6Cu + Al-5Ti-1B), it is unlikely that the preferred twin ORs measured between neighbouring α-Al grains are caused by nucleation on iQCs for the following reasons:

(i) Only a small proportion of grains, ~3%, belong to such grain clusters.

(ii) The above-random proportion of 50° <111> {113} twin boundaries (Figure 5.7) cannot be explained by the nucleation of α-Al on a simple icosahedron.

(iii) In the case of Al-6Cu refined with the Al-5Ti-B master alloy, the α-Al nucleation mechanism is well established: heterogeneous nucleation occurs on TiB_2 particles (or on an Al_3Ti or similar layer on the TiB_2 particles) at low undercooling.

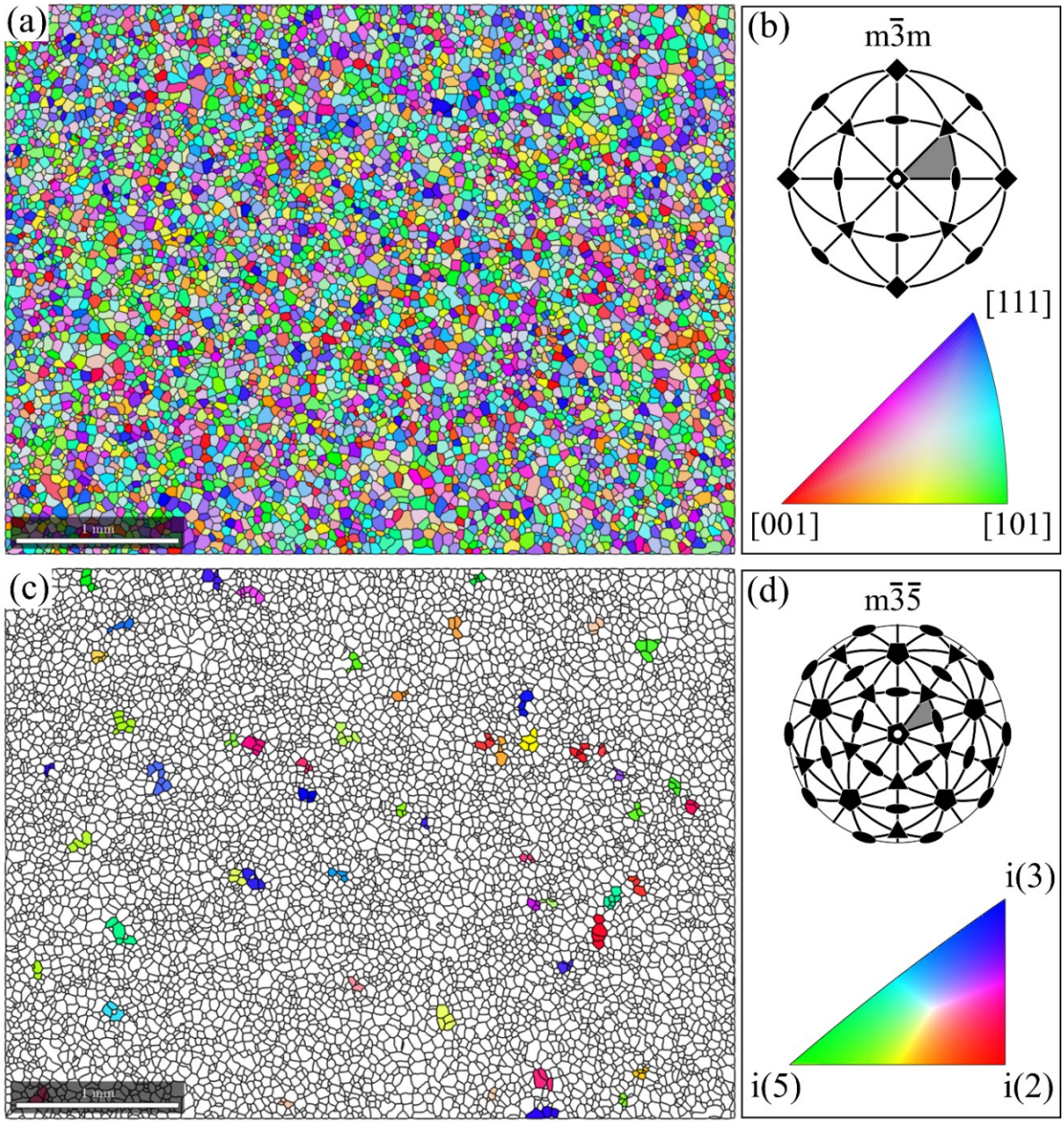

Figure 5.12 Clusters of α-Al equiaxed grains with icosahedron symmetry. (a) EBSD IPF-Z map of Al-6Cu with 1 wt.% Al-5Ti-1B grain refiners containing 7646 α-Al grains. (c) Clusters of 3 or more α-Al grains highlighted from (a) with icosahedron symmetry identified by the algorithm. The clusters are coloured according to the IPF-Z colour key of the icosahedron symmetry. (b) IPF colour key of Al with $m\bar{3}m$ symmetry. (d) IPF colour key of icosahedron with $m\bar{3}\bar{5}$ symmetry.

5.3.1.3 <110> tilt angle preference between equiaxed α-Al grains

According to the DFT calculation in Figure 5.4(d), there are three local energy minima for tilt boundaries along <110> α-Al: 0°, 50.5° and 70.5° where the latter two correspond to {113} and {111} twins, respectively. In order to explore the preferred ORs between neighbouring α-Al grains from an energy perspective, the comparison between the interfacial energy and the occurrence frequency of tilt angle along <110> is shown in Figure 5.13. All grain boundaries with <110> common axes between neighbouring α-Al grains were examined for the three cast Al alloys. The deviation angle between the common <110> directions from two unit cells was set to be less than 5°. For the <110> tilt grain boundaries in the three cast alloys, there are three preferred tilt angles in Figure 5.13: low angle below 10°, ~50° and ~70°. The three peaks are a good match to the three local interfacial energy minima. Figure 5.14 shows the comparison of the tilt angle frequency along <110> between experimental (from Al-20Zn) and simulated untextured α-Al orientations. The large simulated dataset contains 30584 α-Al orientations with 89280 pairs of Al-Al neighbouring grains. There is barely any preference for a particular tilt angle in the simulation except the contrary to the experiment results: it is unlikely to form 60° {111} twinning ORs between random orientations. All of these indicate that the tilting preference along <110> in the cast Al alloys is likely to be attributed to the minimisation of interfacial energy.

According to the study of the solidification OR between Al_3Ti and TiB_2 in Chapter 3, second phase particles can rotate on the growth front to lower the interfacial energy. In the case of equiaxed solidification, 3D stochastic modelling has shown that grain movement can be activated by convection and sedimentation/buoyancy [268]. When two grains come into contact in the mushy zone, the formation of a stable solid-solid interface requires a new grain boundary to have lower energy than the two solid-liquid interfaces it replaces ($\gamma_{S-s} < 2\gamma_{S-L}$) and contacting crystals that do not meet this criterion are expected to be separated by a liquid film [157, 158, 269]. Although the solid-liquid interfacial energy is anisotropic and is a function of temperature and interface composition [270], the typical S-L interfacial energy for Al is set to be 0.1 J/m^2 as in Ref.[157]. The simplified $2\gamma_{S-L}$ value is

plotted as horizontal lines on Figure 5.13(a) and Figure 5.14(a), suggesting that only the solid-solid interfaces below the line would be stable and any other tilt angles would have a liquid film separating the grains. Therefore, it is possible that when grains are separated by liquid films, rotation may be relatively easy but, once rotation brings a pair of grains to a favourable orientation relationship (e.g. a 60° {111} twin), they coalesce to form a grain boundary and further relative rotation becomes more difficult and less likely, so these grains become bonded together whereas other grains can keep rotating until they form a favourable OR with their neighbour. Due to the limited time available and the multiple competing neighbours around each grain, most grains will never reach a favourable OR with their neighbours, but the results indicate it is sufficiently common to give a significantly above-random proportion of special boundaries at the end of equiaxed solidification.

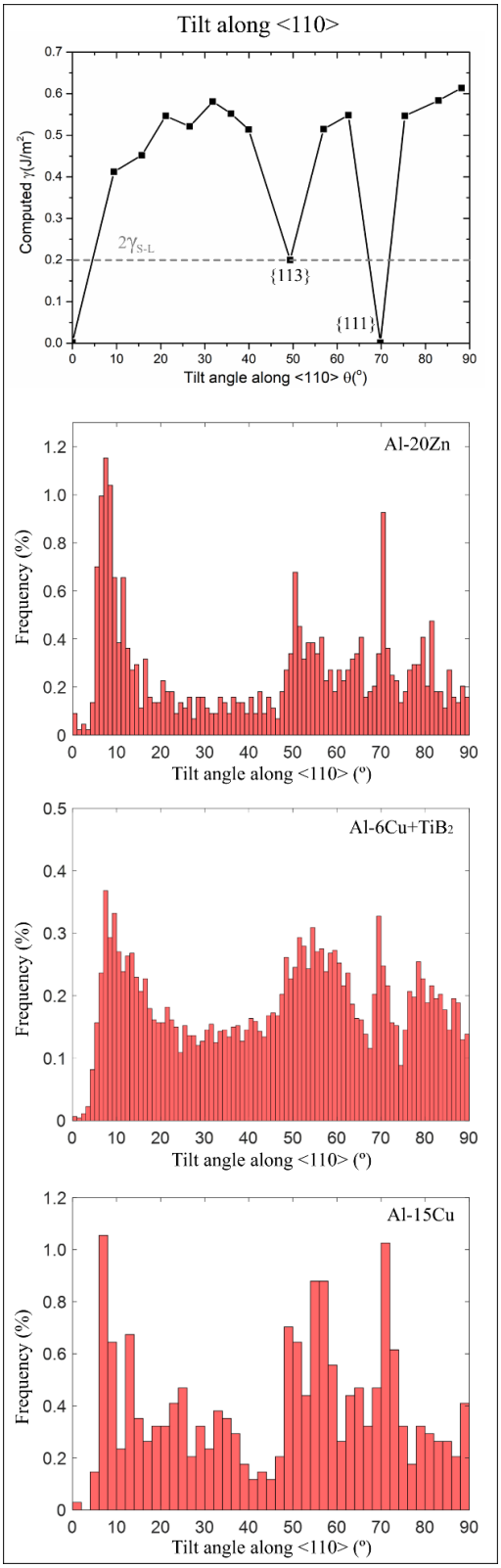

Figure 5.13 The occurrence frequency for α-Al grain boundaries at various tilting angle along <110> for (a) Al-20wt.% Zn, (b) Al-6wt.% Cu with 1 wt.% Al-5Ti-1B additions, (c) Al-15wt.% Cu and (d) untextured simulation.

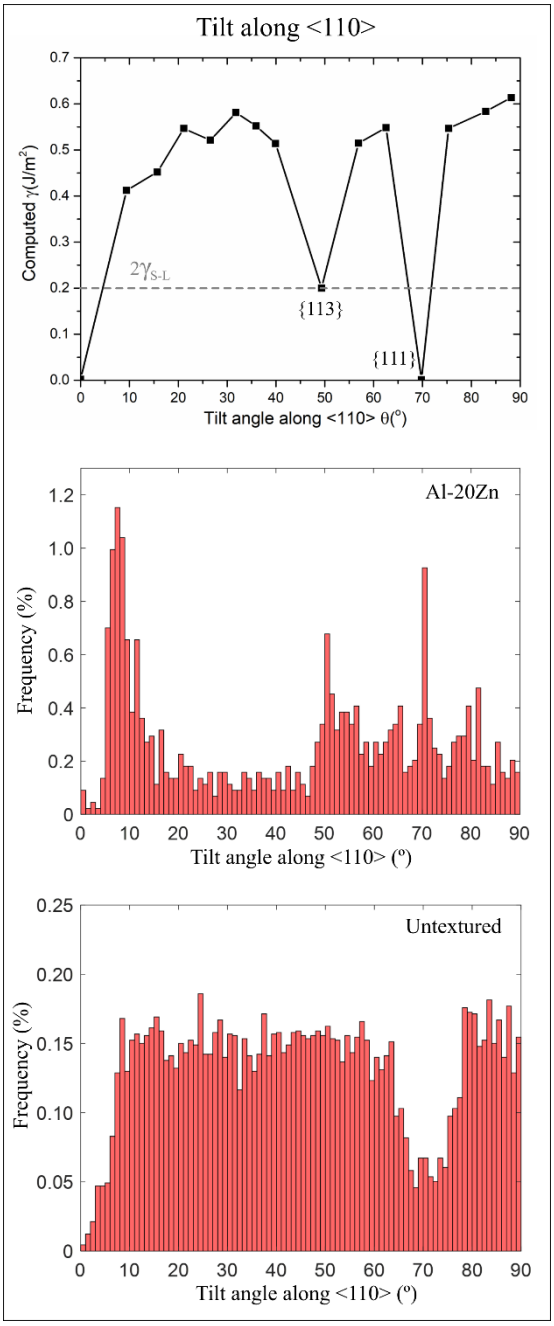

Figure 5.14 Comparison of the tilting frequency along <110> between experimental (Al-20Zn) and simulated untextured α-Al orientations

5.3.2 HCP Mg alloys

5.3.2.1 Preferred grain boundaries in cast Mg alloys

Between equiaxed HCP Mg grains, there were also preferred misorientations at certain angles. Figure 5.15 shows such grain boundary preference for two cast Mg-9wt.%Al-0.7wt.%Zn alloys refined with the addition of $FeCl_3$ and Al_4C_3. From the IPF-Z map plotted by MTEX in Figure 5.15(a) and (d), the Mg grains are equiaxed in both alloys. Certain grain boundaries are preferred in the misorientation frequency histograms superimposed with the Mackenzie curve (Figure 5.15(b) and (e)). Such preference is more obvious after subtracting the Mackenzie curve, as shown in Figure 5.15(c) and (f). Compared to the random uniform texture, the Mg-Mg grain boundaries at low angle (~10°), ~30°, ~60° and ~90° have higher frequency in Mg-9Al-0.7Zn alloys with both refiners.

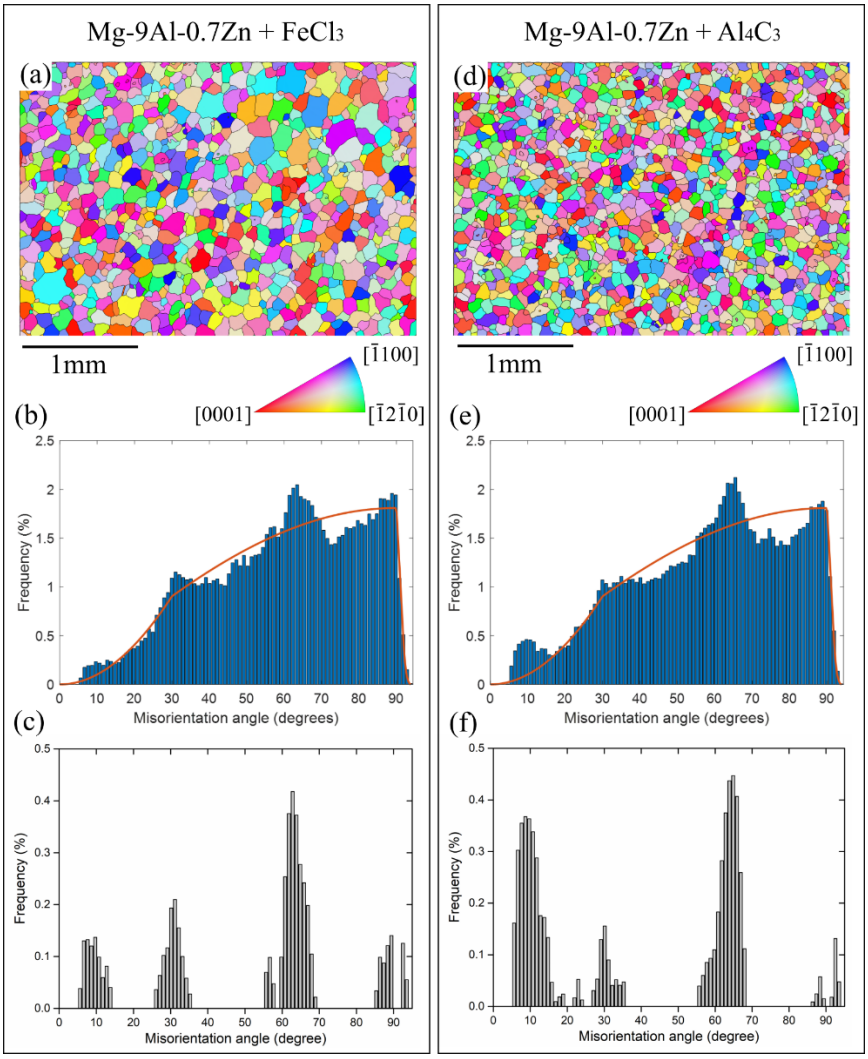

Figure 5.15 The solidification texture of cast Mg-9Al-0.7Zn with $FeCl_3$ ((a)-(c)) and Al_4C_3 ((d)-(f)). (a)(d) EBSD IPF-Z map of cast Mg-9Al-0.7Zn with (a) $FeCl_3$ and (d) Al_4C_3. (b)(e) Misorientation frequency at α-Mg grain boundaries superimposed with the Mackenzie curve for Mg-9Al-0.7Zn with (b) $FeCl_3$ and (e) Al_4C_3. (c)(f) The misorientation fraction above the Mackenzie curve in (b) and (e).

With closer examination of the grain boundaries at the preferred angles, it was found that most of the preferred misorientation angles are associated with twin orientation relationships in HCP alloys. For example, Figure 5.16(a) and (b) show the 34° <$1\bar{1}00$> {$11\bar{2}1$} twin and the 63° <$1\bar{1}00$> {$11\bar{2}2$} twin, and Figure 5.16(c) and (d) show the 86° <$1\bar{2}10$> {$10\bar{1}2$} twin and the 56° <$1\bar{2}10$> {$10\bar{1}1$} twin. All α-Mg grains in Figure 5.16 are coloured with respect to the IPF-Y colour scheme. In Figure 5.16(a) two hexagonal unit cells share a common <$1\bar{1}00$> axis and a common {$11\bar{2}1$} plane. The trace of the interface between these two grains is nearly perpendicular to the plane normal of the common {$11\bar{2}1$}, indicating that the interface is likely to be the common {$11\bar{2}1$} plane. The same match has also been found between the trace of interface in the EBSD map and the common plane normal in the pole figures in Figure 5.16(b) and (d), indicating the interfaces between the α-Mg grains are likely to be the common plane. In Figure 5.16(c) the interface between the two grains comprises multiple crystallographic planes, and part of the interface is likely to be the common {$10\bar{1}2$} plane. It can also be seen in Figure 5.16 that, although most of the interfaces with the twinned orientation relationships are likely to be the common planes, the α-Mg grains do not have simple straight grain boundaries which will unavoidably form interfaces with other crystallographic planes as well.

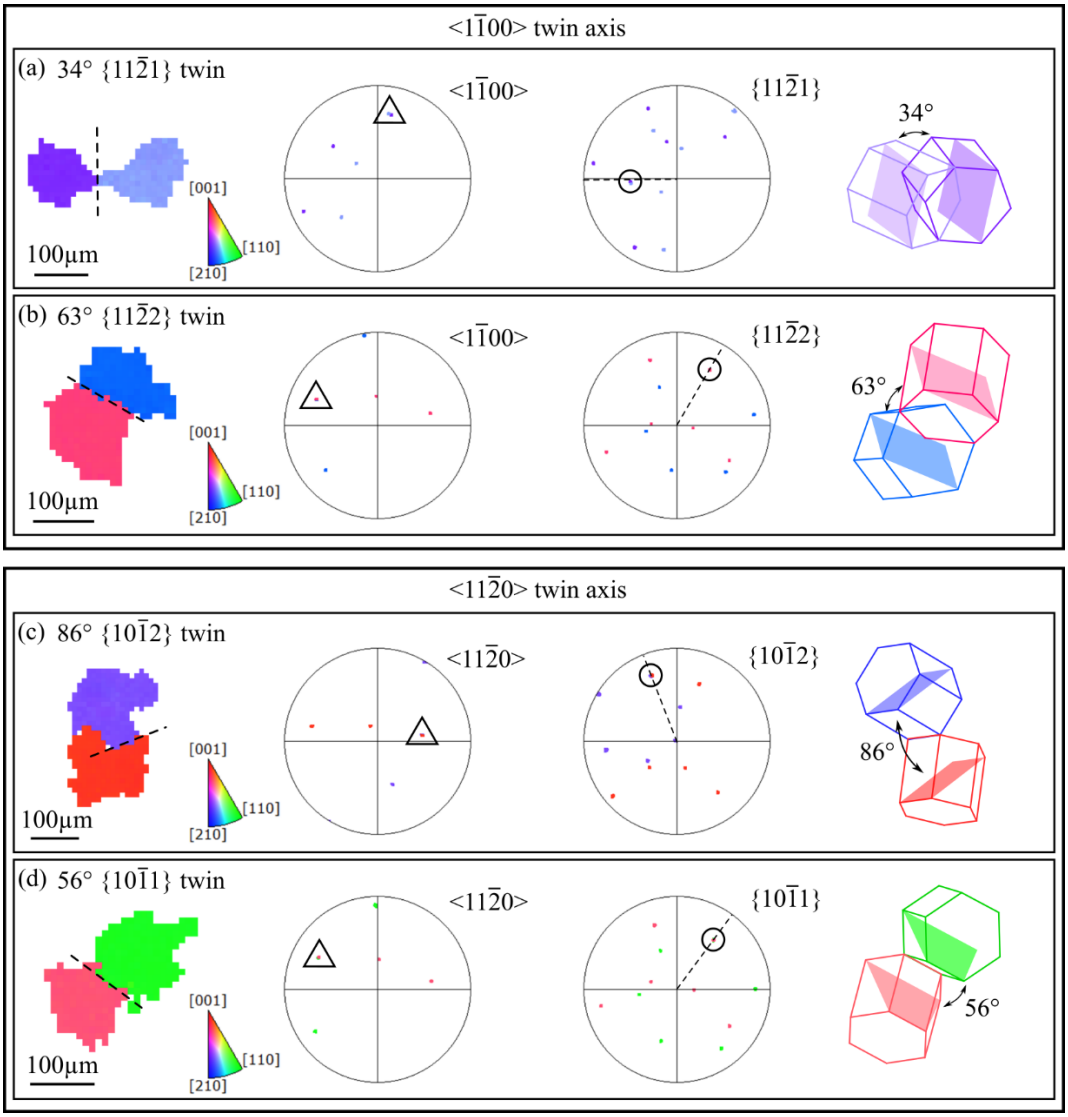

Figure 5.16 Preferred boundaries with twinning orientation relationship in Mg-9Al-0.7Zn. The twin axes are <1 $\bar{1}$00> ((a) and (b)) and <11 $\bar{2}$0> ((c) and (d)), respectively. Four types of twin orientation relationships are plotted: (a) 34° <1 $\bar{1}$00> {11 $\bar{2}$1} twin, (b) 63° <1 $\bar{1}$00> {11 $\bar{2}$2} twin, (c) 86° <11 $\bar{2}$0> {1 $\bar{1}$02} twin and (d) 56° <11 $\bar{2}$0> {1 $\bar{1}$01} twin. The common directions and planes are marked in pole figures. The grains are plotted by EBSD IPF-Y map and unit cell wireframes are plotted based on the Euler angle.

5.3.2.2 Mg grain clusters with combined icosahedron symmetry

Similar to α-Al, the local α-Mg grains may form a combined icosahedron symmetry. However, unlike the simple OR between α-Al and the icosahedron, according to Singh et al. [156], 5 ORs have been measured between α-Mg and icosahedral quasicrystals. Figure 5.17 shows an example where five Mg orientations (the misorientation between grain 2 and 2' is 1.97°) with continuous 34° <$1\bar{1}00$> {$11\bar{2}1$} twins form a fivefold symmetry, and all five orientations share the same OR to an icosahedron orientation. However, grain 1 and 2' do not share any grain boundary with the other four grains. In Figure 5.17(b) all five orientations share a nearly common {$1\bar{1}00$} plane, and the plane normal is parallel to one of the six i(5) of an icosahedron. Five basal planes are nearly at 36° to each other and parallel to the five i(2) which are all perpendicular to the i(5). Therefore, the OR can be written as: {0001} || i(2) with one of the {$1\bar{1}00$} || i(5) (OR2 in Ref. [156]). Figure 5.17(c) illustrates such ORs between the five hexagonal unit cells and a rhombic triacontahedron which is one of the polyhedrons with icosahedral symmetry. In the rhombic triacontahedron, the plane normals of all faces are i(2) and the vectors from the centre to the corners are i(3) or i(5). The colours in Figure 5.17(a) do not contain any meaningful information of how the unit cells are oriented in space. The real orientations are indicated by the unit cell wireframes in Figure 5.17(c).

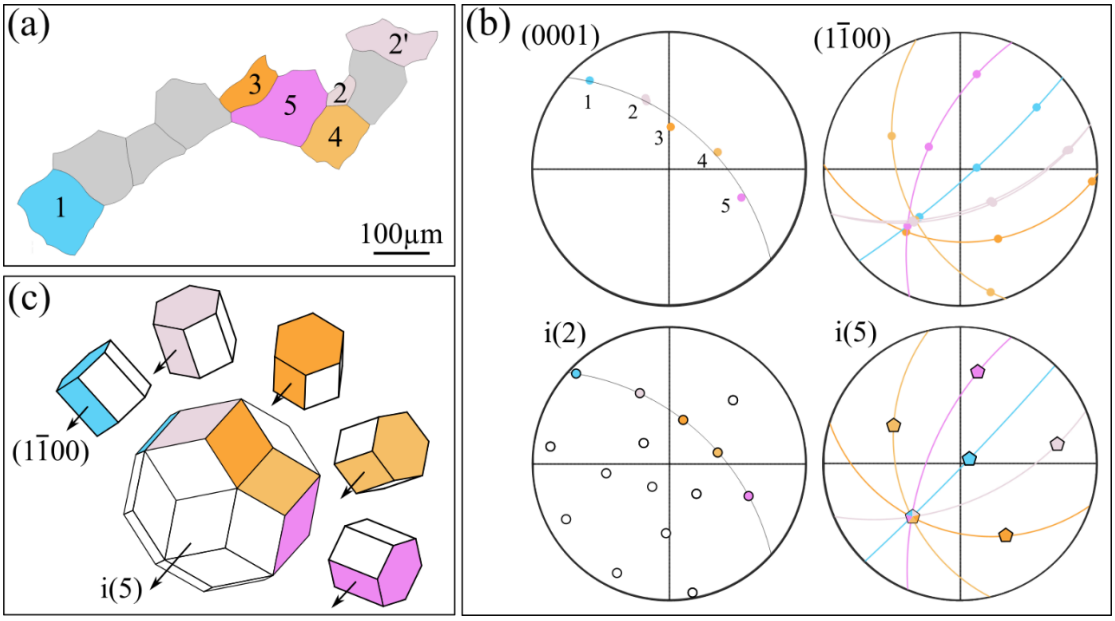

Figure 5.17 Continuous <1$\bar{1}$00> {11$\bar{2}$1} twin forming fivefold symmetry. (a) Six α-Mg grains with five main orientations in Mg-9Al-0.7Zn. (b) {0001} and <1$\bar{1}$00> pole figures of the five orientations. Between every two of them it is 34° rotation along the common <1$\bar{1}$00>. Pole figures of i(2) and i(5) of a standard icosahedron are also plotted, with a simple OR to the α-Mg: {0001} || i(2) with two {1$\bar{1}$00} || i(5). (c) Five hexagonal unit cells with their basal plane parallel to five facets of a rhombic triacontahedron, and the common {1$\bar{1}$00} parallel to an i(5). Note that the colours in (a) are manually chosen to separate different orientations without any meaningful information of how the unit cells are oriented in space. The real orientations are indicated by the unit cell wireframes in (c).

Similarly, other twinned neighbouring α-Mg grains can also be translated into icosahedral symmetry, but it requires Mg grains to have different ORs to the icosahedron. Because of the high symmetry of an icosahedron and in total 48 variants of the 5ORs, it is difficult to identify the relevant grain clusters considering a random Mg orientation could potentially be in one of the 5 reported ORs to the icosahedron.

Similar to the Al-6Cu inoculated with TiB_2 particles, for Mg-9Al-0.7Zn refined with Al_4C_3 particles it is commonly acknowledged that HCP α–Mg nucleates heterogeneously on carbides, which indicates that the measured solidification ORs between neighbouring α-Mg grains is unlikely to be caused by nucleation on an iQC. Similarly, although the nucleation mechanism for the Elfinal process (Mg-9Al-0.7Zn refined with $FeCl_3$) remains unknown, the fact that it shows the same preference as Mg-9Al-0.7Zn refined with Al_4C_3 additions indicates such preferred solidification ORs are also unlikely to be caused by nucleation on iQC.

5.3.2.3 <1$\bar{1}$00> and <11$\bar{2}$0> tilt angle preference between equiaxed α-Mg grains

The tilt angle preference was investigated between α-Mg grains along <1$\bar{1}$00> and <11$\bar{2}$0> directions. For tilting along <1$\bar{1}$00> directions, there are three local energy minima at 0°, 34.2° and 63.2° (Figure 5.6), the latter two corresponding to <1$\bar{1}$00> {11$\bar{2}$1} and <1$\bar{1}$00> {11$\bar{2}$2} twins. After examining the grain boundaries between equiaxed α-Mg grains in cast Mg-9Al-0.7Zn with $FeCl_3$ and Al_4C_3 additions, the occurrence frequency of different tilt angles along the common <1$\bar{1}$00> (deviation angle is set to be less than 5°) is shown in Figure 5.18(b) and (c). There are three preferred tilt boundaries along <1$\bar{1}$00> at (i) low angles less than 10°, (ii) near 34° and (iii) near 63°, which is a good match to the calculated energy preference.

For tilting along <11$\bar{2}$0> direction, there are five local energy minima at 0°, 29.9°, 56.1°, 64.0° and 86.3° (Figure 5.6), and the latter four correspond to the <11$\bar{2}$0> {2$\bar{2}$01}, <11$\bar{2}$0> {1$\bar{1}$01}, <11$\bar{2}$0> {1$\bar{1}$03} and <11$\bar{2}$0> {1$\bar{1}$02} twins, respectively. The five local energy minima also match the occurrence frequency of the tilting angle along <11$\bar{2}$0> for both cast Mg-9Al-0.7Zn alloys, as shown in Figure 5.18(d)-(f).

As discussed in section 5.3.1.3, grain interaction and movement are likely to happen between α-Mg grains during equiaxed solidification to optimise interface. Here for two cast Mg alloys, the good match between the occurrence frequency of tilt grain boundaries along <1$\bar{1}$00> and <11$\bar{2}$0> directions and their interfacial energy preference indicates that α-Mg grains in the two cast alloys are also likely to move during solidification to optimise their interface. The calculated solid-liquid interfacial energy for Mg {0001}, {1$\bar{1}$00} and {11$\bar{2}$0} planes are 88.4, 90.1, 90.8 mJ/m^2 [271], indicating the anisotropic range for the γ_{S-L} of HCP Mg is relatively small compared to faceted crystals [270]. The γ_{S-L} value for Mg is set to be 0.09J/m^2 and $2\gamma_{S-L}$ is plotted as horizontal lines in Figure 5.18(a) and (d). Similar to α-Al, when two Mg grains come into contact with an OR below the horizontal line, then a solid-solid interface is favoured to replace the two solid-liquid interfaces. Otherwise there will be a thin liquid film between the neighbouring grains and rotation is likely to happen to reach an OR with local energy minima. Consequently, a significantly above-random proportion of special boundaries forms at the end of equiaxed solidification.

Therefore, for the special twinning ORs between neighbouring grains produced by grain movement and rotation in cast Al and Mg alloys, it is geometrically possible to form icosahedral symmetry without any iQC-mediated nucleation occurring. These two mechanisms can both lead to grain clusters with the same icosahedral symmetry. Hence, it requires extra caution than simple grain boundary examination to differentiate between grain clusters nucleating from iQC and grain clusters formed by movement and rotation to minimise the interfacial energy.

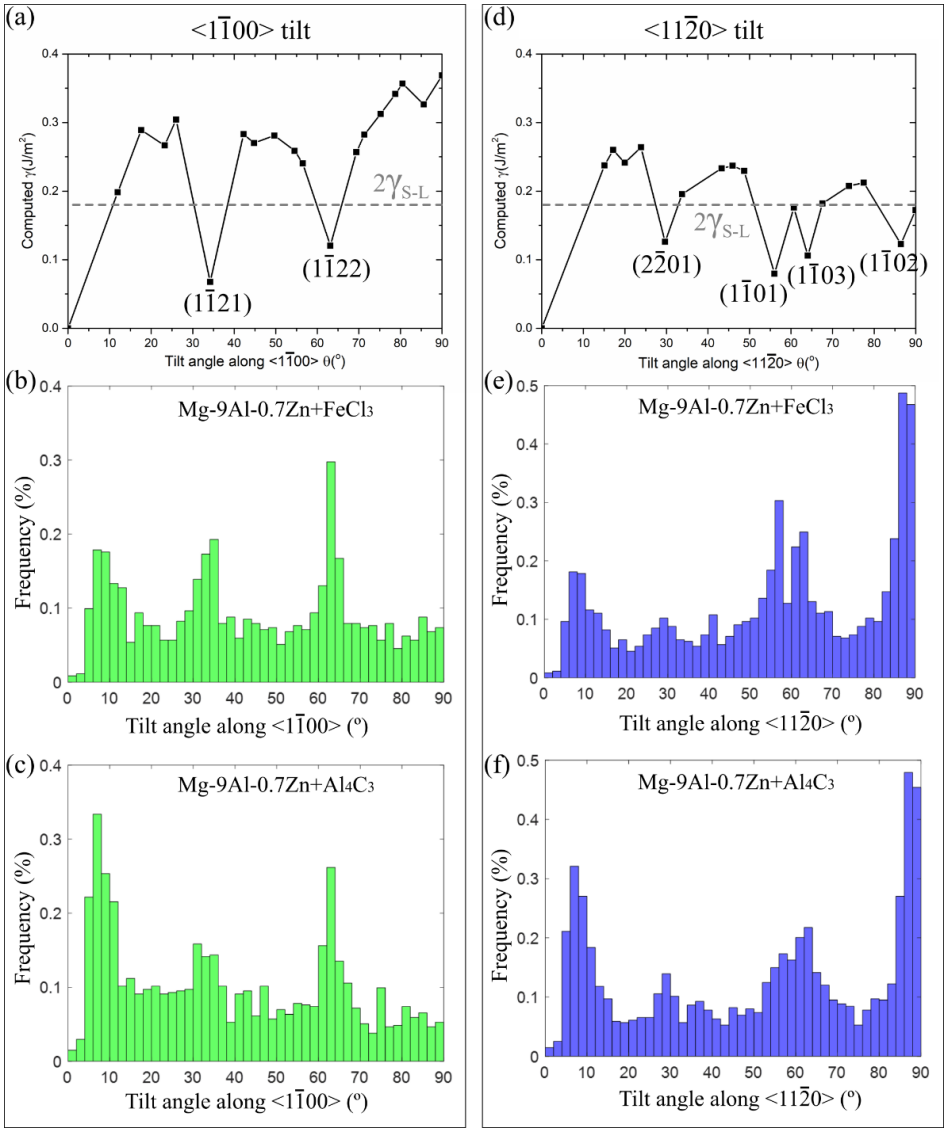

Figure 5.18 The interfacial energy and occurrence frequency for α-Mg grain boundaries at various tilting angle along <1$\bar{1}$00> (a)-(c) and <11$\bar{2}$0> (d)-(f). (a) The interfacial energy tilting from 0° to 90° along <1$\bar{1}$00>. (b)-(c) The occurrence frequency of various tilting angle along <1$\bar{1}$00> for Mg-9Al-0.7Zn with $FeCl_3$ (b) and Al_4C_3 (c) additions. (d) The interfacial energy tilting from 0° to 90° along <11$\bar{2}$0>. (e)-(f) The occurrence frequency of various tilting angle along <11$\bar{2}$0> for Mg-9Al-0.7Zn with $FeCl_3$ (e) and Al_4C_3 (f) additions.

5.4 Conclusions

A study of the solidification texture of (i) equiaxed α-Al grains in three cast Al alloys and (ii) equiaxed α-Mg grains in Mg-9Al-0.7Zn cast with two grain refiner additions has been conducted, combining experiment (EBSD) and simulation (DFT calculations). The main conclusions can be drawn as follows:

- For equiaxed α-Al grains with different shape (globular and dendritic) and size (coarse and refined), there is a significant above-random proportion of grain boundaries with misorientation at 10° to 20° and 50° to 60°.
- For equiaxed α-Mg grains refined with $FeCl_3$ and Al_4C_3, there is a significant above-random proportion of grain boundaries at around 10°, 30°, 60° and 90°.
- Clusters of grains with twin boundaries were observed in both cast Al and Mg alloys forming fivefold symmetry in space. Clusters of α-Al grains with icosahedron symmetry were identified with a simple OR ({111} || i(3) with three <110> || i(5)).
- Through DFT calculation the preferred boundaries with the observed twinning ORs correspond to local interfacial energy minima for both FCC (Al) and HCP (Mg) structures.
- There are two possible coherent interfaces when tilting along the certain directions (<110> for Al and $<1\bar{1}00>$ and $<11\bar{2}0>$ for Mg). Although the exact interface between two grains was not identified in this work, statistical EBSD data treatment and local twinned grain morphologies showed that the lower energy interface is likely to form.
- The tilting preference obtained from large EBSD datasets gives a good match to the theoretically calculated interfacial energy minima. It is likely that the preferred special grain boundaries are formed due to the interaction and movement of grains in the mushy zone to lower the interfacial energy.
- More broadly, during equiaxed solidification, grains are likely to rotate when they contact each other and optimise their interface, forming a solidification texture with a preference for low energy interface orientations instead of being totally random.

- It has been found here that clusters of grains related to each other with icosahedral symmetry exist even in Al alloys cast with Al-5Ti-1B grain refiner where nucleation almost certainly occurred on TiB_2 rather than on an iQC. This geometrical situation is likely to occur when there is an above-random proportion of low energy grain boundaries. This highlights the difficulty in differentiating between grain clusters coming from iQC-mediated nucleation and grain clusters formed by grain rotation to minimise interfacial energy.

Chapter 6 Conclusions and future work

6.1 Conclusions

This thesis has developed a deeper understanding of the formation mechanisms of preferred orientation relationships during alloy solidification. Two main mechanisms were identified. Mechanism (i) involves ORs formed by heterogeneous nucleation on either intentionally added nucleant particles such as Al_3Ti on TiB_2 in Chapter 3, or on metastable precursor phases that led to cyclic twin ORs between the variants of Al_3Ti, Ag_3Sn, $Al_{45}Cr_7$ and $Al_{13}Fe_4$ in Chapter 4. Mechanism (ii) involves the movement and rotations between two contacting grains/particles to lower the interfacial energy. This included ORs created by pushing and engulfment between Al_3Ti and TiB_2 in Chapter 3, and preferred twin ORs between equiaxed neighbouring grains with both FCC and HCP crystal structures in Chapter 5.

There is intensive ongoing research into the grain refinement of alloys by inoculant additions that contain growth restricting solute and numerous heterogeneous nucleant particles. There can be more than one OR formed between growing crystals and nucleants, and multiple mechanisms can generate ORs during solidification, making it difficult to assign each orientation relationship to a formation mechanism. In this work new approaches were developed to link ORs to their formation mechanism using a model system (Al_3Ti and TiB_2). Three reproducible ORs were explored between Al_3Ti and TiB_2 and they were formed by nucleation and pushing & engulfment processes:

$$\{112\}_{Al3Ti} \parallel \{0001\}_{TiB2} \text{ with } <\bar{2}01>_{Al3Ti} \parallel <11\bar{2}0>_{TiB2} \qquad \text{(OR1)}$$

$$\{001\}_{Al3Ti} \parallel \{0001\}_{TiB2} \text{ with } <110>_{Al3Ti} \parallel <11\bar{2}0>_{TiB2} \qquad \text{(OR2)}$$

$$\{100\}_{Al3Ti} \parallel \{0001\}_{TiB2} \text{ with } <010>_{Al3Ti} \parallel <11\bar{2}0>_{TiB2} \qquad \text{(OR3)}$$

The nucleation OR was identified by growing a relatively large TiB_2 crystal and solidifying multiple small Al_3Ti crystals on one (0001) facet of TiB_2. Pushing and engulfment ORs were investigated by statistical analysis of EBSD measurements, density functional theory (DFT) calculations of interface energies, and

imaging of cross-sections of TiB_2 particles being pushed and engulfed by Al_3Ti facets. The lowest energy OR was formed by nucleation as well as by pushing/engulfment. The higher energy ORs, formed by pushing and engulfment, correspond to local interfacial energy minima and can be explained by rotation of TiB_2 particles on Al_3Ti facets during pushing.

To date a wide range of studies on growth twinning of various crystals have been reported. In this work, four IMCs were chosen that are related to different parent structures to study their twinning behaviour and the effect of cooling rate on the formation of multiple twinning ORs during solidification: $D0_{22}$-Al_3Ti, a tetragonal superstructure derived from FCC; $D0_a$-Ag_3Sn, an orthorhombic superstructure derived from HCP; monoclinic $Al_{45}Cr_7$, an icosahedral quasicrystal approximant; and monoclinic $Al_{13}Fe_4$, a decagonal quasicrystal approximant. It was found that these IMCs tend to grow into large single crystal plates (Al_3Ti and Ag_3Sn) and rods ($Al_{45}Cr_7$ and $Al_{13}Fe_4$) at slow cooling rate. Twinned $Al_{45}Cr_7$ and $Al_{13}Fe_4$ crystals were also observed at slow cooling with up to 4 and 2 orientations, respectively. Twin boundaries were found to be commonly coincident with edges and re-entrant corners which gives growth advantage to attain the final twin form. More twinned orientations in the four IMCs were obtained with additional twin types (for $Al_{13}Fe_4$) at higher cooling rate. It is believed that the deeper undercooling induced by higher cooling rate favours the nucleation of metastable phases and/or the formation of short-range order with high symmetry in melt, which then nucleated/transformed into stable phases with all orientation variants. The cyclic twin ORs between the stable IMC variants form combined symmetry of their corresponding parent structure, and the ORs between the stable IMCs and their corresponding parent structure are:

Al_3Ti: $\{001\}_{Al3Ti} \,||\, \{001\}_{ccp}$, with $<100>_{Al3Ti} \,||\, <100>_{ccp}$;

Ag_3Sn: $\{001\}_{Ag3Sn} \,||\, \{1\bar{1}00\}_{hcp}$, with $<100>_{Ag3Sn} \,||\, <0001>_{hcp}$;

$Al_{45}Cr_7$: $<101>_{Al45Cr7} \,||$ *i(5)* and $<110>_{Al45Cr7} \,||$ *i(2)*;

$Al_{13}Fe_4$: $<010>_{Al13Fe4} \,||$ *d(10)*, and $<001>_{Al13Fe4} \,||$ *d(2)*.

In past work, it has been reported that the nucleation of FCC phases from icosahedral quasicrystals formed in undercooled melt can produce a significantly above-random population of 60° twinning grain boundaries in the FCC phase, forming overall icosahedral symmetry after equiaxed solidification. In this work, with the combination of EBSD analysis and DFT calculation, the formation mechanisms for the preferred grain boundaries with special twin ORs between equiaxed neighbouring grains in both FCC (α-Al) and HCP phases (α-Mg) were identified. A significant above-random proportion of 60° {111} and 50.5° {113} twin ORs between neighbouring FCC Al grains were found and clusters of Al grains with multiple 60° {111} twins forming similar icosahedral symmetry were identified. The OR between the FCC Al grains cluster and an icosahedron is the same as the reported nucleation OR between FCC and iQC:

$$\{111\}_{Al} \,||\, i(3) \text{ with three in-plane } \langle 110\rangle_{Al} \,||\, i(5)$$

However, such clusters only contain a small proportion (~3%) of α-Al grains and the 50.5° {113} twins cannot be produced from this simple icosahedron OR. Furthermore, in the case of Al-6Cu refined with the Al-5Ti-B master alloy, the nucleation mechanism is well established: heterogeneous nucleation occurs on TiB_2 particles (or on an Al_3Ti or similar layer on the TiB_2 particles) at low undercooling. Similarly, an above-random population of 34° $\langle 1\bar{1}00\rangle$ $\{11\bar{2}1\}$ twin, 63° $\langle 1\bar{1}00\rangle$ $\{11\bar{2}2\}$ twin, 86° $\langle 1\bar{2}10\rangle$ $\{10\bar{1}2\}$ twin and 56° $\langle 1\bar{2}10\rangle$ $\{10\bar{1}1\}$ twin between neighbouring grains were observed in HCP Mg with known inoculants (carbides) and clusters of Mg grains with multiple twins can also form local icosahedral symmetry with 5 different ORs to the icosahedron. This shows that the above-random proportion of low energy interfaces is not specific to FCC alloys but also occurs for HCP and, for both FCC and HCP, an above random proportion of twin ORs generates clusters of grains with pseudo-icosahedral symmetry. Therefore, it is likely that the measured icosahedral symmetry was formed by the mechanisms that minimise the interfacial energy such as rotation towards low-energy twinned ORs instead of nucleation from iQC. Close examination revealed a good match between the measured tilt angle preference and calculated interfacial energy for both FCC Al and HCP Mg. This interpretation

was further supported by Chapter 3 showing that TiB_2 can rotate on an Al_3Ti growth front to lower the interfacial energy, and previous 3D stochastic modelling that has shown that grain movement can be activated by convection and sedimentation/buoyancy. It is likely that grains can move and rotate to optimise interfaces in the mushy zone and form a significantly above-random proportion of special boundaries at the end of equiaxed solidification. This work also highlights the difficulty in differentiating between grain clusters coming from iQC-mediated nucleation and grain clusters formed by grain rotation to minimise interfacial energy.

6.2 Suggestions for future work

This thesis as a whole studied the broad question of the formation mechanisms of solidification orientation relationships in Al, Sn and Mg alloys. In order to explore this further, the following future work is recommended:

In-situ Synchrotron X-ray Experiments

For detailed observation of the nucleation and subsequent growth of IMCs from metastable phases, and the movement and rotation of neighbouring grains in the mushy zone, synchrotron X-ray tomography combined with in-situ X-ray diffraction could provide useful information about the structure of metastable phases, crystal growth and the misorientation changes between contacting grains. This would require further advances in the time resolution of diffraction tomography experiments that are likely to be feasible within a few years.

iQC-mediated nucleation of IMCs and FCC phases

In order to further explore the iQC-mediated nucleation, it is worth to consider other Al alloys and other FCC systems (Au, Ag etc.) which have the potential for formation of icosahedral quasicrystals and/or icosahedral short-range order. By comparing the FCC phase from iQC mediated nucleation with FCC-Al from movement and rotations during/after equiaxed solidification, useful information can be

gained in terms of differentiating these two formation mechanisms since both of them can produce an above-random proportion of 60° {111} twin ORs between neighbouring FCC grains.

As for the cyclic twinned IMCs nucleating/transforming from icosahedral quasicrystals and/or icosahedral short-range order in the melt, the findings in this thesis with $Al_{45}Cr_7$ could potentially be applied into other systems. For example, α-$Al_{15}(Mn,Fe)_3Si_2$ is often the primary IMC phase in the commonly used Al-Si-Fe-Mn alloys and, similar to $Al_{45}Cr_7$, it contains Mn-centred icosahedral building blocks in its unit cell. Favouring and/or stabilising the formation of icosahedral quasicrystals and/or icosahedral short-range order could potentially be used to trigger more nucleation events and lower the size of α-$Al_{15}(Mn,Fe)_3Si_2$, or cyclic twinning could be used to generate a more compact growth form, both of which could make this phase less deleterious to tensile ductility.

Nucleation of β-Sn on metastable HCP structure

Similar to Ag_3Sn, cyclic twinning often has been observed in β-Sn forming combined hexagonal symmetry. The twinned domains appear to come out (i) from one nucleation event ('beach ball' structure) or (ii) solid state transformation ('interlacing' twin). It may be worth exploring if there is any evidence of a metastable phase forming before β-Sn nucleation, and how to stabilise the metastable phase for further examination. There is a known stable hexagonal phase at the Sn-rich side in Sn-In and Sn-Hg phase diagram, so the addition of In may be a good option for further study.

References

1. Lide, D.R., *Abundance of elements in the Earth's crust and in the sea.* CRC handbook of chemistry and physics, Internet Version, 2005: p. 14-17.
2. Easton, M. and D. StJohn, *Grain refinement of aluminum alloys: Part I. the nucleant and solute paradigms—a review of the literature.* Metallurgical and Materials Transactions A, 1999. **30**(6): p. 1613-1623.
3. Ali, Y., D. Qiu, B. Jiang, F. Pan, and M.-X. Zhang, *Current research progress in grain refinement of cast magnesium alloys: a review article.* Journal of Alloys and Compounds, 2015. **619**: p. 639-651.
4. Easton, M., M. Qian, A. Prasad, and D. StJohn, *Recent advances in grain refinement of light metals and alloys.* Current Opinion in Solid State and Materials Science, 2016. **20**(1): p. 13-24.
5. StJohn, D., M. Easton, M. Qian, and J. Taylor, *Grain refinement of magnesium alloys: a review of recent research, theoretical developments, and their application.* Metallurgical and materials transactions A, 2013. **44**(7): p. 2935-2949.
6. Zhang, Y., H. Wang, N. Ma, and X. Li, *Effect of Fe on grain refining of pure aluminum refined by Al5TiB master alloy.* Materials Letters, 2005. **59**(27): p. 3398-3401.
7. Avedesian, M.M. and H. Baker, *ASM specialty handbook: magnesium and magnesium alloys*. 1999: ASM international.
8. Johnsson, M., *Influence of Si and Fe on the grain refinement of aluminium.* Zeitschrift fur Metallkunde, 1994. **85**(11): p. 781-785.
9. Lee, Y., A. Dahle, D. StJohn, and J. Hutt, *The effect of grain refinement and silicon content on grain formation in hypoeutectic Al–Si alloys.* Materials Science and Engineering: A, 1999. **259**(1): p. 43-52.
10. Hutt, J., D. StJohn, L. Hogan, and A. Dahle, *Equiaxed solidification of Al–Si alloys.* Materials science and technology, 1999. **15**(5): p. 495-500.
11. StJohn, D.H., P. Cao, M. Qian, and M.A. Easton, *A new analytical approach to reveal the mechanisms of grain refinement.* Advanced Engineering Materials, 2007. **9**(9): p. 739-746.
12. Wang, Y., M. Xia, Z. Fan, X. Zhou, and G. Thompson, *The effect of Al8Mn5 intermetallic particles on grain size of as-cast Mg–Al–Zn AZ91D alloy.* Intermetallics, 2010. **18**(8): p. 1683-1689.
13. IZ, R.G.A.Z., *Challenges and advantages of recycling wrought aluminium alloys from lower grades of metallurgically clean scrap.* Materiali in tehnologije, 2013. **47**(1): p. 13-23.
14. Sha, G., K. O'Reilly, B. Cantor, J. Worth, and R. Hamerton, *Growth related metastable phase selection in a 6xxx series wrought Al alloy.* Materials Science and Engineering: A, 2001. **304**: p. 612-616.
15. Rivlin, V. and G. Raynor, *4: Critical evaluation of constitution of aluminium-iran-silicon system.* International Metals Reviews, 1981. **26**(1): p. 133-152.
16. Jirang, C. and H.J. Roven, *Recycling of automotive aluminum.* Transactions of nonferrous metals society of china, 2010. **20**(11): p. 2057-2063.
17. Kumar, S., P. Grant, and K. O'Reilly, *Evolution of Fe bearing intermetallics during DC casting and homogenization of an Al-Mg-Si Al alloy.* Metallurgical and Materials Transactions A, 2016. **47**(6): p. 3000-3014.
18. Kumar, S. and K. O'Reilly, *Influence of Al grain structure on Fe bearing intermetallics during DC casting of an Al-Mg-Si alloy.* Materials Characterization, 2016. **120**: p. 311-322.
19. Verma, A., S. Kumar, P. Grant, and K. O'Reilly, *Influence of cooling rate on the Fe intermetallic formation in an AA6063 Al alloy.* Journal of Alloys and Compounds, 2013. **555**: p. 274-282.
20. Lu, L. and A. Dahle, *Iron-rich intermetallic phases and their role in casting defect formation in hypoeutectic Al-Si alloys.* Metallurgical and materials transactions A, 2005. **36**(3): p. 819-835.
21. Dinnis, C.M., J.A. Taylor, and A.K. Dahle, *As-cast morphology of iron-intermetallics in Al–Si foundry alloys.* Scripta materialia, 2005. **53**(8): p. 955-958.

22. Školáková, A., P. Hanusová, F. Průša, P. Salvetr, P. Novák, and D. Vojtěch, *MICROSTRUCTURE AND THERMAL STABILITY OF Al-Fe-X ALLOYS.* Acta Metallurgica Slovaca, 2018. **24**(3): p. 223-228.
23. Kurtuldu, G., P. Jarry, and M. Rappaz, *Influence of Cr on the nucleation of primary Al and formation of twinned dendrites in Al–Zn–Cr alloys: Can icosahedral solid clusters play a role?* Acta Materialia, 2013. **61**(19): p. 7098-7108.
24. Kurtuldu, G., A. Sicco, and M. Rappaz, *Icosahedral quasicrystal-enhanced nucleation of the fcc phase in liquid gold alloys.* Acta Materialia, 2014. **70**: p. 240-248.
25. Kurtuldu, G., P. Jarry, and M. Rappaz, *Influence of minor Cr-additions to the growth of columnar dendrites in Al-Zn alloys: Influence of Icosahedral Short Range Order in the liquid.* Metallurgical and Materials Transactions A, 2020. **51**(1): p. 279-288.
26. Kurtuldu, G., P. Jarry, and M. Rappaz, *Influence of icosahedral short range order on diffusion in liquids: A study on Al-Zn-Cr alloys.* Acta Materialia, 2016. **115**: p. 423-433.
27. Kurtuldu, G. and M. Rappaz. *Probability of twin boundary formation associated with the nucleation of equiaxed grains on icosahedral quasicrystal templates*. in *IOP Conf. Ser. Mater. Sci. Eng*. 2015.
28. Rappaz, M. and G. Kurtuldu, *Thermodynamic aspects of homogeneous nucleation enhanced by icosahedral short range order in liquid fcc-type alloys.* Jom, 2015. **67**(8): p. 1812-1820.
29. Feng, S., Y. Cui, E. Liotti, A. Lui, C. Gourlay, and P. Grant, *In-situ X-ray radiography of twinned crystal growth of primary Al13Fe4.* Scripta Materialia, 2020. **184**: p. 57-62.
30. Zeng, G., S. Shuai, X. Zhu, S. Ji, J. Xian, and C. Gourlay, *Al 8 Mn 5 in High-Pressure Die Cast AZ91: Twinning, Morphology and Size Distributions.* Metallurgical and Materials Transactions A, 2020: p. 1-13.
31. Zeng, G., J. Xian, and C. Gourlay, *Nucleation and growth crystallography of Al8Mn5 on B2-Al (Mn, Fe) in AZ91 magnesium alloys.* Acta Materialia, 2018. **153**: p. 364-376.
32. Volmer, M. and A. Weber, *Kinetic theory for nucleation of supersaturated structures.* Z. Phys. Chem, 1926. **119**: p. 277.
33. Becker, R. and W. Döring, *The kinetic treatment of nuclear formation in supersaturated vapors.* Ann. Phys, 1935. **24**(719): p. 752.
34. Turnbull, D., *Formation of crystal nuclei in liquid metals.* Journal of Applied Physics, 1950. **21**(10): p. 1022-1028.
35. Turnbull, D. and R. Cech, *Microscopic observation of the solidification of small metal droplets.* Journal of Applied Physics, 1950. **21**(8): p. 804-810.
36. Kelton, K. and A. Greer, *Test of classical nucleation theory in a condensed system.* Physical Review B, 1988. **38**(14): p. 10089.
37. Rappaz, M. and J.A. Dantzig, *Solidification*. 2009: EPFL press.
38. Volmer, M. and A. Weber, *Novel growth mechanism in heteroepitaxial semiconductor growth.* Z. phys. Chem, 1926. **119**: p. 277.
39. Turnbull, D., *Kinetics of heterogeneous nucleation.* The Journal of Chemical Physics, 1950. **18**(2): p. 198-203.
40. Turnbull, D., *Kinetics of solidification of supercooled liquid mercury droplets.* The Journal of chemical physics, 1952. **20**(3): p. 411-424.
41. Porter, D.A. and K.E. Easterling, *Phase transformations in metals and alloys (revised reprint)*. 2009: CRC press.
42. Turnbull, D. and B. Vonnegut, *Nucleation Catalysis.* Industrial & Engineering Chemistry, 1952. **44**(6): p. 1292-1298.
43. Bramfitt, B.L., *The effect of carbide and nitride additions on the heterogeneous nucleation behavior of liquid iron.* Metallurgical Transactions. **1**(7): p. 1987-1995.
44. Kelly, P.M. and M.-X. Zhang, *Edge-to-edge matching—The fundamentals.* Metallurgical and Materials Transactions A, 2006. **37**(3): p. 833-839.

45. Zhang, M.X., P.M. Kelly, M.A. Easton, and J.A. Taylor, *Crystallographic study of grain refinement in aluminum alloys using the edge-to-edge matching model.* Acta Materialia, 2005. **53**(5): p. 1427-1438.
46. Zhang, M.X., P.M. Kelly, M. Qian, and J.A. Taylor, *Crystallography of grain refinement in Mg–Al based alloys.* Acta Materialia, 2005. **53**(11): p. 3261-3270.
47. Mohanty, P. and J. Gruzleski, *Mechanism of grain refinement in aluminium.* Acta Metallurgica et Materialia, 1995. **43**(5): p. 2001-2012.
48. Schumacher, P. and A. Greer, *Enhanced heterogeneous nucleation of α-Al in amorphous aluminium alloys.* Materials Science and Engineering: A, 1994. **181**: p. 1335-1339.
49. Schumacher, P. and A. Greer, *Heterogeneously nucleated α-Al in amorphous aluminium alloys.* Materials Science and Engineering: A, 1994. **178**(1-2): p. 309-313.
50. Schumacher, P. and A. Greer, *Light Metals 1995.* TMS, Warrendale, PA, 1995: p. 869-77.
51. Schumacher, P., A.L. Greer, J. Worth, P.V. Evans, M.A. Kearns, P. Fisher, and A.H. Green, *New studies of nucleation mechanisms in aluminium alloys: implications for grain refinement practice.* Materials Science and Technology, 1998. **14**(5): p. 394-404.
52. Fan, Z., Y. Wang, Y. Zhang, T. Qin, X.R. Zhou, G.E. Thompson, T. Pennycook, and T. Hashimoto, *Grain refining mechanism in the Al/Al–Ti–B system.* Acta Materialia, 2015. **84**: p. 292-304.
53. Greer, A., *Crystallization of amorphous alloys.* Metallurgical and Materials Transactions A, 1996. **27**(3): p. 549-555.
54. Qiu, D., J.A. Taylor, M.X. Zhang, and P.M. Kelly, *A mechanism for the poisoning effect of silicon on the grain refinement of Al–Si alloys.* Acta Materialia, 2007. **55**(4): p. 1447-1456.
55. Quested, T., A.L. Greer, and P. Cooper. *The variable potency of TiB2 nucleant particles in the grain refinement of aluminium by Al-Ti-B additions*. in *Materials Science Forum*. 2002. Trans Tech Publ.
56. Quested, T. and A. Greer, *The effect of the size distribution of inoculant particles on as-cast grain size in aluminium alloys.* Acta materialia, 2004. **52**(13): p. 3859-3868.
57. Greer, A., A. Bunn, A. Tronche, P. Evans, and D. Bristow, *Modelling of inoculation of metallic melts: application to grain refinement of aluminium by Al–Ti–B.* Acta materialia, 2000. **48**(11): p. 2823-2835.
58. Cibula, A., *The grain refinement of al alloy castings by addition of Ti and B.* Journal of the Institute of Metals, 1951. **90**: p. 1-16.
59. Crossley, F. and L. Mondolfo, *Mechanism of grain refinement in aluminum alloys.* J. Metals (New York), 1951. **3**.
60. Jones, G.P. and J. Pearson, *Factors affecting the grain-refinement of aluminum using titanium and boron additives.* Metallurgical Transactions B, 1976. **7**(2): p. 223-234.
61. Johnsson, M., L. Backerud, and G.K. Sigworth, *Study of the mechanism of grain refinement of aluminum after additions of Ti-and B-containing master alloys.* Metallurgical and Materials Transactions A, 1993. **24**(2): p. 481-491.
62. Murty, B., S. Kori, and M. Chakraborty, *Grain refinement of aluminium and its alloys by heterogeneous nucleation and alloying.* International Materials Reviews, 2002. **47**(1): p. 3-29.
63. Cibula, A., *The mechanism of grain refinement of sand castings in aluminium alloys.* Journal of the Institute of Metals, 1949. **76**(4): p. 321-+.
64. Johnsson, M., *On the mechanism of grain refinement of aluminum after additions of Ti and B.* LIGHT METALS-WARRENDALE-, 1993: p. 769-769.
65. Arnberg, L., L. Bäckerud, and H. Klang, *Intermetallic particles in Al–Ti–B–type master alloys for grain refinement of aluminium.* Metals Technology, 1982. **9**(1): p. 7-13.
66. Guzowski, M., G. Sigworth, and D. Sentner, *The role of boron in the grain.* Metallurgical and Materials Transactions A, 1987. **18**(4): p. 603-619.
67. Davies, I., J. Dennis, and A. Hellawell, *The nucleation of aluminum grains in alloys of aluminum with titanium and boron.* Metallurgical Transactions, 1970. **1**(1): p. 275-280.

68. Mohanty, P., F. Samuel, J. Gruzleski, and T. Kosto, *Studies on the Mechanism of Grain refinement in Aluminum.* LIGHT METALS-WARRENDALE-, 1994: p. 1039-1039.
69. Antonio, J.M. and L.M. Lfo, *Grain refinement in aluminum alloyed with titanium and boron.* Metallurgical Transactions, 1971. **2**(2): p. 465-471.
70. Cornish, A., *The influence of boron on the mechanism of grain refinement in dilute aluminium-titanium alloys.* Metal Science, 1975. **9**(1): p. 477-484.
71. Mondolfo, L., S. Farooq, and C. Tse, *Solidification processing 1987.* The Institute of Metals, London, 1988: p. 133-136.
72. Sigworth, G.K., *The grain refining of aluminum and phase relationships in the Al-Ti-B system.* Metallurgical Transactions A, 1984. **15**(2): p. 277-282.
73. Sigworth, G., *THE GRAIN REFINING OF ALUMINUM AND PHASE-RELATIONSHIPS IN THE AL-TI-B SYSTEM-REPLY*. 1986, MINERALS METALS MATERIALS SOC 420 COMMONWEALTH DR, WARRENDALE, PA 15086. p. 349-351.
74. Backerud, L. and S. Yidong, *Grain refining mechanisms in aluminium as a result of additions of titanium and boron. I.* Aluminium, 1991. **67**(7-8): p. 780-785.
75. Bäckerud, L., P. Gustafson, and M. Johnsson, *Grain refining mechanisms in aluminum as a result of additions of titanium and boron, part II.* Aluminium, 1991. **67**(9): p. 910-915.
76. Vader, M. and J. Noordegraaf, *Light metals 1989.* PG. Campbell, ed, 1989.
77. Arnberg, L., L. Bäckerud, and H. Klang, *1: Production and properties of master alloys of Al–Ti–B type and their ability to grain refine aluminium.* Metals Technology, 1982. **9**(1): p. 1-6.
78. Johnsson, M., L. Backerud, and G.K. Sigworth, *Study of the mechanism of grain refinement of aluminum after additions of Ti- and B-containing master alloys.* Metallurgical Transactions A, 1993. **24**(2): p. 481-491.
79. Mohanty, P., R. Guthrie, and J. Gruzleski, *Studies on the fading behaviour of Al-Ti-B master alloys and grain refinement mechanism using LiMCA.* LIGHT MET(WARRENDALE PA), 1995: p. 859-868.
80. Mohanty, P., F. Samuel, and J. Gruzleski, *Studies on addition of inclusions to molten aluminum using a novel technique.* Metallurgical and Materials Transactions B, 1995. **26**(1): p. 103-109.
81. Schumacher, P. and A.L. Greer. *Devitrification Behaviour of the Stable Al-Rich Amorphous Alloy Al85Ni5Y8Co2*. in *Key Engineering Materials*. 1993. Trans Tech Publ.
82. Jones, G., *Solidification processing 1987.* The Institute of Metals, 1988. **1**: p. 496-99.
83. Jones, G., *Int. Seminar on Refining and Alloying of Liquid Aluminum and Ferro-alloys.* Light Metals, 1985. **3**: p. 169-175.
84. Han, Y., Y. Dai, D. Shu, J. Wang, and B. Sun, *First-principles calculations on the stability of Al ／ TiB2 interface.* Applied Physics Letters, 2006. **89**(14): p. 144107.
85. Wearing, D., A.P. Horsfield, W. Xu, and P.D. Lee, *Which wets TiB2 inoculant particles: Al or Al3Ti?* Journal of Alloys and Compounds, 2016. **664**: p. 460-468.
86. Wang, J., A. Horsfield, U. Schwingenschlögl, and P.D. Lee, *Heterogeneous nucleation of solid Al from the melt by TiB 2 and Al 3 Ti: an ab initio molecular dynamics study.* Physical Review B, 2010. **82**(18): p. 184203.
87. Wang, J., A. Horsfield, P.D. Lee, and P. Brommer, *Heterogeneous nucleation of solid Al from the melt by Al 3 Ti: Molecular dynamics simulations.* Physical Review B, 2010. **82**(14): p. 144203.
88. Greer, A.L., A.M. Bunn, A. Tronche, P.V. Evans, and D.J. Bristow, *Modelling of inoculation of metallic melts: application to grain refinement of aluminium by Al–Ti–B.* Acta Materialia, 2000. **48**(11): p. 2823-2835.
89. Quested, T.E. and A.L. Greer, *The effect of the size distribution of inoculant particles on as-cast grain size in aluminium alloys.* Acta Materialia, 2004. **52**(13): p. 3859-3868.
90. Schaffer, P.L., D.N. Miller, and A.K. Dahle, *Crystallography of engulfed and pushed TiB2 particles in aluminium.* Scripta Materialia, 2007. **57**(12): p. 1129-1132.
91. Uhlmann, D.R., B. Chalmers, and K. Jackson, *Interaction between particles and a solid ‐ liquid interface.* Journal of Applied Physics, 1964. **35**(10): p. 2986-2993.

92. Bolling, G.F. and J. Cissé, *A theory for the interaction of particles with a solidifying front.* Journal of Crystal Growth, 1971. **10**(1): p. 56-66.
93. Han, Q., *Redistribution of particles during solidification.* ISIJ international, 1995. **35**(6): p. 693-699.
94. Stefanescu, D., B. Dhindaw, S. Kacar, and A. Moitra, *Behavior of ceramic particles at the solid-liquid metal interface in metal matrix composites.* Metallurgical Transactions A, 1988. **19**(11): p. 2847-2855.
95. Juretzko, F.R., D.M. Stefanescu, B.K. Dhindaw, S. Sen, and P.A. Curreri, *Particle engulfment and pushing by solidifying interfaces: Part 1. Ground experiments.* Metallurgical and Materials Transactions A, 1998. **29**(6): p. 1691-1696.
96. Stefanescu, D.M., F.R. Juretzko, A. Catalina, B.K. Dhindaw, S. Sen, and P.A. Curreri, *Particle engulfment and pushing by solidifying interfaces: Part II. Microgravity experiments and theoretical analysis.* Metallurgical and Materials Transactions A, 1998. **29**(6): p. 1697-1706.
97. Rempel, A.W. and M.G. Worster, *The interaction between a particle and an advancing solidification front.* Journal of Crystal Growth, 1999. **205**(3): p. 427-440.
98. Omenyi, S. and A. Neumann, *Thermodynamic aspects of particle engulfment by solidifying melts.* Journal of Applied Physics, 1976. **47**(9): p. 3956-3962.
99. Hoekstra, P. and R. Miller, *On the mobility of water molecules in the transition layer between ice and a solid surface.* Journal of Colloid and Interface Science, 1967. **25**(2): p. 166-173.
100. Shangguan, D., S. Ahuja, and D. Stefanescu, *An analytical model for the interaction between an insoluble particle and an advancing solid/liquid interface.* Metallurgical Transactions A, 1992. **23**(2): p. 669-680.
101. Azouni, M. and P. Casses, *Thermophysical properties effects on segregation during solidification.* Advances in colloid and interface science, 1998. **75**(2): p. 83-106.
102. Casses, P. and M. Azouni, *Critical velocity of a freezing front interacting with spherical-particles.* INTERNATIONAL COMMUNICATIONS IN HEAT AND MASS TRANSFER, 1995. **22**(4): p. 605-615.
103. Sen, S., F. Juretzko, D. Stefanescu, B. Dhindaw, and P. Curreri, *In situ observations of interaction between particulate agglomerates and an advancing planar solid/liquid interface:: microgravity experiments.* Journal of crystal growth, 1999. **204**(1-2): p. 238-242.
104. Ode, M., J.S. Lee, S.G. Kim, W.T. Kim, and T. Suzuki, *Numerical Simulation of the Critical Velocity for Particle Pushing/Engulfment Transition in Fe–C alloys Using a Phase-Field Model.* ISIJ international, 2000. **40**(2): p. 153-160.
105. Agaliotis, E.M., C.E. Schvezov, M.R. Rosenberger, and A.E. Ares, *A numerical model study of the effect of interface shape on particle pushing.* Journal of Crystal Growth, 2012. **354**(1): p. 49-56.
106. Garvin, J.W. and H.S. Udaykumar, *Drag on a particle being pushed by a solidification front and its dependence on thermal conductivities.* Journal of Crystal Growth, 2004. **267**(3): p. 724-737.
107. Derby, J.J., *The synergy of modeling and novel experiments for melt crystal growth research.* IOP Conference Series: Materials Science and Engineering, 2018. **355**: p. 012001.
108. Shechtman, D., I. Blech, D. Gratias, and J.W. Cahn, *Metallic phase with long-range orientational order and no translational symmetry.* Physical review letters, 1984. **53**(20): p. 1951.
109. Hahn, T. and H. Wondratschek, *Symmetry of crystals: Introduction to International Tables for Crystallography Vol. A.* Acta Cryst, 1997. **53**: p. 252.
110. Pauling, L., *So-called icosahedral and decagonal quasicrystals are twins of an 820-atom cubic crystal.* Physical review letters, 1987. **58**(4): p. 365.
111. Pauling, L., *Evidence from electron micrographs that icosahedral quasicrystals are icosahedral twins of cubic crystals.* Proceedings of the National Academy of Sciences, 1990. **87**(20): p. 7849-7850.
112. Pauling, L., *Apparent icosahedral symmetry is due to directed multiple twinning of cubic crystals.* Nature, 1985. **317**(6037): p. 512-514.

113. Heiney, P., P. Bancel, and P. Horn, *Comment on ''So-called icosahedral and decagonal quasicrystals are twins of an 820-atom cubic crystal''.* Physical Review Letters, 1987. **59**(18): p. 2119.
114. Dunlap, R. and K. Dini, *Formation, structure, and crystallization of metastable quasi-crystalline Al–transition metal alloys prepared by rapid solidification.* Canadian Journal of Physics, 1985. **63**(10): p. 1267-1269.
115. Bendersky, L., R. Schaefer, F. Biancaniello, and D. Shechtman, *Rapidly solidifed Al-Cr alloys: structure and decomposition behaviour.* Journal of materials science, 1986. **21**(6): p. 1889-1896.
116. Lilienfeld, D., M. Nastasi, H. Johnson, D. Ast, and J. Mayer, *The quasicrystalline transformation in the AlCr system.* Journal of Materials Research, 1986. **1**(2): p. 237-242.
117. Bellissent, R., F. Bouree-Vigneron, and P. Sainfort. *Neutron Diffraction Study of the Structure of Some Aluminum--Transition Metal Nonperiodic Crystals*. in *J. Phys., Colloq.* 1986.
118. Cornier-Quiquandon, M., A. Quivy, S. Lefebvre, E. Elkaim, G. Heger, A. Katz, and D. Gratias, *Neutron-diffraction study of icosahedral Al-Cu-Fe single quasicrystals.* Physical Review B, 1991. **44**(5): p. 2071.
119. Guyot, P. and M. Audier, *A quasicrystal structure model for AI-Mn.* Philosophical Magazine B, 1985. **52**(1): p. L15-L19.
120. Katz, A., *Introduction to the Mathematics of Quasicrystals, edited by M. Jaric*. 1989, San Diego: Academic Press.
121. Swamy, V., S. Ranganathan, and K. Chattopadhyay, *Rapidly solidified Al–Cr alloys: Crystalline and quasicrystalline phases.* Journal of Materials Research, 1989. **4**(3): p. 539-551.
122. Inoue, A., H. Kimura, and T. Masumoto, *Formation of AI-Cr-Si quasicrystal with high silicon concentration by rapid quenching and its thermal and electrical properties.* Journal of materials science, 1987. **22**(5): p. 1864-1868.
123. Singh, A. and S. Ranganathan, *A transmission electron microscopic study of icosahedral twins—I. Rapidly solidified Al-Mn-Fe alloys.* Acta metallurgica et materialia, 1995. **43**(9): p. 3539-3551.
124. Van Tendeloo, G., A. Singh, and S. Ranganathan, *Quasicrystals and their crystalline homologues in the Al–Mn–Cu ternary alloys.* Philosophical Magazine A, 1991. **64**(2): p. 413-427.
125. Zhang, H., D. H. Wang, and K. H. Kuo, *Quasicrystals, crystalline phases, and multiple twins in rapidly solidified Al-Cr alloys*. Vol. 37. 1988. 6220-6225.
126. Cooper, M., *The structure of the intermetallic phase ϑ (Cr-Al).* Acta Crystallographica, 1960. **13**(3): p. 257-263.
127. Priputen, P., M. Kusý, M. Kriška, R. Lipka, E. Illeková, P. Švec, J. Buršík, M. Svoboda, J. Dolinšek, and J. Janovec, *Characterization of phases in complex metallic alloys Al73Mn27− xFex (x= 2, 4 and 6).* Intermetallics, 2009. **17**(12): p. 1047-1051.
128. Grin, J., U. Burkhardt, M. Ellner, and K. Peters, *Refinement of the Fe4Al13 structure and its relationship to the quasihomological homeotypical structures*. Vol. 209. 1994. 479-487.
129. Fung, K.K., C. Yang, Y. Zhou, J. Zhao, W. Zhan, and B. Shen, *Icosahedrally related decagonal quasicrystal in rapidly cooled Al-14-at.%-Fe alloy.* Physical review letters, 1986. **56**(19): p. 2060.
130. Zou, X., K. Fung, and K. Kuo, *Orientation relationship of decagonal quasicrystal and tenfold twins in rapidly cooled Al-Fe alloy.* Physical Review B, 1987. **35**(9): p. 4526.
131. Barbier, J.N., N. Tamura, and J.L. Verger-Gaugry, *Monoclinic Al13Fe4 approximant phase: a link between icosahedral and decagonal phases.* Journal of Non-Crystalline Solids, 1993. **153-154**: p. 126-131.
132. Saitoh, K., T. Yokosawa, M. Tanaka, and A.P. Tsai, *Structural studies of monoclinic approximants of Al13Fe4 and τ2-inflated Al13Co4 by the high-angle annular dark-field method.* Microscopy, 1999. **48**(2): p. 105-114.
133. Frank, F.C., *Supercooling of Liquids.* Proceedings of the Royal Society of London. Series A. Mathematical and Physical Sciences, 1952. **215**(1120): p. 43.

134. Schenk, T., D. Holland-Moritz, V. Simonet, R. Bellissent, and D.M. Herlach, *Icosahedral Short-Range Order in Deeply Undercooled Metallic Melts.* Physical Review Letters, 2002. **89**(7): p. 075507.
135. Holland-Moritz, D., T. Schenk, R. Bellissent, V. Simonet, K. Funakoshi, J.M. Merino, T. Buslaps, and S. Reutzel, *Short-range order in undercooled Co melts.* Journal of Non-Crystalline Solids, 2002. **312-314**: p. 47-51.
136. Nelson, D. and F. Spaepen, *Solid State Physics, Vol. 42*. 1989, Academic Press.
137. Schenk, T., V. Simonet, D. Holland-Moritz, R. Bellissent, T. Hansen, P. Convert, and D.M. Herlach, *Temperature dependence of the chemical short-range order in undercooled and stable Al-Fe-Co liquids.* Europhysics Letters (EPL), 2004. **65**(1): p. 34-40.
138. Fang, X., C.-Z. Wang, S. Hao, M.J. Kramer, Y. Yao, M.I. Mendelev, Z. Ding, R.E. Napolitano, and K.-M. Ho, *Spatially resolved distribution function and the medium-range order in metallic liquid and glass.* Scientific reports, 2011. **1**: p. 194.
139. Holland-Moritz, D., T. Schenk, V. Simonet, R. Bellissent, P. Convert, and T. Hansen, *Short-range order in undercooled melts forming quasicrystals and approximants.* Journal of Alloys and Compounds, 2002. **342**(1): p. 77-81.
140. Simonet, V., F. Hippert, M. Audier, and R. Bellissent, *Local order in liquids forming quasicrystals and approximant phases.* Physical Review B, 2001. **65**(2): p. 024203.
141. Simonet, V., F. Hippert, H. Klein, M. Audier, R. Bellissent, H. Fischer, A.P. Murani, and D. Boursier, *Local order and magnetism in liquid Al-Pd-Mn alloys.* Physical Review B, 1998. **58**(10): p. 6273-6286.
142. Kelton, K.F., G.W. Lee, A.K. Gangopadhyay, R.W. Hyers, T.J. Rathz, J.R. Rogers, M.B. Robinson, and D.S. Robinson, *First X-Ray Scattering Studies on Electrostatically Levitated Metallic Liquids: Demonstrated Influence of Local Icosahedral Order on the Nucleation Barrier.* Physical Review Letters, 2003. **90**(19): p. 195504.
143. Nielsen, J.P. and J. Tuccillo, *Grain size in cast gold alloys.* Journal of dental research, 1966. **45**(3): p. 964-969.
144. Ott, D. and C.J. Raub, *Grain size of gold and gold alloys.* Gold Bulletin, 1981. **14**(2): p. 69-74.
145. Renner, H., G. Schlamp, D. Hollmann, H.M. Lüschow, P. Tews, J. Rothaut, K. Dermann, A. Knödler, C. Hecht, and M. Schlott, *Gold, gold alloys, and gold compounds.* Ullmann's Encyclopedia of Industrial Chemistry, 2000.
146. Singh, A. and A. Tsai, *Quasicrystal–crystal interfaces in bulk materials.* Journal of Physics: Condensed Matter, 2008. **20**(31): p. 314002.
147. Bolliger, B., V. Dmitrienko, M. Erbudak, R. Lüscher, H.-U. Nissen, and A. Kortan, *Epitactic textures of fcc Al on icosahedral Al-Pd-Mn quasicrystal.* Physical Review B, 2001. **63**(5): p. 052203.
148. Lüscher, R., M. Erbudak, and Y. Weisskopf, *Al nanostructures on quasicrystalline Al-Pd-Mn.* Surface science, 2004. **569**(1-3): p. 163-175.
149. Beeli, C., T. Ishimasa, and H.-U. Nissen, *Orientation relation between icosahedral and crystalline phases in Al-Mn alloys.* Philosophical Magazine B, 1988. **57**(5): p. 599-608.
150. Loiseau, A. and G. Lapasset, *Crystalline and quasi-crystalline structures in an Al-Li-Cu-Mg alloy.* Le Journal de Physique Colloques, 1986. **47**(C3): p. C3-331-C3-340.
151. Loiseau, A. and G. Lapasset, *Relations between quasicrystals and crystalline phases in Al—Li—Cu—Mg alloys: A new class of approximant structures.* Philosophical magazine letters, 1987. **56**(5): p. 165-171.
152. Elser, V. and C.L. Henley, *Crystal and quasicrystal structures in Al-Mn-Si alloys.* Physical review letters, 1985. **55**(26): p. 2883.
153. Christopher, L. Henley, and V. Elser, *Quasicrystal structure of (Al, Zn) 49Mg32.* Philosophical Magazine B, 1986. **53**(3): p. L59-L66.

154. Audier, M., P. Sainfort, and B. Dubost, *A simple construction of the AlCuLi quasicrystalline structure related to the (Al, Zn) 49 Mg32 cubic structure type.* Philosophical Magazine B, 1986. **54**(4): p. L105-L111.
155. Yu-Zhang, K., J. Bigot, J. Chevalier, D. Gratias, G. Martin, and R. Portier, *Dodecahedral-shaped quasicrystalline precipitates in dilute Al-Mn solid solutions.* Philosophical Magazine B, 1988. **58**(1): p. 1-13.
156. Singh, A., M. Watanabe, A. Kato, and A.P. Tsai, *Twinning and the orientation relationships of icosahedral phase with the magnesium matrix.* Acta Materialia, 2005. **53**(17): p. 4733-4742.
157. Rappaz, M., A. Jacot, and W.J. Boettinger, *Last-stage solidification of alloys: theoretical model of dendrite-arm and grain coalescence.* Metallurgical and Materials Transactions A, 2003. **34**(3): p. 467-479.
158. Mathier, V., A. Jacot, and M. Rappaz, *Coalescence of equiaxed grains during solidification.* Modelling and simulation in materials science and engineering, 2004. **12**(3): p. 479.
159. Miller, W. and G. Chadwick, *On the magnitude of the solid/liquid interfacial energy of pure metals and its relation to grain boundary melting.* Acta metallurgica, 1967. **15**(4): p. 607-614.
160. Hasson, G. and C. Goux, *Interfacial energies of tilt boundaries in aluminium. Experimental and theoretical determination.* Scripta metallurgica, 1971. **5**(10): p. 889-894.
161. Vernede, S., P. Jarry, and M. Rappaz, *A granular model of equiaxed mushy zones: Formation of a coherent solid and localization of feeding.* Acta Materialia, 2006. **54**(15): p. 4023-4034.
162. Vernede, S. and M. Rappaz, *Transition of the mushy zone from continuous liquid films to a coherent solid.* Philosophical Magazine, 2006. **86**(24): p. 3779-3794.
163. Read, W.T. and W. Shockley, *Dislocation models of crystal grain boundaries.* Physical review, 1950. **78**(3): p. 275.
164. Biloni, H., *SUBSTRUCTURES AND DISLOCATIONS PRODUCED DURING SOLIDIFICATION OF ALUMINUM.* Canadian Journal of Physics, 1961. **39**(10): p. 1501-1507.
165. Falleiros, I., *Qualitative evidence of solute redistribution during grain boundary migration.* Metallography, 1972. **5**(2): p. 125-137.
166. Campbell, J., *Castings*. 2003: Elsevier.
167. Tedman-Jones, S., S. McDonald, M. Bermingham, D. StJohn, and M. Dargusch, *Investigating the morphological effects of solute on the β-phase in as-cast titanium alloys.* Journal of Alloys and Compounds, 2019. **778**: p. 204-214.
168. Gertsman, V.Y., J. Li, S. Xu, J.P. Thomson, and M. Sahoo, *Microstructure and second-phase particles in low-and high-pressure die-cast magnesium alloy AM50.* Metallurgical and Materials Transactions A, 2005. **36**(8): p. 1989-1997.
169. Pigenko, A., T. Chernyshova, M.K. Shorshorov, and A.Y. Dontsova, *Structure formation in cast and deposited maraging steel N18K8M3TYu.* Metal Science and Heat Treatment, 1975. **17**(9): p. 751-754.
170. Matsuda, F., H. Nakagawa, S. Ogata, and S. Katayama, *Fractographic investigation on solidification crack in the varestraint test of fully austenitic stainless steel: Studies on fractography of welded zone (III).* Transactions of JWRI, 1978. **7**(1): p. 59-70.
171. Matsuda, F., H. Nakagawa, T. Uehara, S. Katayama, and Y. Arata, *A New Explanation for Role of Delta-Ferrite Improving Weld Solidification Crack Susceptibility in Austenitic Stainless Steel (Materials, Metallurgy, Weldability).* Transactions of JWRI, 1979. **8**(1): p. 105-112.
172. Shibata, S. and T. Watanabe, *The effect of the surface on grain boundary migration in austenitic stainless steel weld metal.* Metallurgical and Materials Transactions A, 2001. **32**(6): p. 1453-1458.
173. Shibata, S.-i., T. Watanabe, S. Mekaru, and I. Fukumoto, *Effect of Various Factors on Grain Boundary Migration in the Weld Metal of an Austenitic Stainless Steel.* QUARTERLY JOURNAL OF THE JAPAN WELDING SOCIETY, 1997. **15**(1): p. 100-107.

174. Otarawanna, S., C.M. Gourlay, H.I. Laukli, and A.K. Dahle, *Agglomeration and bending of equiaxed crystals during solidification of hypoeutectic Al and Mg alloys.* Acta Materialia, 2010. **58**(1): p. 261-271.
175. Sannes, S., L. Arnberg, and M.C. Flemings. *Orientational relationships in semi-solid Al-6.5wt% Si*. in *Light Metals: Proceedings of Sessions, TMS Annual Meeting (Warrendale, Pennsylvania)*. 1996.
176. Dake, J.M., J. Oddershede, H.O. Sørensen, T. Werz, J.C. Shatto, K. Uesugi, S. Schmidt, and C.E. Krill, *Direct observation of grain rotations during coarsening of a semisolid Al–Cu alloy.* Proceedings of the National Academy of Sciences, 2016. **113**(41): p. E5998-E6006.
177. Dake, J., *Experimental Investigations of Microstructural Coarsening in 3D using X-Ray Microscopy*. 2020, Universität Ulm.
178. Lejcek, P., *Grain boundary segregation in metals*. Vol. 136. 2010: Springer Science & Business Media.
179. Buckett, M.I. and K.L. Merkle, *Determination of grain boundary volume expansion by HREM.* Ultramicroscopy, 1994. **56**(1): p. 71-78.
180. Rohrer, G.S., D.M. Saylor, B.E. Dasher, B.L. Adams, A.D. Rollett, and P. Wynblatt, *The distribution of internal interfaces in polycrystals.* Zeitschrift für Metallkunde, 2004. **95**(4): p. 197-214.
181. Saylor, D.M., B.S. El-Dasher, B.L. Adams, and G.S. Rohrer, *Measuring the five-parameter grain-boundary distribution from observations of planar sections.* Metallurgical and Materials Transactions A, 2004. **35**(7): p. 1981-1989.
182. Rohrer, G.S., *The distribution of grain boundary planes in polycrystals.* JOM, 2007. **59**(9): p. 38-42.
183. Marquardt, K., G.S. Rohrer, L. Morales, E. Rybacki, H. Marquardt, and B. Lin, *The most frequent interfaces in olivine aggregates: the GBCD and its importance for grain boundary related processes.* Contributions to Mineralogy and Petrology, 2015. **170**(4): p. 40.
184. Bennett, T.A., C.S. Kim, G.S. Rohrer, and A.D. Rollett. *Five-parameter grain boundary character distribution in Fe-1% Si*. in *Materials Science Forum*. 2004. Trans Tech Publ.
185. Kim, C.-S., Y. Hu, G.S. Rohrer, and V. Randle, *Five-parameter grain boundary distribution in grain boundary engineered brass.* Scripta materialia, 2005. **52**(7): p. 633-637.
186. Randle, V., G. Rohrer, and Y. Hu, *Five-parameter grain boundary analysis of a titanium alloy before and after low-temperature annealing.* Scripta Materialia, 2008. **58**(3): p. 183-186.
187. Randle, V., G. Rohrer, H. Miller, M. Coleman, and G. Owen, *Five-parameter grain boundary distribution of commercially grain boundary engineered nickel and copper.* Acta materialia, 2008. **56**(10): p. 2363-2373.
188. Dillon, S.J., H. Miller, M.P. Harmer, and G.S. Rohrer, *Grain boundary plane distributions in aluminas evolving by normal and abnormal grain growth and displaying different complexions.* International journal of materials research, 2010. **101**(1): p. 50-56.
189. Khorashadizadeh, A., D. Raabe, S. Zaefferer, G. Rohrer, A. Rollett, and M. Winning, *Five‐Parameter Grain Boundary Analysis by 3D EBSD of an Ultra Fine Grained CuZr Alloy Processed by Equal Channel Angular Pressing.* Advanced Engineering Materials, 2011. **13**(4): p. 237-244.
190. Fang, X., Z. Liu, M. Tikhonova, A. Belyakov, R. Kaibyshev, G. Rohrer, and W. Wang, *Grain boundary plane distributions in 304 steel annealed at high temperature after a parallel processing of multiple forging and direct rolling.* Acta Metallurgica Sinica(China), 2012. **48**(8): p. 895-906.
191. Beladi, H. and G.S. Rohrer, *The distribution of grain boundary planes in interstitial free steel.* Metallurgical and Materials Transactions A, 2013. **44**(1): p. 115-124.
192. Liu, X., D. Choi, H. Beladi, N.T. Nuhfer, G.S. Rohrer, and K. Barmak, *The five-parameter grain boundary character distribution of nanocrystalline tungsten.* Scripta Materialia, 2013. **69**(5): p. 413-416.

193. Ratanaphan, S., Y. Yoon, and G.S. Rohrer, *The five parameter grain boundary character distribution of polycrystalline silicon.* Journal of materials science, 2014. **49**(14): p. 4938-4945.
194. Farabi, E., P.D. Hodgson, G.S. Rohrer, and H. Beladi, *Five-parameter intervariant boundary characterization of martensite in commercially pure titanium.* Acta Materialia, 2018. **154**: p. 147-160.
195. Saylor, D.M., B.S. El Dasher, A.D. Rollett, and G.S. Rohrer, *Distribution of grain boundaries in aluminum as a function of five macroscopic parameters.* Acta Materialia, 2004. **52**(12): p. 3649-3655.
196. Beladi, H., A. Ghaderi, and G.S. Rohrer, *Five-parameter grain boundary characterisation of randomly textured AZ31 Mg alloy.* Philosophical Magazine, 2020. **100**(4): p. 456-466.
197. Kim, C.-S., A.D. Rollett, and G.S. Rohrer, *Grain boundary planes: New dimensions in the grain boundary character distribution.* Scripta materialia, 2006. **54**(6): p. 1005-1009.
198. Sholl, D. and J.A. Steckel, *Density functional theory: a practical introduction*. 2011: John Wiley & Sons.
199. Griffiths, D.J. and D.F. Schroeter, *Introduction to quantum mechanics*. 2018: Cambridge University Press.
200. Schrödinger, E., *An undulatory theory of the mechanics of atoms and molecules.* Physical review, 1926. **28**(6): p. 1049.
201. Hohenberg, P. and W. Kohn, *Inhomogeneous electron gas.* Physical review, 1964. **136**(3B): p. B864.
202. Kohn, W. and L.J. Sham, *Self-consistent equations including exchange and correlation effects.* Physical review, 1965. **140**(4A): p. A1133.
203. Munro, R.G., *Material properties of titanium diboride.* Journal of Research of the National Institute of Standards and Technology, 2000. **105**(5): p. 709.
204. Norby, P. and A.N. Christensen, *Preparation and structure of Al 3 Ti.* Acta chemica scandinavica, Series A, 1986. **40**: p. 157.
205. Aparicio-Fernández, R., H. Springer, A. Szczepaniak, H. Zhang, and D. Raabe, *In-situ metal matrix composite steels: Effect of alloying and annealing on morphology, structure and mechanical properties of TiB2 particle containing high modulus steels.* Acta Materialia, 2016. **107**: p. 38-48.
206. Bachmann, F., R. Hielscher, and H. Schaeben, *Texture Analysis with MTEX – Free and Open Source Software Toolbox.* Solid State Phenomena, 2010. **160**: p. 63-68.
207. Hafner, J., *Ab-initio simulations of materials using VASP: Density-functional theory and beyond.* Journal of Computational Chemistry, 2008. **29**(13): p. 2044-2078.
208. Kresse, G. and D. Joubert, *From ultrasoft pseudopotentials to the projector augmented-wave method.* Physical Review B, 1999. **59**(3): p. 1758-1775.
209. Perdew, J.P., K. Burke, and M. Ernzerhof, *Generalized Gradient Approximation Made Simple.* Physical Review Letters, 1996. **77**(18): p. 3865-3868.
210. Methfessel, M. and A.T. Paxton, *High-precision sampling for Brillouin-zone integration in metals.* Physical Review B, 1989. **40**(6): p. 3616-3621.
211. Cooper, A.S., *Precise lattice constants of germanium, aluminum, gallium arsenide, uranium, sulphur, quartz and sapphire.* Acta Crystallographica, 1962. **15**(6): p. 578-582.
212. Wood, R., *The lattice constants of high purity alpha titanium.* Proceedings of the Physical Society, 1962. **80**(3): p. 783.
213. Switendick, A. and B. Morosin. *Electronic charge density and bonding in α‐boron: An experimental‐theoretical comparison*. in *AIP Conference Proceedings*. 1991. AIP.
214. Li, J., M. Zhang, Y. Zhou, and G. Chen, *First-principles study of Al/A13Ti heterogeneous nucleation interface.* Applied Surface Science, 2014. **307**: p. 593-600.
215. Colinet, C. and A. Pasturel, *Structural stability of one-dimensional long-period structures in the TiAl 3 compound.* Journal of Physics: Condensed Matter, 2002. **14**(26): p. 6713.

216. Nassik, M., F.Z. Chrifi-Alaoui, K. Mahdouk, and J.C. Gachon, *Calorimetric study of the aluminium–titanium system.* Journal of Alloys and Compounds, 2003. **350**(1): p. 151-154.
217. Jain, A., R. Pankajavalli, S. Anthonysamy, K. Ananthasivan, R. Babu, V. Ganesan, and G.S. Gupta, *Determination of the thermodynamic stability of TiB2.* Journal of Alloys and Compounds, 2010. **491**(1): p. 747-752.
218. Yanfeng, H., D. Yongbing, S. Da, W. Jun, and S. Baode, *First-principles study of TiB 2 (0001) surfaces.* Journal of Physics: Condensed Matter, 2006. **18**(17): p. 4197.
219. Liu, L.M., S.Q. Wang, and H.Q. Ye, *First-principles study of polar Al/TiN(111) interfaces.* Acta Materialia, 2004. **52**(12): p. 3681-3688.
220. Han, Y.F., Y.B. Dai, J. Wang, D. Shu, and B.D. Sun, *First-principles calculations on Al/AlB2 interfaces.* Applied Surface Science, 2011. **257**(17): p. 7831-7836.
221. Chandra, N. and P. Dang, *Atomistic simulation of grain boundary sliding and migration.* Journal of Materials Science, 1999. **34**(4): p. 655-666.
222. Saha, S., T.Z. Todorova, and J.W. Zwanziger, *Temperature dependent lattice misfit and coherency of Al3X (X=Sc, Zr, Ti and Nb) particles in an Al matrix.* Acta Materialia, 2015. **89**: p. 109-115.
223. Azouni, M.A. and P. Casses, *Thermophysical properties effects on segregation during solidification.* Advances in Colloid and Interface Science, 1998. **75**(2): p. 83-106.
224. Youssef, Y.M., R.J. Dashwood, and P.D. Lee, *Effect of clustering on particle pushing and solidification behaviour in TiB2 reinforced aluminium PMMCs.* Composites Part A: Applied Science and Manufacturing, 2005. **36**(6): p. 747-763.
225. Catalina, A.V., S. Sen, D.M. Stefanescu, and W.F. Kaukler, *Interaction of porosity with a planar solid/liquid interface.* Metallurgical and Materials Transactions A, 2004. **35**(5): p. 1525-1538.
226. Stefanescu, D.M., *The Multidisciplinary Facets of Particle Engulfment and Pushing.* Transactions of the Indian Institute of Metals, 2007. **60**(2): p. 79-86.
227. Turnbull, D., *Theory of catalysis of nucleation by surface patches.* Acta Metallurgica, 1953. **1**(1): p. 8-14.
228. Greer, A., *Grain refinement of alloys by inoculation of melts.* Philosophical Transactions of the Royal Society of London. Series A: Mathematical, Physical and Engineering Sciences, 2003. **361**(1804): p. 479-495.
229. Greer, A.L., P.S. Cooper, M.W. Meredith, W. Schneider, P. Schumacher, J.A. Spittle, and A. Tronche, *Grain refinement of aluminium alloys by inoculation.* Advanced Engineering Materials, 2003. **5**(1‐2): p. 81-91.
230. Hornfeck, W., R. Kobold, M. Kolbe, M. Conrad, and D. Herlach, *Quasicrystal nucleation and 𝕫 module twin growth in an intermetallic glass-forming system.* Nature Communications, 2018. **9**(1): p. 4054.
231. Rossi, P.J., N. Zotov, and E.J. Mittemeijer, *Redetermination of the crystal structure of the Ag3Sn intermetallic compound.* Zeitschrift für Kristallographie-Crystalline Materials, 2016. **231**(1): p. 1-9.
232. Buchanan, K., J. Ribis, J. Garnier, and K. Colas, *Identification of monoclinic θ′-phase dispersoids in a 6061 aluminium alloy.* Philosophical Magazine Letters, 2016. **96**(4): p. 121-131.
233. Tsuchimori, M., T. Ishimasa, and Y. Fukano, *Crystal structures of small Al-rich Fe alloy particles formed by a gas-evaporation technique.* Philosophical Magazine B, 1992. **66**(1): p. 89-108.
234. Black, P., *The structure of FeAl3. II.* Acta Crystallographica, 1955. **8**(3): p. 175-182.
235. Springer, H., R. Aparicio Fernandez, M.J. Duarte, A. Kostka, and D. Raabe, *Microstructure refinement for high modulus in-situ metal matrix composite steels via controlled solidification of the system Fe–TiB2.* Acta Materialia, 2015. **96**: p. 47-56.
236. Srinivasan, S., P. Desch, and R. Schwarz, *Metastable phases in the Al3X (X= Ti, Zr, and Hf) intermetallic system.* Scripta metallurgica et materialia, 1991. **25**.

237. Ellner, M., *Polymorphic phase transformation of Fe4Al13 causing multiple twinning with decagonal pseudo-symmetry.* Acta Crystallographica Section B: Structural Science, 1995. **51**(1): p. 31-36.
238. Louis, E., R. Mora, and J. Pastor, *Nature of star-shaped clusters of FeAl3 in aluminium–iron alloys.* Metal Science, 1980. **14**(12): p. 591-594.
239. Skjerpe, P., *An electron microscopy study of the phase Al3Fe.* Journal of Microscopy, 1987. **148**(1): p. 33-50.
240. Ma, X., H. Liebertz, and U. Köster, *Multiple Twins of Monoclinic Al13Fe4 Showing Pseudo‐Orthorhombic and Fivefold Symmetries.* physica status solidi (a), 1996. **158**(2): p. 359-367.
241. Chen, R., Y.-f. Shi, Q.-y. Xu, and B.-c. Liu, *Effect of cooling rate on solidification parameters and microstructure of Al− 7Si− 0.3 Mg− 0.15 Fe alloy.* Trans. Nonferrous Met. Soc. China, 2014. **24**(6): p. 1645-1652.
242. Yang, B., Y. Gao, C. Zou, Q. Zhai, A. Abyzov, E. Zhuravlev, J. Schmelzer, and C. Schick, *Cooling rate dependence of undercooling of pure Sn single drop by fast scanning calorimetry.* Applied Physics A, 2011. **104**(1): p. 189-196.
243. Gao, Y., E. Zhuravlev, C. Zou, B. Yang, Q. Zhai, and C. Schick, *Calorimetric measurements of undercooling in single micron sized SnAgCu particles in a wide range of cooling rates.* Thermochimica Acta, 2009. **482**(1-2): p. 1-7.
244. Nývlt, J., *Kinetics of nucleation in solutions.* Journal of Crystal Growth, 1968. **3**: p. 377-383.
245. Xian, J., S. Belyakov, M. Ollivier, K. Nogita, H. Yasuda, and C. Gourlay, *Cu6Sn5 crystal growth mechanisms during solidification of electronic interconnections.* Acta Materialia, 2017. **126**: p. 540-551.
246. Wanbing, G., G. Yulai, Z. Qijie, and X. Kuangdi, *DSC study on the undercooling of droplet solidification of metal melt.* Chinese Science Bulletin, 2005. **50**(9): p. 929.
247. Buerger, M., *The genesis of twin crystals.* American Mineralogist: Journal of Earth and Planetary Materials, 1945. **30**(7-8): p. 469-482.
248. Hahn, T. and H. Klapper, *Twinning of crystals. Sect. 3.3.* International Tables for Crystallography, 2013. **500**.
249. Senechal, M., *The genesis of growth twins.* Sov. Phys. Crystallogr, 1980. **25**: p. 520-524.
250. Van Tendeloo, G. and S. Amelinckx, *Group-theoretical considerations concerning domain formation in ordered alloys.* Acta Crystallographica Section A: Crystal Physics, Diffraction, Theoretical and General Crystallography, 1974. **30**(3): p. 431-440.
251. Lehman, L., Y. Xing, T. Bieler, and E. Cotts, *Cyclic twin nucleation in tin-based solder alloys.* Acta Materialia, 2010. **58**(10): p. 3546-3556.
252. Larsson, A.-K., L. Stenberg, and S. Lidin, *The superstructure of domain-twinned η'-Cu6Sn5.* Acta Crystallographica Section B: Structural Science, 1994. **50**(6): p. 636-643.
253. Okamoto, N.L., J. Okumura, M. Higashi, and H. Inui, *Crystal structure of η'-Fe3Al8; low-temperature phase of η-Fe2Al5 accompanied by an ordered arrangement of Al atoms of full occupancy in the c-axis chain sites.* Acta Materialia, 2017. **129**: p. 290-299.
254. Laughlin, D.E., K. Srinivasan, M. Tanase, and L. Wang, *Crystallographic aspects of L10 magnetic materials.* Scripta Materialia, 2005. **53**(4): p. 383-388.
255. Cui, Y., D. King, A. Horsfield, and C. Gourlay, *Solidification orientation relationships between Al3Ti and TiB2.* Acta Materialia, 2020. **186**: p. 149-161.
256. Majumdar, A. and B. Muddle, *Microstructure in rapidly solidified Al-Ti alloys.* Materials Science and Engineering: A, 1993. **169**(1-2): p. 135-147.
257. Guo, J., K. Ohtera, K. Kita, T. Shibata, A. Inoue, and T. Masumoto, *New metastable phases in rapidly solidified Al-Zr and Al-Ti alloys with high solute contents.* Materials Science and Engineering: A, 1994. **181**: p. 1397-1404.
258. Furushiro, N. and S. Hori, *A possible mechanism of phase transformation of Al3Hf from Ll2 to DO22 during aging in a rapidly solidified Al-3Hf-0.3 Si alloy.* Acta Metallurgica, 1985. **33**(5): p. 867-872.

259. Bancel, P.A. and P.A. Heiney, *Icosahedral aluminum–transition-metal alloys.* Physical Review B, 1986. **33**(12): p. 7917.
260. Fung, K., X. Zou, and C. Yang, *Transmission electron microscopy study of Al13Fe4 tenfold twins in rapidly cooled Al–Fe alloys.* Philosophical magazine letters, 1987. **55**(1): p. 27-32.
261. Christian, J.W., *The Theory of Transformations in Metals and Alloys. I.* Equilibrium and general kinetic theory, 1975. **586**.
262. Herlach, D.M., *Solidification from undercooled melts.* Materials Science and Engineering: A, 1997. **226**: p. 348-356.
263. Kelton, K., *Quasicrystals: Structure and stability.* International materials reviews, 1993. **38**(3): p. 105-137.
264. Hasson, G., J.-Y. Boos, I. Herbeuval, M. Biscondi, and C. Goux, *Theoretical and experimental determinations of grain boundary structures and energies: Correlation with various experimental results.* Surface Science, 1972. **31**: p. 115-137.
265. Ni, C., H. Ding, M. Asta, and X. Jin, *Computational study of <11¯00> symmetric tilt grain boundaries in Mg and Ti.* Scripta Materialia, 2015. **109**: p. 94-99.
266. Wang, J., I. Beyerlein, and C. Tomé, *An atomic and probabilistic perspective on twin nucleation in Mg.* Scripta Materialia, 2010. **63**(7): p. 741-746.
267. Wang, J. and I.J. Beyerlein, *Atomic structures of symmetric tilt grain boundaries in hexagonal close packed (hcp) crystals.* Modelling and Simulation in Materials Science and Engineering, 2012. **20**(2): p. 024002.
268. Charbon, C., A. Jacot, and M. Rappaz, *3D stochastic modelling of equiaxed solidification in the presence of grain movement.* Acta metallurgica et materialia, 1994. **42**(12): p. 3953-3966.
269. Tzimas, E. and A. Zavaliangos, *Evolution of near-equiaxed microstructure in the semisolid state.* Materials Science and Engineering: A, 2000. **289**(1-2): p. 228-240.
270. Woodruff, D., *The Solid-Liquid Interface, Cambridge, Univ*. 1973, Press Londen.
271. Bai, Y., *Molecular Dynamics Simulation Study of Solid-liquid Interface Properties of Hcp Magnesium*. 2012.

Copyright permission

My Orders My Library My Profile Welcome yi.cui15@imperial.ac.uk Log out | Help

My Orders > Orders > All Orders

License Details

This Agreement between Mr. Yi Cui ("You") and Springer Nature ("Springer Nature") consists of your license details and the terms and conditions provided by Springer Nature and Copyright Clearance Center.

Print Copy

License Number	4952120509521
License date	Nov 18, 2020
Licensed Content Publisher	Springer Nature
Licensed Content Publication	Metallurgical and Materials Transactions A
Licensed Content Title	Iron-rich intermetallic phases and their role in casting defect formation in hypoeutectic Al–Si alloys
Licensed Content Author	L. Lu et al
Licensed Content Date	Dec 31, 1969
Type of Use	Thesis/Dissertation
Requestor type	academic/university or research institute
Format	print and electronic
Portion	figures/tables/illustrations
Number of figures/tables/illustrations	1
Will you be translating?	no
Circulation/distribution	1 - 29
Author of this Springer Nature content	no
Title	Solidification orientation relationships in Al and Mg alloys
Institution name	Imperial College London
Expected presentation date	Nov 2020
Portions	Figure 8(a)
Requestor Location	Mr. Yi Cui Department of Materials South Kensington Campus, Imperial College London London, other SW7 2AZ United Kingdom Attn: Mr. Yi Cui
Total	0.00 GBP

BACK

License Details

This Agreement between Mr. Yi Cui ("You") and Elsevier ("Elsevier") consists of your license details and the terms and conditions provided by Elsevier and Copyright Clearance Center.

Print Copy

License Number	4952431131558
License date	Nov 19, 2020
Licensed Content Publisher	Elsevier
Licensed Content Publication	Scripta Materialia
Licensed Content Title	As-cast morphology of iron-intermetallics in Al–Si foundry alloys
Licensed Content Author	Cameron M. Dinnis,John A. Taylor,Arne K. Dahle
Licensed Content Date	Oct 1, 2005
Licensed Content Volume	53
Licensed Content Issue	8
Licensed Content Pages	4
Type of Use	reuse in a thesis/dissertation
Portion	figures/tables/illustrations
Number of figures/tables/illustrations	1
Format	both print and electronic
Are you the author of this Elsevier article?	No
Will you be translating?	No
Title	Solidification orientation relationships in Al and Mg alloys
Institution name	Imperial College London
Expected presentation date	Nov 2020
Portions	Figure 4
Requestor Location	Mr. Yi Cui Department of Materials South Kensington Campus, Imperial College London London, other SW7 2AZ United Kingdom Attn: Mr. Yi Cui
Publisher Tax ID	GB 494 6272 12
Total	0.00 GBP

BACK

License Details

This Agreement between Mr. Yi Cui ("You") and Elsevier ("Elsevier") consists of your license details and the terms and conditions provided by Elsevier and Copyright Clearance Center.

Print Copy

License Number	4952450866505
License date	Nov 19, 2020
Licensed Content Publisher	Elsevier
Licensed Content Publication	Scripta Metallurgica
Licensed Content Title	Interfacial energies of tilt boundaries in aluminium. Experimental and theoretical determination
Licensed Content Author	G.C. Hasson,C. Goux
Licensed Content Date	Oct 1, 1971
Licensed Content Volume	5
Licensed Content Issue	10
Licensed Content Pages	6
Type of Use	reuse in a thesis/dissertation
Portion	figures/tables/illustrations
Number of figures/tables/illustrations	1
Format	both print and electronic
Are you the author of this Elsevier article?	No
Will you be translating?	No
Title	Solidification orientation relationships in Al and Mg alloys
Institution name	Imperial College London
Expected presentation date	Nov 2020
Portions	Figure 1
Requestor Location	Mr. Yi Cui Department of Materials South Kensington Campus, Imperial College London London, other SW7 2AZ United Kingdom Attn: Mr. Yi Cui
Publisher Tax ID	GB 494 6272 12
Total	0.00 GBP

BACK

License Details

This Agreement between Mr. Yi Cui ("You") and Elsevier ("Elsevier") consists of your license details and the terms and conditions provided by Elsevier and Copyright Clearance Center.

Print Copy

License Number	4952460049991
License date	Nov 19, 2020
Licensed Content Publisher	Elsevier
Licensed Content Publication	Acta Materialia
Licensed Content Title	Crystallographic study of grain refinement in aluminum alloys using the edge-to-edge matching model
Licensed Content Author	M.-X. Zhang,P.M. Kelly,M.A. Easton,J.A. Taylor
Licensed Content Date	Mar 1, 2005
Licensed Content Volume	53
Licensed Content Issue	5
Licensed Content Pages	12
Type of Use	reuse in a thesis/dissertation
Portion	figures/tables/illustrations
Number of figures/tables/illustrations	1
Format	both print and electronic
Are you the author of this Elsevier article?	No
Will you be translating?	No
Title	Solidification orientation relationships in Al and Mg alloys
Institution name	Imperial College London
Expected presentation date	Nov 2020
Portions	Figure 1
Requestor Location	Mr. Yi Cui Department of Materials South Kensington Campus, Imperial College London London, other SW7 2AZ United Kingdom Attn: Mr. Yi Cui
Publisher Tax ID	GB 494 6272 12
Total	0.00 GBP

BACK

License Details

This Agreement between Mr. Yi Cui ("You") and Elsevier ("Elsevier") consists of your license details and the terms and conditions provided by Elsevier and Copyright Clearance Center.

Print Copy

License Number	4952460339335
License date	Nov 19, 2020
Licensed Content Publisher	Elsevier
Licensed Content Publication	Acta Materialia
Licensed Content Title	Icosahedral quasicrystal-enhanced nucleation of the fcc phase in liquid gold alloys
Licensed Content Author	Güven Kurtuldu,Alberto Sicco,Michel Rappaz
Licensed Content Date	May 15, 2014
Licensed Content Volume	70
Licensed Content Issue	n/a
Licensed Content Pages	9
Type of Use	reuse in a thesis/dissertation
Portion	figures/tables/illustrations
Number of figures/tables/illustrations	2
Format	both print and electronic
Are you the author of this Elsevier article?	No
Will you be translating?	No
Title	Solidification orientation relationships in Al and Mg alloys
Institution name	Imperial College London
Expected presentation date	Nov 2020
Portions	Figure 1, Figure 8
Requestor Location	Mr. Yi Cui Department of Materials South Kensington Campus, Imperial College London London, other SW7 2AZ United Kingdom Attn: Mr. Yi Cui
Publisher Tax ID	GB 494 6272 12
Total	**0.00 USD**

BACK

License Details

This Agreement between Mr. Yi Cui ("You") and Elsevier ("Elsevier") consists of your license details and the terms and conditions provided by Elsevier and Copyright Clearance Center.

Print Copy

License Number	4952461318551
License date	Nov 19, 2020
Licensed Content Publisher	Elsevier
Licensed Content Publication	Acta Materialia
Licensed Content Title	A granular model of equiaxed mushy zones: Formation of a coherent solid and localization of feeding
Licensed Content Author	Stéphane Vernède,Philippe Jarry,Michel Rappaz
Licensed Content Date	Sep 1, 2006
Licensed Content Volume	54
Licensed Content Issue	15
Licensed Content Pages	12
Type of Use	reuse in a thesis/dissertation
Portion	figures/tables/illustrations
Number of figures/tables/illustrations	1
Format	both print and electronic
Are you the author of this Elsevier article?	No
Will you be translating?	No
Title	Solidification orientation relationships in Al and Mg alloys
Institution name	Imperial College London
Expected presentation date	Nov 2020
Portions	Figure 4
Requestor Location	Mr. Yi Cui Department of Materials South Kensington Campus, Imperial College London London, other SW7 2AZ United Kingdom Attn: Mr. Yi Cui
Publisher Tax ID	GB 494 6272 12
Total	**0.00 GBP**

BACK

License Details

This Agreement between Mr. Yi Cui ("You") and Elsevier ("Elsevier") consists of your license details and the terms and conditions provided by Elsevier and Copyright Clearance Center.

Print Copy

License Number	4952470215226
License date	Nov 19, 2020
Licensed Content Publisher	Elsevier
Licensed Content Publication	Journal of Alloys and Compounds
Licensed Content Title	Investigating the morphological effects of solute on the β-phase in as-cast titanium alloys
Licensed Content Author	S.N. Tedman-Jones,S.D. McDonald,M.J. Bermingham,D.H. StJohn,M.S. Dargusch
Licensed Content Date	Mar 25, 2019
Licensed Content Volume	778
Licensed Content Issue	n/a
Licensed Content Pages	11
Type of Use	reuse in a thesis/dissertation
Portion	figures/tables/illustrations
Number of figures/tables/illustrations	2
Format	both print and electronic
Are you the author of this Elsevier article?	No
Will you be translating?	No
Title	Solidification orientation relationships in Al and Mg alloys
Institution name	Imperial College London
Expected presentation date	Nov 2020
Portions	Figure 2, Figure 12
Requestor Location	Mr. Yi Cui Department of Materials South Kensington Campus, Imperial College London London, other SW7 2AZ United Kingdom Attn: Mr. Yi Cui
Publisher Tax ID	GB 494 6272 12
Total	**0.00 GBP**

BACK

Copyright Clearance Center Marketplace™

Order Number: 1078519
Order Date: 19 Nov 2020

Payment Information

Yi Cui
yi.cui15@imperial.ac.uk
Payment method: Invoice

Billing Address:
Mr. Yi Cui
Department of Materials
South Kensington Campus, Imperial College London
London, SW7 2AZ
United Kingdom

+44 7907908204
yi.cui15@imperial.ac.uk

Customer Location:
Mr. Yi Cui
Department of Materials
South Kensington Campus, Imperial College London
London, SW7 2AZ
United Kingdom

Order Details

1. Modelling and Simulation in Materials Science and Engineering

Billing Status: Open

Order license ID	1078519-1
Order detail status	Completed
ISSN	0965-0393
Type of use	Republish in a thesis/dissertation
Publisher	IOP Publishing
Portion	Image/photo/illustration

0.00 GBP
Republication Permission

LICENSED CONTENT

Publication Title	Modelling and Simulation in Materials Science and Engineering	**Country**	United Kingdom of Great Britain and Northern Ireland
Author/Editor	Institute of Physics (Great Britain)	**Rightsholder**	IOP Publishing, Ltd
		Publication Type	Journal
Date	01/01/1992		
Language	English		

REQUEST DETAILS

Portion Type	Image/photo/illustration	**Distribution**	Worldwide
		Translation	Original language of publication
Number of images / photos / illustrations	1		
		Copies for the disabled?	No
Format (select all that apply)	Print,Electronic		
		Minor editing privileges?	No
Who will republish the content?	Academic institution		
		Incidental promotional use?	No

License Details

This Agreement between Mr. Yi Cui ("You") and Elsevier ("Elsevier") consists of your license details and the terms and conditions provided by Elsevier and Copyright Clearance Center.

Print Copy

License Number	4952520473931
License date	Nov 19, 2020
Licensed Content Publisher	Elsevier
Licensed Content Publication	Scripta Materialia
Licensed Content Title	Grain boundary planes: New dimensions in the grain boundary character distribution
Licensed Content Author	Chang-Soo Kim,Anthony D. Rollett,Gregory S. Rohrer
Licensed Content Date	Mar 1, 2006
Licensed Content Volume	54
Licensed Content Issue	6
Licensed Content Pages	5
Type of Use	reuse in a thesis/dissertation
Portion	figures/tables/illustrations
Number of figures/tables/illustrations	1
Format	both print and electronic
Are you the author of this Elsevier article?	No
Will you be translating?	No
Title	Solidification orientation relationships in Al and Mg alloys
Institution name	Imperial College London
Expected presentation date	Nov 2020
Portions	Figure 1
Requestor Location	Mr. Yi Cui Department of Materials South Kensington Campus, Imperial College London London, other SW7 2AZ United Kingdom Attn: Mr. Yi Cui
Publisher Tax ID	GB 494 6272 12
Total	0.00 GBP

BACK

License Details

This Agreement between Mr. Yi Cui ("You") and Springer Nature ("Springer Nature") consists of your license details and the terms and conditions provided by Springer Nature and Copyright Clearance Center.

Print Copy

License Number	4952520748182
License date	Nov 19, 2020
Licensed Content Publisher	Springer Nature
Licensed Content Publication	Contributions to Mineralogy and Petrology
Licensed Content Title	The most frequent interfaces in olivine aggregates: the GBCD and its importance for grain boundary related processes
Licensed Content Author	Katharina Marquardt et al
Licensed Content Date	Oct 14, 2015
Type of Use	Thesis/Dissertation
Requestor type	academic/university or research institute
Format	print and electronic
Portion	figures/tables/illustrations
Number of figures/tables/illustrations	1
Will you be translating?	no
Circulation/distribution	1 - 29
Author of this Springer Nature content	no
Title	Solidification orientation relationships in Al and Mg alloys
Institution name	Imperial College London
Expected presentation date	Nov 2020
Portions	Figure 1
Requestor Location	Mr. Yi Cui Department of Materials South Kensington Campus, Imperial College London London, other SW7 2AZ United Kingdom Attn: Mr. Yi Cui
Total	0.00 GBP

BACK

License Details

This Agreement between Mr. Yi Cui ("You") and Elsevier ("Elsevier") consists of your license details and the terms and conditions provided by Elsevier and Copyright Clearance Center.

Print Copy

License Number	4952521194138
License date	Nov 19, 2020
Licensed Content Publisher	Elsevier
Licensed Content Publication	Acta Materialia
Licensed Content Title	Distribution of grain boundaries in aluminum as a function of five macroscopic parameters
Licensed Content Author	David M Saylor,Bassem S El Dasher,Anthony D Rollett,Gregory S Rohrer
Licensed Content Date	Jul 12, 2004
Licensed Content Volume	52
Licensed Content Issue	12
Licensed Content Pages	7
Type of Use	reuse in a thesis/dissertation
Portion	figures/tables/illustrations
Number of figures/tables/illustrations	3
Format	both print and electronic
Are you the author of this Elsevier article?	No
Will you be translating?	No
Title	Solidification orientation relationships in Al and Mg alloys
Institution name	Imperial College London
Expected presentation date	Nov 2020
Portions	Figure 2, Figure 3, Figure 4
Requestor Location	Mr. Yi Cui Department of Materials South Kensington Campus, Imperial College London London, other SW7 2AZ United Kingdom Attn: Mr. Yi Cui
Publisher Tax ID	GB 494 6272 12
Total	0.00 GBP

BACK

License Details

This Agreement between Mr. Yi Cui ("You") and Elsevier ("Elsevier") consists of your license details and the terms and conditions provided by Elsevier and Copyright Clearance Center.

Print Copy

License Number	4952551143230
License date	Nov 19, 2020
Licensed Content Publisher	Elsevier
Licensed Content Publication	Materials Letters
Licensed Content Title	Effect of Fe on grain refining of pure aluminum refined by Al5TiB master alloy
Licensed Content Author	Yijie Zhang,Haowei Wang,Naiheng Ma,Xianfeng Li
Licensed Content Date	Nov 1, 2005
Licensed Content Volume	59
Licensed Content Issue	27
Licensed Content Pages	4
Type of Use	reuse in a thesis/dissertation
Portion	figures/tables/illustrations
Number of figures/tables/illustrations	1
Format	both print and electronic
Are you the author of this Elsevier article?	No
Will you be translating?	No
Title	Solidification orientation relationships in Al and Mg alloys
Institution name	Imperial College London
Expected presentation date	Nov 2020
Portions	Figure 1
Requestor Location	Mr. Yi Cui Department of Materials South Kensington Campus, Imperial College London London, other SW7 2AZ United Kingdom Attn: Mr. Yi Cui
Publisher Tax ID	GB 494 6272 12
Total	0.00 GBP

BACK